Interfacial Thermodynamics of Liquid Crystals: Applications to Capillary Instabilities

Ae-Gyeong Cheong

Department of Chemical Engineering

McGill University, Montreal

April 2004

A thesis submitted to the Faculty of Graduate and Postdoctoral Studies
in partial fulfillment of the requirements for the degree of Doctor of Philosophy

Your file Votre référence
ISBN: 0-612-98226-2
Our file Notre référence
ISBN: 0-612-98226-2

To my mother,

a woman of great faith and perseverance

Foreword

The present author chooses the manuscript-based thesis option according to the Guidelines for Thesis Preparation given by the Faculty of Graduate Studies and Research. The following is excerpts from the Guidelines for Thesis Preparation:

Candidates have the option of including, as part of the thesis, the text of papers submitted, or to be submitted, for publication, or the clearly-duplicated text (not the reprints) of one or more published papers. These texts must be bound together as an integral part of the thesis. (Reprints of published papers can be included in the appendices at the end of the thesis.)

In general, when co-authored papers are included in a thesis the candidate must have made a substantial contribution to all papers included in the thesis. In addition, the candidate is required to make an explicit statement in the thesis as to who contributed to such work and to what extent. This statement should appear in a single section entitled "Contributions of Authors" as a preface to the thesis. The supervisor must attest to the accuracy of this statement at the doctoral oral defence. Since the task of the examiners is made more difficult in these cases, it is in the candidate's interest to clearly specify the responsibilities of all the authors of the co-authored papers.

When previously published copyright material is presented in a thesis, the candidate must include signed waivers from the publishers and submit these to the Graduate and Postdoctoral Studies Office with the final deposition, if not submitted previously. The candidate must also include signed waivers from any co-authors of unpublished manuscripts.

Contributions of Authors

Contents of chapters 2 to 5 of the present thesis are adopted or revised from the papers that have been published or submitted for publication in scientific journals under the normal supervision of my research supervisor, Professor A. D. Rey, who is also a co-author. In chapter 3, Professor P. T. Mather pursued experimental verification of non-axisymmetric capillary instability using rheological microscopy methods, and he is a co-author of the corresponding paper.

I, Alejandro D. Rey, hereby give copyright clearance of the following papers, of which I am a co-author, in the doctoral thesis of Ae-Gyeong Cheong.

- Chapter 2: A.-G. Cheong and A. D. Rey, *Cahn-Hoffman capillarity vector thermodynamics for liquid crystal interfaces*, Physical Review E **66**, 021704 (2002).
- Chapter 2: A.-G. Cheong and A. D. Rey, *Cahn-Hoffman capillarity vector thermodynamics for curved liquid crystal interfaces with applications to fiber instabilities*, Journal of Chemical Physics **117**, 5062-5071 (2002).
- Chapter 3: A.-G. Cheong, A. D. Rey, and P. T. Mather, *Capillary instabilities in thin nematic liquid crystalline fibers*, Physical Review E **64**, 041701 (2001).
- Chapter 3: A.-G. Cheong and A. D. Rey, *Capillary instabilities in a thin nematic liquid crystalline fiber embedded in a viscous matrix*, Continuum Mechanics and Thermodynamics **14**, 263-279 (2002).
- Chapter 4: A.-G. Cheong and A. D. Rey, *Temperature effects on capillary instabilities in a thin nematic liquid crystalline fiber embedded in a viscous matrix*, European Physical Journal E **9**, 171-193 (2002).
- Chapter 5: A.-G. Cheong and A. D. Rey, *Texture dependence of capillary instabilities in nematic liquid crystalline fibers*, accepted in Liquid Crystals (2004).

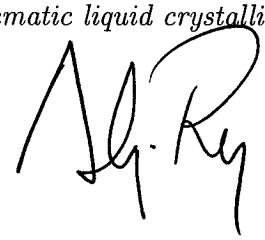

Alejandro D. Rey

James McGill Professor

Department of Chemical Engineering

McGill University

Montreal, Quebec, Canada

Dear Ae-Gyeong Cheong:

Thank you for requesting permission to reproduce material from American Institute of Physics publications.

Permission is granted for the following material:

Ae-Gyeong Cheong and Alejandro D. Rey, *Cahn-Hoffman capillarity vector thermodynamics for curved liquid crystal interfaces with applications to fiber instabilities*, J. Chem. Phys. **117**, 5062 (2002)

to be used as part of your Ph.D. thesis.

Full credit to the original publication must appear in the new use.

Thank you.

Sincerely,

Susann Brailey

~~~~~~~~~~~~

Office of the Publisher, Journals and Technical Publications

Rights & Permissions

American Institute of Physics

Suite 1NO1

2 Huntington Quadrangle

Melville, NY 11747-4502

516-576-2268 TEL

516-576-2450 FAX

rights@aip.org
~~~~~~~~~~~~

Dear Ae-Gyeong Cheong,

We are pleased to grant you the permission requested for

Ae-Gyeong Cheong and Alejandro D. Rey, *Capillary instabilities in a thin nematic liquid crystalline fiber embedded in a viscous matrix*, Cont. Mech. Therm. **14**, 263 (2002),

provided full credit (Springer journal title, article title, name(s) of author(s), volume, page, figure number(s), year of publication, Springer copyright notice) is given to the publication in which the material was originally published.

With kind regards,

Rosita Sturm (Ms.)

****

Rights & Permissions

Springer-Verlag GmbH & Co. KG

Tiergartenstrasse 17

69121 Heidelberg

GERMANY

Tel: ++ 49 (0) 6221 - 487 8228

Fax: ++ 49 (0) 6221 - 487 8100

e-mail: Sturm@springer.de

internet: www.springer.de/rights

Abstract

Most current applications and uses of liquid crystalline materials involve surfaces and interfaces. Prominent examples are high performance carbonaceous mesophase fibers, liquid crystal polymer fibers, and thermoplastic/liquid crystal polymer in-situ composites. Fundamental surface science and engineering principles are needed to optimize and design fibers and composites derived from liquid crystalline precursors. Currently non-equilibrium liquid crystal surface phenomena are not well understood. Force balance equations describing static and dynamical interfacial phenomena are available but have not been adequately used to describe the mechanics of fiber and film microstructures.

This thesis explores the mechanics and stability of nematic liquid crystalline fibers embedded in inviscid and viscous matrices. A new theoretical framework for liquid crystal surface mechanics is formulated and used to model pattern formation and instability driven processes in fibers and fibrillar composites and blends. The liquid crystal *Herring's formula* and *Laplace equation* are derived and the role of liquid crystallinity is elucidated. In order to systematically analyze the role of the fundamental processes, linear stability analyses of capillary instabilities in nematic liquid crystalline fibers are performed by formulating and solving the governing nemato-capillary equations. An essential characteristic of liquid crystals, in contrast to isotropic liquids, is their mechanical anisotropy. Thus, the main parameters affecting the capillary instabilities are the isotropic and anisotropic surface tensions, the anisotropic viscosities, the bulk orientational elasticity, the isotropic viscosity of the matrix, and the surface bending modulus. Two asymptotic regimes are investigated: (a) the thin-fiber regime characterized by homogeneous bulk orientation and storage of surface elasticity, and (b) the thick-fiber regime characterized by bulk orientation distortions without surface elastic storage. Novel capillary instability mechanisms and symmetries of the instability modes for a nematic fiber embedded in a matrix are characterized. The predicted ability of capillary instabilities in nematic fibers to produce surface structures of well-defined symmetry and length scales, as well as chiral microstructures, is an important result that augments the pathways for targeted pattern formation. Deviations from classical Rayleigh capillary instabilities are identified and quantified in terms of liquid crystalline order.

Résumé

La plupart des applications et utilisations courantes des matériaux cristallins liquides impliquent des surfaces et des interfaces. D'importants exemples sont les fibres carbonées à hautes performances issues de mésophase, les fibres en polymère cristallin liquide, et les composés de polymère thermoplastique/cristallin liquide in-situ. Les principes fondamentaux de la science et de l'ingénierie des surfaces sont nécessaires pour optimiser et concevoir des fibres et des composés dérivés de précurseurs cristallins liquides. Actuellement les phénomènes surfaciques des cristaux liquides en déséquilibre ne sont pas bien compris. Les équations d'équilibre de force décrivant les phénomènes statiques et dynamiques sont disponibles mais n'ont pas été jusque ici employées de façon appropriée pour décrire la mécanique de microstructure des films et des fibres.

Cette thèse explore les mécanismes et la stabilité des fibres cristallines liquides nématiques incorporées dans les matrices non visqueuses et visqueuses. Un nouveau cadre théorique pour la mécanique de surface des cristaux liquides est formulé et employé pour modéliser les patterns de formation et les procédés conduits par les instabilités dans les fibres, les composés fibrillaires et les mélanges. *La formule d'Herring* pour cristaux liquides et *l'équation de Laplace* sont dérivées et le rôle de la cristallinité liquide est élucidé. Afin d'analyser systématiquement le rôle des procédés fondamentaux, des analyses linéaires de stabilité des instabilités capillaires, dans les fibres cristallines liquides nématiques, sont effectuées en formulant et en résolvant les équations de nemato-capillarité. Une caractéristique essentielle des cristaux liquides, contrairement aux liquides isotropes, est leur anisotropie mécanique. Ainsi, les principaux paramètres affectant les instabilités capillaires sont les tensions superficielles isotropes et anisotropes, les viscosités anisotropes, l'élasticité orientationelle intérieure, la viscosité isotrope de la matrice, et le module de recourbement surfacique. Deux régimes asymptotiques sont étudiés : (a) le régime de fibre mince caractérisé par une orientation interne homogène et un stockage d'élasticité surfacique, et (b) le régime de fibre épaisse caractérisé par des déformations de l'orientation interne sans stockage élastique de surface. De nouveaux mécanismes d'instabilité capillaires pour une fibre nématique incorporée dans une matrice sont caractérisés. La capacité prévue des instabilités capillaires dans les fibres nématiques de produire des structures surfaciques de symétrie et de dimensions bien définies, ainsi que des microstructures chirales, est un résultat important qui

augmente les voies pour la génération visée de pattern de formation. Des déviations depuis les instabilités capillaires classiques de Rayleigh sont identifiées et mesurées en termes de l'ordre cristallin liquide.

Acknowledgements

I am delighted for this opportunity to acknowledge all the people who have showed their support in many different ways during the continuously demanding time of my Ph.D. study.

My heartfelt thanks are due to my research supervisor, Professor Alejandro D. Rey, of immense knowledge, scholarly conscience, and fairness, for his constant research guidance from which I have been academically and ethically shaped as a researcher knowledgeable in a fascinating research field as well as responsible for processes and results of my research.

I would like to thank my colleagues in the research group, who have diverse national and research backgrounds, for I have enjoyed multicultural conversations in our get-togethers as well as discussions on a variety of exciting research topics through our group seminars. I would especially like to thank Gino who kindly translated the thesis abstract into French, and Benjamin who read the first and last chapters and pointed out potential improvements.

I am also thankful for the financial support from McGill Major Fellowship for three years.

I would like to express my gratitude to Barbara and Professor Rey for occasionally inviting all our group members to wonderful dinners and providing a cozy atmosphere with interesting conversations.

I am grateful to my Korean friends who have studied as graduate students for years together in Montreal. We shared our experiences at school and exchanged ideas about living in a foreign country while celebrating many memorable occasions. I became more objectively aware of cons and pros of Korean society and, at the same time, more appreciating Korean cultural heritage.

I would also like to thank my friends in the church circle, who are devoted Catholics by living out their faith and have listened to me patiently. I am sincerely grateful to Fr. Eric for cheering me up by his spiritual guidance with deep understanding of my difficulties, to Jeanne and Sr. Madeleine for always remembering and inviting me with their warmth, care, and thoughtful generosity, and to Mary Grace for constantly encouraging me during the slow process of preparing the thesis manuscript.

Most of all, I thank my family members and relatives for their whole-hearted support: Deepest gratitude to my mother who is always behind me, patiently waiting and praying for me, to my brother's family who enabled me to study abroad by willingly taking all the responsibility in Korea, and to my aunt and cousin with whom I have often talked about the way of faith.

Contents

List of Tables

List of Figures

Chapter 1

General Introduction

1.1 Thesis Motivation

Surfaces and interfaces involving liquid crystalline materials play a fundamental role in a wide variety of applications, and hence understanding liquid crystal surface physics is crucial. An essential characteristic of liquid crystals (LCs), in contrast to isotropic liquids, is their mechanical anisotropy [1]. Thus, this thesis explores the effects of the anisotropic characteristic of liquid crystals on interfacial phenomena, specifically on capillary instabilities of liquid crystalline fibers and fibrillar composites.

1.1.1 Anisotropic properties of liquid crystals

LCs flow like a liquid but possess orientational order like a solid. The orientational order at least in one dimension causes some degree of anisotropy in the mechanical and symmetry properties of LCs. Hence, the anisotropic viscosity and elasticity of LCs are measured for relative molecular orientations. The anisotropies in the viscoelastic bulk properties of LCs are well understood theoretically [2, 3] and experimentally [1], and the anisotropies in the surface elastic properties of LCs are also well-characterized [4, 5]. It is known that the surface tension of LCs contains anisotropic contributions [6, 7, 8] known as ordering and anchoring energies [1, 4, 5] as well as an isotropic contribution.

1.1.2 Surfaces and interfaces in liquid crystal applications

The current wide use of liquid crystal thin fibers, films, foams and multiphase material systems demands a fundamental understanding of capillary hydrodynamics, interfacial thermodynamics, and interfacial transport phenomena [9, 10, 11]. In addition, many new LC applications which have dominant interfacial effects, such as mesophase fiber spinning [12] and the formation of in-situ liquid crystalline polymer (LCP) composites [13], likewise require a fundamental understanding of capillary hydrodynamics. The following examples are LC applications where surfaces/interfaces are important because of the large surface to volume ratio: polymer-dispersed LCs and liquid crystal displays (LCDs), LC fibers and films, and LC lubricants and surfactants.

Electro-optic applications of liquid crystals

Electro-optic applications of LCs are based on the fact that low voltages can orient LCs [14, 15, 16]. For example, the twisted nematic display (TND) takes advantage of the Frederiks transition of a confined nematic LC cell between crossed polarizers [15, 16]. In the absence of an electric field, a parallel alignment of the LC on the cell plates causes LC to twist 90° from one plate to another, which results in incoming polarized light to travel through the 90° twisted LC and to get through the second polarizer. The presence of an electric field with its voltage above the threshold Frederiks transition value changes the alignment of the LC to be parallel to the applied electric field rather than the cell plates, so that the polarized light is blocked by the second polarizer. When the alignment of the LC with the plates relies on surface treatment, designing surfaces is important as it leads to many new LC applications. Another example of an electro-optic LC application is the polymer-dispersed liquid crystal (PDLC) display, in which micron- or submicron-size LC droplets are dispersed in a rigid polymer matrix [14, 15]. Without the external electric field, the bipolar texture inside the droplets scatters light intensely due to lack of LC alignment. By applying an electric field across the PDLC film, using an LC with a refractive index that matches that of the polymer matrix, the film becomes transparent because the bipolar texture inside the droplets is replaced by a fully aligned LC. Again, since the PDLC system has a large surface to volume ratio, the surface boundary effects of the droplets are inevitably important.

Liquid crystalline fibers

Fiber spinning and in-situ composites are involved in forming LC fibrillar structures. For LCP solutions, fibers with high mechanical properties, such as Kevlar, are spun by wet or dry spinning [17]. Carbon fibers can be produced by melt spinning of mesophase pitch since molecules inside the pitch filaments are well aligned through the melt spinning process [18]. A processing window depending on spinning conditions exists to form unbroken filaments. For instance, by controlling spinning temperature, the filaments at a high temperature may break up into droplets in the spinneret while fractures of the filaments occur at a low temperature due to high tensile strength in the threadline. In natural systems, spider silk is a focus of current interest because of not only its outstanding mechanical properties but also ambient spinning conditions [19]. The silk proteins solution to be spun is liquid crystalline, and the formation of the fibrillar structure of the proteins during silk processing is essential to obtain high-performance silk [20]. Meanwhile, in-situ composites consist of a thermoplastic (polymer) matrix and LC reinforcing fibers that are formed from LCP droplets during processing [21]. Since the mechanical properties of the composites, such as polypropylene/Vectra, strongly depend on the fibrillar morphology of LCP [21], a fundamental understanding of the mechanism of LCP fiber instability in a polymer matrix during processing is required.

Liquid crystalline foams and films

Carbonaceous mesophase foams are suitable for foam-core sandwich structures in thermal management applications owing to their high thermal conductivity and low weight [22]. The carbon foams provide an interconnected network of graphitic ligaments which are highly oriented during a foam forming process, and hence result in a specific conductivity up to six times greater than that of copper [22]. Freely suspended liquid crystalline (FSLC) films also show pronounced surface effects because of the long-range orientational molecular order in thin films with a thickness ranging from several hundred $\AA$ to several tens of μm [23]. The problems of film stability are important, e.g., for production of various foams and emulsions in the chemical and cosmetics industries [23].

Liquid crystalline lubricants and biomembranes

LCs are also used as lubricants and lubricant additives in petroleum-based and synthetic oils, e.g., siloxanes, and a simulating lubricant of a natural synovial fluid of living joints [24]. Addition of LCs considerably increases the lubricity of lubricants due to the formation of LC layers on friction surfaces [24]. In living cells, surfaces are dominating and consist of self-assembled lipid bilayers to which proteins and other components are bound [16, 25]. The bilayer biomembranes in the LC state, due to their fluidity, are permeable to water-soluble molecules while the membranes are not permeable in the gel state that is solid-like [25]. Therefore, controlling gel-to-LC phase transition is important to determine the properties of biomembranes.

Among the examples given above, this thesis focuses on LC fibers and fibrillar composites.

1.2 Classification of Liquid Crystals

Most materials exhibit three distinct phases according to the surrounding temperature and pressure: (i) solid crystalline, (ii) liquid, and (iii) gaseous. The degree of order in the material distinguishes one state of matter from another. Certain organic materials possess more condensed phases intermediate between the solid and liquid states called mesophases. These mesophases can be orientationally or conformationally disordered crystals, plastic crystals, or liquid crystalline phases [26]. If LC phases are formed in pure materials by heating from their solid states or by cooling from their isotropic liquid states, the materials are referred to as thermotropic LCs. If LC phases are induced by a solvent and hence by changes in concentration in a certain temperature interval, the materials are referred to as lyotropic LCs [15, 16, 27, 28].

Materials which can exist in LC phases are called mesogens. They are composed of rod-like, disc-shaped, or banana-shaped molecules, and are called calamitic, discotic, and banana LCs, respectively [26]. Figure 1-1 shows examples of calamitic (a-c), banana (d), and discotic (e) mesogens: (a) 4-*n*-4′-pentyl-4-cyanobiphenyl (5CB), (b) *p*-azoxyanisole (PAA), (c) N-(*p*-methoxybenzylidene)-*p*-butylaniline (MBBA), (d) 2-nitro-1-3-phenylene bis[4-(4-*n*-alkyloxyphenyliminomethyl)benzoates] and (e) hexa-heptyloxybenzoate.

Thermotropic LCs are usually formed by calamitic and discotic mesogens. Figure 1-2 shows a schematic of the crystal, liquid crystal, and liquid phases. Solid crystals possess long-range,

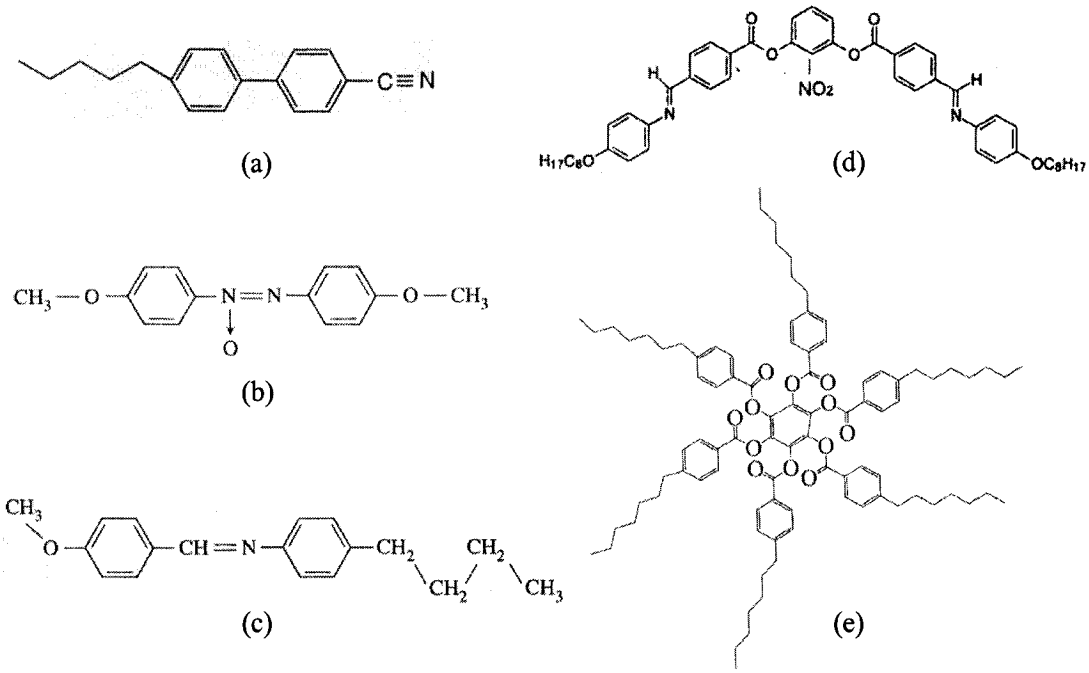

Figure 1-1: Examples of calamitic (a-c), banana (d), and discotic (e) mesogens.

three-dimensional, positional order, whereas isotropic liquids possess neither positional nor orientational order. For rod-like molecules, a preferred orientation of molecules, called the director, is shown as **n** for the LC phase. Exhibiting order intermediate between crystalline and liquid phases, thermotropic LCs are further classified into three main types: nematics, cholesterics, and smectics. Figure 1-3 shows schematic diagrams of calamitic nematic (a), cholesteric (b), and smectic-A and -C (c), and discotic nematic (d) and columnar (e) LC phases [15, 17]. As seen in figure 1-3(a), nematics are least ordered since they have orientational order but no positional order, i.e., molecules are only aligned in a preferred direction known as the director. Twisted nematic devices are used extensively in liquid crystal displays (LCDs) for watches, pocket calculators, car dashboards, and mobile phones. Figure 1-3(b) shows that cholesterics, often called chiral nematics, are similar to nematics on a local scale, but here the average molecular orientation (director) denoted by small arrows in the figure tends to form a helix in space, with a well-defined pitch. This helical distortion is due to the presence of a chiral centre in the molecule, and thus exhibits left- or right-handedness. The pitch of the

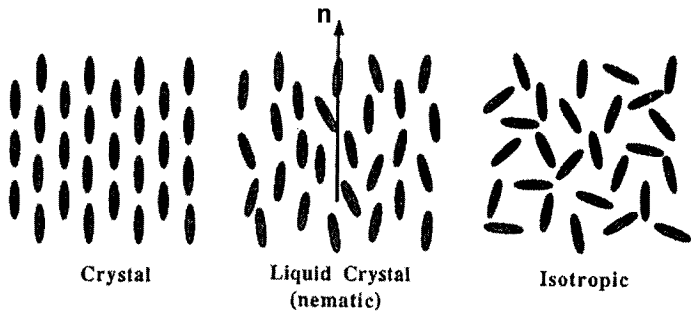

Figure 1-2: Schematic of the crystal, liquid crystal, and liquid phases. For rod-like molecules, a preferred orientation of molecules is shown as **n** in the liquid crystalline phase.

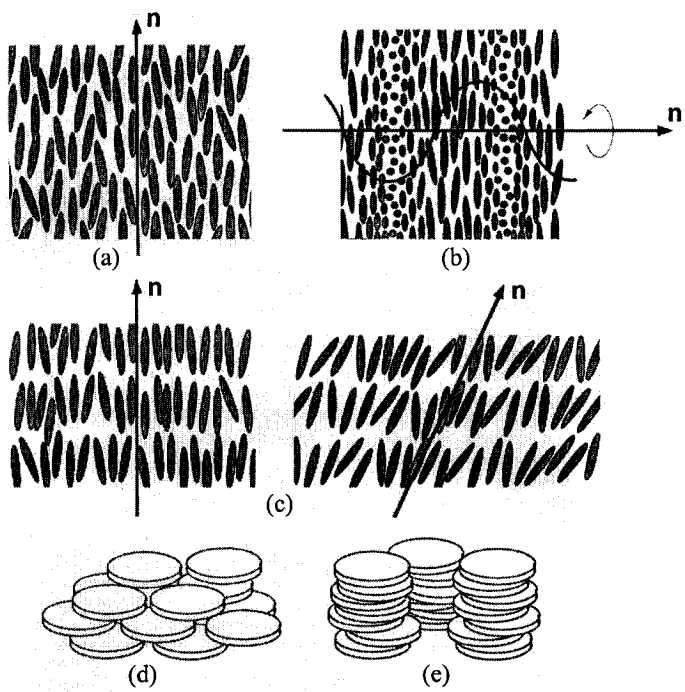

Figure 1-3: Schematic diagrams of calamitic (a-c) and discotic (d-e) liquid crystals: (a, d) nematic, (b) cholesteric, (c) smectic-A and -C, and (e) columnar phases.

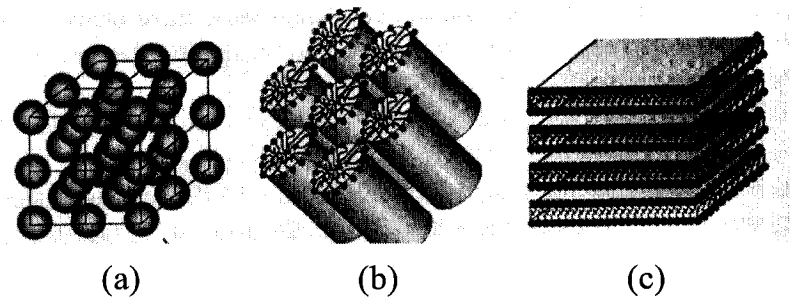

Figure 1-4: Lyotropic liquid crystalline phases: (a) cubic, (b) hexagonal, and (c) lamellar.

helix is often of the same order as the wavelength of light, which allows for the cholesterics' striking optical display effects. Unlike nematics, smectics possess long-range one-dimensional positional order as well as long-range orientational order. As seen in figure 1-3(c), the molecules are segregated into layers, and the layer spacing is of the same order as the molecular length. Two common types of smectics are smectics A, in which the director is parallel to the layer normal, and smectics C, in which the director is tilted away from the layer normal. Figure 1-3(d) shows that discotic LCs also form a nematic phase in which the director is perpendicular to the molecular plane. As shown in figure 1-3(e), when discotic molecules are stacked on top of one another to form columns, a columnar phase possessing two-dimensional positional order as well as orientational order is formed.

Lyotropic LCs are formed in solutions of amphiphilic molecules such as soaps, detergents, and phospholipids. Soap molecules in aqueous solution, for instance, tend to self-assemble to form spherical or cylindrical micelles, bilayers, and vesicles. As the concentration of amphiphile increases, a cubic phase formed by spherical micelles, a hexagonal phase formed by cylindrical micelles, and a lamellar phase formed by bilayers can be obtained sequentially [16]. Figure 1-4 shows lyotropic LC phases: cubic (a), hexagonal (b), and lamellar (c) [16].

This thesis focuses on LCs of nematic rod-like molecules since this simplest and least ordered LC phase shows all of the interesting effects that are due to its anisotropic properties. In the following section, the anisotropic mechanical properties of nematics are explained.

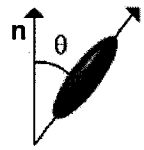

Figure 1-5: A rod-like molecule makes an angle θ with the director $\mathbf{n}$.

1.3 Mechanical Properties of Nematic Liquid Crystals

1.3.1 Scalar order parameter

For nematic LCs of rod-like molecules, the average molecular orientation denoted by director $\mathbf{n}$ does not represent the degree of alignment of LC molecules. Instead, the degree of alignment can be measured by introducing a distribution function $f(\theta)$ by which the angular distribution of the rod-like molecules around the preferred direction $\mathbf{n}$ is expressed. Figure 1-5 shows a rod-like molecule making an angle θ with the director $\mathbf{n}$. More conveniently, since the directions $\mathbf{n}$ and $-\mathbf{n}$ are indistinguishable, the degree of alignment is defined by the scalar order parameter S, which was first introduced by Tsvetkov, as [29, 30]

$$S = \frac{1}{2}\left\langle 3\cos^2\theta - 1\right\rangle = 2\pi \int_0^{\pi} \frac{1}{2}\left(3\cos^2\theta - 1\right) f(\theta)\sin\theta d\theta \ , \tag{1.1}$$

where θ is the angle between the long molecular axis and the director, and the angular brackets denote a statistical average over all molecular orientations. In an isotropic liquid, $S = 0$ due to random orientations of molecules, while $S = 1$ for a perfect crystal since $\theta = 0$. In the nematic phase, S has an intermediate value which is strongly dependent on temperature because of kinetic molecular motion; typically $0.3 < S < 0.9$ [15]. Figure 1-6 shows the order parameter S as a function of temperature [15]. There is a weak first-order phase transition at the nematic-isotropic point T_{NI} above which the long-range orientational order vanishes.

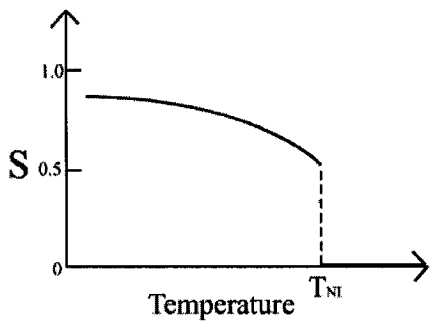

Figure 1-6: Order parameter S as a function of temperature. Above the nematic-isotropic point T_{NI}, the long-range orientational order vanishes.

1.3.2 Bulk anisotropy

Frank orientational distortion elasticity

When a stress is applied to a nematic LC, the long-range order of the LC can be distorted, which causes an increase in the elastic energy of the LC. However, if the long-range order of the LC is not distorted by the stress, e.g., under a simple shear, there is no increase in elastic energy but flow occurs [16]. Therefore, a mechanical characteristic of nematic LCs is their viscoelasticity, which is anisotropic.

Long-range orientational distortions can be described using a tensor order parameter $\mathbf{Q}$ that is symmetric and traceless [1]. In a weakly distorted system, nematic LCs are considered as uniaxial in which the degree of molecular alignment S remains unchanged while the orientation of the director $\mathbf{n}$ gradually changes. The tensor order parameter is given in the uniaxial nematic state by

$$\mathbf{Q} = S(T)\left(\mathbf{nn} - \frac{1}{3}\mathbf{I}\right), \tag{1.2}$$

where $\mathbf{I}$ is the unit tensor. The distortion is then described in terms of the space gradients of $\mathbf{n}$, and the elastic distortion free-energy density is expressed with three elastic constants:

$$F_d = \frac{1}{2}K_1\left(\nabla\cdot\mathbf{n}\right)^2 + \frac{1}{2}K_2\left[\mathbf{n}\cdot\left(\nabla\times\mathbf{n}\right)\right]^2 + \frac{1}{2}K_3\left[\mathbf{n}\times\left(\nabla\times\mathbf{n}\right)\right]^2, \tag{1.3}$$

where F_d is the Frank distortion free energy density and $\{K_i\}$, $i = 1, 2, 3$, are the Frank elastic

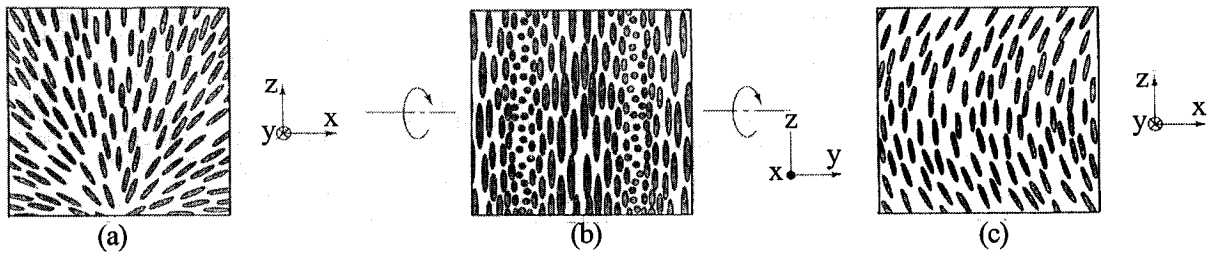

Figure 1-7: Three types of distortion in nematic liquid crystals. The director distortion is in the x-direction as (a) splay, (b) twist, and (c) bend.

constants corresponding to splay, twist, and bend distortions, respectively. Figure 1-7 shows the three types of distortion in nematic LCs. The director distortion is in the x-direction as (a) splay, $(\partial n_x/\partial x)$; (b) twist, $(\partial n_x/\partial y)$; and (c) bend, $(\partial n_x/\partial z)$ [17]. For typical low molecular-weight rod-like LCs such as PAA, MBBA, and 5CB (see figure 1-1), the elastic constants are of order $10^{-7} \sim 10^{-6} dyne$, and the bending constant K_3 is normally larger than the other two [1, 31]. It is also noticed that as temperature increases, the magnitude of each elastic constant decreases but the ratio K_3/K_1 is independent of temperature. Meanwhile, nematic liquid crystalline polymers can have elastic constants with orders of magnitude up to $10^{-3} dyne$ [32]. For mesophase carbon pitches, elastic constants were estimated to be on the order of $10^{-3} dyne$ [33]. Finally, near the nematic/smectic-A transition, the bend elastic constant diverges [1, 34].

Miesowicz viscosities

The anisotropic viscosity of nematic LCs was first determined by Miesowicz who measured effective viscosities for relative director orientations to the flow direction [29, 30]. Figure 1-8 shows three Miesowicz geometries in which nematic LCs with the director $\mathbf{n}$ fixed by a strong magnetic field are confined between a stationary bottom plate and a top plate moving with a constant velocity $\mathbf{v}$: (a) $\mathbf{n}$ parallel to the velocity gradient, (b) $\mathbf{n}$ parallel to the velocity, and (c) $\mathbf{n}$ parallel to the vorticity direction, which are corresponding to Miesowicz viscosity coefficients, η_1, η_2, and η_3, respectively [35]. For rod-like nematics, the relative magnitude of the three Miesowicz viscosities is $\eta_1 > \eta_3 > \eta_2$. The viscosity η_3 corresponds to the case where the nematic behaves as an isotropic fluid. For low molecular nematics, the ratio η_2/η_1 is

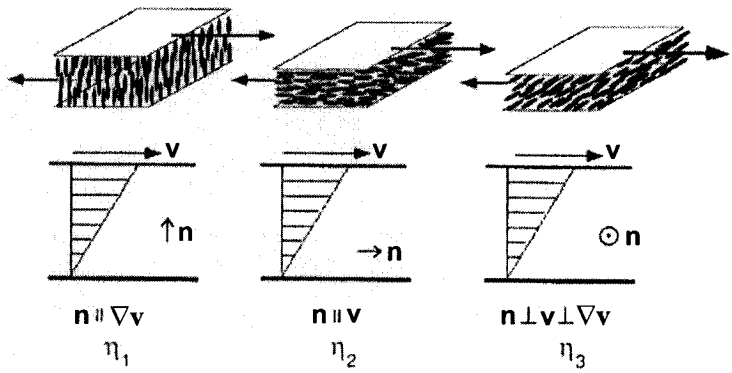

Figure 1-8: Three Miesowicz geometries: (a) **n** parallel to the velocity gradient, (b) **n** parallel to the velocity, and (c) **n** parallel to the vorticity direction, which are corresponding to Miesowicz viscosity coefficients, η_1, η_2, and η_3, respectively.

approximately 0.18 for 5CB and MBBA and approximately 0.26 for PAA [29, 30].

1.3.3 Surface anisotropy

Surface free energy

When a nematic LC is in contact with another solid or liquid phase, the LC molecular orientation at the surface is generally different from the bulk nematic orientation. At the surface, the director has a preferred orientation, and the macroscopic orientation of the LC, imposed by the surface, is called anchoring [36]. If the surface is assumed to be uniaxial, as given in Eq. (1.2), the surface free energy density γ can be written as [5, 7]

$$\gamma = \gamma_{is} + w_0(S) + w_2(S)\cos^2\theta + w_4(S)\cos^4\theta, \tag{1.4}$$

where γ_{is} is the isotropic surface tension, $\{w_i(S)\}$, $i = 0, 2, 4$, represent the anisotropic contribution due to the nematic ordering S, defined in Eq. (1.1), and θ is the tilt angle between the surface director and the surface unit normal vector. The free energy associated with changes in tilt angle, the third and fourth terms on the right-hand side, is known as the anchoring energy. Depending on the signs and values of w_2 and w_4, planar, conical, or homeotropic surface orientation may occur [7]. For strong anchoring, the surface director orientation, e.g., planar

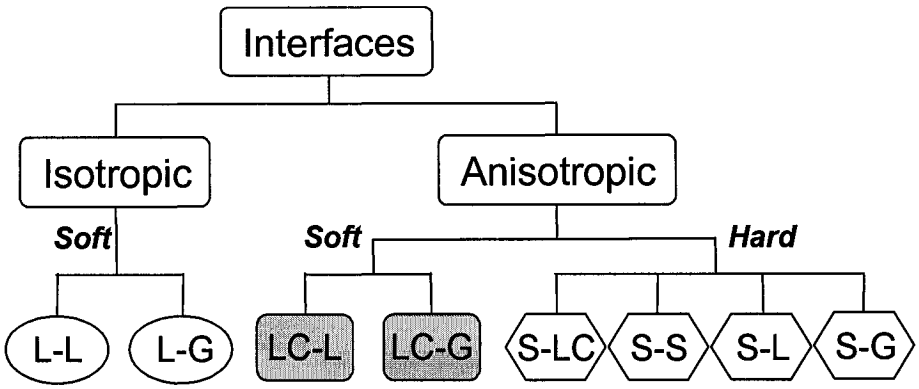

Figure 1-9: Interfaces can be classified into two groups: isotropic and anisotropic interfaces. L represents liquid, G gas, LC liquid crystal, and S solid.

or homeotropic, is fixed as a function of temperature and does not change due to bulk director fields since changes to the surface energy due to surface director orientation requires large surface torques. For weak anchoring, on the other hand, the surface director orientation is easily subjected to changes in temperature and to bulk director fields [7, 37, 38].

Unlike isotropic liquids, the anisotropies both in the viscoelastic bulk and at the surface are essential characteristics of LCs and are, therefore, crucial to understanding the real behaviors of LCs.

1.3.4 Classification of interfaces

Figure 1-9 shows two classes of interfaces: isotropic and anisotropic. In the figure, L represents liquid, G gas, LC liquid crystal, and S solid. When one of the contact phases is an anisotropic phase such as liquid crystal or solid, the interfaces generated are anisotropic. The easy axis of the nematic surface, which is the preferred director orientation at the surface since it minimizes the surface free energy, depends on the nature of the contact phase [1].

For the interface of nematic LC-solid substrate, the anchoring mechanism depends on three main classes of substrate [36]: smooth surfaces, interpenetrable layers, and topographies. Smooth substrates include crystal, glasses, and polymer films. The effect of these substrates on the LC is limited to the surface layer through the short-range interaction of LC molecules at the surface. Planar degenerate, in which more than one easy axis in the plane of the surface

exists, is often observed. Substrates with interpenetrable layers are prepared by grafting polar molecules with a long tail, such as surfactants. LC molecules penetrate into the layer and adopt a homeotropic or conical (degenerate tilted) anchoring depending on the orientation of the chains in the layer. Specific topography for a surface can be obtained by rubbing the surface with a hard material, such as rubbed glass or surfactant-coated glass, or by anisotropic vapor deposition, such as an evaporated SiO film. The topography of a surface introduces distortions along the plane of the surface, and the LC adopts an anchoring direction that minimizes these distortions. Grooved surfaces, for instance, induce an anchoring direction parallel to the grooves for PAA.

The interface of nematic LC-isotropic liquid or -gas involves no interaction with a substrate. For the free surface of PAA, a planar degenerate orientation, in which all directions in the plane of the surface are the easy axes, is observed. A conical anchoring occurs along the free surface for MBBA, whereas the anchoring is homeotropic for nCB. At the LC-liquid interface, the surface director is tilted, with the surface tilt angle ranging from 50° to 80°.

Among the interfaces shown above, this thesis treats soft anisotropic (LC-L, LC-G) interfaces.

1.3.5 Experimental measurements of capillary and interfacial properties

Anchoring energy

The most commonly used analytical approximation for the surface free energy of a nematic LC is given by Rapini-Papoular form [4, 37, 38]:

$$\gamma = \gamma_{is} + \frac{W(T)}{2} \cos^2 \theta, \tag{1.5}$$

where the term accounting for changes in tilt angle θ is the anchoring energy, and $W(T)$ is the surface anchoring strength. The tilt angle θ is an angle between the surface director and the easy axis that is an energetically preferable direction for the surface orientation. Figure 1-10 shows temperature dependences for the anchoring strength in nematic and isotropic phases of 5CB with planar anchoring, for different cell thicknesses d: $d = 14.7\mu m$ (curve 1), $30.2\mu m$ (curve 2), $24.0\mu m$ (curve 3) [4]. In the nematic phase, $T < T_{NI}$, the anchoring strength decreases

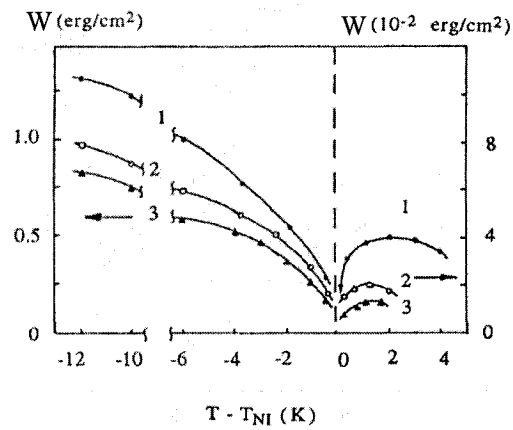

Figure 1-10: Temperature dependences of the anchoring strength in nematic and isotropic phases of 5CB with planar anchoring condition for different cell thicknesses d: d =14.7μm (curve 1), 30.2μm (curve 2), 24.0μm (curve 3) [4].

with increasing temperature. At the nematic-isotropic transition T_{NI}, the anchoring strength is close to zero. In the isotropic phase, $T > T_{NI}$, the anchoring strength is about two orders of magnitude lower than in the nematic phase. Therefore, the nematic ordering is preserved in the surface layer of molecular thickness, several nm, even in the isotropic phase.

Surface tension Figure 1-11 shows temperature dependences of the surface tension in nematic and isotropic phases of three different LCs: (a) PAA, (b) p-anisaldazine, and (c) 5CB [29]. It is well known that the temperature gradient of the surface tension is directly related to the surface excess entropy per unit area, s_{excess}, by [29, 30]

$$s_{\text{excess}} = -\frac{d\gamma}{dT}. \tag{1.6}$$

If the molecular interactions of LCs near the surface become weaker, a positive surface excess entropy, $s_{\text{excess}} > 0$, is expected. Thus, the surface tension γ decreases with temperature T, which is observed for many systems. However, in some cases the very presence of the interface induces an additional order. Then, $s_{\text{excess}} < 0$ and γ increases with T. Inversions of the slope $d\gamma/dT$ are often observed near phase transitions in LCs. It has been suggested that there are two competing effects on the orientational order near the surface [29, 30]: (1) the disordering

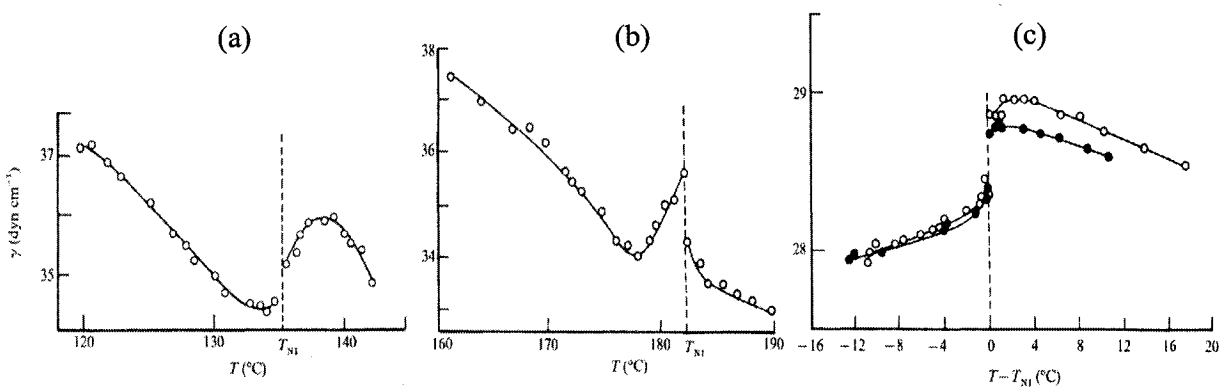

Figure 1-11: Temperature dependences of the surface tension in nematic and isotropic phases of three different LCs: (a) PAA, (b) p-anisaldazine, and (c) 5CB [29].

effect of the spatial delocalization across the liquid-gas transition zone, which is assumed to be proportional to the density profile across the interface; (2) the ordering effect of a surface torque field, which is assumed to be proportional to the density gradient profile across the interface. The relative strengths of these two opposing effects and their temperature dependence may result in variations of the surface tension with temperature for different LCs, as seen in Fig. 1-11.

Surface order parameter

The surface order parameter strongly depends on the character of the solid substrate and can remain, to some degree, in the isotropic phase near the nematic-isotropic transition temperature. Figure 1-12 shows typical temperature dependences of the bulk (S_b) and surface (S_s) order parameters for 7CB [4]. At the nematic-isotropic transition temperature T_{NI}, the bulk order parameter undergoes an abrupt jump to zero through the first-order phase transition while the surface order parameter gradually decreases to about 0.15 and remains constant even in the isotropic phase.

Capillary rise

Capillary rise is a measure of the surface tension of a liquid. The height of the liquid rise in a capillary above the level of the flat surface of the liquid in a large dish is measured. For

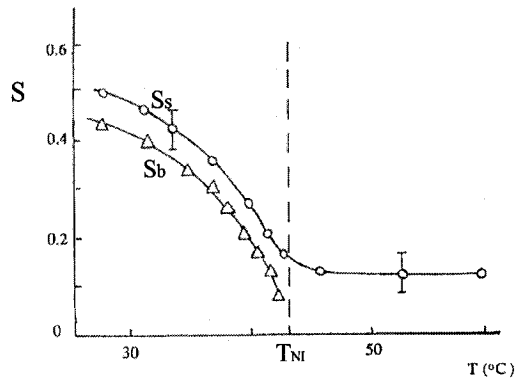

Figure 1-12: Typical temperature dependences of the bulk (S_b) and surface (S_s) order parameters for 7CB [4].

isotropic liquids, the height of the liquid rise, h, is related to the surface tension γ by equating the hydrostatic pressure obtained from the capillary rise to the Young-Laplace equation which describes the pressure jump due to the curved surface at the meniscus [39]:

$$\Delta\rho gh = \frac{2\gamma}{R} = \frac{2\gamma\cos\theta}{R_c}, \tag{1.7}$$

where $\Delta\rho$ is the density difference between the liquid and the ambient gas, g is the gravitational acceleration, R is the radius of the meniscus curvature, R_c is the capillary radius, and θ is the contact angle measured at the junction of the liquid-gas interface and the solid wall. However, since the surface tension of LCs is anisotropic, the effect of orienting surfaces at the capillary wall must be measured differently. Experiments on MBBA found that, by imposing strong anchoring at the capillary surface, the height of the LC rise for planar anchoring is much larger than that for homeotropic anchoring [40]. When using a capillary with thickness of $100\mu m$, planar wall orientation resulted in a $75mm$ capillary rise while homeotropic orientation only $65mm$. These experimental observations have been theoretically explained [41]. Three anisotropic contributions of LCs to the capillary rise are identified: surface anchoring strength and two long-range elasticities due to orientation gradients, respectively, in the bulk and at the contact line that forms at the intersection of three phases (capillary wall-LC-gas). The third contribution appears to be the most significant.

Disjoining pressure

When the thickness of a liquid film is very small, i.e., in the mesoscopic range (submicron and nanometer), the molecular interactions between the two interfacial layers can overlap and some long-range forces become relevant. This leads to excess pressure Π, called disjoining pressure, acting normal to the film. The disjoining pressure Π can be either positive due to repulsive forces, tending to thicken the film, or negative due to attractive forces, tending to thin the film [30]. For isotropic liquid films, there are two main components of Π: the electrostatic disjoining pressure originating in repulsive electrostatic forces acting between the double ion layers at the film surface, and the van der Waals disjoining pressure due to attractive van der Waals forces. For LC films, there exist anisotropic contributions to Π: the elastic disjoining pressure due to the elastic torques caused by deformations of the director field inside the film, and the structural disjoining pressure caused by the layered molecular ordering inside the film. For instance, the elastic disjoining pressures of nCB and MBBA films, respectively, between a solid substrate and air were experimentally measured by imposing strong planar anchoring on the solid substrate and homeotropic anchoring for the nCB free surface, with tilted anchoring for the MBBA free surface. The disjoining pressures of nCB and MBBA were about $200 \sim 500 Nm^{-2}$, at the film thickness of the order of $100nm$ [42], where the isotropic components of Π can be neglected [23].

Partial wetting

Spreading of a liquid drop over a solid surface results in two types of wetting [43]. In cases of complete wetting, the liquid spreads freely over the solid surface and forms a very thin film. The disjoining pressure is of crucial importance to describe the mesoscopic interactions involved in the thin film. In cases of partial wetting, the liquid does not spread completely and remains as a drop on the solid. A contact line forms where three phases intersect, and thus three interfacial tensions are involved: γ_{LG}, γ_{SL}, and γ_{SG}, which are the liquid-gas (L-G), solid-liquid (S-L), and solid-gas (S-G) interfacial tensions, respectively. A contact angle is defined as an angle between the L-G and S-L interfaces. For isotropic liquid, the salient features of the partial wetting, e.g., the shape of the liquid drop and the contact angle, can be described by the so-called classical capillarity such as the Young-Laplace equation and the Young's law that gives a relation of

the contact angle to the three interfacial tensions. Classical capillarity predicts that liquids completely wet solid substrates when $\gamma_{SG} \geq \gamma_{SL} + \gamma_{LG}$. Hence, solid surfaces with very high surface tension, such as mica, give rise to complete wetting by all organic liquids [44]. However, recent experiments found that nematic MBBA does not completely wet mica but forms a liquid drop with the contact angle 14° at 23°C [45]. Both the long-range elasticity due to orientation gradients in the bulk and the discontinuity in the director orientation at the contact line appear to influence wettability of LCs.

As described by the experimental observations above, the presence of anisotropy in LCs is evident and important to: (i) Surface anchoring energy and surface orientational order contributions to surface tension; (ii) Long-range elasticity contribution due to bulk orientational gradients to disjoining pressure; (iii) Long-range elasticity contributions due to bulk orientational gradients and due to contact-line orientational gradients to partial wetting; (iv) Long-range elasticity and surface anchoring contributions to capillary rise. Thus, we know that interfacial phenomena in LCs are highly anisotropic, strongly coupled with bulk properties through the Frank orientational distortion elasticity and with surface properties affected by the surface anchoring and surface orientational order. Therefore, classical interfacial theories are inappropriate to describe liquid crystal phenomena and new theories and formalisms are necessary.

1.3.6 Liquid jet instabilities

Stability and break-up of capillary jets are important in a wide variety of engineering applications such as mixing, spraying, fuel injection, ink-jet printing, fiber spinning, and silicon chip technology. A liquid jet emanating from a nozzle is subjected to a hydrodynamic instability that leads to break-up of the liquid jet. There are two main regimes of the break-up caused by interfacial instability: drop formation and spray formation, which are controlled by different physical mechanisms [46]. When a liquid jet becomes unstable to peristaltic (axisymmetric) surface disturbances, the break-up of the jet results in a trail of drops comparable in size to the jet diameter, known as the Rayleigh or capillary instability. When atomization, in which much smaller droplets than the jet diameter are stripped off from the jet surface, occurs due to a high velocity of the jet, the instability is referred as the Taylor mode.

Axisymmetric modes

When a thin liquid jet slowly moves in a medium, e.g., a surrounding gas or another liquid, the surface tension of the jet overcomes inertia and tends to minimize the surface area. As a result, axisymmetric disturbances dominate the jet, and thus jet break-up forms a trail of drops. This low-speed jet is also known as a capillary jet because the capillary force is predominant in jet instability. The Rayleigh instability is widely observed in low- and high-viscosity isotropic liquids and in viscoelastic liquids. A highly extended fluid filament, often suspended in another fluid, at rest is also subject to the Rayleigh mode since the surface area can be reduced by infinitesimal surface disturbances: break-up of an isotropic Newtonian thread [47] and a lyotropic LC thread [48] immersed in an isotropic viscoelastic liquid. Linear stability theory describes the onset of break-up and was first developed by Rayleigh, demonstrating that there is a certain wavelength at which surface disturbances grow fastest, resulting in a specific size of drops after the jet break-up. Although the dynamics near break-up, e.g., pinching and formation of satellite drops, is highly non-linear, cylindrical symmetry is still preserved because any azimuthal disturbances give rise to a relative increase in surface area and are thus stable [49]. During the break-up of a Vectra (thermotropic LCP) fiber in a polypropylene (thermoplastic) matrix, for example, calculated shape changes from fiber to drop, based on the Rayleigh mechanism, closely predicted actual shapes [50]. The linear approach is also applicable to anisotropic systems such as pinched tubular vesicles, where not only surface tension but also entropic forces due to the curvature of membranes exist [51].

The Rayleigh instability can be modified by the Marangoni effect induced by non-uniformity of surface tension in the presence of temperature or chemical gradients across the jet surface. Surface convection across these gradients perturbs the interfacial temperature or concentration, and thus creates a non-uniform surface tension, resulting in surface tractions which induce bulk fluid motions. For example, in the case of surface-tension reducing solutes, e.g., surfactants, the Marangoni effect associated with the non-uniform surface tension is destabilizing by increasing solute concentration at the troughs while decreasing solute concentration at the crests [52]. On the other hand, surface convection gives rise to a stabilizing Marangoni effect, i.e., the surface contracts at the crests and dilates at the troughs. Therefore, the Rayleigh instability of the jet is modified by the two competing Marangoni effects. Break-up of a molten solder

(liquid metal) jet shows a drastic effect of surface tension in the Rayleigh mode. In a nitrogen environment, a solder jet breaks up into a series of uniform drops, whereas the jet becomes stable by changing the ambient gas to air [53]. Oxide formation on the surface of the liquid metal decreases the surface tension significantly by at least an order of magnitude. Meanwhile, morphological stability of a solid metal-solid metal interface under interfacial diffusion control shows that an interfacial perturbation grows when the wavelength of the perturbation is smaller than the mean diffusion distance of solute in the matrix [54]. Also, an interesting observation on jet branching was reported that a liquid jet bifurcates into a two-, three-, and multi-pronged jet by oscillating the nozzle along its long axis at a successively higher frequency [55, 56]. The two-pronged jet, for instance, breaks up and two streams of drops form, placing drops alternatively in each stream every half-cycle of the jet oscillation [55].

Non-axisymmetric modes

Unlike low-speed jets, high-speed jets may result in chiral (non-axisymmetric) instabilities with a quantized azimuthal wavenumber m different than zero. In a liquid jet moving in an ambient gas, for instance, sinuous (helical) disturbances ($m = 1$) may develop due to aerodynamic form drag. The gas pressure difference between lower pressure at convex sections of the jet surface and the higher pressure at concave sections gives rise to a distributed lift force, promoting the sinuous instability [57]. When the Weber (We) number, or the ratio of surface force to the inertial force, is lower than a critical value, non-axisymmetric modes become unstable [58]. The critical We depends on the wavelength of the disturbance and the density ratio between the liquid and the gas. As the jet speed further increases, droplets are stripped off from the jet surface due to local atomization [59], and then a diverging spray is observed with a higher jet speed due to complete atomization of the jet [46]. Aerodynamic forces caused by the velocity difference between the liquid and the gas are attributed to non-axisymmetric modes with high values of m, which are unstable for sufficiently low We [58]. As a result, catastrophic instabilities appear as short wavelength disturbances [60].

Non-axisymmetric modes are also observed in a smectic mesophase that grows in helical filament shapes: in a lyotropic smectic phase of chiral amphiphilic molecules or of achiral molecules [61, 62]; in a thermotropic smectic phase of achiral banana-shaped molecules [63].

The formation of helical filaments at the isotropic-smectic transition is due to chiral smectic structures. For achiral molecules, chiral smectic phases are induced by symmetry breaking instabilities, e.g., polar molecular packing and molecular tilt in achiral banana-shaped molecules [63]. Meanwhile, cylindrical tubules and helical ribbons are the most interesting self-assembled morphologies of chiral amphiphilic molecules. Tubules are bilayer or multilayer membranes of amphiphilic molecules in a cylindrical shape and observed in lipids [64, 65], biles [66], surfactants [67], and glutamates [68]. Tubules in these systems often exhibit a twisted ripple pattern on the surface of the cylinder [69], which is similar to non-axisymmetric modes with $m \geq 2$. Helical ribbons consist of long strips of membranes. If a helical ribbon keeps an optimum width but grows longer, the ribbon is stable. If the ribbon grows wider over its optimum size, the helical ribbon becomes unstable and forms a tubule. An interesting observation on mixtures of rod-like viruses and polymers was recently reported that a smectic ribbon of $1\mu m$ width corresponding to one smectic layer is formed and grows into a helical shape out of a nematic ellipsoid which forms initially in the isotropic-smectic transition [70].

1.3.7 Surface extrapolation length

The equilibrium of a bounded LC is found by minimizing the total energy that includes bulk elastic and surface anchoring terms. On the other hand, approximations based on a qualitative comparison of the different terms are often useful to obtain an important physical parameter for the system. For a nematic LC fiber of a characteristic size R embedded in a matrix, for example, representative physical properties of the LC fiber are the bulk elastic constant K and the surface anchoring strength W. The surface extrapolation length l is defined as $l \equiv K/W$. For strong anchoring, the surface extrapolation length l is comparable with the coherence length that is associated with the nematic-isotropic transition, whereas l is much larger than the coherence length for weak anchoring [1, 4, 14]. The bulk director orientation of the nematic LC fiber is also different in two regimes [30]. A thin fiber for $R \ll l$ prefers a uniform director orientation, i.e., $\mathbf{n}$ =constant, since the bulk elastic energy involving the variation of the bulk orientation is even more costly compared with the surface anchoring energy driven by surface director deviation from the easy axis under the weak anchoring condition in this regime. A thick fiber for $R \gg l$, on the other hand, prefers director variation in the bulk since strong anchoring is imposed at

the surface and hence any director deviation from the surface easy axis is costly. It is noted that using the data for K and W, given in the previous sections, l ranges from an order of nm to an order of mm, and hence both weak and strong anchoring conditions are applicable. For a nematic fiber of an order of μm in radius, for example, both thin- and thick-fiber regimes are accessible.

1.4 Thesis Objectives

The objectives of this thesis are to formulate a new theoretical framework for liquid crystal surface mechanics and to use it to model pattern formation and instability driven processes in individual liquid crystalline fibers in contact with a viscous matrix, as in fibrillar composites and blends, or air (free surfaces). The particular objectives of this thesis can be summarized as follows:

1. To develop a new thermodynamic formalism for anisotropic liquid crystal surfaces and interfaces, which takes into account the essential elastic anisotropies.

2. To use the new thermodynamic formalism to derive rigorous capillary pressure equations at liquid crystal interfaces.

3. To use the formulated theory to model capillary instabilities in nematic liquid crystalline fibers embedded in viscid and inviscid matrices, and to characterize the contributions of isotropic surface tension, surface anchoring energy, surface ordering energy, bulk orientational elasticity, anisotropic viscosities, and matrix viscosity for composites, respectively.

4. To characterize all possible resulting morphologies and fiber surface patterns in capillary instabilities of nematic liquid crystalline fibers: drops, surface fibrillation, and helical or chiral fibers with twisted ripple patterns on the surface.

5. To formulate fundamental processing principles to control the formation of drops, fibrils, and chiral microstructures.

1.5 Methodology and Thesis Organization

To properly analyze interfacial processes in liquid crystals, the governing equations should consist of the bulk and interfacial linear momentum balances, internal angular momentum

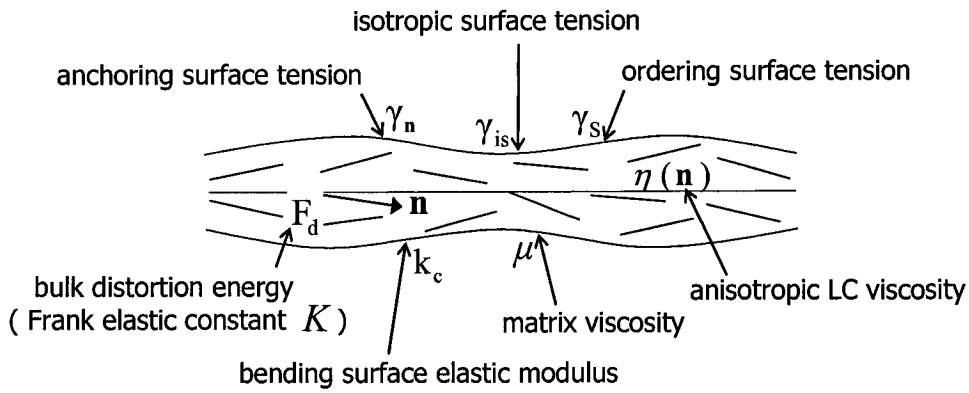

Figure 1-13: Three surface (isotropic, anchoring, and ordering) energies and bulk distortion energy in nematic LCs are taken into account in the thesis. The LC viscosity is considered orientation-dependent while the matrix viscosity is isotropic. The effect of the bending surface elastic modulus is also studied.

balance (director torque balance), and constitutive equations for the stresses and for viscous and elastic torques, which take into account the full viscoelastic anisotropies of the system. For embedded liquid crystalline fibers in viscous fluids, the role of dissipation in the viscous matrix has to be incorporated. Such a program is unfeasible due to a multitude of length scales and time scales, and a number of coupling processes. Moreover, the development of computational codes for the calculation of free-surface flows from first principles has technical difficulties involved in implementing both moving boundaries and surface tension. Therefore, modeling nonlinear processes is beyond the scope of this thesis. Instead, the methodology used in the thesis is to analyze systematically the role of the fundamental processes by adopting linear stability theory which governs the early stage of capillary instabilities but still captures essential features of capillary instabilities such as instability mode selection and resulting morphologies. Figure 1-13 shows all the components to be considered in the fundamental processes: four energies, i.e., γ_{is}, $\gamma_{\mathbf{n}}$, γ_S, and F_d, associated with capillary instability of nematic LCs; the anisotropic viscosity $\eta(\mathbf{n})$ for the liquid crystalline fiber and the isotropic viscosity μ for the matrix; and the bending surface elastic modulus k_c from the interface curvature effects.

The procedure of analyzing the fundamental processes is presented in the thesis organization as follows (see Figure 1-14):

Chapter 1 presents a general background of the thesis including thesis motivation, anisotropic

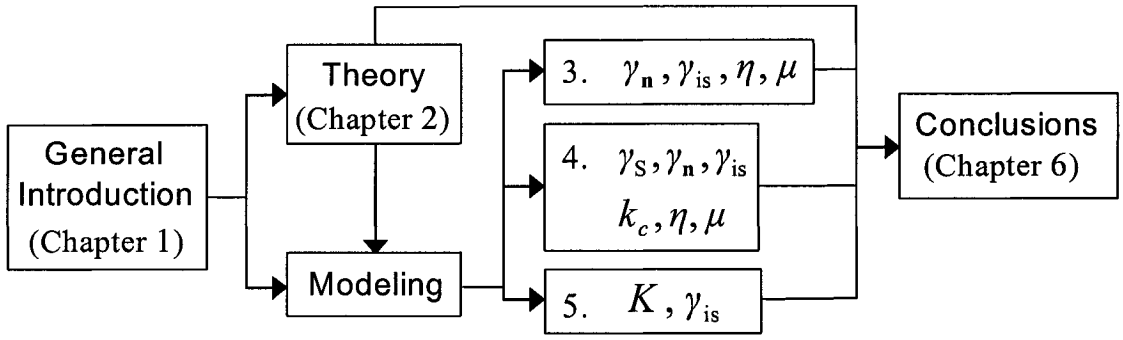

Figure 1-14: Schematic of the thesis organization.

properties and surface phenomena of nematic liquid crystals, and a comprehensive introduction to liquid jet instabilities. It also presents the thesis objectives.

Chapter 2 focuses on formulation of a new thermodynamic formalism for curved anisotropic liquid crystal surfaces and interfaces, which takes into account the essential elastic anisotropies. This formalism is derived and expressed in terms of nematic surface energies, and used to derive a capillary pressure equation at liquid crystal interfaces. The application of the fundamental theory to the capillary instability in thin nematic liquid crystalline fibers is also presented.

Two asymptotic regimes are investigated independently: in chapters 3 and 4, thin-fiber regime where the bulk orientation is uniform and all elastic storage comes from the surface; in chapter 5, thick-fiber regime where strong anchoring is imposed and all elastic storage comes from the bulk. Chapters 3 and 4 present the modeling of capillary instabilities in nematic liquid crystalline fibers embedded in viscid and inviscid matrices as main applications of the theory presented in chapter 2.

In chapter 3, nemato-capillary equations implementing a nemato-capillary pressure are formulated. The capillary pressure equation at the liquid crystal surface accounts for the surface anchoring energy contribution as well as the isotropic surface tension. The viscosity of the liquid crystalline fiber is considered orientation-dependent. Capillary instability mechanisms and symmetry of instability modes in a thin nematic fiber are characterized. The presented study is then extended to the liquid crystalline fiber embedded in an immiscible viscous matrix for which the nemato-capillary equations are reformulated to take into account the viscous stress at the interface due to the presence of the viscous matrix. The contribution of the viscosity

ratio, i.e., matrix viscosity/fiber viscosity, to the capillary instabilities is investigated.

In chapter 4, the nemato-capillary equations formulated in chapter 3 are used in conjunction with a newly formulated capillary pressure equation which accounts for the surface ordering energy, as a function of temperature, and anchoring energy contributions as well as the isotropic surface tension. The critical role of the surface ordering energy in the instability mode selection is fully characterized. It is also discovered that the non-axisymmetric instability mechanism is regulated by taking account of the surface bending moment, implemented through the surface stress tensor.

In chapter 5, comprehensive analysis of bulk distortion elasticity effects on axisymmetric capillary instabilities in textured liquid crystalline fibers is presented using the equations of nemato-statics and inviscid nemato-dynamics. Instability mechanisms explaining deviations from the classical Rayleigh instability are characterized.

Chapter 6 presents the conclusions and the contributions to original knowledge.

Bibliography

[1] P. G. de Gennes and J. Prost, *The Physics of Liquid Crystals* (Oxford University Press, London, 1993).

[2] H. Ehrentraut and S. Hess, Phys. Rev. E, **51**, 2202 (1995).

[3] R. G. Larson, *The Structure and Rheology of Complex Fluids* (Oxford University Press, New York, 1999).

[4] A. A. Sonin, *The Surface Physics of Liquid Crystals* (Gordon and Breach Publishers, Amsterdam, 1995).

[5] H. Yokoyama, in *Handbook of Liquid Crystal Research*, edited by P. J. Collins and J. S. Patel (Oxford University Press, New York, 1997).

[6] W. J. A. Goossens, Mol. Cryst. Liq. Cryst., **124**, 305 (1985).

[7] T. J. Sluckin and A. Poniewierski, in *Fluid Interfacial Phenomena*, edited by C. A. Croxton (John Wiley & Sons, Chichester, 1986).

[8] G. Barbero, Z. Gabbasova, and M. A. Osipov, J. Phys. II, **1**, 691 (1991).

[9] D. A. Edwards, H. Brenner, and D. T. Wasan, *Interfacial Transport Processes and Rheology* (Butterworths-Heinemann, Boston, 1989).

[10] V. G. Levich, *Physicochemical Hydrodynamics* (Prentice-Hall, Englewood Cliffs, 1962).

[11] J. C. Slattery, *Interfacial Transport Phenomena* (Springer-Verlag, New York, 1990).

[12] D. D. Edie and E.G. Stoner, in *Carbon-Carbon Materials and Composites*, edited by J. D. Buckley and D. D. Edie (Noyes, Park Ridge, 1993).

[13] A. D. Rey, Ind. Eng. Chem. Res., **36**, 1114 (1997).

[14] M. Kreuzer and R. Eidenschink, in *Liquid Crystals in Complex Geometries*, edited by G. P. Crawford and S. Zumer (Taylor & Francis, London, 1996).

[15] P. J. Collings, *Liquid Crystals* (Princeton University Press, Princeton, 2002).

[16] R. A. L. Jones, *Soft Condensed Matter* (Oxford University Press, Oxford, 2002).

[17] A. M. Donald and A. H. Windle, *Liquid Crystalline Polymers* (Cambridge University Press, Cambridge, 1992).

[18] D. D. Edie and M. G. Dunham, Carbon, **27**, 647 (1989).

[19] F. Vollrath and D. P. Knight, Nature, **410**, 541 (2001).

[20] H.-J. Jin and D. L. Kaplan, Nature, **424**, 1057 (2003).

[21] Y. Qin, Polym. Adv. Technol., **7**, 151 (1996).

[22] J. Klett, R. Hardy, E. Romine, C. Walls, and T. Burchell, Carbon, **38**, 953 (2000).

[23] A. A. Sonin, *Freely Suspended Liquid Crystalline Films* (John Wiley & Sons, Chichester, 1998).

[24] B. I. Kupchinov, V. G. Rodnenkov, S. F. Ermakov, and V. P. Parkalov, Tribology International, **24**, 25 (1991).

[25] J. F. Rusling, Microporous Materials, **3**, 1 (1994).

[26] M. Baron and R. F. T. Stepto, Pure Appl. Chem., **74**, 493 (2002).

[27] I. C. Khoo, *Liquid Crystals: Physical properties and nonlinear optical phenomena* (John Wiley & Sons, New York, 1995).

[28] S. Kumar, *Liquid Crystals: Experimental Study of Physical Properties and Phase Transitions* (Cambridge University Press, Cambridge, 2001).

[29] S. Chandrasekhar, *Liquid Crystals* (Cambridge University Press, Cambridge, 1992).

[30] M. Kleman and O. D. Lavrentovich, *Soft Matter Physics: An Introduction* (Springer-Verlag, New York, 2003).

[31] D. A. Dunmur, in *Physical Properties of Liquid Crystals: Nematics*, edited by D. Dunmur, A. Fukuda, and G. Luckhurst (INSPEC, London, 2001).

[32] T. De'neve, M. Kleman, and P. Navard, Liq. Cryst., **18**, 67 (1994).

[33] O. Fleurot and D. D. Edie, J. Rheol., **42**, 781 (1998).

[34] L. Cheung and R. B. Meyer, Phys. Lett. A, **43**, 261 (1973).

[35] J. Janik, R. Tadmor, and J. Klein, Langmuir, **17**, 5476 (2001).

[36] B. Jerome, in *Physical Properties of Liquid Crystals*, edited by D. Demus, J. Goodby, G. W. Gray, H.-W. Spiess and V. Vill (Wiley-VCH, Weinheim, 1999).

[37] G. Barbero and L. R. Evangelista, *An Elementary Course on the Continuum Theory for Nematic Liquid Crystals* (World Scientific, Singapore, 2001).

[38] G. Barbero and G. Durand, in *Liquid Crystals in Complex Geometries*, edited by G. P. Crawford and S. Zumer (Taylor and Francis, London, 1996).

[39] P. C. Hiemenz and R. Rajagopalan, *Principles of Colloid and Surface Chemistry* (Marcel Dekker, New York, 1997).

[40] V. A. Tsvetkov, O. V. Tsvetkov, and V. A. Balandin, Mol. Cryst. Liq. Cryst., **329**, 305 (1999).

[41] A. D. Rey, Langmuir, **19**, 3677 (2003).

[42] E. Perez, J. E. Proust, and L. Ter-Minassian-Saraga, in *Thin Liquid Films: Fundamentals and Applications*, edited by I. B. Ivanov (Marcel Dekker, New York, 1988).

[43] L. Leger and J. F. Joanny, Rep. Prog. Phys., **55**, 431 (1992).

[44] P. G. de Gennes, Rev. Mod. Phys., **57**, 827 (1985).

[45] C.-M. Lin, P. Neogi, and R. M. Ybarra, Chem. Eng. Sci., **55**, 37 (2000).

[46] S. P. Lin, *Breakup of Liquid Sheets and Jets* (Cambridge University Press, Cambridge, 2003).

[47] V. T. Tsakalos, P. Navard, and E. Peuvrel-Disdier, J. Rheol., **42**, 1403 (1998).

[48] V. T. Tsakalos, P. Navard, and E. Peuvrel-Disdier, Liq. Cryst., **21**, 663 (1996).

[49] J. Eggers, Rev. Mod. Phys., **69**, 865 (1997).

[50] A. Boersma, M. Wubbenhorst, and J. Turnhout, Macromol., **30**, 2915 (1997).

[51] R. Bar-Ziv and E. Moses, Phys. Rev. Lett., **73**, 1392 (1994).

[52] G. O. Collantes, E. Yariv, and I. Frankel, J. Fluid Mech., **474**, 95 (2003).

[53] D. B. Wallace, J. Fluids Eng., **115**, 529 (1993).

[54] J. M. Howe, *Interfaces in Materials* (John Wiley & Sons, New York, 1997).

[55] S. P. Lin and R. D. Webb, Phys. Fluids, **6**, 2671 (1994).

[56] S. P. Lin and D. R. Woods, Phys. Fluids A, **3**, 241 (1991).

[57] A. L. Yarin, *Free Liquid Jets and Films: Hydrodynamics and Rheology* (Longman Scientific & Technical, New York, 1993).

[58] H. Q. Yang, Phys. Fluids A, **4**, 681 (1992).

[59] J. W. Hoyt and J. J. Taylor, J. Fluid Mech., **83**, 119 (1977).

[60] D. D. Joseph, *Fluid Dynamics of Viscoelastic Liquids* (Springer-Verlag, New York, 1990).

[61] M. Todorokihara, K. Fujihara, and H. Naito, Int. Liq. Cryst. Conference (2002).

[62] R. Pratibha and N. V. Madhusudana, J. Phys. II France, **2**, 383 (1992).

[63] A. Jakli, Ch. Lischka, W. Weissflog, G. Pelzl, and A. Saupe, Liq. Cryst., **27**, 1405 (2000).

[64] J. Georger, C. Singh, and R. Price, J. Am. Chem. Soc., **109**, 6169 (1987).

[65] A. Singh et al., Chem. Phys. Lipids, **47**, 135 (1988).

[66] D. S. Chung, G. B. Benedek, F. M. Konikoff, and J. M. Donovan, Proc. Natl. Acad. Sci., **90**, 11341 (1993).

[67] T. Tachibana, S. Kitazawa, and H. Takeno, Bull. Chem. Soc. Jpn., **43**, 2418 (1970).

[68] N. Nakashima, S. Asakuma, and T. Kunitake, J. Am. Chem. Soc., **107**, 509 (1985).

[69] J. V. Selinger, F. C. MacKintosh, and J. M. Schnur, Phys. Rev. E, **53**, 3804 (1996).

[70] Z. Dogic and S. Fraden, Phil. Trans. R. Soc. Lond. A, **359**, 997 (2001).

Chapter 2

Cahn-Hoffman Capillarity Vector Thermodynamics for Curved Liquid Crystal Interfaces with Applications to Fiber Instabilities

2.1 Summary

The classical Cahn-Hoffman capillarity vector formalism for anisotropic interfaces, widely used to analyze capillary and surface patterning processes in metallic systems, is applied to nematic liquid crystalline surfaces.

Firstly, the nematic capillarity vector is derived and expressed in terms of nematic surface energies. Expressions for surface tension forces on surface line elements are derived and shown to include the usual tangential forces as well as normal forces driven by surface tension anisotropy. The connection between interfacial rotational effects, surface tension anisotropy, and bending stresses is established. The vector formalism is shown to be a tractable and simple method to analyze capillarity processes in nematic liquid crystals.

Secondly, the Cahn-Hoffman capillarity vector thermodynamics for curved anisotropic interfaces is adapted to soft liquid crystalline interfaces. The formalism is used to derive the

Herring's capillary pressure equation for liquid crystal interfaces, where the role of anchoring energy of liquid crystals is made explicitly. It is shown in detail that liquid crystal interfaces have three distinct contributions to capillary pressure: (i) area reduction, (ii) area rotation, and (iii) orientation curvature. General expressions representing these three mechanisms in terms of isotropic and anisotropic surface tensions are derived and used to analyze the Rayleigh capillary instability in thin fibers. It is shown that liquid crystal fibers and filaments are unstable to peristaltic and chiral surface ripple modes. The peristaltic mode leads to droplet formation, whereas chiral modes produce ripples in the curvature of the fiber. The role of liquid crystal orientation and anchoring energy on mode selection is elucidated and quantified.

2.2 Introduction

The surface physics of nematic liquid crystals is currently an active area of research [1, 2, 3, 4, 5, 6] since many applications of liquid crystalline materials involve multiphase systems, where interfaces play significant roles. Interfacial orientation phenomena and orientational transitions in well-defined geometries are well characterized experimentally [1, 2, 3] and theoretically [4, 5, 6, 7, 8]. On the other hand, deforming interphases and shape characterization are less characterized. The first part of this chapter deals with capillarity models of interfacial forces that drive shape determination in anisotropic nematic liquid crystalline materials. Examples of applications of the capillarity models include determination of contact angles, droplet shapes, and triple line phenomena. Although static and dynamical interfacial models for nematic liquid crystals (NLCs) have been presented [4, 5, 6, 7, 8, 9, 10, 11, 12, 13, 14], still there is a need to formulate simple and more tractable models. The first part of this chapter presents a capillarity model based on the widely used Cahn-Hoffman formalism of capillarity vector for anisotropic surfaces [14]. Since the Cahn-Hoffman formalism was developed for anisotropic surfaces, it follows that the formalism is also applicable to anisotropic NLCs. The main objectives of the first part are to: (1) adapt the widely used Cahn-Hoffman formalism to NLCs surfaces and interfaces, and (2) establish the correspondence between the nematic Cahn-Hoffman equations and the classical interfacial mechanics of NLCs presented in Refs. [12, 13].

Meanwhile, liquid crystals exhibit anisotropy in both their bulk and interfacial properties

[15]. It is well-known that anisotropic interfacial properties play a significant role in metallurgical systems, where contact angles, grain boundaries, triple lines, and capillary instabilities are affected by surface tension anisotropy [16]. A capillarity vector thermodynamics for anisotropic materials was developed by Cahn-Hoffman, and the formalism is now part of classical interfacial material science [14, 16, 17]. The capillarity vector $\boldsymbol{\zeta}$ is the fundamental quantity in this formalism and takes into account the orientation dependence of the surface tension γ: $\gamma = \gamma(\mathbf{N})$, where $\mathbf{N}$ is the surface unit normal. The surface tension force as well as the capillary pressure is shown to depend on the orientation of the surface since surface energy can be reduced by reducing the surface area or by rotation of the surface. This effect is captured in the well-known Herring's equation [16, 17, 18]. Since liquid crystals are anisotropic materials, the Cahn-Hoffman capillarity vector thermodynamic formalism is also applicable to these soft but anisotropic materials. In addition, the Cahn-Hoffman formalism provides a direct and transparent way to elucidate the role of anisotropy in capillary pressure and its role in particle shape determination.

The stability of fibers and filaments arises in a variety of multiphase material systems, such as metal [16, 18], polymer [19], and ceramic [20] composites, and polymer gels [21], as well as in the fiber forming process [19]. Most of the analysis for fiber stability is based on extensions of the Rayleigh capillary instability, which is driven by the area reduction when a fiber breaks into an array of droplets. The instability modes are always axisymmetric and known as peristaltic modes [21]. This result is based on the assumption of isotropic interfacial tension, and since non-axisymmetric instabilities always increase surface area, they are never observed. Exceptions are jet instabilities under strong inertia [22], where the disintegration process is analyzed in terms of chiral modes. Since anisotropic systems can decrease energy by surface contraction or by surface rotation, materials with orientational order such as liquid crystals are likely to exhibit chiral instabilities. Figure 2-1 shows schematics of characteristic peristaltic and chiral instability modes. Chiral instabilities of tubules driven by anisotropic surface energies have been studied in the literature and apparently explain geometric features of certain biomaterials [23, 24, 25]. In this chapter, we use the liquid crystal Cahn-Hoffman formalism [14, 17] to analyze peristaltic and chiral capillary instabilities of thin liquid crystalline fibers.

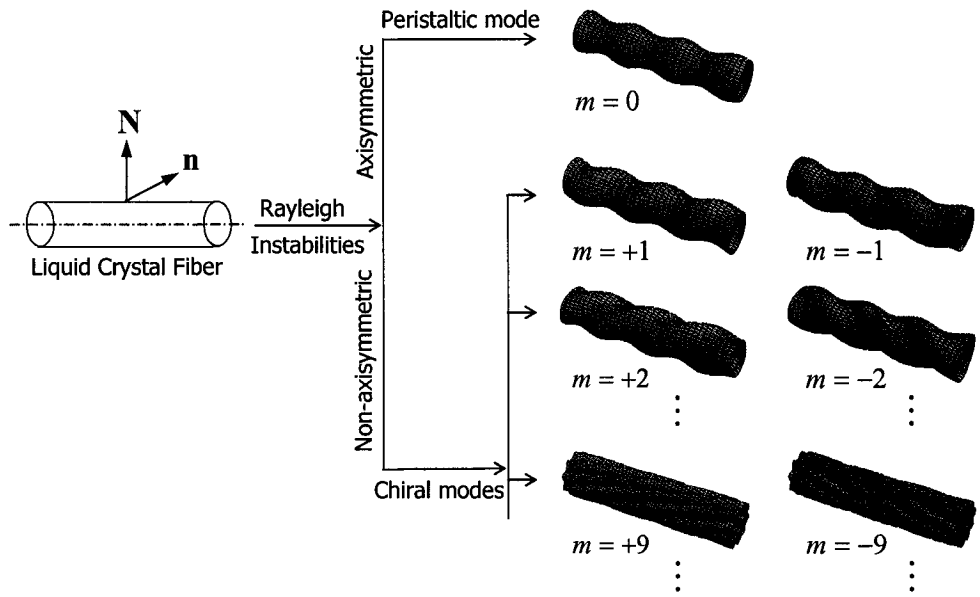

Figure 2-1: Schematic of capillary instability modes in nematic liquid crystalline fibers. Top figure: peristaltic (axisymmetric) mode, $m = 0$. Bottom figures: chiral (non-axisymmetric) modes, $m = \pm 1, \pm 2, \cdots$.

The organization of this chapter is as follows. The first part consists of sections 2.3 – 2.5: Section 2.3 presents the main derivations and results of the Cahn-Hoffman equations; Section 2.4 presents the derivation of the nematic Cahn-Hoffman equations; Section 2.5 presents the correspondence between the nematic Cahn-Hoffman equation and the surface stress tensor equation presented in [12, 13]. The second part consists of sections 2.6 and 2.7: Section 2.6 presents the Cahn-Hoffman capillarity vector thermodynamics for curved anisotropic interfaces following Refs. [14, 17], and for curved nematic liquid crystal interfaces; Section 2.7 presents the application of the Cahn-Hoffman formalism to Rayleigh instabilities in thin nematic liquid crystalline fibers. Section 2.8 presents the conclusions.

2.3 Cahn-Hoffman Capillarity Vector for Anisotropic Surfaces

This section summarizes the Cahn-Hoffman formalism as given in [14, 16, 17, 18]. For anisotropic systems, the surface free energy density γ is a function of the surface unit normal $\mathbf{N}$: $\gamma(\mathbf{N})$.

The capillarity vector $\boldsymbol{\zeta}(\mathbf{N})$ is defined by the gradient of the scalar field $r\gamma$:

$$\boldsymbol{\zeta}(\mathbf{N}) = \nabla[r\gamma(\mathbf{N})], \qquad \mathbf{r} = r\mathbf{N}, \tag{2.1}$$

where r is the distance from the origin in a fixed reference frame and is denoted by the magnitude of the surface position vector $\mathbf{r}$. Noticing that $\boldsymbol{\zeta}(\mathbf{N})$, the gradient of $r\gamma$, yields

$$d(r\gamma) = \nabla(r\gamma)\cdot d\mathbf{r}, \qquad rd\gamma + \gamma dr = \boldsymbol{\zeta}\cdot d(r\mathbf{N}) = r\boldsymbol{\zeta}\cdot d\mathbf{N} + \boldsymbol{\zeta}\cdot\mathbf{N}dr, \tag{2.2}$$

and therefore

$$d\gamma = \boldsymbol{\zeta}\cdot d\mathbf{N}, \qquad \gamma = \boldsymbol{\zeta}\cdot\mathbf{N}. \tag{2.3}$$

Since the surface free energy density γ is a function of surface orientation, i.e., of the angles describing the orientation of $\mathbf{N}$ in a fixed reference frame, using Eq. (2.3), it follows that

$$\boldsymbol{\zeta}\cdot\frac{d\mathbf{N}}{d\theta} = \frac{d\gamma}{d\theta}, \qquad \boldsymbol{\zeta}_{\perp} = \boldsymbol{\zeta}\cdot\mathbf{NN} = \gamma\mathbf{N}, \tag{2.4}$$

where $d\mathbf{N}$ represents a change in orientation by the small rotation angle $d\theta = |d\mathbf{N}|$. Since the unit tangent vector is given by $\mathbf{t} = d\mathbf{N}/d\theta$, then $\zeta_{\shortparallel} = \boldsymbol{\zeta}\cdot\mathbf{t} = d\gamma/d\theta$. The selected tangential component of $\boldsymbol{\zeta}$ is the one that maximizes the increase of surface energy with rotation, and hence

$$\boldsymbol{\zeta}_{\shortparallel} = \boldsymbol{\zeta}\cdot\mathbf{I}_s = \left(\frac{d\gamma}{d\theta}\right)_{\max}\mathbf{t}_0, \tag{2.5}$$

where $\mathbf{I}_s$ is the 2×2 unit surface dyadic and $\mathbf{t}_0$ is the unit tangent vector along which $d\gamma/d\theta$ has the maximum rate of increase. For anisotropic surfaces there is a principal orthogonal coordinate frame ($\mathbf{t}_0$, $\mathbf{c}_0$), and rotation of $\mathbf{N}$ around $\mathbf{c}_0$ produces the maximum increase in surface energy. The principal frame is selected by the main anisotropic axes of the surface. Anisotropic surfaces can change surface energy by dilation and by rotation. Figure 2-2 shows an element of area $A = \mathbf{A}\cdot\mathbf{N}$ and surface unit normal $\mathbf{N}$ that undergoes expansion and rotation. Since γ is a function of $\mathbf{N}$, the surface energy γ can increase by expansion and by rotation of $\mathbf{N}$. Figure 2-3 shows the components of $\boldsymbol{\zeta}$ and their magnitudes in the principal frame ($\mathbf{t}_0$, $\mathbf{c}_0$). Figure 2-4 shows a schematic of the capillarity vectors $\boldsymbol{\zeta}$ and $-\boldsymbol{\zeta}$, and the normal $-\boldsymbol{\zeta}_{\perp}$ and

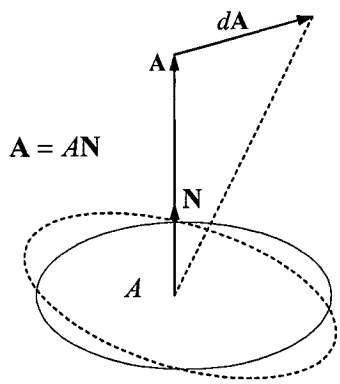

Figure 2-2: Schematic of a surface patch indicating the two modes of surface energy increase: (a) Dilation increases the surface area A; (b) Rotation tilts the area vector $\mathbf{A}$. Adapted from Ref. [14].

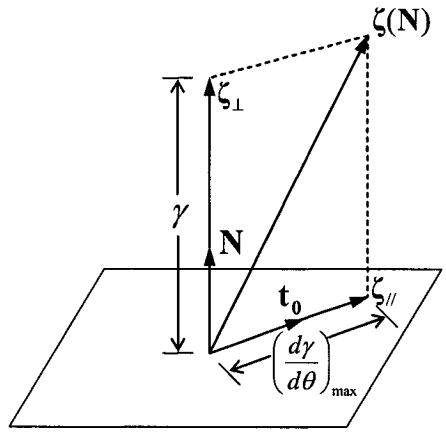

Figure 2-3: Schematic of the capillarity vector $\boldsymbol{\zeta}$, and its normal $\boldsymbol{\zeta}_\perp$ and tangential $\boldsymbol{\zeta}_{||}$ components in the principal surface coordinate frame $(\mathbf{t}_0, \mathbf{c}_0)$. Adapted from Ref. [14].

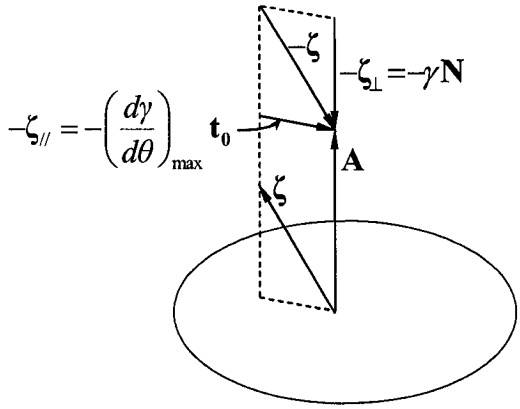

Figure 2-4: Schematic of the effect of the capillarity vector $-\boldsymbol{\zeta}$ and its components on the surface area vector $\mathbf{A}$. The normal component $-\boldsymbol{\zeta}_\perp$ tends to shrink the area, while the tangential component $-\boldsymbol{\zeta}_{||}$ tends to rotate the area vector to reduce surface energy. Adapted from Ref. [14].

tangential $-\boldsymbol{\zeta}_{||}$ components of $-\boldsymbol{\zeta}$. The vector $-\boldsymbol{\zeta}$ represents the surface force acting on the area vector $\mathbf{A}$, tending to shrink ($-\boldsymbol{\zeta}_\perp$) and rotate ($-\boldsymbol{\zeta}_{||}$) the surface. For isotropic surface, $\boldsymbol{\zeta}_{||} = 0$ and no rotational effects appear.

The capillarity vector $\boldsymbol{\zeta}$ is needed to compute the surface tension force density $\boldsymbol{\sigma}$. The surface tension force per unit length, $\boldsymbol{\sigma}$, acting on a line element oriented along a unit tangent vector $\mathbf{l}$ is $\boldsymbol{\sigma} = \boldsymbol{\zeta} \times \mathbf{l}$, from which the following tangential and normal components are obtained:

$$\boldsymbol{\sigma}_{||} = \boldsymbol{\zeta}_\perp \times \mathbf{l} = \gamma (\mathbf{N} \times \mathbf{l}) = \gamma \boldsymbol{\nu}, \qquad \boldsymbol{\nu} = \mathbf{N} \times \mathbf{l}, \tag{2.6}$$

$$\boldsymbol{\sigma}_\perp = \boldsymbol{\zeta}_{||} \times \mathbf{l} = \left(\frac{d\gamma}{d\theta}\right)_{max} (\mathbf{t}_0 \times \mathbf{l}) \, . \tag{2.7}$$

Since $\boldsymbol{\nu} = \mathbf{N} \cdot \mathbf{l}$ for any $\mathbf{l}$, the magnitude of the tangential surface force $\boldsymbol{\sigma}_{||}$ is always γ. On the other hand, the normal surface force $\boldsymbol{\sigma}_\perp$ depends on the vector $\mathbf{t}_0 \times \mathbf{l}$. Thus $\boldsymbol{\sigma}_\perp = \mathbf{0}$ for $\mathbf{t}_0 \,||\, \mathbf{l}$ and $\boldsymbol{\sigma}_\perp = (\boldsymbol{\sigma}_\perp)_{max}$ for $\mathbf{t}_0 \perp \mathbf{l}$.

2.4 Cahn-Hoffman Capillarity Vector for Nematic Surfaces

For a nematic liquid crystal surface the nematic ordering is defined by the three-component orientation vector known as the director, $\mathbf{n} = \mathbf{n}(\mathbf{r})$, where $\mathbf{n} \cdot \mathbf{n} = 1$, $\mathbf{r} = r\mathbf{N}$ is the surface position vector, and $\mathbf{N}$ is the surface unit normal, as before. A useful decomposition of the

surface director field into tangential and normal components is $\mathbf{n}_{\shortparallel} = \mathbf{I}_s \cdot \mathbf{n}$ and $\mathbf{n}_{\perp} = \mathbf{NN} \cdot \mathbf{n}$, where $\mathbf{I}_s = \mathbf{I} - \mathbf{NN}$ is the 2×2 unit surface dyadic, and $\mathbf{I}$ is the 3×3 volumetric unit tensor. To develop the Cahn-Hoffman capillarity vector for nematic surfaces, we use the well-known Rapini-Papoular surface free energy density γ given by [26]

$$\gamma(\mathbf{n}\cdot\mathbf{N}, T) = \gamma_{is}(T) + \gamma_{an}(\mathbf{n}\cdot\mathbf{N}, T)\,, \qquad \gamma_{an}(\mathbf{n}\cdot\mathbf{N}, T) = \frac{w(T)}{2}(\mathbf{n}\cdot\mathbf{N})^2\,, \tag{2.8}$$

where γ_{is} is the isotropic contribution, γ_{an} is the anisotropic contribution due to anchoring energy, and w is the anchoring energy coefficient. Higher-order expansions are easily incorporated into Eq. (2.8) [4], but the present expression suffices for the scope of this chapter. To find the nematic capillarity vector $\boldsymbol{\zeta}$, we use definition (2.1):

$$\boldsymbol{\zeta}(\mathbf{n}, \mathbf{N}) = \nabla[r\gamma(\mathbf{N})]\,, \tag{2.9}$$

where the director $\mathbf{n}$ in the surface energy is kept constant: $\gamma(\mathbf{n}, \mathbf{N}) = \gamma(\mathbf{N})$. Computing the gradient of $r\gamma$ using $r = r(\mathbf{r}(\mathbf{N}))$ and $\mathbf{N} = \mathbf{N}(\mathbf{r})$ gives

$$\boldsymbol{\zeta}(\mathbf{n}, \mathbf{N}) = \nabla[r\gamma(\mathbf{N})] = \gamma\frac{\partial r}{\partial \mathbf{r}} + r\frac{\partial \gamma}{\partial \mathbf{r}} = \gamma\mathbf{N} + \mathbf{I}_s \cdot \frac{d\gamma}{d\mathbf{N}}\,, \tag{2.10}$$

where the following results have been used:

$$\frac{\partial r}{\partial \mathbf{r}} = \mathbf{N}\,, \qquad \frac{\partial \gamma}{\partial \mathbf{r}} = \mathbf{I}_s \cdot \frac{d\gamma}{d\mathbf{N}} \cdot \frac{\partial \mathbf{N}}{\partial \mathbf{r}} = \mathbf{I}_s \cdot \frac{d\gamma}{d\mathbf{N}}\frac{1}{r}\,. \tag{2.11}$$

Thus the components of capillarity vector for nematic surfaces and interfaces are

$$\boldsymbol{\zeta}_{\perp}(\mathbf{n}, \mathbf{N}) = \boldsymbol{\zeta}\cdot\mathbf{NN} = \gamma\mathbf{N}\,, \qquad \boldsymbol{\zeta}_{\shortparallel}(\mathbf{n}, \mathbf{N}) = \mathbf{I}_s \cdot \frac{d\gamma}{d\mathbf{N}} = \frac{d\gamma}{d(\mathbf{n}\cdot\mathbf{N})}(\mathbf{I}_s \cdot \mathbf{n}) = \gamma'\mathbf{n}_{\shortparallel}\,, \tag{2.12}$$

where $\gamma' = d\gamma/d(\mathbf{n}\cdot\mathbf{N})$. To put $\boldsymbol{\zeta}_{\shortparallel}$ in the Cahn-Hoffman form, Eq. (2.5), we let θ be the angle between the unit normal $\mathbf{N}$ and the director $\mathbf{n}$ in Eq. (2.12) and get

$$\boldsymbol{\zeta}_{\shortparallel} = \gamma'\mathbf{n}_{\shortparallel} = \left(\frac{d\gamma}{d\theta}\right)_{\max}\mathbf{t}_0\,; \qquad \left(\frac{d\gamma}{d\theta}\right)_{\max} = -\frac{d\gamma}{d\theta}\,, \qquad \mathbf{t}_0 = \frac{\mathbf{n}_{\shortparallel}}{|\mathbf{n}_{\shortparallel}|}\,. \tag{2.13}$$

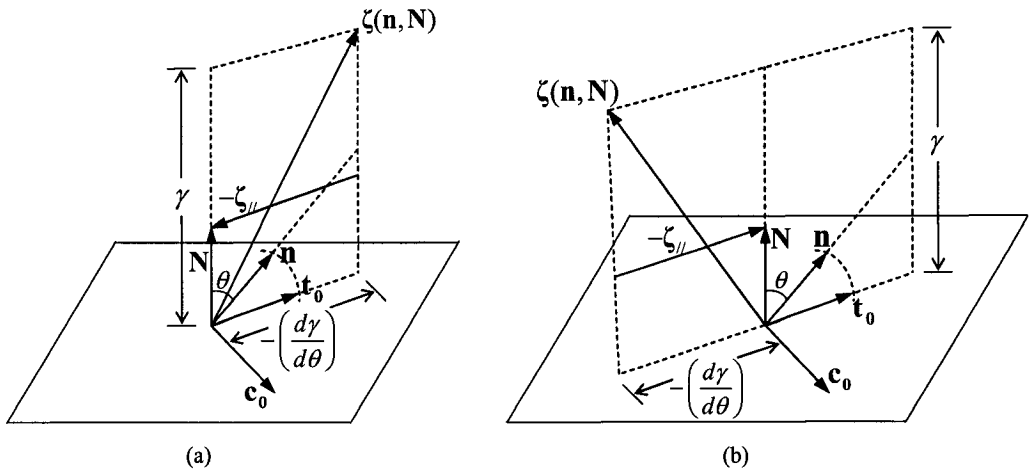

Figure 2-5: Schematic of the main vectors in the nematic Cahn-Hoffman vector thermodynamics for (a) planar easy axis ($-d\gamma/d\theta > 0$), and (b) homeotropic easy axis ($-d\gamma/d\theta < 0$). The principal surface frame ($\mathbf{t}_0$, $\mathbf{c}_0$) is selected by the director orientation.

Thus the selected tangential vector $\mathbf{t}_0$ is the tangential unit vector along the surface projection of the director $\mathbf{n}_{||}$, and the maximum rate of increase of γ is just $-d\gamma/d\theta$ (see Figure 2-5 below). In nematic interfaces the principal frame ($\mathbf{t}_0$, $\mathbf{c}_0$) is defined by the intersection of the **N**-**n** plane and the surface. Therefore, nematic surfaces may decrease the surface energy by contraction or by rotation of the surface unit normal around an axis (parallel to $\mathbf{c}_0$) that is perpendicular to the surface projection of the director. The nematic surface behavior is isotropic only if

$$\boldsymbol{\zeta}_{||} = \mathbf{n}_{||} \frac{d\gamma}{d(\mathbf{n}\cdot\mathbf{N})} = \mathbf{0}, \tag{2.14}$$

which is possible when $n_{||} = 0$ or when $d\gamma/d(\mathbf{n}\cdot\mathbf{N}) = 0$. When $n_{||} = 0$, i.e., $\mathbf{n} \parallel \mathbf{N}$, the surface is isotropic as when $n_{||} = 1$, i.e., $\mathbf{n} \perp \mathbf{N}$. The director $\mathbf{n}^*$ corresponding to the stable extrema of γ is known as the easy axis, and is (i) planar; $w > 0$, $n_{||}^* = 1$, or (ii) homeotropic; $w < 0$, $n_{||}^* = 0$ [4]. The two cases are shown in Figure 2-5: $\mathbf{n}$, $\mathbf{N}$, $\mathbf{t}_0$, $\mathbf{c}_0$, $\boldsymbol{\zeta}$, $-\boldsymbol{\zeta}_{||}$ vectors for a planar easy axis (a) and for a homeotropic easy axis (b). Rotation of $\mathbf{N}$ around $\mathbf{c}_0$ in the direction imposed by $-\boldsymbol{\zeta}_{||}$ gives the fastest rate of decrease in anchoring energy: (a) $-d\gamma/d\theta > 0$ and (b) $-d\gamma/d\theta < 0$.

For a nematic surface, the components of the surface tension force per unit length, $\boldsymbol{\sigma}$, acting

on a line element oriented along a unit tangent vector $\mathbf{l}$, in Eqs. (2.6) and (2.7), are rewritten as

$$\boldsymbol{\sigma}_{\shortparallel} = \boldsymbol{\zeta}_{\perp} \times \mathbf{l} = \gamma (\mathbf{N} \times \mathbf{l}) = \gamma \boldsymbol{\nu}, \qquad \boldsymbol{\sigma}_{\perp} = \boldsymbol{\zeta}_{\shortparallel} \times \mathbf{l} = \frac{d\gamma}{d(\mathbf{n} \cdot \mathbf{N})} (\mathbf{n}_{\shortparallel} \times \mathbf{l}) \,. \tag{2.15}$$

Thus the normal surface tension force per unit length acting on a line oriented along $\mathbf{l}$ is zero only if $\boldsymbol{\zeta}_{\shortparallel} = \mathbf{0}$ or if $\mathbf{n} \parallel \mathbf{l}$. Barring these possibilities, a line on a nematic surface is subjected to a normal force, $\boldsymbol{\sigma}_{\perp}$, unlike isotropic surfaces. This normal force plays a role in the balance of forces at contact lines and triple lines, where if one of the intersecting surfaces is nematic, the classical Neumann tangential capillarity vector equation must be augmented to include the normal vector force $\boldsymbol{\sigma}_{\perp}$ [12].

2.5 Correspondence between Cahn-Hoffman Capillarity Vector and Surface Elastic Stress Tensor

The previous model of interfacial nemato-statics [12, 13] is based on the surface elastic stress tensor $\mathbf{t}^{\mathrm{se}}$. This fundamental quantity defines the capillary pressure p_c, $p_c = -(\nabla_s \cdot \mathbf{t}^{\mathrm{se}}) \cdot \mathbf{N}$, and the surface tension force $\boldsymbol{\sigma}$ on a surface line along $\mathbf{l}$, $\boldsymbol{\sigma} = \boldsymbol{\nu} \cdot \mathbf{t}^{\mathrm{se}}$, where $\boldsymbol{\nu} \perp \mathbf{l}$. The expression of the surface elastic stress tensor $\mathbf{t}^{\mathrm{se}}$ is found basically by noting that $\gamma = \gamma(\mathbf{N})$ and by using the identity $\mathbf{t}^{\mathrm{se}} = \mathbf{I}_s \cdot \mathbf{t}^{\mathrm{se}}$. The surface elastic stress tensor $\mathbf{t}^{\mathrm{se}}$ is given by the usual 2×2 symmetric interfacial tension contribution $\mathbf{t}^{\mathrm{se}}_N$ (normal stresses) and the 2×3 anisotropic contribution $\mathbf{t}^{\mathrm{se}}_B$ (bending stresses):

$$\mathbf{t}^{\mathrm{se}} = \mathbf{t}^{\mathrm{se}}_N + \mathbf{t}^{\mathrm{se}}_B \;; \qquad \mathbf{t}^{\mathrm{se}}_N = \gamma \mathbf{I}_s \,, \qquad \mathbf{t}^{\mathrm{se}}_B = -\mathbf{I}_s \cdot \left(\frac{\partial \gamma}{\partial \mathbf{N}} \mathbf{N} \right) = -\gamma' \mathbf{n}_{\shortparallel} \mathbf{N} \,. \tag{2.16}$$

Comparing Eqs. (2.12), (2.13), and (2.16) we find that the correspondence between the surface elastic stress tensor $\mathbf{t}^{\mathrm{se}}$ and the Cahn-Hoffman capillarity vector $\boldsymbol{\zeta}$ is

$$\mathbf{t}^{\mathrm{se}} = \boldsymbol{\zeta} \cdot \boldsymbol{\Psi} \,, \qquad \boldsymbol{\Psi} = \mathbf{N}\mathbf{I}_s - \mathbf{I}_s \mathbf{N} \,, \tag{2.17}$$

$$\mathbf{t}^{\mathrm{se}}_N = \boldsymbol{\zeta}_{\perp} \cdot \mathbf{N}\mathbf{I}_s \,, \qquad \mathbf{t}^{\mathrm{se}}_B = -\boldsymbol{\zeta}_{\shortparallel} \mathbf{N} = \frac{d\gamma}{d\theta} \mathbf{t}_0 \mathbf{N} \,. \tag{2.18}$$

The bending coefficient $d\gamma/d\theta$ is the fastest rate of decrease in anchoring energy, and $\mathbf{t}_B^{se}$ has only one component in the principal frame. Figure 2-6(a) shows the bending stress cylinder, presenting $\mathbf{n}$, $\mathbf{N}$, $\mathbf{t}_0$, $\mathbf{c}_0$ vectors and $|d\gamma/d\theta|$. The arrows denote the direction and magnitude of the bending stresses acting on a surface patch where the orthogonal frame is any arbitrary orthogonal $(\mathbf{t}, \mathbf{c})$. The magnitude of the bending stress at any point on the circle is

$$\mathbf{t} \cdot \mathbf{t}_B^{se} \cdot \mathbf{N} = \frac{d\gamma}{d\theta} (\mathbf{t} \cdot \mathbf{t}_0) = \frac{d\gamma}{d\theta} \cos\varphi \,, \tag{2.19}$$

where φ is the angle between $\mathbf{t}_0$ and $\mathbf{t}$. Figure 2-6(b) shows that for the principal frame $(\mathbf{t}_0, \mathbf{c}_0)$ there is only one component, i.e., principal bending stress of magnitude $|d\gamma/d\theta|$, acting on the surface direction normal to $\mathbf{t}_0$. Figure 2-6(c) shows that for any other frame $(\mathbf{t}, \mathbf{c})$ there are two bending stress components whose magnitudes depend on the rotation angle φ between the principal frame $(\mathbf{t}_0, \mathbf{c}_0)$ and the $(\mathbf{t}, \mathbf{c})$ frame.

2.6 Herring's Formula for Capillary Pressure Derived from Cahn-Hoffman Capillarity Vector

In this section, the Cahn-Hoffman capillarity vector thermodynamics for curved anisotropic interfaces is adapted to soft liquid crystal interfaces. The formalism is used to derive the Herring's capillary pressure equation for liquid crystal interfaces, where the role of anchoring energy of liquid crystals is made explicitly. It is shown in detail that liquid crystal interfaces have three distinct contributions to capillary pressure: (i) area reduction, (ii) area rotation, and (iii) director curvature.

To derive the Herring's equation for curved anisotropic interfaces, it is necessary to introduce surface curvature as follows. The mean curvature H and the surface curvature tensor $\mathbf{b}$ of curved interfaces are given by

$$H = -\frac{1}{2}\nabla_s \cdot \mathbf{N} = \frac{1}{2}\mathbf{I}_s : \mathbf{b} = -\frac{1}{2}\mathbf{I}_s : \nabla_s \mathbf{N} = \frac{1}{2}(\kappa_1 + \kappa_2) \,, \tag{2.20}$$

$$\mathbf{b} = -\nabla_s \mathbf{N} = \kappa_1 \mathbf{e}_1\mathbf{e}_1 + \kappa_2 \mathbf{e}_2\mathbf{e}_2 \,, \tag{2.21}$$

where $\nabla_s = \mathbf{I}_s \cdot \nabla$ is the surface gradient , $\mathbf{I}_s$ is the 2×2 unit surface dyadic, $\mathbf{b}$ is a 2×2

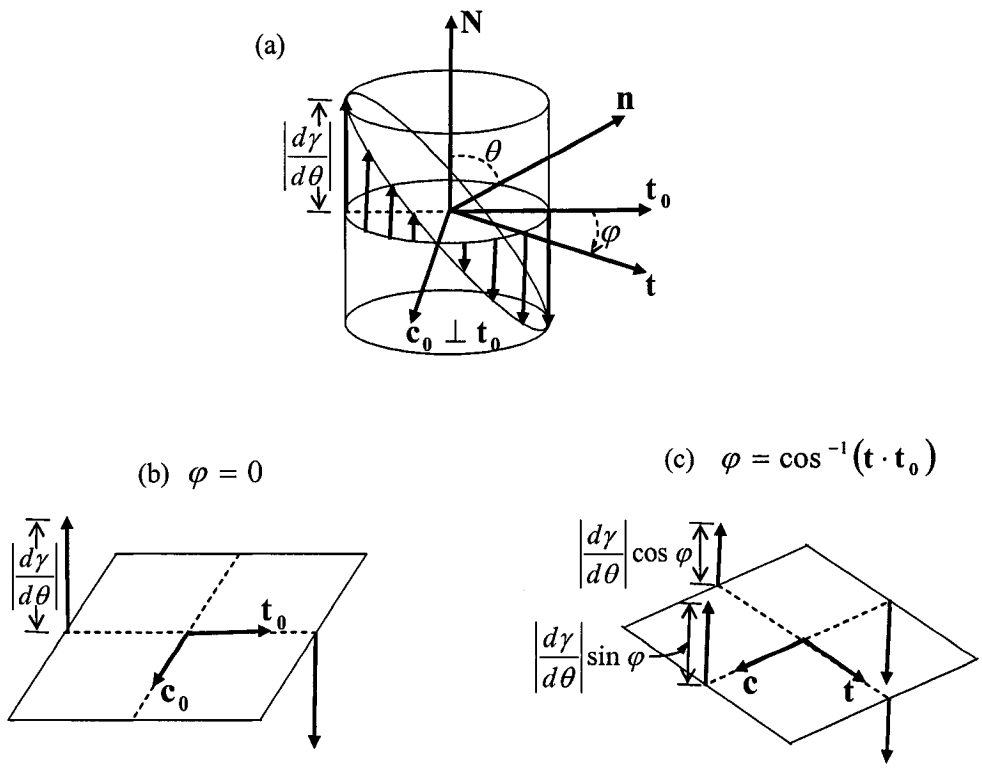

Figure 2-6: (a) Schematic of the bending stress cylinder $\mathbf{t}_B^{se}$ in relation to the main surface vectors and main frame ($\mathbf{t}_0$, $\mathbf{c}_0$). (b) Schematic of the single principal bending stress on a surface element oriented along the principal frame ($\mathbf{t}_0$, $\mathbf{c}_0$). (c) Schematic of the two bending stresses on a surface element oriented along the principal frame ($\mathbf{t}_0$, $\mathbf{c}_0$).

symmetric tensor, and where $\{\kappa_i\}$ and $\{\mathbf{e}_i\}$, $i = 1, 2$, are the eigenvalues and eigenvectors of $\mathbf{b}$. The surface divergence of $\mathbf{I}_s$ is a normal vector: $\nabla_s \cdot \mathbf{I}_s = 2H\mathbf{N}$. Using Eq. (2.3) the total surface free energy F_s is

$$\int_A \gamma dA = \int_A \boldsymbol{\zeta} \cdot \mathbf{N} dA \,. \tag{2.22}$$

The variation of the total surface free energy δF_s due to a displacement δu normal to the interface is

$$\delta F_s = \int_A p_c \delta u \, dA + \oint_C f_e \delta u \, dl \,, \tag{2.23}$$

where p_c is the capillary pressure and f_e is the component of the edge force along the contour C. As shown in Ref. [17], δF_s is given by

$$\delta F_s = \int_A (\nabla_s \cdot \boldsymbol{\zeta}) \, \delta u \, dA - \oint_C (\mathbf{N} \times \boldsymbol{\zeta}_{\shortparallel}) \cdot \boldsymbol{\eta} \delta u \, dl \,, \tag{2.24}$$

where $\boldsymbol{\eta}$ is the unit tangent to C. Thus the capillary pressure is $p_c = \nabla_s \cdot \boldsymbol{\zeta}$. The divergence of the capillarity vector follows the rule

$$p_c = \nabla_s \cdot \boldsymbol{\zeta} = \nabla_s \cdot \left(\boldsymbol{\zeta}_\perp + \boldsymbol{\zeta}_{\shortparallel}\right) = \frac{\partial \boldsymbol{\zeta}_\perp}{\partial \mathbf{N}} : \nabla_s \mathbf{N} + \frac{\partial \boldsymbol{\zeta}_{\shortparallel}}{\partial \mathbf{N}} : \nabla_s \mathbf{N} = -\left(\frac{\partial \boldsymbol{\zeta}_\perp}{\partial \mathbf{N}} + \frac{\partial \boldsymbol{\zeta}_{\shortparallel}}{\partial \mathbf{N}}\right) : \mathbf{b} \,. \tag{2.25}$$

The contribution from the normal component $\boldsymbol{\zeta}_\perp$ is the classical term

$$-\frac{\partial \boldsymbol{\zeta}_\perp}{\partial \mathbf{N}} : \mathbf{b} = -\gamma \mathbf{I}_s : \mathbf{b} = -\gamma \left(\kappa_1 + \kappa_2\right) \,. \tag{2.26}$$

According to Eq. (2.5),

$$\frac{\partial \boldsymbol{\zeta}_{\shortparallel}}{\partial \mathbf{N}} = \mathbf{I}_s \cdot \left\{ \frac{\partial}{\partial \mathbf{N}} \left(\mathbf{I}_s \cdot \frac{\partial \gamma}{\partial \mathbf{N}} \right) \right\} = \mathbf{I}_s \cdot \frac{\partial^2 \gamma}{\partial \mathbf{N}^2} - \mathbf{I}_s \left(\mathbf{N} \cdot \frac{\partial \gamma}{\partial \mathbf{N}} \right) \,. \tag{2.27}$$

Using Eqs. (2.5), (2.21), and (2.27) the contribution to p_c from the tangential component is

$$-\frac{\partial \boldsymbol{\zeta}_{\shortparallel}}{\partial \mathbf{N}} : \mathbf{b} = -\left(\frac{\partial^2 \gamma}{\partial \theta_1^2} \kappa_1 + \frac{\partial^2 \gamma}{\partial \theta_2^2} \kappa_2 \right) \,, \tag{2.28}$$

$$\frac{\partial^2 \gamma}{\partial \theta_1^2} = \mathbf{e}_1 \mathbf{e}_1 : \frac{\partial^2 \gamma}{\partial \mathbf{N}^2} - \mathbf{N} \cdot \frac{\partial \gamma}{\partial \mathbf{N}} \,, \qquad \frac{\partial^2 \gamma}{\partial \theta_2^2} = \mathbf{e}_2 \mathbf{e}_2 : \frac{\partial^2 \gamma}{\partial \mathbf{N}^2} - \mathbf{N} \cdot \frac{\partial \gamma}{\partial \mathbf{N}} \,. \tag{2.29}$$

Collecting results in Eqs. (2.26), (2.28), and (2.29), the following well-known Herring's equation [16, 17] is obtained from Eq. (2.25):

$$-p_c = -\nabla_s \cdot \boldsymbol{\zeta} = \left(\gamma + \frac{\partial^2 \gamma}{\partial \theta_1^2}\right) \kappa_1 + \left(\gamma + \frac{\partial^2 \gamma}{\partial \theta_2^2}\right) \kappa_2 = \gamma \left(\kappa_1 + \kappa_2\right) + \left(\frac{\partial^2 \gamma}{\partial \theta_1^2} \kappa_1 + \frac{\partial^2 \gamma}{\partial \theta_2^2} \kappa_2\right) . \quad (2.30)$$

The area size change is driven by geometric curvature. The rotation effect creates capillary pressure only on curved surfaces. The curvatures $\partial^2 \gamma / \partial \theta_i^2$ renormalize the surface tension, and since their sign is unrestricted, negative effective surface tension can arise.

To derive the liquid crystal Herring's formula for the capillary pressure, we use the definition (2.25) and find

$$-p_c = -\nabla_s \cdot \boldsymbol{\zeta} = -\nabla_s \cdot \left(\boldsymbol{\zeta}_\perp + \boldsymbol{\zeta}_{\shortparallel}\right) = \frac{\partial \boldsymbol{\zeta}_\perp}{\partial \mathbf{N}} : \mathbf{b} + \frac{\partial \boldsymbol{\zeta}_{\shortparallel}}{\partial \mathbf{N}} : \mathbf{b} - \frac{\partial \boldsymbol{\zeta}_{\shortparallel}}{\partial \mathbf{n}} : \nabla_s \mathbf{n} , \quad (2.31)$$

where the additional contribution to the capillary pressure arises from director curvature since the nematic capillarity vector is a function of both the director and the normal, i.e., $\boldsymbol{\zeta} = \boldsymbol{\zeta}(\mathbf{n}, \mathbf{N})$. Flat planar liquid crystal interfaces generate capillary pressure by director curvature [11, 12, 13]. The contribution from the area size change is the classical term (2.26). Using Eq. (2.12)

$$\boldsymbol{\zeta}_{\shortparallel} = \gamma' \left(\mathbf{I}_s \cdot \mathbf{n}\right) = \gamma' \left[\mathbf{n} - \mathbf{N} \left(\mathbf{n} \cdot \mathbf{N}\right)\right] , \quad (2.32)$$

the area rotation contribution becomes

$$\frac{\partial \boldsymbol{\zeta}_{\shortparallel}}{\partial \mathbf{N}} : \mathbf{b} = \gamma'' \left[\mathbf{nn} - \left(\mathbf{n} \cdot \mathbf{N}\right)^2 \mathbf{I}\right] : \mathbf{b} = \gamma'' \left\{ \left[\left(\mathbf{n} \cdot \mathbf{e}_1\right)^2 - \left(\mathbf{n} \cdot \mathbf{N}\right)^2\right] \kappa_1 + \left[\left(\mathbf{n} \cdot \mathbf{e}_2\right)^2 - \left(\mathbf{n} \cdot \mathbf{N}\right)^2\right] \kappa_2 \right\} . \quad (2.33)$$

The director curvature contribution is found using the equality $\gamma' = \gamma'' \left(\mathbf{n} \cdot \mathbf{N}\right)$ to obtain

$$-\frac{\partial \boldsymbol{\zeta}_{\shortparallel}}{\partial \mathbf{n}} : \nabla_s \mathbf{n} = -\gamma'' \left[tr \left(\mathbf{Nn}\right) tr \left(\nabla_s \mathbf{n}\right) + tr \left(\mathbf{Nn} \nabla_s \mathbf{n}\right)\right] . \quad (2.34)$$

Collecting terms (2.26), (2.33), and (2.34)and using $\gamma'' = w$, we finally obtain the liquid crystal

Herring equation for capillary pressure from Eq. (2.31):

$$\begin{aligned} -p_c &= \left\{\gamma + w\left[(\mathbf{n}\cdot\mathbf{e}_1)^2 - (\mathbf{n}\cdot\mathbf{N})^2\right]\right\}\kappa_1 + \left\{\gamma + w\left[(\mathbf{n}\cdot\mathbf{e}_2)^2 - (\mathbf{n}\cdot\mathbf{N})^2\right]\right\}\kappa_2 \\ &\quad -w\left[tr\left(\mathbf{Nn}\right)tr\left(\nabla_s\mathbf{n}\right) + tr\left(\mathbf{Nn}\nabla_s\mathbf{n}\right)\right], \end{aligned} \tag{2.35}$$

where the contributions due to area change, area rotation, and director curvature are

$$\begin{aligned} -p_c &= \underbrace{\gamma\left(\kappa_1+\kappa_2\right)}_{\text{area size change}} + \underbrace{w\left\{\left[(\mathbf{n}\cdot\mathbf{e}_1)^2 - (\mathbf{n}\cdot\mathbf{N})^2\right]\kappa_1 + \left[(\mathbf{n}\cdot\mathbf{e}_2)^2 - (\mathbf{n}\cdot\mathbf{N})^2\right]\kappa_2\right\}}_{\text{area rotation}} \\ &\quad \underbrace{-w\left[\left(\mathbf{N}\cdot\mathbf{n}\right)\left(\nabla_s\cdot\mathbf{n}\right) + \mathbf{Nn}:\nabla_s\mathbf{n}\right]}_{\text{director curvature}}. \end{aligned} \tag{2.36}$$

In the absence of director curvature, the classical expression of the Herring equation, Eq. (2.30), is obtained since

$$\frac{\partial^2\gamma}{\partial\theta_i^2} = \mathbf{e}_i\mathbf{e}_i : \frac{\partial^2\gamma}{\partial\mathbf{N}^2} - \mathbf{N}\cdot\frac{\partial\gamma}{\partial\mathbf{N}} = w\left[(\mathbf{n}\cdot\mathbf{e}_i)^2 - (\mathbf{n}\cdot\mathbf{N})^2\right], \qquad i = 1,2\,. \tag{2.37}$$

For flat planar interfaces the capillary pressure is driven by director curvature:

$$-p_c = -w\left[\left(\mathbf{N}\cdot\mathbf{n}\right)\left(\nabla_s\cdot\mathbf{n}\right) + \mathbf{Nn}:\nabla_s\mathbf{n}\right]. \tag{2.38}$$

For curved surfaces and orientation along the principal axis, say $\mathbf{n} = \mathbf{e}_1$, the capillary pressure p_c is

$$-p_c = \left(\gamma_{is} + w\right)\kappa_1 + \gamma_{is}\kappa_2 - w\left(\mathbf{Ne}_1:\nabla_s\mathbf{e}_1\right), \tag{2.39}$$

which shows that the effective surface tension corresponding to curvature κ_1 is renormalized from γ_{is} to $\gamma_{is} + w$. Since the sign of w is undetermined [4], competition or cooperation may result. In addition, planar orientation on curved interfaces results in capillary pressure. For curved interfaces and orientation along the unit normal, $\mathbf{n} = \mathbf{N}$,

$$-p_c = \gamma\left(\kappa_1+\kappa_2\right) - w\left(\kappa_1+\kappa_2\right) + 2Hw = 2H\left(\gamma_{is} + \frac{w}{2}\right), \tag{2.40}$$

and the classical form of Laplace equation for isotropic interfaces results since the surface it-

self is isotropic because the anisotropic axis is along the normal. Clearly, capillary pressure in anisotropic liquid crystal interfaces includes a number of novel interfacial effects: (a) capillary pressure even for flat surfaces, (b) orientation-dependent renormalization of the surface tension coefficients due to anchoring energy, (c) orientation-driven transitions between classical (Laplace pressure) and non-classical behaviors, and (d) Laplace-type capillary pressure due to orientation curvature. We next analyze the stability of thin nematic liquid crystal fibers, where the manifestations of these novel phenomena clearly emerge.

2.7 Application of Cahn-Hoffman Capillarity Vector Thermodynamics to the Rayleigh Fiber Instability

The classical Rayleigh liquid fiber instability is driven by area reduction. Consider a liquid cylinder of length L with axis along the z-direction of constant radius a. Axisymmetric perturbations of infinitesimal amplitude and axial wave number k of the type

$$R(z) = a\sqrt{1 - \frac{\xi_0^2}{2a^2}} + \xi_0 \cos kz \approx a\left(1 - \frac{\xi_0^2}{4a^2}\right) + \xi_0 \cos kz \tag{2.41}$$

conserve the volume and change the original total surface area $A_i = 2\pi aL$ to

$$A_f = A_i\left\{1 + \frac{\xi_0^2}{4a^2}\left[(ka)^2 - 1\right]\right\}, \tag{2.42}$$

and when $ka < 1$, the area is reduced, and the liquid fiber undergoes a peristaltic instability that eventually leads to the formation of spherical droplets (see Fig. 2-1). Since nematic interfaces change the surface energy through area reduction, area rotation, and director curvature, new non-axisymmetric (chiral) instability modes beyond the classical peristaltic mode are expected (see Fig. 2-1). We must therefore consider the following volume-conserving non-axisymmetric perturbations of infinitesimal amplitude ξ_0:

$$R(\theta, z) = R_0 + \xi(\theta, z), \qquad R_0 = a\sqrt{1 - \frac{\xi_0^2}{2a^2}} \approx a\left(1 - \frac{\xi_0^2}{4a^2}\right), \qquad \xi(\theta, z) = \xi_0 \cos\left(kz + m\theta\right), \tag{2.43}$$

where $m = \pm 1, \pm 2, \cdots$ is the quantized azimuthal wave number that gives rise to chiral surface patterns. For these non-axisymmetric perturbations we next show that the surface area always increases, and hence these instability modes are not observed in isotropic systems. The surface position vector $\mathbf{P}(\theta, z)$ is

$$\mathbf{P}(\theta, z) = (R\cos\theta, R\sin\theta, z) \ . \tag{2.44}$$

To compute the total surface area A_{fm} of a deformed cylinder of length L we use cylindrical coordinates $(u = R_0\theta, v = z)$ and integrate,

$$A_{fm} = \int_0^L \int_0^{2\pi} \sqrt{EG - F^2} du dv \,, \tag{2.45}$$

$$E = \sum_i \left(\frac{\partial P_i}{\partial v}\right)^2 = 1 + \left(\frac{\partial \xi}{\partial v}\right)^2 , \qquad F = \sum_i \frac{\partial P_i}{\partial v}\frac{\partial P_i}{\partial u} = \frac{\partial \xi}{\partial v}\frac{\partial \xi}{\partial u} \,, \tag{2.46}$$

$$G = \sum_i \left(\frac{\partial P_i}{\partial u}\right)^2 = \left(1 + \frac{\xi}{R_0}\right)^2 + \left(\frac{\partial \xi}{\partial u}\right)^2 , \tag{2.47}$$

$$\begin{aligned} EG - F^2 &= \left(1 + \frac{\xi}{R_0}\right)^2 \left[1 + \left(\frac{\partial \xi}{\partial v}\right)^2 + \frac{\left(\frac{\partial \xi}{\partial u}\right)^2}{\left(1 + \frac{\xi}{R_0}\right)^2}\right] \approx \left(1 + \frac{\xi}{R_0}\right)^2 \left[1 + \left(\frac{\partial \xi}{\partial v}\right)^2 + \left(\frac{\partial \xi}{\partial u}\right)^2\right], \\ \sqrt{EG - F^2} &\approx \left(1 + \frac{\xi}{R_0}\right) \left[1 + \frac{1}{2}\left\{\left(\frac{\partial \xi}{\partial v}\right)^2 + \left(\frac{\partial \xi}{\partial u}\right)^2\right\}\right]. \end{aligned} \tag{2.48}$$

Computing the derivatives the final area A_{fm} is found to be

$$A_{fm} = A_i \left\{1 + \frac{\xi_0^2}{4a^2}\left[(ka)^2 + m^2 - 1\right]\right\} \,, \tag{2.49}$$

where the calculation is valid to second order in ξ. Thus for $m \geq 1$ the area increases quadratically with m. Next we show how chiral instabilities emerge driven by area rotation and director curvature modes.

The capillary pressure p_c is the variation of the surface energy density under a small perturbation of the orientation, surface area, and surface rotation. Introducing an infinitesimal

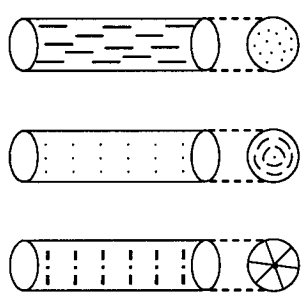

Figure 2-7: Schematic of the three fiber textures: (a) axial ($\mathbf{n}_z = 1$), (b) onion ($\mathbf{n}_\theta = 1$), (c) radial ($\mathbf{n}_r = 1$) textures.

perturbation $\xi(\theta, z)$ of the type (2.43) creates a capillary pressure given by

$$-p_c = -\nabla_s \cdot \boldsymbol{\zeta} = D + \Delta(\xi) \,, \tag{2.50}$$

where D is a perturbation-independent constant and does not contribute to the growth rate equation for the perturbation (see Chapter 3 for details) while $\Delta(\xi)$ contains all the perturbation-dependent terms. A perturbation $\xi(\theta, z)$ decreases the surface energy when

$$\Delta(\xi) > 0 \,. \tag{2.51}$$

Next we analyze all the possible instability modes of thin nematic fibers by establishing the conditions that lead to positive values of the perturbation-dependent contribution to $-p_c$.

We consider the three characteristic orientation states in a nematic fiber of initial constant radius a subjected to infinitesimal perturbation $\xi(\theta, z)$, as given in Eq. (2.43). Figure 2-7 shows the schematic of the three fiber textures: (a) axial ($n_z = 1$), (b) onion ($n_\theta = 1$), and (c) radial ($n_r = 1$) textures. The phenomena are described in a cylindrical coordinate system (θ, z, r), and the director field $\mathbf{n}$ is specified by $\mathbf{n}(\theta, z, r) = (n_\theta, n_z, n_r)$. The principal surface frame is given by the unit vectors: $\mathbf{e}_1 = \boldsymbol{\delta}_\theta$, $\mathbf{e}_2 = \boldsymbol{\delta}_z$, the unit surface normal $\mathbf{N}$ by

$$\mathbf{N}(\theta, z) = -\frac{\partial_\theta R}{R}\boldsymbol{\delta}_\theta - \partial_z R \boldsymbol{\delta}_z + \boldsymbol{\delta}_r \,, \tag{2.52}$$

and the principal curvatures $\chi_{\theta r}$ and χ_{zr} by

$$\kappa_1 \equiv \chi_{\theta r} = -\frac{1}{a} + \frac{\partial_{\theta\theta}\xi}{a^2} + \frac{\xi}{a^2} = -\frac{1}{a} + \frac{\xi}{a^2}\left(1 - m^2\right), \qquad \kappa_2 \equiv \chi_{zr} = \partial_{zz}\xi = -k^2\xi\,. \quad (2.53)$$

Thus Eq. (2.35) is rewritten as

$$-p_c = \left(\gamma + \frac{\partial^2\gamma}{\partial\theta_\theta^2}\right)\chi_{\theta r} + \left(\gamma + \frac{\partial^2\gamma}{\partial\theta_z^2}\right)\chi_{zr} - w\left[(\mathbf{N}\cdot\mathbf{n})\left(\nabla_s\cdot\mathbf{n}\right) + \mathbf{Nn}:\nabla_s\mathbf{n}\right], \quad (2.54)$$

where the curvatures of the surface energy are

$$\frac{\partial^2\gamma}{\partial\theta_\theta^2} = w\left[(\mathbf{n}\cdot\boldsymbol{\delta}_\theta)^2 - (\mathbf{n}\cdot\mathbf{N})^2\right], \qquad \frac{\partial^2\gamma}{\partial\theta_z^2} = w\left[(\mathbf{n}\cdot\boldsymbol{\delta}_z)^2 - (\mathbf{n}\cdot\mathbf{N})^2\right]. \quad (2.55)$$

Substituting Eq. (2.53) into Eqs. (2.54) yields the general Rayleigh instability condition:

$$\Delta(\xi) = \left(\gamma + \frac{\partial^2\gamma}{\partial\theta_\theta^2}\right)\left(1 - m^2\right) - \left(\gamma + \frac{\partial^2\gamma}{\partial\theta_z^2}\right)(ka)^2 - \frac{wa^2}{\xi}\left[(\mathbf{N}\cdot\mathbf{n})\left(\nabla_s\cdot\mathbf{n}\right) + \mathbf{Nn}:\nabla_s\mathbf{n}\right] > 0\,. \quad (2.56)$$

The four mechanisms that operate in the Rayleigh instabilities in nematic fibers are explicitly shown below:

$$\underbrace{\gamma\left[\left(1-m^2\right) - (ka)^2\right]}_{\text{area reduction (AR)}} + \underbrace{\frac{\partial^2\gamma}{\partial\theta_\theta^2}\left(1-m^2\right)}_{\text{area rotation around } \boldsymbol{\delta}_z\ (R_z)} - \underbrace{\frac{\partial^2\gamma}{\partial\theta_z^2}(ka)^2}_{\text{area rotation around } \boldsymbol{\delta}_\theta\ (R_\theta)}$$

$$\underbrace{-\frac{wa^2}{\xi}\left[(\mathbf{N}\cdot\mathbf{n})\left(\nabla_s\cdot\mathbf{n}\right) + \mathbf{Nn}:\nabla_s\mathbf{n}\right]}_{\text{director curvature (DC)}} > 0 \quad (2.57)$$

denoted as area reduction (AR), area rotation around $\boldsymbol{\delta}_z$ (R_z), area rotation around $\boldsymbol{\delta}_\theta$ (R_θ), and director curvature (DC). Whether a mechanism drives or quenches the instability depends on its sign. The AR mechanism is stabilizing for $m \geq 1$, and destabilizing for $m = 0$ and $ka < 1$. The rotation and DC mechanisms can drive or quench the instabilities since the sign of anchoring energy coefficient w is not fixed. The emergence of chiral modes ($m \geq 1$) is possible only if

$$\frac{\partial^2\gamma}{\partial\theta_\theta^2} = w\left[(\mathbf{n}\cdot\boldsymbol{\delta}_\theta)^2 - (\mathbf{n}\cdot\mathbf{N})^2\right] < 0\,, \quad (2.58)$$

Table 2.1: Anisotropic contributions to the Rayleigh instabilities according to Eq.(2.60).

Texture	α_{R_z}: rotation around $\boldsymbol{\delta}_z$	α_{R_θ}: rotation around $\boldsymbol{\delta}_\theta$	$\alpha_{\rm DC}$: director curvature
Axial $\mathbf{n} = \boldsymbol{\delta}_z$	0	+1	0
Onion $\mathbf{n} = \boldsymbol{\delta}_\theta$	+1	0	+1
Radial $\mathbf{n} = \boldsymbol{\delta}_r$	$-\frac{1}{2}$	$-\frac{1}{2}$	−1

and the two characteristic cases are

$$\text{(i) } \mathbf{n} = \mathbf{N},\ w > 0\,;\ \ \frac{\partial^2 \gamma}{\partial \theta_\theta^2} = -w\ < 0\,, \qquad \text{(ii) } \mathbf{n} = \boldsymbol{\delta}_\theta,\ w < 0\,;\ \ \frac{\partial^2 \gamma}{\partial \theta_\theta^2} = w\ < 0\,. \tag{2.59}$$

Chiral modes arise (i) when the director is homeotropic ($\mathbf{n} = \mathbf{N}$) and the easy axis is planar ($w > 0$), and (ii) when the director is along the azimuthal direction ($\mathbf{n} = \boldsymbol{\delta}_\theta$) but the easy axis is homeotropic ($w < 0$). For the three characteristic director textures, i.e., axial ($\mathbf{n} = \boldsymbol{\delta}_z$), onion ($\mathbf{n} = \boldsymbol{\delta}_\theta$), and radial ($\mathbf{n} = \mathbf{N} = \boldsymbol{\delta}_r$), the general Rayleigh instability condition (2.57) simplifies to

$$\left(\gamma_{is} + \alpha_{R_z} w\right)\left(1 - m^2\right) - \left(\gamma_{is} + \alpha_{R_\theta} w\right)(ka)^2 - \alpha_{\rm DC} w > 0\,, \tag{2.60}$$

and in dimensionless form, by setting $\tau \equiv w/\gamma_{is}$,

$$\left(1 + \alpha_{R_z} \tau\right)\left(1 - m^2\right) - \left(1 + \alpha_{R_\theta} \tau\right)(ka)^2 - \alpha_{\rm DC} \tau > 0\,, \tag{2.61}$$

where the coefficients $\{\alpha_i\}$, $i = \alpha_{R_z}$, α_{R_θ}, $\alpha_{\rm DC}$ are equal to 0, $-1/2$, or ± 1, depending on the director orientation, as shown in Table 2.1. For the axial texture $\mathbf{n} = \boldsymbol{\delta}_z$, the director has no curvature: $\alpha_{R_z} = 0$, $\alpha_{R_\theta} = 1$, $\alpha_{\rm DC} = 0$. For the onion texture $\mathbf{n} = \boldsymbol{\delta}_\theta$, the director has bending curvature: $\alpha_{R_z} = 1$, $\alpha_{R_\theta} = 0$, $\alpha_{\rm DC} = 1$. For the radial texture $\mathbf{n} = \boldsymbol{\delta}_r$, the director has splay curvature: $\alpha_{R_z} = -1/2$, $\alpha_{R_\theta} = -1/2$, $\alpha_{\rm DC} = -1$. Clearly a rotation mechanism is activated when the director has a projection normal to a given rotation axis. For radial textures, two orthogonal rotations are equally likely and thus $\alpha_{R_z} = \alpha_{R_\theta} = -1/2$. We next discuss the thresholds and parametric dependence of the Rayleigh instabilities for each texture. We will consider peristaltic (axisymmetric) and chiral (non-axisymmetric) modes, as well as bounded ($D > ka > 0$; D is finite) and unbounded modes ($ka > 0$). Unbounded modes denote Hadamard catastrophic instabilities that are regularized, for instance, by viscoelastic modes not included

here but further investigated in the following chapters. Chiral bounded modes arise sequentially since m is quantized, and are denoted as chiral sequential modes. It is interesting to note that unbounded instabilities in anisotropic systems were already discussed by Cahn [18]. In what follows we use the following nomenclature for instability modes: peristaltic bounded (PB), peristaltic unbounded (PU), chiral sequential (CS), and chiral unbounded (CU). The azimuthal wave numbers for these modes are peristaltic bounded modes, $m_{\mathrm{PB}} = 0$; peristaltic unbounded modes, $m_{\mathrm{PU}} = 0$; chiral bounded modes, $m_{\mathrm{CB}} \geq 1$; and chiral unbounded modes, $m_{\mathrm{CU}} \geq 1$. A summary of all the instability modes, their parametric dependence, and main driving forces for the three characteristic fiber textures are given in Tables 2.2–2.4, and discussed in detail in the following:

(1) *Axial textures* (Table 2.2). When $\mathbf{n} = \boldsymbol{\delta}_z$, the instability equation (2.61) is

$$\left(1 - m^2\right) - (1 + \tau)\,(ka)^2 > 0 \tag{2.62}$$

and leads to the two following axisymmetric (peristaltic) and non-axisymmetric (chiral) instability modes:

(a) Peristaltic bounded mode (PB)

$$\tau > -1\,; \quad \frac{1 - m_{\mathrm{PB}}^2}{1+\tau} > (ka)^2 > 0\,, \tag{2.63}$$

where the driving force is the area reduction (AR).

(b) Peristaltic and chiral unbounded modes (PU, CU)

$$-2 < \tau < -1\,; \qquad (ka)^2 > 0 \;\text{ for } m = 0, 1\,, \qquad (ka)^2 > \frac{m_{\mathrm{CU}}^2 - 1}{|1+\tau|} \;\text{ for } m \geq 2\,, \tag{2.64}$$

where the driving forces are the area reduction (AR) and rotations (R_θ) for $m = 0$, and only rotations (R_θ) for $m \geq 1$. Since the area reduction mechanism is weaker as m increases, higher-order modes arise at shorter wavelengths (lager wavenumbers).

(2) *Onion textures* (Table 2.3). When $\mathbf{n} = \boldsymbol{\delta}_\theta$, the instability equation (2.61) is

$$(1 + \tau)\left(1 - m^2\right) - (ka)^2 - \tau > 0 \tag{2.65}$$

Table 2.2: Axial texture (AT).

Instability mechanisms	Rotation around $\boldsymbol{\delta}_\theta$ (R_θ)	Area reduction (AR)	Director curvature (DC)
Schematics of instability mechanisms	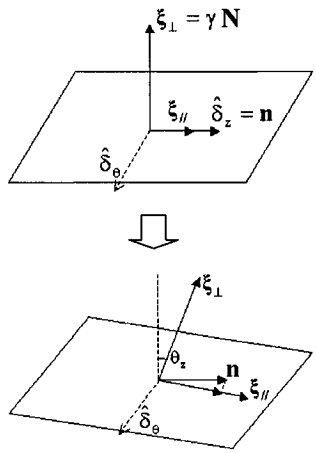	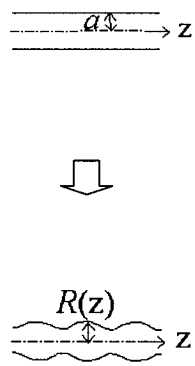	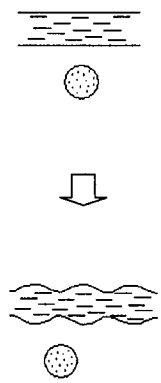
$-p_c$	$\frac{\partial^2 \gamma}{\partial \theta_z^2} \chi_{zr} = -w\,(ka)^2$	$\gamma\,(\chi_{\theta r} + \chi_{zr}) =$ $\gamma_{is}\left[\left(1-m^2\right) - (ka)^2\right]$	None
Driving force	$w < 0\,;\ -w\,(ka)^2$	$m = 0\,;\ \gamma_{is}$	None
Instability condition	$\left(1-m^2\right) - (1+\tau)\,(ka)^2 > 0$		
Instability type	$-2 < \tau < -1\,;\quad m_{\mathrm{PU}} = 0,\, m_{\mathrm{CU}} \geq 1$ Peristaltic and Chiral Unbounded		$\tau > -1\,;\quad m_{\mathrm{PB}} = 0$ Peristaltic Bounded
Schematics of unstable fibers	 $m_{\mathrm{PU}} = 0$ $m_{\mathrm{CU}} = 1$		 $m_{\mathrm{PB}} = 0$

Table 2.3: Onion texture (OT).

Instability mechanisms	Rotation around $\boldsymbol{\delta}_z$ (R_z)	Area reduction (AR)	Director curvature (DC)
Schematics of instability mechanisms	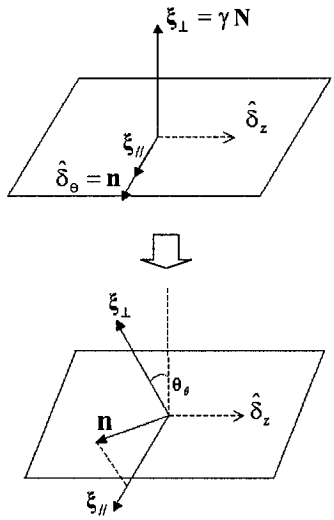	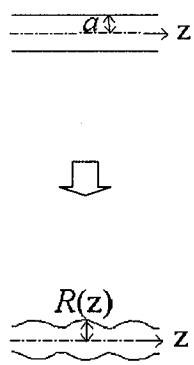	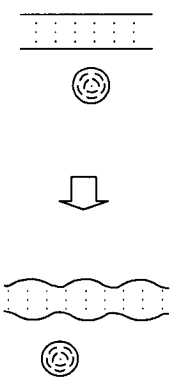
$-p_c$	$\frac{\partial^2 \gamma}{\partial \theta_\theta^2} \chi_{\theta r} = -w\left(1-m^2\right)$	$\gamma\left(\chi_{\theta r}+\chi_{zr}\right) = \gamma_{is}\left[\left(1-m^2\right)-(ka)^2\right]$	$-w$
Driving force	$m=0$, $w>0$ $\Big\}$ w $m \geq 1$, $w<0$ $\Big\}$ $w\left(1-m^2\right)$	$m=0$; γ_{is}	$w<0$; $-w$
Instability condition	$(1+\tau)\left(1-m^2\right)-(ka)^2-\tau>0$		
Instability type	$-2<\tau<0$; Peristaltic Bounded, $m_{\mathrm{PB}}=0$ Chiral Sequential, $m_{\mathrm{CS}} \geq 1$		$\tau \geq 0$; $m_{\mathrm{PB}}=0$ Peristaltic Bounded
Schematics of unstable fibers	 $m_{\mathrm{PB}}=0$ $m_{\mathrm{CS}}=1$ $m_{\mathrm{CS}}=2$		 $m_{\mathrm{PB}}=0$

and leads to the following axisymmetric (peristaltic) and non-axisymmetric (chiral) bounded modes:

(a) Peristaltic bounded modes (PB)

$$\tau > -2\,;\quad 0 < (ka)^2 < (1+\tau)\left(1 - m_{\mathrm{PB}}^2\right) - \tau = 1\,, \tag{2.66}$$

where the driving force is the area reduction (AR), for $\tau < 0$ also director curvature (DC), and for $\tau > 0$ also rotation (R_z).

(b) Chiral sequential bounded modes (CS)

$$m_{\mathrm{CS}} \geq 1\,,\ \tau \leq \tau_{cm} < 0\,;\quad 0 < (ka)^2 < -\left|1 - m_{\mathrm{CS}}^2\right|(1+\tau) - \tau\,,\quad \tau_{cm} = \frac{-\left|1 - m_{\mathrm{CS}}^2\right|}{1 + \left|1 - m_{\mathrm{CS}}^2\right|}\,, \tag{2.67}$$

where τ_{cm} is the upper critical value of emergence for the mode m. For $m = 1$ the instability is driven by director curvature. For $m > 1$, the instability driving force is the R_z rotation and director curvature. When $\tau < 0$ the easy axis is homeotropic and a surface rotation around $\boldsymbol{\delta}_z$ can lower the energy. The $m = 2$ mode is ignited when $\tau \leq \tau_{c2} = -3/4$, the $m = 3$ mode when $\tau \leq \tau_{c3} = -8/9$, and so on. As $m \longrightarrow \infty$, $\tau_{c\infty} \longrightarrow -1$, and hence when $\tau < -1$ all modes ($m \geq 0$) are unstable (see Figure 2-8 and discussion below).

(3) *Radial textures* (Table 2.4). When $\mathbf{n} = \boldsymbol{\delta}_r$, the instability equation (2.61) is

$$\left(1 - \frac{\tau}{2}\right)\left[\left(1 - m^2\right) - (ka)^2\right] + \tau > 0 \tag{2.68}$$

and leads to the following axisymmetric (peristaltic) and non-axisymmetric (chiral) bounded modes:

(a) Peristaltic bounded modes (PB)

$$-2 < \tau < 2\,;\quad 0 < (ka)^2 < \frac{(2-\tau)\left(1 - m_{\mathrm{PB}}^2\right) + 2\tau}{|\tau - 2|} = \frac{\tau + 2}{|\tau - 2|}\,, \tag{2.69}$$

where the driving forces are the area reduction (AR), for $\tau > 0$ also director curvature (DC) and rotation mode (R_θ), and for $\tau < 0$ also rotation mode (R_z).

Table 2.4: Radial texture (RT).

Instability mechanisms	Rotation (R_θ)	Rotation (R_z)	Area reduction (AR)	Director curvature (DC)
Schematics of instability mechanisms	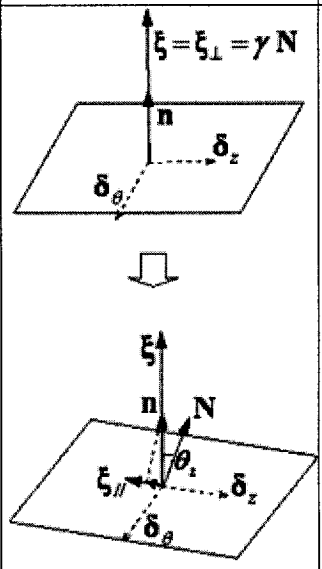	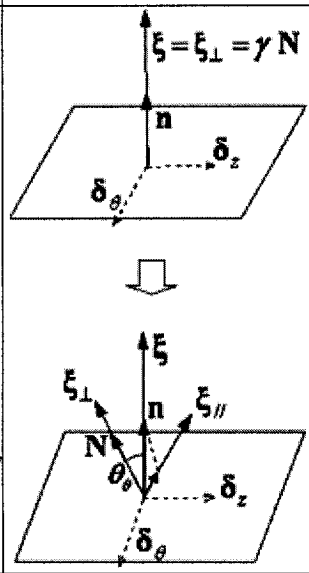	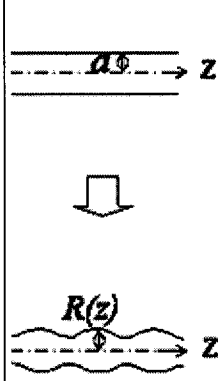	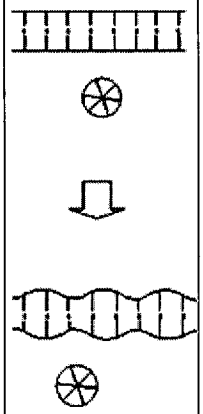
$-p_c$	$\frac{\partial^2\gamma}{\partial\theta_z^2}\chi_{rz} = w(ka)^2$	$\frac{\partial^2\gamma}{\partial\theta_\theta^2}\chi_{r\theta} = -w(1-m^2)$	$\gamma(\chi_{r\theta}+\chi_{rz}) =$ $\gamma[(1-m^2)-(ka)$ $(\gamma=\gamma_{is}+w/2)$	w
Driving force	$w>0$; $w(ka)^2$	$\begin{Bmatrix} m=0 \\ w<0 \end{Bmatrix} -w$ $\begin{Bmatrix} m\geq 1 \\ w>0 \end{Bmatrix} -w(1-m^2)$	$m=0$; γ	$w>0$; w
Instability condition	$\left(1-\frac{\tau}{2}\right)\left[(1-m^2)-(ka)^2\right]+\tau \ >0$			
Instability type	$-2<\tau\leq 0$ $m_{PB}=0$	$0<\tau<2$ $m_{PB}=0,\ m_{CS}\geq 1$	$\tau\geq 2$ $m_{PU}=0,\ m_{CU}\geq 1$	
Schematics of unstable fibers	 $m_{PB}=0$	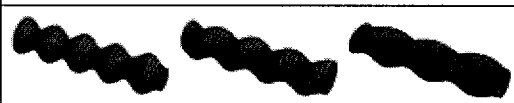 $m_{PB}=0$ $m_{CS}=1$ $m_{CS}=2$	 $m_{PU}=0$ $m_{CU}=1$	

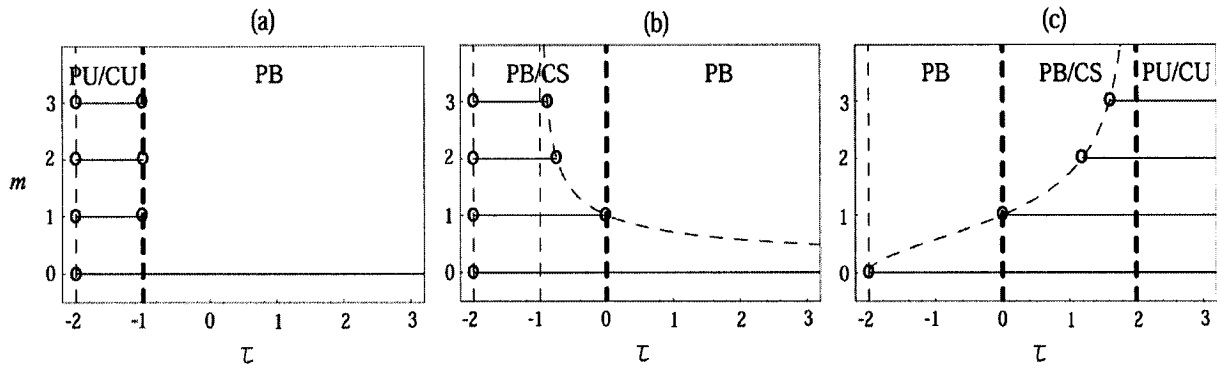

Figure 2-8: Azimuthal wavenumber m as a function of dimensionless anchoring energy τ for (a) axial, (b) onion, and (c) radial textures. The captions (PB, PB/CS, PU/CU) refer to the instability types of Tables 2.2-2.4, and the instability regions are divided by thick dashed lines. In (b) and (c), the dashed curves indicate either the upper or the lower critical value, τ_{cm}, for the emergence of each instability mode m.

(b) Peristaltic and chiral unbounded modes (PU, CU)

$$\tau \geq 2; \quad (ka)^2 > 0 \ \text{ for } m \geq 0, \tag{2.70}$$

where the driving forces are the area reduction (AR), director curvature (DC), and rotation mode (R_θ).

(c) Chiral sequential bounded modes (CS)

$$m_{\rm CS} \geq 1, \quad 0 < \tau \leq \tau_{cm} < 2; \quad (ka)^2 < \frac{2\tau}{(2-\tau)} - \left|1 - m_{\rm CS}^2\right|, \quad \tau_{cm} = \frac{2\left|1 - m_{\rm CS}^2\right|}{2 + \left|1 - m_{\rm CS}^2\right|}, \tag{2.71}$$

where the driving forces are rotation (R_z, R_θ) and director curvature (DC). As τ becomes positive and increases, the $m = 1$ mode arises at $\tau_{c1} = 0$, then the $m = 2$ mode at $\tau_{c2} = 6/5$, and then the $m = 3$ mode at $\tau_{c3} = 16/10$, and as $m \longrightarrow \infty$, $\tau_{c\infty} \longrightarrow 2$ (see Figure 2-8 and discussion below).

Figure 2-8 shows the azimuthal wavenumber m as a function of dimensionless anchoring energy τ for (a) axial, (b) onion, and (c) radial textures. The captions (PB, PB/CS, PU/CU) refer to the instability types of Tables 2.2–2.4, and the instability regions are divided by thick dashed lines. In Figs. 2-8(b) and 2-8(c), the dashed curves indicate either the upper or the

lower critical value, τ_{cm}, for the emergence of each instability mode m. Figure 2-8(a) shows the transition of instability mechanisms from PB to PU/CU at $\tau = -1$ in the axial texture. Figure 2-8(b) shows that for the onion texture CS modes emerge when $\tau < 0$, and the instability creation curve diverges as $\tau \longrightarrow -1^{+}$, indicating that in this limit, represented by the vertical dashed line at $\tau = -1$, all m modes are unstable. For the radial texture CS modes emerge when $\tau > 0$, and the instability creation curve diverges as $\tau \longrightarrow 2^{-}$, indicating that all m modes are unstable in this limit and even become unbounded.

2.8 Conclusions

The Cahn-Hoffman capillarity vector thermodynamics formalism for anisotropic surfaces has been adapted to nematic liquid crystal surfaces, and its connection with the classical stress tensor model has been established. The Cahn-Hoffman capillarity vector formalism offers a clear and tractable methodology to analyze capillarity forces in nematic surfaces. The existence of rotational forces and their connection to gradients of anchoring energy and bending stresses has been established. The potential minimization of anchoring energy leads to surface rotations and bending stresses. The nematic Cahn-Hoffman capillarity vector is an efficient tool to analyze shape selection and surface patterning processes in liquid crystals.

The Cahn-Hoffman capillarity vector thermodynamics on curved anisotropic interfaces can be adapted to liquid crystal interfaces since the interfacial tension of liquid crystals is orientation dependent. The anchoring energy of liquid crystals appears as the property that renormalizes the isotropic component of the interfacial tension and promotes the rotation of the interface. Since the orientational order of liquid crystals on curved interfaces can exhibit gradients, the classical Herring's formula for capillary pressure contains four contributions: surface area reduction, two surface area rotations, and director curvature. Rayleigh capillary instabilities in isotropic materials display only peristaltic mode, since they are driven by area reduction. Other anisotropic systems such as liquid crystals also exhibit chiral capillary instabilities that lead to an increase of the surface area. The chiral modes produce twisted microstructures driven by area rotation and director curvature mechanisms. Chiral modes emerge whenever orientation along the azimuthal direction tends to rotate the surface or when splay or bend orientation

curvature is too costly to produce. The chiral modes are capillary instabilities that lead to novel structuring and patterning of anisotropic fibers.

Bibliography

[1] A. A. Sonin, *The Surface Physics of Liquid Crystals* (Gordon and Breach Publishers, Amsterdan, 1995).

[2] B. Jerome, in *Handbook of Liquid Crystals*, edited by D. Demus, J. Goodby, G. W. Gray, H.-W. Spiess, and V. Vill (Wiley-VCH, Weinheim, 1998).

[3] H. Yokoyama, in *Handbook of Liquid Crystal Research*, edited by P. J. Collins and J. S. Patel (Oxford University Press, New York, 1997).

[4] T. J. Sluckin and A. Poniewierski, in *Fluid Interfacial Phenomena*, edited by C. A. Croxton (Wiley, Chichester, 1986).

[5] S. Faetti, in *Physics of Liquid Crystalline Materials*, edited by I-C Khoo and F. Simoni (Gordon and Breach, Philadelphia, 1991).

[6] E. G. Virga, *Variational Theories for Liquid Crystals* (Chapman Hall, London, 1994).

[7] A. K. Sen and D. E. Sullivan, Phys. Rev A. **35**, 1391 (1987).

[8] G. Barbero and G. Durand, in *Liquid Crystals in Complex Geometries*, edited by G. P. Crawford and S. Zumer (Taylor and Francis, London, 1996).

[9] J. T. Jenkins and P. J. Barrat, Quart. J. Mech. Appl. Math. **27**,111 (1974).

[10] J. L. Ericksen, in *Advances in Liquid Crystals*, edited by G. H. Brown (Academic, New York, 1979), vol.4.

[11] C. Papenfuss and W. Muschik, Mol. Mater. **2**, 1 (1992).

[12] A. D. Rey, J. Chem. Phys. **113**, 10820 (2000).

[13] A. D. Rey, Phys. Rev. E **61**, 1540 (2000).

[14] D. W. Hoffman and J. W. Cahn, Surf. Sci. **31**, 368 (1972).

[15] P. G. de Gennes and J. Prost, *The Physics of Liqid Crystals* (Oxford University Press, London, 1993).

[16] A. P. Sutton and R. W. Balluffi, *Interfaces in Crystalline Materials* (Oxford Science Clarendon Press, New York, 1995).

[17] J. W. Cahn and D. W. Hoffman, Acta Metall. **22**, 1205 (1974).

[18] J. W. Cahn, Scr. Metall. **13**, 1069 (1979).

[19] S. Middleman, *Modeling Axisymmetric Flows: Dynamics of Films, Jets, and Drops* (Academic Press, San Diego, 1995).

[20] A. M. Glaeser, Interface Sci. **9**, 65 (2001).

[21] B. Barriere, K. Sekimoto, and L. Leibler, J. Chem. Phys. **105**, 1735 (1996).

[22] X. Li, Atomization and Sprays **5**, 89 (1995).

[23] J. V. Selinger, F. C. MacKintosh, and J. M. Schnur, Phys. Rev. E **53**, 3804 (1996).

[24] A. Tardieu, V. Luzzati, and F. C. Reman, J. Mol. Biol. **75**, 711 (1973).

[25] J. A. N. Zasadzinski, J. Schneir, J. Gurley, V. Elings, and P. K. Hansma, Science **239**, 1013 (1988).

[26] A. Rapini and M. Papoular, J. Phys. (Paris), Colloq. C4, **30**, 54 (1969).

Chapter 3

Capillary Instabilities in a Thin Nematic Liquid Crystalline Fiber Embedded in Viscid and Inviscid Matrices

3.1 Summary

A complete identification and characterization of three distinct capillary instabilities in nematic liquid crystalline fibers is presented. Linear stability analysis of capillary instabilities in a thin nematic liquid crystalline cylindrical fiber embedded in immiscible viscid and inviscid matrices is performed by formulating and solving the governing nemato-capillary equations. In the case of a viscous matrix, the governing nemato-capillary equations include the effect of interfacial viscous shear forces due to flow in the viscous matrix. A representative axial nematic orientation texture is studied. The surface disturbance is expressed in normal modes, which include the azimuthal wavenumber m to take into account non-axisymmetric modes of the disturbance. Capillary instabilities in nematic fibers reflect the anisotropic nature of liquid crystals, such as the orientation contribution to the surface elasticity and surface bending stresses. Surface gradients of bending stresses provide additional anisotropic contributions to the capillary pressure

that may renormalize the classical displacement and curvature forces that exist in any fluid fiber. The exact nature (stabilizing and destabilizing) and magnitude of the renormalization of the displacement and curvature forces depend on the nematic orientation and the anisotropic contribution to the surface energy. Accordingly, capillary instabilities may be axisymmetric or non-axisymmetric, with finite or unbounded wavelengths. Thus, the classical fiber-to-droplet transformation is one of several possible instability pathways while others include surface fibrillation. The contribution of the viscosity ratio to the capillary instabilities of a thin nematic fiber in a viscous matrix is analyzed by two parameters, the fiber and matrix Ohnesorge numbers, which represent the ratio between viscous and surface forces in each phase. The capillary instabilities of a thin nematic fiber in a viscous matrix are suppressed by increasing either fiber or matrix Ohnesorge number, but estimated droplet sizes after fiber break-up in axisymmetric instabilities decrease with increasing matrix Ohnesorge number.

3.2 Introduction

This chapter is concerned with the mechanics and stability of a thin nematic liquid crystalline fiber embedded in viscid and inviscid matrices. In the first part of this chapter, capillary instabilities in a liquid crystalline fiber in an inviscid matrix are analyzed, and we extend this work in the second part of this chapter to include viscous matrix effects.

A question of fundamental importance in capillary instabilities of thin fibers is the nature of the modes that arise as driven by surface tension forces. In isotropic fluid fibers, the fiber-to-droplet transformation is well understood and known as the Rayleigh instability [1, 2, 3]. In this case, displacement capillary forces drive the fiber break-up, while curvature dependent forces resist the instability thus setting a lower cutoff in the resulting droplet sizes. Since in these materials surface tension is isotropic, only axisymmetric mode emerges, eventually generating spherical droplets. On the other hand, an essential characteristic of nematic liquid crystals is mechanical anisotropy [4]. The anisotropies in the viscoelastic bulk properties of nematic liquid crystals are well understood theoretically [5, 6] and experimentally [4], and the anisotropies in the surface elastic properties of nematics are also well-characterized [7, 8]. It is well-known that the surface tension of nematics contains an isotropic contribution as well

as an anisotropic contribution, known as the anchoring energy [7, 8, 4]. The role of anchoring energy on capillary instabilities has been partially studied [9, 10] with simplified versions of the governing interfacial linear momentum balance equations. The study of capillary instabilities is based on analysis of macroscopic flow produced by gradients in capillary pressure [1, 10]. The capillary pressure is found by projecting the surface gradient of the surface stress tensor along the unit surface normal vector. Thus, the nature of surface stress tensor is at the center of capillary instabilities. For isotropic fluids, the surface stress tensor is a diagonal 2×2 tensor, the capillary pressure is isotropic, and non-axisymmetric modes of thin cylindrical fibers are thus stable because curvature dampens such costly deformation [2] (Isotropic jets, on the other hand, may develop non-axisymmetric disturbances but only through inertia effects [11, 12, 13]). For nematic liquid crystals, the surface stress tensor is a 2×3 tensor, exhibiting both *normal* and *bending* stresses [14]. Bending stresses arise because the surface energy depends on the nematic orientation at the surface. The bending stresses attempt to deform the surface if the surface energy can be lowered in doing so. In the first part of this chapter, we show that gradients in bending stresses renormalize the capillary pressure effects, creating new axisymmetric and non-axisymmetric capillary instabilities.

Tomotika [15] has analyzed capillary fiber instabilities of isotropic viscous fluids in an isotropic viscous matrix, and in particular its dependence on the fiber-to-matrix viscosity ratio. It was shown that the fastest growing wavelength of the instability, i.e., the wavelength corresponding to the maximum (fastest) growth rate of the instability, as a function of the viscosity ratio had a local maximum, implying that smallest droplets after fiber break-up were expected at a finite viscosity ratio. Meanwhile, the fastest growing wavelength increased to infinity as the viscosity ratio approached zero, e.g., inviscid fiber/viscous matrix, or infinity, e.g., viscous fiber/inviscid matrix as in earlier Rayleigh's study [16]. Kinoshita [17] recently extended Tomotika's work by enlarging the parameter space, taking into account the fiber Ohnesorge number and the matrix-to-fiber viscosity ratio. Good agreement among several studies [15, 17, 18] were reported. In the classical Tomotika's work [15], the only parameter is the viscosity ratio since different groups of parameters are chosen in the process of derivation and non-dimensionalization of the growth rate equation. In the other studies [17, 18] and in the present work, the model contains two parameters, the matrix-to-fiber viscosity ratio and

the fiber Ohnesorge number. According to Ref. [17], Tomotika's results underestimate the maximum dimensionless wavenumber for a given viscosity ratio because the Ohnesorge number is not included in the model. In this work, we include the Ohnesorge number and find results in qualitative agreement with Refs. [17, 18]. In the second part of this chapter, we adopt the nemato-capillary equation for the fiber which further contains the viscous stress force at the interface, and thus show the effect of the viscosity ratio on the capillary instabilities using the natural fiber and the matrix Ohnesorge numbers. It is also shown with this novel approach that a possible path in our parametric plane yields results in good agreement with other computational models found in the literature for Newtonian fluids [15, 17, 18].

The specific objectives of this chapter are to: (1) derive a general equation that describes capillary instabilities in a thin nematic liquid crystal fiber embedded in viscid and inviscid matrices; (2) characterize all the possible capillary instability modes and elucidate the physical mechanisms that drive and quench the instabilities; (3) characterize the fundamental role of anisotropic surface elasticity and bending stresses in capillary instabilities; (4) establish parametric conditions that lead to axisymmetric and non-axisymmetric capillary instabilities; and (5) characterize the contribution of the matrix-to-fiber viscosity ratio and the fiber Ohnesorge number to capillary instabilities.

The organization of this chapter is as follows. In Section 3.3, we present the governing nemato-capillary equations and derive the instability criteria for a representative nematic texture. In Section 3.4, we characterize all possible instability modes and the geometry of the evolving unstable fiber. The instability mechanisms are clearly identified and discussed in terms of capillary forces. All results are summarized in compact tabular form and discussed in detail, emphasizing the physical as well as mathematical aspects. Representative computed visualizations of unstable fibers are included to complement the tabulated and graphical information. In Section 3.5, we further investigate the stabilizing effects of the viscous matrix when the contribution of the stress tensor in the viscous matrix evaluated at the surface is included. Section 3.6 presents conclusions.

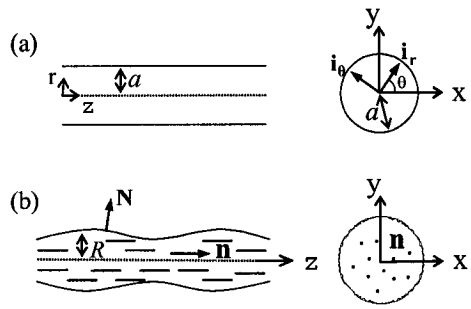

Figure 3-1: (a) Unperturbed fiber with radius a is aligned in the z-axis of cylindrical coordinates (r, θ, z). Cross-sectional view in Cartesian coordinates (x, y) shows the unit vectors $\mathbf{i}_r$ and $\mathbf{i}_\theta$ in azimuthal angle θ. (b) Unit surface normal $\mathbf{N}$ and director field $\mathbf{n}$ ($n_z = 1$) of the axial nematic fiber with surface disturbances. Fiber radius R and unit surface normal $\mathbf{N}$ change along the z- and θ-directions. In the cross-section, the director field $\mathbf{n}$ is shown as dots and θ-directional surface disturbances as small-amplitude wrinkles at the surface.

3.3 Governing Equations

3.3.1 Geometry and texture of nematic liquid crystalline fibers

To completely define the state of a nematic liquid crystalline fiber, both the geometry of the fiber and the spatial orientational order of the nematic liquid crystal must be specified. More specifically, Nematic Liquid Crystalline Fiber $\equiv \{\mathbf{n}, R, \mathbf{N}\}$, where $\mathbf{n}$ is the nematic director field [4], R is the fiber radius, and $\mathbf{N}$ is the unit surface normal vector. For an isotropic material fiber, only the geometry is necessary, i.e., $\{R, \mathbf{N}\}$.

Figure 3-1 shows definitions of the fiber geometry and nematic texture. Figure 3-1(a) shows that the fiber is initially a uniform cylinder with radius a, and the fiber axis is collinear with the z-axis of a cylindrical coordinate system. The fiber nematic texture is expressed by the director field using unit vectors $\mathbf{i}_r$, $\mathbf{i}_\theta$, and $\mathbf{i}_z$ in the direction of the r-, θ-, and z-axes, respectively. In this chapter, we restrict our analysis to a nematic texture with a fixed director field, denoted as axial texture, and the nematic fiber with the axial texture is called 'axial fiber'. Figure 3-1(b) shows the axial fiber with surface disturbances. In the cross-sectional view of Fig. 3-1(b), the director field $\mathbf{n}$ is shown as dots and the θ-directional surface disturbances as small-amplitude wrinkles at the surface, although in real the surface noise is too small to be visually detected. The fiber radius R and the unit surface normal $\mathbf{N}$ change along the z- and θ-directions. In the

axial texture, the director is oriented along the fiber axis and it is given by

$$\mathbf{n} = \mathbf{i}_z \,. \tag{3.1}$$

The fiber shape at any time t and position z and θ is given by

$$R(z,\theta,t) = a + \xi(z,\theta,t) \,. \tag{3.2}$$

The surface disturbance ξ is expressed by taking normal modes of the form [19, 20]

$$\xi(z,\theta,t) = \xi_0 \exp\left[\alpha t + i\left(kz + m\theta\right)\right] \,, \tag{3.3}$$

where ξ_0 is the initial amplitude of the disturbance, α the growth rate for real and positive values, k the axial wavenumber, and m the azimuthal wavenumber. The wave vector (k, m) is composed of two wave numbers. Due to rotational periodicity, the azimuthal wavenumber m is an integer and specifies the disturbance mode in the azimuthal (θ-) direction. Axisymmetric modes correspond to $m = 0$, while non-axisymmetric modes correspond to $m \neq 0$, i.e., $m = \pm 1, \pm 2, \cdots$. During a capillary instability the fiber geometry evolution is captured by the fiber's radius (R), the principal radii of curvature ($R_{r\theta}$, R_{rz}), and its unit surface normal ($\mathbf{N}$). To discuss capillary instabilities it is also useful to introduce the following expression for the mean curvature H in cylindrical coordinates:

$$\begin{aligned} H &= -\frac{1}{2}\nabla_s \cdot \mathbf{N} = -\frac{1}{2}\left(\frac{1}{R_{r\theta}} + \frac{1}{R_{rz}}\right) \\ &= \frac{-1}{2\sqrt{\left(1 + \frac{R_{,\theta}^2}{R^2} + R_{,z}^2\right)^3}} \left[\begin{array}{l} \frac{1}{R}\left(1 + \frac{2R_{,\theta}^2}{R^2} + R_{,z}^2\right) - \left(1 + R_{,z}^2\right)\frac{R_{,\theta\theta}}{R^2} \\ -\left(1 + \frac{R_{,\theta}^2}{R^2}\right) R_{,zz} + \frac{2}{R^2} R_{,\theta} R_{,z} R_{,\theta z} \end{array} \right] , \end{aligned} \tag{3.4}$$

where ∇_s is the surface gradient operator, $R_{,\theta} = \partial R/\partial\theta$, $R_{,z} = \partial R/\partial z$, $R_{,\theta\theta} = \partial^2 R/\partial\theta^2$, $R_{,zz} = \partial^2 R/\partial z^2$, and $R_{,\theta z} = \partial^2 R/\left(\partial\theta\partial z\right)$. A linearized expression for H is given below (see Eq. (3.24)).

3.3.2 Linear bulk and surface momentum balance equations

We consider the stability of a thin, initially axisymmetric, cylindrical nematic fiber surrounded by an inviscid matrix. The nematic liquid crystal is assumed to be incompressible, and its orientation is homogeneous and constant. Linear stability analysis is used to analyze the complete set of axisymmetric and non-axisymmetric capillary instabilities in nematic liquid crystal fibers. Since the director is fixed, only the surface and bulk linear momentum balance equations define the evolution of the fiber's shape. In this work, the mechanical response of the nematic fluid is that of an anisotropic viscoelastic material [21, 4], where the bulk is viscous and the surface is elastic.

The bulk linear momentum balance equation for this system is given by

$$\rho \frac{\partial \mathbf{v}}{\partial t} = \nabla \cdot \mathbf{t}\,, \tag{3.5}$$

where ρ is the density, $\mathbf{v}$ the velocity vector, $\mathbf{t}$ the total stress tensor. Inertia is neglected. The total stress tensor $\mathbf{t}$ is defined as

$$\mathbf{t} = -p\mathbf{I} + \mathbf{t}^v, \tag{3.6}$$

where p is the pressure, $\mathbf{I}$ the unit tensor, and $\mathbf{t}^v$ the viscous stress tensor. Although nematic liquid crystals have bulk Frank elasticity due to orientation gradients, in this chapter no elastic stresses arise because $\mathbf{n}$ is held constant. Thus, the viscous stress tensor $\mathbf{t}^v$ is expressed by Ericksen's Transversely Isotropic Fluid (TIF) constitutive equation [6]:

$$\mathbf{t}^v = 2\eta_2 \mathbf{A} + \eta_3 \mathbf{A} : \mathbf{nnnn} + 2\left(\eta_1 - \eta_2\right)\left(\mathbf{A}\cdot\mathbf{nn} + \mathbf{nn}\cdot\mathbf{A}\right)\,, \tag{3.7}$$

where η_1, η_2, and η_3 are viscosity coefficients, and $\mathbf{A}$ is the rate of deformation tensor given by

$$\mathbf{A} = \frac{1}{2}\left[\nabla\mathbf{v} + (\nabla\mathbf{v})^{\mathrm{T}}\right]\,, \tag{3.8}$$

where the superscript $^{\mathrm{T}}$ denotes the transpose. When $\eta_1 = \eta_2$ and $\eta_3 = 0$, the constitutive equation for Newtonian fluids is recovered. The TIF equation thus describes an anisotropic viscous material, whose viscosity depends on the director orientation. The continuity equation

for this system is written as

$$\frac{\partial v_z}{\partial z} + \frac{1}{r}\frac{\partial (r v_r)}{\partial r} = 0\,. \tag{3.9}$$

Since the fiber's shape is evolving, a kinematic boundary condition is applied through the radial velocity of the free surface:

$$v_r\,|_R = \frac{\partial R}{\partial t}\,, \tag{3.10}$$

which is used when deriving Eq. (3.33).

In addition to the *bulk* linear momentum balance equation, the presence of an evolving free surface involves the action of surface forces, and thus the *surface* linear momentum balance equation enters the description. The surface linear momentum balance equation is given by [1, 22]

$$-\mathbf{N}\cdot\left(\mathbf{t}^{\mathrm{M}} - \mathbf{t}\right) = \nabla_s \cdot \mathbf{t}^{\mathrm{se}}, \tag{3.11}$$

where $\mathbf{t}^{\mathrm{se}}$ is the surface elastic stress tensor. On the right hand side of Eq. (3.11), the surface viscous stresses are ignored since they are insignificant in relation to the surface elastic stresses. The shape of the evolving fiber depends only on the normal component of the surface linear momentum balance equation, and thus the shape equation is

$$-\mathbf{N}\cdot\left(\mathbf{t}^{\mathrm{M}} - \mathbf{t}\right)\cdot\mathbf{N} = \left(\nabla_s \cdot \mathbf{t}^{\mathrm{se}}\right)\cdot\mathbf{N}\,. \tag{3.12}$$

To make further progress, an expression for the surface elastic stress tensor, $\mathbf{t}^{\mathrm{se}}$, is required. Since nematic liquid crystals are anisotropic viscoelastic materials, anisotropy is an essential feature of $\mathbf{t}^{\mathrm{se}}$. Moreover, surface elastic stresses are defined by constrained variations of the surface energy, which we now discuss.

The simplest expression for the surface free energy of the nematic liquid crystal is given by the Rapini-Papoular constitutive equation [23, 22, 4]:

$$\gamma = \gamma_{is} + \gamma_{an} = \gamma_{is} + \frac{w}{2}\left(\mathbf{n}\cdot\mathbf{N}\right)^2 = \gamma_{is}\left[1 + \frac{\tau}{2}\left(\mathbf{n}\cdot\mathbf{N}\right)^2\right]\,, \tag{3.13}$$

where γ_{is} is the isotropic surface tension, γ_{an} is the anchoring energy due to the nematic orientation at the surface, w is the anchoring energy coefficient, and $\tau = w/\gamma_{is}$ is the ratio of

the anchoring energy to isotropic surface tension. Since the surface free energy and the isotropic surface tension are always positive, τ is restricted to a value greater than -2. If $\tau = 0$, the surface anisotropy vanishes. Depending on the signs of τ, different surface orientations are energetically favorable [24]. For $\tau > 0$, the surface "easy axis", that which minimizes the surface free energy, is parallel to the surface (planar anchoring) and perpendicular to the surface normal vector. For $\tau < 0$, the surface easy axis is perpendicular to the surface (homeotropic anchoring) and parallel to the surface normal vector. Extensions of the Rapini-Papoular formula are used in the literature, specifically to describe thermally-induced surface orientation transitions [25], but these thermal effects are beyond the scope of this chapter.

The expression for the surface elastic stress tensor $\mathbf{t}^{\mathrm{se}}$ is obtained by considering the energetic penalty of constrained variations in γ and is given by the sum of the normal (tension) $\mathbf{t}^{\mathrm{se}}_N$ and the bending $\mathbf{t}^{\mathrm{se}}_B$ contributions [14, 22]:

$$\mathbf{t}^{\mathrm{se}}_N = \gamma \mathbf{I}_s \,, \qquad \mathbf{t}^{\mathrm{se}}_B = -\mathbf{I}_s \cdot \left(\frac{\partial \gamma}{\partial \mathbf{N}} \mathbf{N} \right) . \tag{3.14}$$

Parametrizing the interface with orthonormal unit surface base vectors $(\mathbf{i}_1, \mathbf{i}_2)$, the normal and bending surface elastic stresses become

$$\mathbf{t}^{\mathrm{se}}_N = \left[\gamma_{is} + \frac{w}{2} (\mathbf{n} \cdot \mathbf{N})^2 \right] (\mathbf{i}_1 \mathbf{i}_1 + \mathbf{i}_2 \mathbf{i}_2) \,, \qquad \mathbf{t}^{\mathrm{se}}_B = B^{\mathrm{NI}}_{13} \mathbf{i}_1 \mathbf{N} + B^{\mathrm{NI}}_{23} \mathbf{i}_2 \mathbf{N} \,, \tag{3.15}$$

where the superscript $^{\mathrm{NI}}$ denotes the interface between the nematic liquid crystal (N) and isotropic fluid (I), which is inviscid in this study, and where the bending coefficients $\{B^{\mathrm{NI}}_{13}, B^{\mathrm{NI}}_{23}\}$ are given by

$$B^{\mathrm{NI}}_{13} = -w (\mathbf{n} \cdot \mathbf{N}) (\mathbf{n} \cdot \mathbf{i}_1) \,, \qquad B^{\mathrm{NI}}_{23} = -w (\mathbf{n} \cdot \mathbf{N}) (\mathbf{n} \cdot \mathbf{i}_2) \,. \tag{3.16}$$

The bending coefficients are proportional to the anchoring energy and to the director's projections along the unit normal and along the surface base vectors. The largest magnitudes of the bending coefficients, for given w, arise at $\pi/4$ angles from the interface, and they vanish at the planar and homeotropic orientations. In matrix form, the 2×3 surface elastic stress tensor $\mathbf{t}^{\mathrm{se}}$ is

$$\mathbf{t}^{\mathrm{se}} = \begin{bmatrix} \gamma & 0 & B^{\mathrm{NI}}_{13} \\ 0 & \gamma & B^{\mathrm{NI}}_{23} \end{bmatrix} . \tag{3.17}$$

Clearly the surface stress tensor is asymmetric. Moreover, such bending stresses are intrinsic to nematic interfaces and result in forces normal to the interface, even in the absence of curvature, for a director field not parallel or perpendicular to the interface. The bending stresses play a crucial role in the capillary instability of nematic fibers. Isotropic surface tension leads to axisymmetric capillary instabilities, but anisotropic surface tension leads, through the generation of bending stresses, to non-axisymmetric modes. The reason behind this statement is that forces normal to the interface depend on surface orientation and exist even in the absence of curvature [26, 14].

Using the expression for the surface elastic stress tensor $\mathbf{t}^{\mathrm{se}}$, we find the following expression for the interfacial elastic force $\mathbf{f}^{\mathrm{e}}$ [14]:

$$\begin{aligned}\mathbf{f}^{\mathrm{e}} &= \nabla_s \cdot \mathbf{t}^{\mathrm{se}} = \nabla_s \cdot \mathbf{t}_N^{\mathrm{se}} + \nabla_s \cdot \mathbf{t}_B^{\mathrm{se}} \\ &= \underbrace{\left\{\left[\left(\frac{\partial\gamma}{\partial\mathbf{n}}\right)\cdot\left(\nabla_s\mathbf{n}\right)^{\mathrm{T}}\right]\cdot\mathbf{I}_s + (2H\gamma)\,\mathbf{N}\right\}}_{\text{normal stress contribution}} + \underbrace{\left\{\left[-2H\left(\frac{\partial\gamma}{\partial\mathbf{N}}\cdot\mathbf{N}\right) - \nabla_s\cdot\left(\frac{\partial\gamma}{\partial\mathbf{N}}\right)\right]\mathbf{N}\right\}}_{\text{bending stress contribution}} \end{aligned} \tag{3.18}$$

Eq. (3.18) shows that surface gradients in the normal (tension) surface stress $\mathbf{t}_N^{\mathrm{se}}$ give rise to tangential (perpendicular to $\mathbf{N}$) and normal forces (parallel to $\mathbf{N}$), while surface gradients of bending stress $\mathbf{t}_B^{\mathrm{se}}$ give rise only to normal forces. It is shown in Eq. (3.18) that normal forces from surface gradients of bending stress persist even in the absence of curvature ($H = 0$). Meanwhile, tangential forces have been shown to drive Marangoni nematic flows [14].

The normal component of Eq. (3.18) is known as the generalized Laplace equation [1]:

$$-\mathbf{N}\cdot\left(\mathbf{t}^{\mathrm{M}} - \mathbf{t}\right)\cdot\mathbf{N} = \left(\nabla_s\cdot\mathbf{t}^{\mathrm{se}}\right)\cdot\mathbf{N} = -p_c\,, \tag{3.19}$$

where the superscript $^{\mathrm{M}}$ denotes the matrix fluid, and p_c is the magnitude of the interfacial normal force originating from the surface gradients of the normal and bending stresses, called as the capillary pressure. According to Eq. (3.18) the capillary pressure p_c is given by

$$-p_c = 2H\gamma - 2H\left(\frac{\partial\gamma}{\partial\mathbf{N}}\cdot\mathbf{N}\right) - \nabla_s\cdot\left(\frac{\partial\gamma}{\partial\mathbf{N}}\right)\,. \tag{3.20}$$

Thus, the normal and bending stress contributions to the capillary forces are

$$p_c|_{\text{normal stresses}} = -2H\gamma\,, \qquad p_c|_{\text{bending stresses}} = 2H\left(\frac{\partial\gamma}{\partial\mathbf{N}}\cdot\mathbf{N}\right) + \nabla_s\cdot\left(\frac{\partial\gamma}{\partial\mathbf{N}}\right). \tag{3.21}$$

Thus, the anchoring energy γ_{an} contributes to the capillary pressure through both the *normal* and *bending* stresses. Nevertheless, when considering the linear regime of capillary instability of a nematic liquid crystal fiber, second order terms involving $H\,(\mathbf{n}\cdot\mathbf{N})^2$ cancel out and the only remaining anisotropic contribution to the capillary pressure is that from the bending stresses. Thus, any model that attempts to capture the linear regime of capillary instability in a nematic liquid crystal fiber must include all contributions arising from the bending stress tensor.

3.3.3 Simplifying assumptions

The assumptions made to describe the linear regime of the capillary instability in incompressible, isothermal nematic fibers are:

(a) For sufficiently thin fibers, the surface elastic energy is insignificant with respect to the bulk Frank elasticity [4]. Thus, the orientational elasticity originates not from director variation in the bulk but from surface director deviation from the easy axis; the director field does not change even if the fiber shape evolves through the linear instability process.

(b) In the long wavelength approximation, the wavelength of a dominant surface disturbance is assumed to be much longer than the fiber radius, and the axial velocity is considerably larger than the other velocity components. In the present case, an order of magnitude calculation obtained using the continuity equation yields $v_z \gg v_r,\, v_\theta$ [2]. Thus, only the axial velocity v_z is significant.

(c) In the absence of surrounding matrix effects and in the long wavelength approximation, the radial dependence of axial velocity is ignored so that the axial velocity is considered as a function only of the axial coordinate and time: $v_z\,(z,t)$ [2].

(d) The analysis is restricted to the linear regime of the capillary instability. This restriction is obeyed when $\frac{\xi}{a} \ll 1$.

In the next section, we develop the governing equations for the capillary instabilities of nematic fibers when the director is aligned along the fiber axis ($n_z = 1$).

3.3.4 Governing equations for an axial nematic fiber

In this section, the governing equation of the surface disturbance $\xi(z,\theta,t)$, Eq. (3.3), is derived for the axial fiber by combining the linear momentum balance equation, Eq. (3.5), and the normal stress boundary condition, Eq. (3.19).

During non-axisymmetric capillary instability, the principal radii of the curvature ($R_{r\theta}$, R_{rz}) and the unit surface normal vector $\mathbf{N}$ are obtained in the linear regime using the assumptions stated in the previous section:

$$\frac{1}{R_{r\theta}} = \frac{1}{R} - \frac{1}{R^2}\left(\frac{\partial^2 R}{\partial \theta^2}\right), \qquad \frac{1}{R_{rz}} = -\frac{\partial^2 R}{\partial z^2}, \tag{3.22}$$

$$\mathbf{N} = \mathbf{i}_r - \frac{1}{R}\frac{\partial R}{\partial \theta}\mathbf{i}_\theta - \frac{\partial R}{\partial z}\mathbf{i}_z. \tag{3.23}$$

Note that the radii of curvature are θ-dependent: $R_{r\theta} = R_{r\theta}(z,\theta,t)$, $R_{rz} = R_{rz}(z,\theta,t)$. Thus, the mean curvature H in Eq. (3.4) is expressed as [3]

$$H = -\frac{1}{2}\left(\frac{1}{R_{r\theta}} + \frac{1}{R_{rz}}\right) = -\frac{1}{2}\left[\frac{1}{R} - \frac{1}{R^2}\left(\frac{\partial^2 R}{\partial \theta^2}\right) - \frac{\partial^2 R}{\partial z^2}\right]. \tag{3.24}$$

Under the assumed kinematical conditions, the only non-zero component of $\mathbf{A}$ is

$$A_{zz} = \frac{\partial v_z}{\partial z}. \tag{3.25}$$

The viscous stress tensor, obtained by substituting Eqs. (3.1) and (3.25) into Eq. (3.7), is

$$t^v_{zz} = 2\eta\frac{\partial v_z}{\partial z}, \tag{3.26}$$

where $\eta = \eta_2 + \eta_3/2 + 2(\eta_1 - \eta_2)$. Substituting Eq. (3.26) into Eq. (3.6), the total stress tensor becomes

$$t_{zz} = -p + 2\eta\frac{\partial v_z}{\partial z}. \tag{3.27}$$

Using Eqs. (3.23) and (3.24) in Eq. (3.20), the capillary pressure p_c becomes

$$p_c = \gamma_{is}\left[\frac{1}{a} - \frac{1}{a^2}\xi - \left(\frac{1}{a^2}\frac{\partial^2 \xi}{\partial \theta^2} + \frac{\partial^2 \xi}{\partial z^2}\right) - \tau\frac{\partial^2 \xi}{\partial z^2}\right], \tag{3.28}$$

which properly reduces to the Newtonian capillary pressure when $\tau = 0$, i.e., when surface tension is isotropic. Importantly, when the bending stress contributes to the capillary pressure of an axial fiber, a force $p_c|_{bf}$ appears to be

$$p_c|_{bf} = -\gamma_{is}\tau\frac{\partial^2\xi}{\partial z^2}\,, \tag{3.29}$$

which can compete or cooperate with the usual isotropic contribution since the sign of τ is not fixed. Thus, τ in Eq. (3.28) can be positive, negative, or zero.

The pressure in Eq. (3.27) can be expressed in terms of the capillary pressure [2]:

$$p = -\frac{1}{3}\left(t_{zz} + t_{\theta\theta} + t_{rr}\right) = -\frac{1}{3}\left(t_{zz} - 2p_\gamma\right)\,, \tag{3.30}$$

where following boundary conditions are applied: $t_{rr} = -p_c$, $t_{\theta\theta} = t_{rr}$ at $r = a$. Substituting Eq. (3.30) into Eq. (3.27), the total stress tensor is rewritten as [2]

$$t_{zz} = -p_c + 3\eta\frac{\partial v_z}{\partial z}\,. \tag{3.31}$$

Using Eq. (3.31), the axial momentum balance equation, Eq. (3.5), is found to be [2]

$$\rho\frac{\partial v_z}{\partial t} = -\frac{\partial p_c}{\partial z} + 3\eta\frac{\partial_z^2 v}{\partial z^2}\,. \tag{3.32}$$

By integrating the continuity equation, Eq. (3.9), across the cross section of the fiber, we obtain[1]

$$\frac{\partial R}{\partial t} + \frac{R}{2}\frac{\partial v_z}{\partial z} = 0\,. \tag{3.33}$$

Thus, using Eq. (3.2) the axial velocity can be expressed in terms of ξ [2, 27]:

$$\frac{\partial v_z}{\partial z} = -\frac{2}{a}\frac{\partial \xi}{\partial t}\,. \tag{3.34}$$

Combining Eqs. (3.32) and (3.34) in conjunction with Eq. (3.28) gives the differential equation for ξ:

$$\frac{\partial^2 \xi}{\partial t^2} - \frac{3\eta}{\rho}\frac{\partial^3 \xi}{\partial z^2 \partial t} + \frac{\gamma_{is} a}{2\rho}\frac{\partial^2}{\partial z^2}\left[\frac{\xi}{a^2} + \left(\frac{\partial^2 \xi}{\partial z^2} + \frac{1}{a^2}\frac{\partial^2 \xi}{\partial \theta^2}\right) + \tau\frac{\partial^2 \xi}{\partial z^2}\right] = 0\,. \tag{3.35}$$

By substituting Eq. (3.3) into Eq. (3.35), a quadratic equation for the dimensionless growth rate, $\alpha^* = \alpha\sqrt{\rho a^3/\gamma_{is}}$, is obtained:

$$\alpha^{*2} + 3Oh\,(ka)^2\,\alpha^* - \frac{(ka)^2}{2}\left[1 - m^2 - (1+\tau)\,(ka)^2\right] = 0\,, \tag{3.36}$$

---

[1] We derive Eq. (3.33) using Eq. (3.9). Integrating the continuity equation, Eq. (3.9), across the cross-section of the fiber gives

$$\begin{aligned}
\int_0^{R(z,t)} [\frac{\partial v_z}{\partial z} + \frac{1}{r}\frac{\partial (r v_r)}{\partial r}] r dr &= 0 \\
\int_0^R \frac{\partial v_z}{\partial z} r dr + \int_0^R \partial (r v_r) &= 0 \\
\frac{\partial}{\partial z}\int_0^R v_z r dr - R\frac{\partial R}{\partial z} v_z\,|_R + R\, v_r\,|_R &= 0 \\
\frac{\partial}{\partial z}\left(\frac{R^2}{2} v_z\,|_R\right) - R\frac{\partial R}{\partial z} v_z\,|_R + R\, v_r\,|_R &= 0 \\
\frac{R^2}{2}\frac{\partial (v_z\,|_R)}{\partial z} + R\, v_r\,|_R &= 0
\end{aligned}$$

by using the assumption (c) in section 3.3.3 and the Leibniz rule as follows

$$\begin{aligned}
\frac{\partial}{\partial z}\int_0^{R(z,t)} v_z r dr &= \int_0^{R(z,t)} \frac{\partial}{\partial z}[v_z r]\, dr + \frac{\partial R}{\partial z}[v_z r]\,|_R \\
&= \int_0^R \frac{\partial v_z}{\partial z} r dr + R\frac{\partial R}{\partial z} v_z\,|_R\,.
\end{aligned}$$

Applying the kinematic boundary condition in the linear regime of the capillary instability, Eq. (3.10), i.e. $v_r\,|_R = \frac{\partial R}{\partial t}$, we finally obtain Eq. (3.33):

$$\frac{R}{2}\frac{\partial v_z}{\partial z} + \frac{\partial R}{\partial t} = 0\,.$$

where ka is the dimensionless wavenumber and $Oh = \eta/\sqrt{\rho a \gamma_{is}}$ is the Ohnesorge number, or the ratio of the viscous force to the surface force. Solving the quadratic equation for α^*, Eq. (3.36), we find

$$\alpha^* = \frac{1}{2}\left\{-3Oh\,(ka)^2 + \sqrt{\left[3Oh\,(ka)^2\right]^2 + 2\,(ka)^2\left[1 - m^2 - (1+\tau)\,(ka)^2\right]}\right\}. \tag{3.37}$$

Thus, the axial fibers are unstable when the following inequality is satisfied:

$$-3Oh\,(ka)^2 + \sqrt{\left[3Oh\,(ka)^2\right]^2 + 2\,(ka)^2\left[1 - m^2 - (1+\tau)\,(ka)^2\right]} > 0\,. \tag{3.38}$$

The maximum growth rate $\alpha^*_{\max}$ and the corresponding wavenumber $ka_{\max}$, obtained by solving Eq. (3.36), are

$$\alpha^*_{\max} = \left[2\sqrt{2}\sqrt{\frac{1+\tau}{(1-m^2)^2}} + \frac{6Oh}{(1-m^2)}\right]^{-1}, \quad ka_{\max} = \left[\sqrt{\frac{2\,(1+\tau)}{(1-m^2)} + 3\sqrt{2}Oh\sqrt{\frac{1+\tau}{(1-m^2)^2}}}\right]^{-1}, \tag{3.39}$$

which reduce to the results for Newtonian fluids if the viscoelastic anisotropy and the non-axisymmetric dependence vanish; i.e., $\eta_1 = \eta_2$, $\eta_3 = 0$, $\tau = 0$, and $m = 0$: for the highly viscous fiber, $\alpha^*_{\max} = 1/(6Oh)$ and $ka_{\max} = 1/\sqrt{3\sqrt{2}Oh}$; for the inviscid fiber, $\alpha^*_{\max} = 1/\left(2\sqrt{2}\right)$ and $ka_{\max} = 1/\sqrt{2}$. In particular, when only axisymmetric disturbances become unstable, i.e., $m = 0$, the results from Eq. (3.39) predict the axial fiber break-up into droplets with a characteristic size of $2\pi/\left(ka_{\max}\right)$ [10].

The physics of capillary instabilities in axial nematic fibers can be elucidated by rewriting Eq. (3.28) as

$$p_c = \gamma_{is}\left[\frac{1}{a} - \frac{1}{a^2}\xi - \left(\frac{1}{a^2}\frac{\partial^2\xi}{\partial\theta^2} + \frac{\partial^2\xi}{\partial z^2}\right) - \tau\frac{\partial^2\xi}{\partial z^2}\right] = \frac{\gamma_{is}}{a} + f_d + f_c\,, \tag{3.40}$$

$$f_d = -\frac{1}{a^2}C_\xi\xi\,, \qquad f_c = -\frac{1}{a^2}C_{\xi_{\theta\theta}}\xi_{\theta\theta} - C_{\xi_{zz}}\xi_{zz}\,, \qquad C_\xi = C_{\xi_{\theta\theta}} = \gamma_{is}\,, \qquad C_{\xi_{zz}} = \gamma_{is}\,(1+\tau)\,. \tag{3.41}$$

The capillary pressure contains two (ξ-dependent) deformation effects: a displacement force, f_d, and a curvature force, f_c. Capillary instabilities occur because a spatially periodic pressure

gradient develops, inducing macroscopic flow. The driving force for creating a pressure gradient is denoted as a destabilizing force, while a force resisting it is denoted as a stabilizing force. The nature of the two capillary forces depends only on the sign of their coefficients, C_ξ, $C_{\xi_{\theta\theta}}$, and $C_{\xi_{zz}}$, which are the effective surface tensions for both forces. Thus the displacement force is destabilizing (stabilizing) for $C_\xi > 0$ ($C_\xi < 0$), while the curvature force is stabilizing (destabilizing) for $C_{\xi_{\theta\theta}} > 0$ and $C_{\xi_{zz}} > 0$ ($C_{\xi_{\theta\theta}} < 0$ and $C_{\xi_{zz}} < 0$). In isotropic fibers ($\tau = 0$), the displacement force is always destabilizing and the curvature force is always stabilizing, thus explaining the existence of lower cutoff in the instability wavelength, as in the classical Rayleigh fiber instability (see Figure 3-3 and discussion below). This occurs because the stabilizing curvature force for sufficiently short wavelengths overpowers the driving displacement force. Since for axial fibers $C_\xi > 0$, the displacement force is always destabilizing. On the other hand, since $\tau \geq -2$, the curvature force from ξ_{zz} can be destabilizing if $\tau < -1$ because $C_{\xi_{zz}} < 0$ or stabilizing if $\tau > -1$ because $C_{\xi_{zz}} > 0$, although the curvature force from $\xi_{\theta\theta}$ is always stabilizing. Thus, when the curvature force from ξ_{zz} is destabilizing ($\tau < -1$), a lower cutoff wavelength does not exist and the instability must be of the Hadamard type (see Figure 3-2 and discussion below). Since τ is the bending force coefficient (see Eq. (3.29)), the described phenomenology of capillary instabilities in axial fibers is attributed to anisotropic effects arising from surface gradients of bending stresses.

3.4 Results and Discussion

The characterization of capillary instabilities in nematic fibers requires the specification of two features: (i) Instability mechanism; (ii) Symmetry of deformation modes. These two features are embedded in Eq. (3.37) and must be considered separately.

(i) *Instability mechanism*

The capillary instabilities in nematic liquid crystalline fibers are found to follow two different routes: Modified Rayleigh and Catastrophic instability mechanisms.

(a) Modified Rayleigh (MR) instability mechanism

The modified Rayleigh instability is characterized by a single $m = 0$ mode. Setting in

Eqs. (3.37) and (3.39), we find that the nematic fibers are MR-unstable whenever

$$2a^*\left(m=0\right)=-3Oh\left(ka\right)^2+\sqrt{\left[3Oh\left(ka\right)^2\right]^2+2\left(ka\right)^2\left[1-\left(1+\tau\right)\left(ka\right)^2\right]}\;>0\,, \tag{3.42}$$

$$\alpha^*_{\max}\left(m=0\right)=\left[2\sqrt{2}\sqrt{1+\tau}+6Oh\right]^{-1}\;>0\,, \tag{3.43}$$

$$0<\;ka_{\max}\left(m=0\right)=\left[\sqrt{2\left(1+\tau\right)+3\sqrt{2}Oh\sqrt{1+\tau}}\right]^{-1}\;<\;ka_{\text{cutoff}}\,, \tag{3.44}$$

where ka_{cutoff} is an upper cutoff wavenumber above which disturbances do not grow. The axial fibers have no azimuthal dependence and thus axisymmetric.

(b) Catastrophic (C) simultaneous instability mechanism

In the catastrophic simultaneous instability mechanism, unstable modes follow the classical short wave (small wavelength) instability [28], which is characterized by simultaneous occurrence of all azimuthal modes m with unbounded growth rate. Using Eq. (3.37), we find that the nematic fibers are C-unstable whenever

$$2\alpha^*=-3Oh\left(ka\right)^2+\sqrt{\left[3Oh\left(ka\right)^2\right]^2+2\left(ka\right)^2\left[1-m^2-\left(1+\tau\right)\left(ka\right)^2\right]}\;>0\,,\quad\frac{d\alpha^*}{d\left(ka\right)}\;>0\,, \tag{3.45}$$

where $ka\;>\;0$ for a catastrophic instability without upper ka_{cutoff}. Under this instability mechanism, the following ordering in growth rates is found:

$$\alpha^{*0}>\alpha^{*1}>\cdots>\alpha^{*n}>\alpha^{*n+1}>\cdots\,, \tag{3.46}$$

where $\alpha^*\left(m_n\right)\equiv\alpha^{*n}$ while m_n represents $m=n$ mode hereafter.

(ii) *Symmetry of deformation modes*

The symmetry of the deformation in this chapter is restricted to axisymmetric and non-axisymmetric modes, axisymmetric modes being rotationally invariant. It is noted that for axial fibers the $m=0$ mode is, as usual, an axisymmetric mode.

Based on this general discussion, the criteria required to classify the capillary instability are given by specification of: Instability mechanism/Symmetry. The following three cases emerge:

(a) Modified Rayleigh/Axisymmetric (MR/A)

(b) Catastrophic/Axisymmetric (C/A)

Table 3.1: Capillary instabilities in axial fibers according to Eqs.(3.38) and (3.62).

Instability type	Region I ($\tau > -1$)	Criticality ($\tau = -1$)	Region II ($-1 > \tau \geq -2$)
MR/A	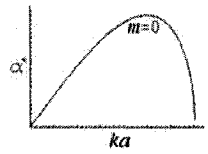	No	No
C/A	No	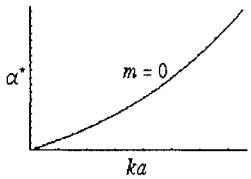	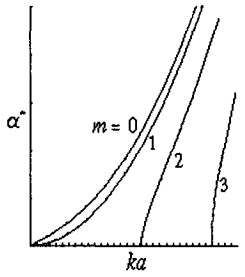
C/NA	No	No	$(\alpha^{*0} > \alpha^{*1} > \alpha^{*2} > \cdots)$

(c) Catastrophic/Non-axisymmetric (C/NA).

In what follows we discuss these three different capillary instabilities in axial fibers, and determine the parametric dependence of the deformation and growth rates.

3.4.1 Capillary instabilities in axial fibers

Table 3.1[2] summarizes the complete phenomenology of the three capillary instabilities in axial fibers, as computed from Eqs. (3.42)-(3.45). There are three regimes according to the values of τ. The first column shows the instability type, and the entries show characteristic growth rate curves for each instability mechanism. For the MR instability in the second column, the growth rate curve is bounded, and an upper ka_{cutoff} exists. For the C instabilities of all modes in the fourth column, the growth rate curves are unbounded, and lower modes grow faster than higher modes. We next discuss in detail the physical and mathematical aspects of the tabulated information.

[2] MR/A: Modified Rayleigh/Axisymmetric instability
C/A: Catastrophic/Axisymmetric instability
C/NA: Catastrophic/Non-axisymmetric instability
α^{*i}: Growth rate of ith mode for C instabilities

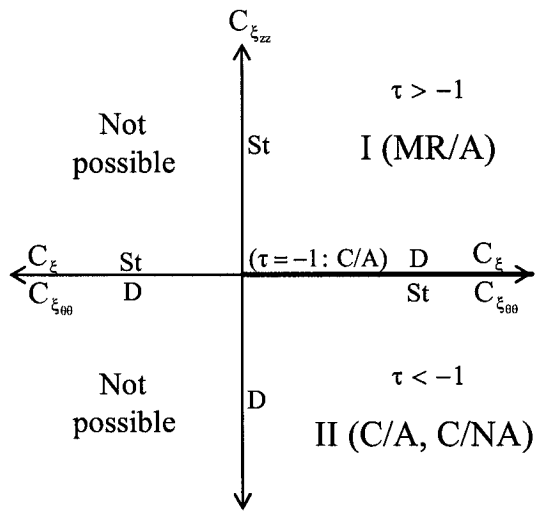

Figure 3-2: Instability phase diagram in terms of the displacement force coefficient, C_ξ, and the curvature force coefficients, $C_{\xi_{\theta\theta}}$ and $C_{\xi_{zz}}$. Roman numerals (I, II) refer to the two regions of Table 3.1, and the captions (MR/A, C/A, C/NA) to the instability types of Table 3.1. On the axes St and D denote stabilizing and destabilizing, respectively.

Instability characterization in axial fibers

As explained above the physics of capillary instabilities in axial fibers, as summarized in Table 3.1, is elucidated by considering the sign of the displacement and curvature force coefficients or effective surface tensions (see Eqs. (3.41)). Figure 3-2 presents an instability phase diagram spanned by the displacement force coefficient, C_ξ, and the curvature force coefficients, $C_{\xi_{\theta\theta}}$ and $C_{\xi_{zz}}$. The roman numerals (I, II) refer to the two regions of Table 3.1, and the captions (MR/A, C/A, C/NA) to the instability types of Table 3.1. The figure captures the nature of the driving forces and identifies when and why an instability occurs. For the axial fiber, since C_ξ ($C_{\xi_{\theta\theta}}$) is always positive and thus destabilizing (stabilizing), the sign of $C_{\xi_{zz}}$ determines instability mechanisms: The first quadrant corresponds to instabilities with an upper ka_{cutoff} since the curvature forces are stabilizing; in the fourth quadrant, curvature from ξ_{zz} destabilizes and catastrophic instabilities occur; the second and third quadrants are thermodynamically inaccessible since C_ξ and $C_{\xi_{\theta\theta}}$ are always positive. By crossing the boundary between the first and fourth quadrants ($\tau = -1$), the fiber under MR instability in Region I becomes susceptible to catastrophic instability for mode $m = 0$. And then, in Region II the fiber is C-unstable

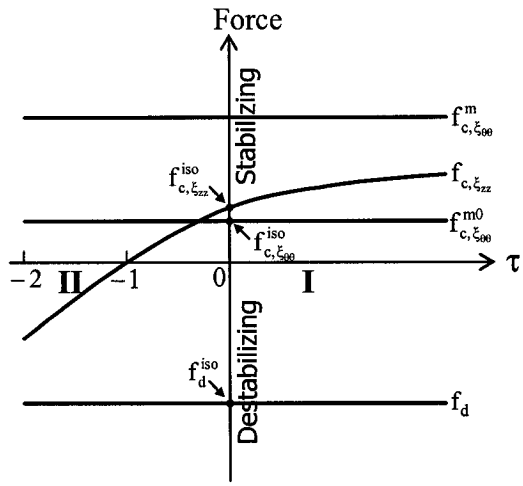

Figure 3-3: Representative schematic of the displacement (f_d) and curvature ($f_{c,\xi_{zz}}$, $f^{m0}_{c,\xi_{\theta\theta}}$, $f^{m}_{c,\xi_{\theta\theta}}$) forces as a function of the dimensionless anchoring energy τ, where $f_{c,\xi_{zz}}$ represents the curvature forces from ξ_{zz}, $f^{m0}_{c,\xi_{\theta\theta}}$ the curvature force from $\xi_{\theta\theta}$ for $m = 0$ mode, and $f^{m}_{c,\xi_{\theta\theta}}$ for $m \geq 1$ modes. In the figure, $f^{\rm iso}_{d}$ represents the displacement force, and $f^{\rm iso}_{c,\xi_{\theta\theta}}$ and $f^{\rm iso}_{c,\xi_{zz}}$ the curvature forces for isotropic fibers ($\tau = 0$). The figure provides the reasons of the existence of the two regions (I and II), and observation of the relative magnitudes of the stabilizing and destabilizing forces explains the phenomenology of Table 3.1.

for modes $m \geq 1$ as well as $m = 0$. Figure 3-3 shows a representative schematic of the displacement (f_d) and curvature ($f_{c,\xi_{zz}}$, $f^{m0}_{c,\xi_{\theta\theta}}$, $f^{m}_{c,\xi_{\theta\theta}}$) forces as a function of the dimensionless anchoring energy τ, where $f_{c,\xi_{zz}}$ represents the curvature forces from ξ_{zz}, $f^{m0}_{c,\xi_{\theta\theta}}$ the curvature force from $\xi_{\theta\theta}$ for $m = 0$ mode, and $f^{m}_{c,\xi_{\theta\theta}}$ for $m \geq 1$ modes. The figure again provides the reasons of the existence of the two regions (I and II), and observation of the sign and relative magnitudes of the stabilizing and destabilizing forces explains the phenomenology of Table 3.1. In short, the displacement forces (f_d) are always destabilizing, while the curvature forces from $\xi_{\theta\theta}$ ($f^{m0}_{c,\xi_{\theta\theta}}$, $f^{m}_{c,\xi_{\theta\theta}}$) always stabilizing, showing the smaller curvature force for $m = 0$ than for $m \geq 1$. Meanwhile, the curvature forces from ξ_{zz} ($f_{c,\xi_{zz}}$) are stabilizing only for $\tau > -1$. In Fig. 3-3, the stabilizing forces for the non-axisymmetric modes ($f^{m}_{c,\xi_{\theta\theta}}$) are sufficiently strong to quench the instability if $\tau > -1$, and thus only $m = 0$ is unstable. In other words, it is energetically costly to cause instability modes $m \geq 1$ for $\tau > -1$ as seen by comparing the magnitude of stabilizing forces with that of destabilizing forces. For $\tau = -1$, since the

destabilizing f_d cannot overcome the stabilizing $f^m_{c,\xi_{\theta\theta}}$ and $f_{c,\xi_{zz}}$ is no longer stabilizing, only $m = 0$ undergoes catastrophic instability. The figure also shows that for isotropic fibers ($\tau = 0$) the curvature forces $f^{\text{iso}}_{c,\xi_{\theta\theta}}$ and $f^{\text{iso}}_{c,\xi_{zz}}$ are always stabilizing while the displacement force f^{iso}_d is always destabilizing, and thus the upper ka_{cutoff} exists since the magnitude of the destabilizing force is relatively greater than that of the total stabilizing curvature forces.

The nature of non-axisymmetric instabilities is explained as follows. For the cylindrical axial fiber, the surface orientation of the nematic texture is planar anchoring. Since for $\tau > 0$ the easy axis of the surface is planar anchoring, the misalignment between the surface orientation and the easy axis is not high enough to cause the non-axisymmetric instability by bending stresses. On the other hand, for $\tau < 0$ the misalignment between the actual director and the easy axis (homeotropic) is large, and if the anchoring energy (τ) is strong enough (large negative value), the bending stresses may even cause non-axisymmetric deformation in order to relieve the high misalignment and align the director with the easy axis by means of surface deformations and rotations. These observations on the symmetry of the unstable modes can be made quantitative, as follows. When the growth rate a^* is real and positive, the surface disturbances become unstable and grow with time. In the Newtonian fiber ($\tau = 0$) the positive real a^* is obtained only for the axisymmetric disturbances ($m = 0$), from Eq. (3.37). For the axial fiber, by solving Eq. (3.37) positive real a^* solutions are obtained when the following condition is satisfied:

$$1 - m^2 - (1 + \tau)(ka)^2 \ > 0\,. \tag{3.47}$$

For isotropic fibers, $\tau = 0$ and inequality Eq. (3.47) is never fulfilled for $m \geq 1$, but for nematic fibers it can be. Inequality Eq. (3.47) is satisfied when $\tau < -1$, where the following condition is also satisfied:

$$0 < \frac{1 - m^2}{1 + \tau} < (ka)^2\,. \tag{3.48}$$

In other words, when the magnitude of the stabilizing curvature force $f_{c,\xi_{zz}}$ is sufficiently reduced by bending forces, and eventually $f_{c,\xi_{zz}}$ becomes destabilizing because the effective surface tension is negative, non-axisymmetric modes emerge under catastrophic Hadamard instabilities. Since curvature from ξ_{zz} is destabilizing, there is no upper cutoff but lower cutoff wavenumber for $m \geq 2$ from Eq. (3.48).

For axial fibers we then have two instability regions:

(a) MR/A: $\tau > -1$, Region I

This case corresponds to the second column of Table 3.1. When $\tau > -1$ only the modified Rayleigh instability with a single unstable m_0 mode is present. The mode is axisymmetric. In this case, the effective surface tensions are positive and the instability follows the classical Rayleigh mode.

(b) C/NA and C/A: $-2 \leq \tau < -1$, Region II

This case corresponds to the fourth column of Table 3.1. There are two possible instabilities: C/NA and C/A. The catastrophic instability mechanism controls the fiber: All modes are unstable, and the short wave instability is dominant. The lower modes grow faster than the higher modes at constant τ, which means lower mode disturbances with short wavelengths are more likely to cause the fiber instability. In this regime destabilizing forces dominate, and the negative effective surface tension of curvature force $f_{c,\xi_{zz}}$ allows for surface fibrillation.

(c) Criticality: $\tau = -1$

The third column in Table 3.1 shows that when $\tau = -1$ there is a critical state involving C/A instability. In the limit $\tau = -1^+$ the growth rate of the MR/A instability becomes maximized. On the other hand, in the limit $\tau = -1^-$ the C/A and C/NA instabilities shrink to the only C/A instability with a smaller slope of growth rate. Thus, decreasing τ through the value of -1 denotes the extinction of the bounded MR instability, and the birth of the unbounded C instabilities.

Symmetry of deformation modes in axial fibers

In this study, surface disturbances are classified by the mode m in the azimuthal direction given in Eq. (3.3). Because m is an integer, positive and negative signs are equally possible for each value of m. In axial fibers, the sign selects the handedness of the shape deformation but does not affect the growth rate curves due to the m^2 dependence of the growth rate in Eq. (3.37). A positive sign imprints a left-handed rotation to the surface pattern and thus these are chiral modes. The mode m_0, which is a so-called varicose mode, represents the well-known axisymmetric disturbance. Likewise, the m_1 mode is called the sinuous mode, and modes with $m \geq 2$, fluted modes. Under the mode m_1 instability, the center of the fiber moves along a

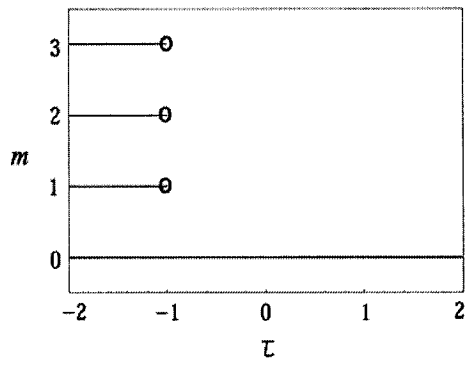

Figure 3-4: Azimuthal wavenumber m as a function of the dimensionless anchoring energy τ. At $\tau = -1$, the figure shows the transition of instability mechanisms from MR to C. Only the m_0 mode is unstable in the whole range of τ. The instability creation curve diverges as $\tau \to -1^+$, and thus the m_0 mode undergoes from MR for $\tau > -1$ to C for $\tau \leq -1$. Non-axisymmetric catastrophic instabilities also emerge when $\tau < -1$.

spiral trajectory around the z-axis. For $m \geq 2$, the cross-sectional shape has a regular pattern identified by m axes of rotational symmetry, and the shape rotates along the z-axis. The axial rotation of the anisotropic cross-sectional shape for $m \geq 2$, produces chiral surface ripple modes.

It is noted that while values $Oh > 0$ change the maximum growth rate and the corresponding wavenumber, they have no effect on the surface deformation pattern. For the classical m_0 mode, $\lambda = 2\pi/(ka)$ is the dimensionless wavelength of the varicose shape in the z-direction. The fiber cross-section is always circular but periodically expands and contracts when traversing the axial fiber direction. Thus, for the m_0 mode the formation of droplets with a characteristic size λ is predicted.

Parametric effects on capillary instabilities in axial fibers

Figure 3-4 shows the azimuthal wavenumber m as a function of the dimensionless surface anchoring energy τ. At $\tau = -1$, the figure shows the transition of instability mechanisms from MR to C. Only the MR mode m_0 persists for $\tau > -1$ because the stabilizing curvature forces $f^m_{c,\xi_{\theta\theta}}$ for modes $m \geq 1$ are sufficiently strong, while if $\tau < -1$ all C modes arise simultaneously since curvature forces $f_{c,\xi_{zz}}$ are destabilizing and thus total destabilizing forces are greater than total stabilizing forces for all modes (see Fig. 3-3). The instability creation curve diverges as

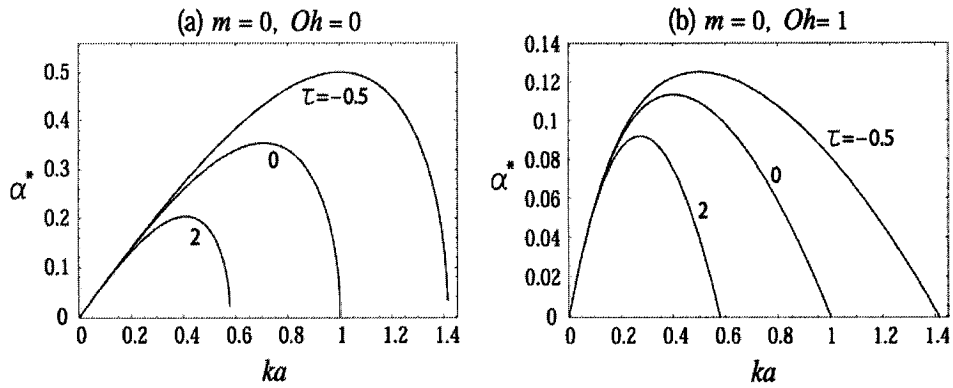

Figure 3-5: Dimensionless growth rate curves a^* as a function of dimensionless wavenumber ka, for m_0 at $\tau = -0.5, 0, 2$, for (a) $Oh = 0$ and (b) $Oh = 1$. This figure corresponds to Region I in Table 3.1 and the only m_0 mode is MR-unstable.

$\tau \to -1^+$, indicating that in this $\tau = -1$ limit, the m_0 mode becomes C-unstable.

Figure 3-5 shows the dimensionless growth rate curves a^* as a function of dimensionless wavenumber ka, for m_0 at $\tau = -0.5, 0, 2$, for (a) $Oh = 0$ and (b) $Oh = 1$. This figure corresponds to Region I in Table 3.1. According to Eq. (3.42), at three values of τ, $\tau = -0.5, 0, 2$, the only unstable mode is m_0. It is seen in Fig. 3-5 that the cutoff wavenumber, which is given as $ka_{\text{cutoff}} = 1/\sqrt{1+\tau}$, is not a function of Oh. In addition to decreasing the maximum growth rate, the effect of increasing Oh is to shift horizontally the maximum growth rate to lower ka values, meaning that viscosity increases the length scales of the unstable mode.

Figure 3-6(a) shows the maximum growth rate α^*_{max}, and Fig. 3-6(b) the corresponding maximum dimensionless wavenumber ka_{max} as a function of dimensionless anchoring energy τ, for m_0 and $Oh = 0, 1, 10$. This figure corresponds to Region I in Table 3.1, and to the MR/A instability. The suppressing effect of the viscosity is again evident in both figures. The figure shows that as τ increases α^*_{max} and ka_{max} decrease sharply until $\tau = 0$, and then they decrease at a much slower rate. The sensitivity of the instability with respect to τ has already been explained in the previous section in terms of the misalignment between the surface orientation and the easy axis.

Figure 3-7 shows the dimensionless cutoff wavenumber ka_{cutoff} as a function of the dimensionless anchoring energy τ, for m_0. This figure corresponds to Region I in Table 3.1, and to the

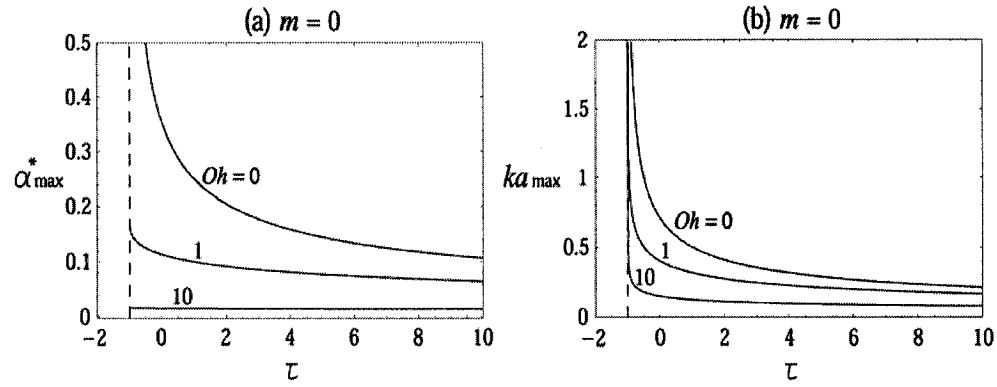

Figure 3-6: (a) Maximum growth rate $\alpha^*_{\max}$ and (b) the corresponding maximum dimensionless wavenumber $ka_{\max}$ as a function of dimensionless anchoring energy τ, for m_0 and $Oh = 0, 1, 10$. This figure corresponds to Region I in Table 3.1, and to the MR/A instability.

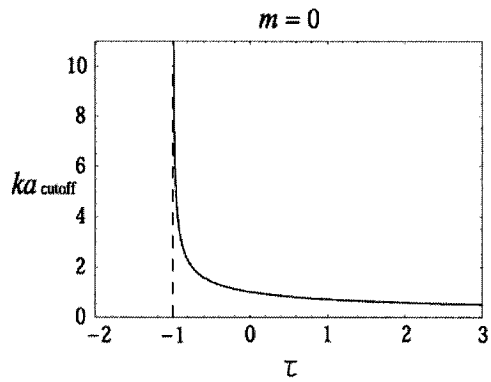

Figure 3-7: Dimensionless cutoff wavenumber ka_{cutoff} as a function of the dimensionless anchoring energy τ, for m_0. This figure corresponds to Region I in Table 3.1, and to the MR/A instability.

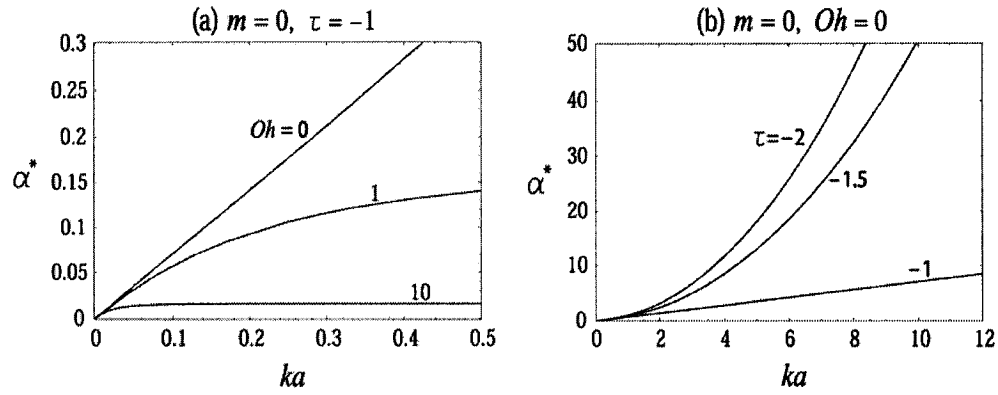

Figure 3-8: Dimensionless growth rate curves α^* as a function of dimensionless wavenumber ka, for m_0, and (a) $Oh = 0, 1, 10$, and $\tau = -1$, and (b) $\tau = \tau = -2, -1.5, -1$, and $Oh = 0$. (a) corresponds to the transition (C/A instability) between Regions I and II, and (b) to the transition and Region II in Table 3.1.

MR/A instability. The ka_{cutoff} decreases with τ in the same pattern as in Fig. 3-6(b). Similar to the viscous effect, if $\tau > -1$, the surface elasticity τ tends to stabilize the fiber, as explained above.

Figure 3-8 shows the dimensionless growth rate curves α^* as a function of dimensionless wavenumber ka, for m_0, and (a) $Oh = 0, 1, 10$, and $\tau = -1$, and (b) $\tau = -2, -1.5, -1$, and $Oh = 0$. Fig. 3-8(a) corresponds to the transition (C/A instability) between Regions I and II in Table 3.1. According to Eq. (3.45), for $\tau = -1$ the only unstable mode is m_0, and the growth rate increases with wavenumber ka without ka_{cutoff}, signaling that axisymmetric catastrophic instability occurs but increasing Oh suppresses the slope of growth rate by means of the stabilization effect of viscosity. Fig. 3-8(b) corresponds to the transition and Region II in Table 3.1. According to Eq. (3.45), as τ decreases from $\tau = -1$, the growth rate of mode m_0 increases faster with wavenumber ka under the catastrophic instability.

Figure 3-9 shows the dimensionless growth rate curves α^* as a function of dimensionless wavenumber ka, for m_0 at $\tau = -0.99, -1, -1.01$, and (a) $Oh = 0$, and (b) $Oh = 1$, dramatically revealing the critical point at $\tau = -1$. The dimensionless anisotropic elasticity values are close to $\tau = -1$ (transition between Regions I and II in Table 3.1), when controlled by the MR

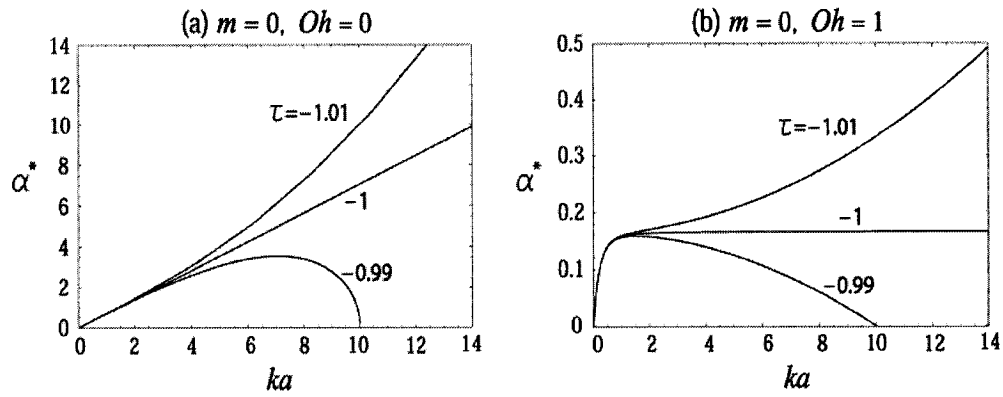

Figure 3-9: Dimensionless growth rate curves α^* as a function of dimensionless wavenumber ka, for m_0 at $\tau = -0.99, -1, -1.01$, and (a) $Oh = 0$, and (b) $Oh = 1$, dramatically revealing the critical point at $\tau = -1$. The dimensionless anisotropic elasticity values are close to $\tau = -1$ (transition between Regions I and II in Table 3.1), when controlled by the MR ($\tau = -0.99$; Region I in Table 3.1) and C ($\tau = -1.01$; Region II in Table 3.1) instability mechanisms, respectively.

($\tau = -0.99$; Region I in Table 3.1) and C ($\tau = -1.01$; Region II in Table 3.1) instability mechanisms, respectively. The growth rate curves are bounded at ka_{cutoff} for $\tau = -0.99$ while the short wave instabilities are seen for $\tau = -1$ and -1.01. Although, considering that the MR instability is maximized as $\tau \rightarrow -1^+$ while the catastrophic instability is minimized as $\tau \rightarrow -1^-$, the latter is always more unstable in the whole range of ka. The phenomena mentioned above hold qualitatively for any range of viscosity, although the shapes of the growth rate curves look different in Fig. 3-9(a) and (b) as higher viscosity shifts α^*_{max} and ka_{max} toward significantly smaller values, i.e., a quantitative effect. When $Oh > 0$, for $\tau = -1$ the growth rate increases with wavenumber but, after leveling off, it is almost bounded without ka_{cutoff} (see also Fig. 3-8(a)).

Figure 3-10 shows the dimensionless growth rate curves α^* as a function of dimensionless wavenumber ka, for m_0 to m_5, when $Oh = 0$, for (a) $\tau = -1.01$ and (b) $\tau = -2$. The dimensionless anisotropic elasticity range corresponds to C instability mechanism (Region II in Table 3.1). The short wave instabilities are seen for all modes, but only six among all C modes are presented in the figure, clearly showing that lower modes grow faster than higher modes. In

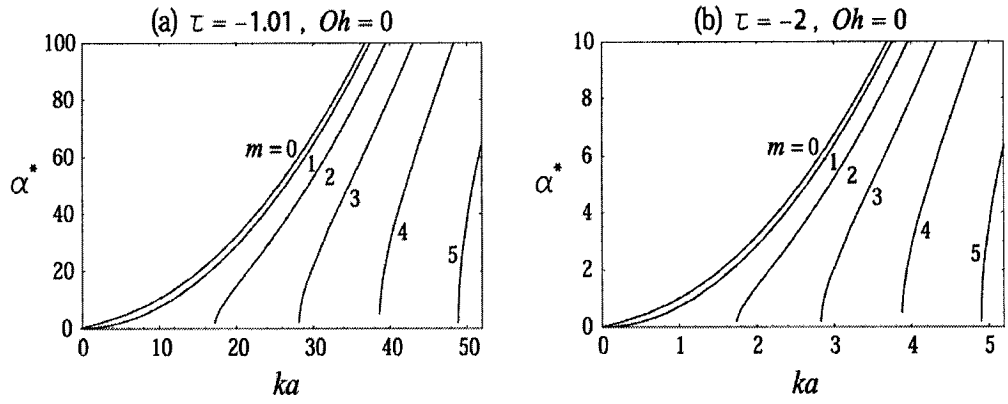

Figure 3-10: Dimensionless growth rate curves α^* as a function of dimensionless wavenumber ka, for m_0 to m_5, when $Oh = 0$, for (a) $\tau = -1.01$ and (b) $\tau = -2$. The dimensionless anisotropic elasticity range corresponds to C instability mechanism (Region II in Table 3.1): $\tau = -1.01$ (just below the criticality $\tau = -1$) and $\tau = -2$ (the thermodynamic limit).

Fig. 3-10(a) and (b), the growth rate curves for m_0 to m_5 show the same pattern for $\tau = -1.01$ (just below the criticality $\tau = -1$) and $\tau = -2$ (the thermodynamic limit), showing that the C instability for $\tau = -2$ grows much faster than that for $\tau = -1.01$ (see also Fig. 3-8(b)). Further, it is shown that for $\tau < -1$ the "lower" ka_{cutoff} exist for the C modes only when $m \geq 2$, as explained in Eq. 3.48).

Figure 3-11 shows representative structures that summarize capillary instabilities in axial fibers (see Table 3.1). Axial fibers display three types of linear instabilities, whose symmetry and existence are controlled by the magnitude and sign of the dimensionless surface anchoring energy τ. Large negative values of τ (Region II) ignite catastrophic axisymmetric and non-axisymmetric Hadamard instabilities, leading to fibrillation phenomena, as the effective surface tension coefficient, $C_{\xi_{zz}}$, for curvature forces, $f_{c,\xi_{zz}}$, is negative. Intermediate negative values close to zero and positive values of τ (Region I) lead to the axisymmetric Rayleigh instability, and to an eventual fiber break-up into droplets, because destabilizing displacement forces f_d overcome stabilizing curvature forces $f_{c,\xi_{zz}}$ and $f^{m0}_{c,\xi_{\theta\theta}}$, but $f^{m}_{c,\xi_{\theta\theta}}$. At the critical state of $\tau = -1$, the fiber instability is of catastrophic axisymmetric type. The only effect of viscosity is to slow the growth rate and increase the wavelength of the unstable modes.

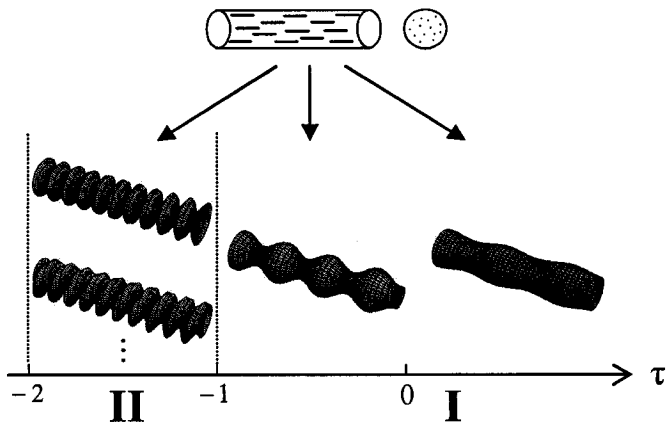

Figure 3-11: Representative structures that summarize capillary instabilities in axial fibers (see Table 3.1). Axial fibers display three types of linear instabilities, whose symmetry and existence are controlled by the magnitude and sign of the dimensionless surface anchoring energy τ. Varicose deformations emerge at positive and Intermediate negative values of τ (Region I), and surface fibrillation at large negative values of τ (Region II).

3.5 Viscous Matrix Effects on Capillary Instabilities

3.5.1 Modified governing equations

In this section we further investigate the stabilizing effects of the viscous matrix when the contribution of the stress tensor in the viscous matrix evaluated at the surface is included. The governing nemato-capillary equation is modified by the fact that the surface force due to the presence of the viscous matrix only exists at the interface.

The linear momentum balance equation for the system, where a thin axial fiber is embedded in an immiscible viscous matrix, is given as

$$\int_V (\rho \frac{\partial \mathbf{v}}{\partial t} - \nabla \cdot \mathbf{t} - \mathbf{F}_V^{\mathrm{M}})\, dV = 0, \tag{3.49}$$

where $\mathbf{t}$ is the total stress tensor for the fiber, and $\mathbf{F}_V^{\mathrm{M}}$ is the volume force density due to viscous matrix. Nonlinear inertia is neglected. At the interface, the surface force density from the viscous stress acting on the fiber is given as

$$\mathbf{F}_S^{\mathrm{M}} = \mathbf{N} \cdot \mathbf{t}^{\mathrm{M}} \,|_R\,, \tag{3.50}$$

where $\mathbf{t}^{\mathrm{M}}\,|_R$ is the stress tensor in the viscous matrix evaluated at the surface. To find $\mathbf{F}_V^{\mathrm{M}}$ we use the following equality:

$$\int_V \mathbf{F}_V^{\mathrm{M}} dV = \int_A \mathbf{F}_S^{\mathrm{M}} dA, \tag{3.51}$$

where $dA = Rd\theta dz$ and $dV = rdrd\theta dz$. Then it follows that

$$\mathbf{F}_V^{\mathrm{M}} = \mathbf{F}_S^{\mathrm{M}} \delta\left(r - R\right), \tag{3.52}$$

where $\delta(r)$ is the Dirac delta function, and thus the surface force only exists at the interface, $r = R$. Using Eq. (3.50) we finally find

$$\mathbf{F}_V^{\mathrm{M}} = \mathbf{N} \cdot \mathbf{t}^{\mathrm{M}}\,|_R\, \delta\left(r - R\right). \tag{3.53}$$

Thus, Eq. (3.49) is rewritten as

$$\int_V \left(\rho \frac{\partial \mathbf{v}}{\partial t} - \bigtriangledown \cdot \mathbf{t} - \mathbf{F}_V^{\mathrm{M}}\right) rdrd\theta dz = 0. \tag{3.54}$$

Since the viscous matrix effect exists only at the interface, Eq. (3.54) can be rewritten by substituting Eq. (3.53) into Eq. (3.54) as

$$\int_0^L \int_0^{2\pi} \left[\left(\rho \frac{\partial \mathbf{v}}{\partial t} - \bigtriangledown \cdot \mathbf{t}\right) \frac{R^2}{2} - \mathbf{N} \cdot \mathbf{t}^{\mathrm{M}}\,|_R\, R\right] d\theta dz = 0, \tag{3.55}$$

where L is the fiber length and the definite integration of the Dirac delta function, i.e., $\int_0^R \delta\left(r - R\right) rdr = R$, is used. Then, the momentum balance equation for this system becomes

$$\rho \frac{\partial \mathbf{v}}{\partial t} = \bigtriangledown \cdot \mathbf{t} + \frac{2}{R}\left(\mathbf{N} \cdot \mathbf{t}^{\mathrm{M}}\,|_R\right). \tag{3.56}$$

Using Eq. (3.31), the axial momentum balance equation, Eq. (3.56), is found to be [2]

$$\rho \frac{\partial v_z}{\partial t} = -\frac{\partial p_c}{\partial z} + 3\eta \frac{\partial^2 v_z}{\partial z^2} + \frac{2}{R} N_r t_{rz}^{\mathrm{M}}. \tag{3.57}$$

By assuming that the surface shear due to the existence of the matrix does not affect the macroscopic bulk flow in the fiber, the only remaining surface shear component for the slightly

disturbed surface is given by [29]

$$t_{rz}^{\mathrm{M}} = -\frac{2\mu}{k^2a^2}\frac{\partial^2\xi}{\partial z\partial t}. \tag{3.58}$$

Combining Eqs. (3.57), (3.34), (3.58) and in conjunction with Eq. (3.28) gives the differential equation for ξ:

$$\frac{\partial^2\xi}{\partial t^2} - \left(\frac{3\eta}{\rho} + \frac{2\mu}{\rho k^2a^2}\right)\frac{\partial^3\xi}{\partial z^2\partial t} + \frac{\gamma_{is}a}{2\rho}\frac{\partial^2}{\partial z^2}\left[\frac{\xi}{a^2} + \left(\frac{\partial^2\xi}{\partial z^2} + \frac{1}{a^2}\frac{\partial^2\xi}{\partial\theta^2}\right) + \tau\frac{\partial^2\xi}{\partial z^2}\right] = 0. \tag{3.59}$$

Eq. (3.59) properly reduces to the Newtonian fiber embedded in a Newtonian matrix, already derived in Ref. [29]. By substituting Eq. (3.3) into Eq. (3.59), a quadratic equation for the dimensionless growth rate, $\alpha^* = \alpha\sqrt{\rho a^3/\gamma_{is}}$, is obtained:

$$\alpha^{*2} + \left[3Oh\,(ka)^2 + 2Oh_m\right]\alpha^* - \frac{(ka)^2}{2}\left[1 - m^2 - (1+\tau)\,(ka)^2\right] = 0, \tag{3.60}$$

where ka is the dimensionless wavenumber, $Oh = \eta/\sqrt{\rho a\gamma_{is}}$ the fiber Ohnesorge number, and $Oh_m = \mu/\sqrt{\rho a\gamma_{is}}$ the matrix Ohnesorge number. These two Ohnesorge numbers are the ratios of the viscous to surface forces. Solving the quadratic equation for α^*, Eq. (3.60), we find

$$\alpha^* = \frac{1}{2}\left\{-\left[3Oh\,(ka)^2 + 2Oh_m\right] + \sqrt{\left[3Oh\,(ka)^2 + 2Oh_m\right]^2 + 2\,(ka)^2\left[1 - m^2 - (1+\tau)\,(ka)^2\right]}\right\}. \tag{3.61}$$

Thus, the axial fibers are unstable when the following inequality is satisfied:

$$-\left[3Oh\,(ka)^2 + 2Oh_m\right] + \sqrt{\left[3Oh\,(ka)^2 + 2Oh_m\right]^2 + 2\,(ka)^2\left[1 - m^2 - (1+\tau)\,(ka)^2\right]} > 0\,. \tag{3.62}$$

The maximum growth rate $\alpha^*_{\max}$ and the corresponding wavenumber $ka_{\max}$ are obtained by solving Eq. (3.60), which properly reduce to the well-known results for Newtonian fluids surrounded by an inviscid matrix when the viscoelastic anisotropy and the non-axisymmetric dependence vanish; i.e., $\mu = 0$, $\eta_1 = \eta_2$, $\eta_3 = 0$, $\tau = 0$, and $m = 0$. In more detail, the asymptotic results for the highly viscous fiber are $\alpha^*_{\max} = 1/(6Oh)$ and $ka_{\max} = 1/\sqrt{3\sqrt{2}Oh}$, whereas the asymptotic results for the inviscid fiber are $\alpha^*_{\max} = 1/\left(2\sqrt{2}\right)$ and $ka_{\max} = 1/\sqrt{2}$. Moreover, when only axisymmetric disturbances become unstable, i.e., $m = 0$, the results predict the axial fiber

break-up into droplets with a characteristic size of $2\pi/(ka_{\max})$ [10].

3.5.2 Parametric effects on capillary instabilities in axial fibers

Table 3.1 again summarizes the complete phenomenology of the three capillary instabilities in axial fibers, as computed from Eq. (3.61).

It is noted that while different values of Oh and Oh_m change the maximum growth rate and the corresponding wavenumber, they have no effect on the surface deformation pattern.

The contribution of the viscosity ratio to the capillary instabilities of a thin nematic fiber in a viscous matrix is analyzed by two parameters, the fiber and matrix Ohnesorge numbers, where viscosity ratio is defined as

$$VR = \frac{\mu}{\eta} = \frac{Oh_m}{Oh}. \tag{3.63}$$

Following convention, either Oh_m or VR is used to display the results of the effect of viscosities on the capillary instabilities when setting Oh equal to a constant value.

Figure 3-12 shows the dimensionless growth rate curves α^* as a function of dimensionless wavenumber ka, for m_0 at $\tau = 0$, for (a) $Oh = 0, 0.1, 1, 10$ when $Oh_m = 0$, (b) $Oh_m = 0, 0.1, 1, 10$ when $Oh = 0$ ($VR \rightarrow \infty$), and (c) $VR = 0, 1, 10$ when $Oh = 0.1$. The dashed curve in Fig. 3-12(c) denotes the growth rate for $Oh = 0$ and $Oh_m = 0$. Fig. 3-12 corresponds to Region I in Table 3.1, and to the MR/A instability. It is seen in Fig. 3-12(a) and (b) that increasing Oh decreases the maximum growth rate and shifts it to lower ka values, meaning that fiber viscosity increases the length scales of the unstable mode, while increasing Oh_m decreases the maximum growth rate but does not affect the corresponding wavenumber for an inviscid fiber ($Oh = 0$). Fig. 3-12(c) shows that for a viscous fiber ($Oh = 0.1$), increasing VR (increasing Oh_m) decreases the maximum growth rate and shifts it to higher ka values, meaning that matrix viscosity decreases the length scales of the unstable mode.

Figure 3-13 shows the dimensionless growth rate curves α^* as a function of dimensionless wavenumber ka, for m_0 to m_4, for $Oh_m = 0$ (solid curves) and $Oh_m = 1$ (dashed curves), when (a, b) $Oh = 0$ and (c, d) $Oh = 0.1$, for (a, c) $\tau = -1.01$ and (b, d) $\tau = -2$. The dimensionless anisotropic elasticity range corresponds to C instability mechanism (Region II in Table 3.1). The short wave instabilities are seen for all modes, but only five among all C modes are presented in the figure, clearly showing that lower modes grow faster than higher modes.

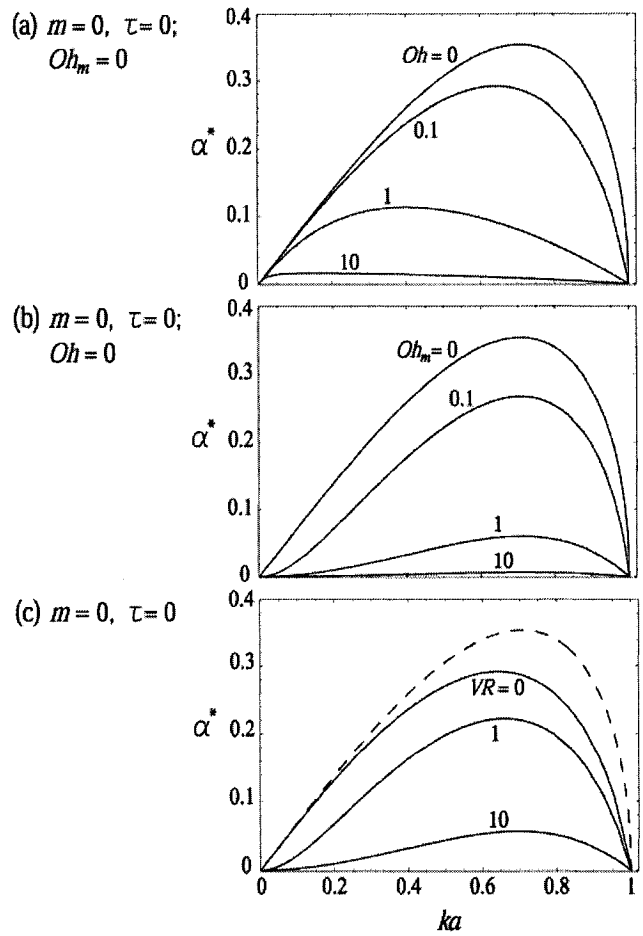

Figure 3-12: Dimensionless growth rate curves α^* as a function of dimensionless wavenumber ka, for m_0 at $\tau = 0$, for (a) $Oh = 0, 0.1, 1, 10$ when $Oh_m = 0$, (b) $Oh_m = 0, 0.1, 1, 10$ when $Oh = 0$ ($VR \to \infty$), and (c) $VR = 0, 1, 10$ when $Oh = 0.1$. The dashed curve in (c) denotes the growth rate for $Oh = 0$ and $Oh_m = 0$. The figure corresponds to Region I in Table 3.1, and to the MR/A instability.

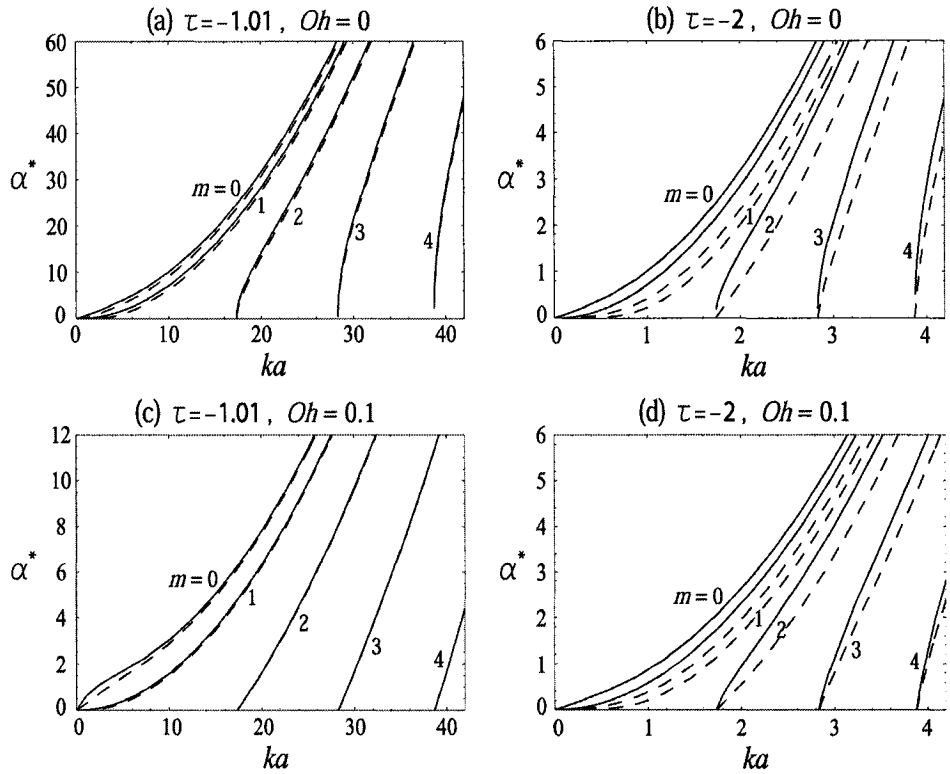

Figure 3-13: Dimensionless growth rate curves α^* as a function of dimensionless wavenumber ka, for m_0 to m_4, for $Oh_m = 0$ (solid curves) and $Oh_m = 1$ (dashed curves), when (a, b) $Oh = 0$ and (c, d) $Oh = 0.1$, for (a, c) $\tau = -1.01$ and (b, d) $\tau = -2$. The figure corresponds to Region II in Table 3.1, and to the C/A and C/NA instabilities.

In the figure the growth rate curves for m_0 to m_4 show the same pattern for $\tau = -1.01$ (just below the criticality) and $\tau = -2$ (the thermodynamic limit), showing that the C instability for $\tau = -2$ grows much faster than that for $\tau = -1.01$ (see also Fig. 3-14(b, d)). Further, it is shown that for $\tau < -1$ the "lower" ka_{cutoff} exist for the C modes only when $m \geq 2$, as explained in Eq. (3.48). For each unstable mode the growth rate decreases as Oh_m increases, and the Oh_m effect is more clearly seen for long wavelengths (small wavenumbers), and thus in lower modes, because the instability grows much faster at short wavelengths (large wavenumbers) under the C instability mechanism. When comparing Fig. 3-13(c, d) with Fig. 3-13(a, b), the growth rate decreases with increasing Oh as well as increasing Oh_m. The suppressing effect of the fiber viscosity Oh is even more evident at $\tau = -1.01$ than at $\tau = -2$, showing that instabilities with slower growth rates can be dampened more easily.

Figure 3-14 shows the dimensionless growth rate curves α^* as a function of dimensionless wavenumber ka, for m_0 and $Oh_m = 0$ (solid curves), 0.1 (dash-dot curves), 1 (dashed curves), when (a, b) $Oh = 0$ and (c, d) $Oh = 0.1$, for (a, c) $\tau = -0.5, 0, 2$, and (b, d) $\tau = -2, -1.01, -1, -0.99$. Fig. 3-14(a, c) corresponds to Region I in Table 3.1. According to Eq. (3.61), at three values of τ, $\tau = -0.5$, 0, and 2, the only unstable mode is m_0. The cutoff wavenumber ka_{cutoff}, which is given as $ka_{\text{cutoff}} = 1/\sqrt{1+\tau}$, is a function of neither Oh nor Oh_m. It is clearly shown that as Oh_m increases the maximum growth rate decreases but the corresponding wavenumber does not change for an inviscid fiber, $Oh = 0$ (see also Fig. 3-15(a)). It is also noted that the growth rate curves for $\tau = 0$ in Fig. 3-14(a) correspond to those in Fig. 3-12(b). Fig. 3-14(b, d) dramatically reveals the critical point at $\tau = -1$. The dimensionless anisotropic elasticity values are close to $\tau = -1$ (transition between Regions I and II in Table 3.1), when controlled by the MR ($\tau = -0.99$; Region I in Table 3.1) and C ($\tau = -1.01$; Region II in Table 3.1) instability mechanisms, respectively. The growth rate curves are bounded at ka_{cutoff} for $\tau = -0.99$ while the short wave instabilities are seen for $\tau = -1$ and below. Although, considering that the MR instability is maximized as $\tau \to -1^+$ while the catastrophic instability is minimized as $\tau \to -1^-$, the latter is always more unstable in the whole range of ka. The phenomena mentioned above hold qualitatively for any range of viscosity. It is also shown that the Oh_m effect is more clearly seen for smaller negative values of τ since instabilities with slower growth rates can be more easily dampened as explained above.

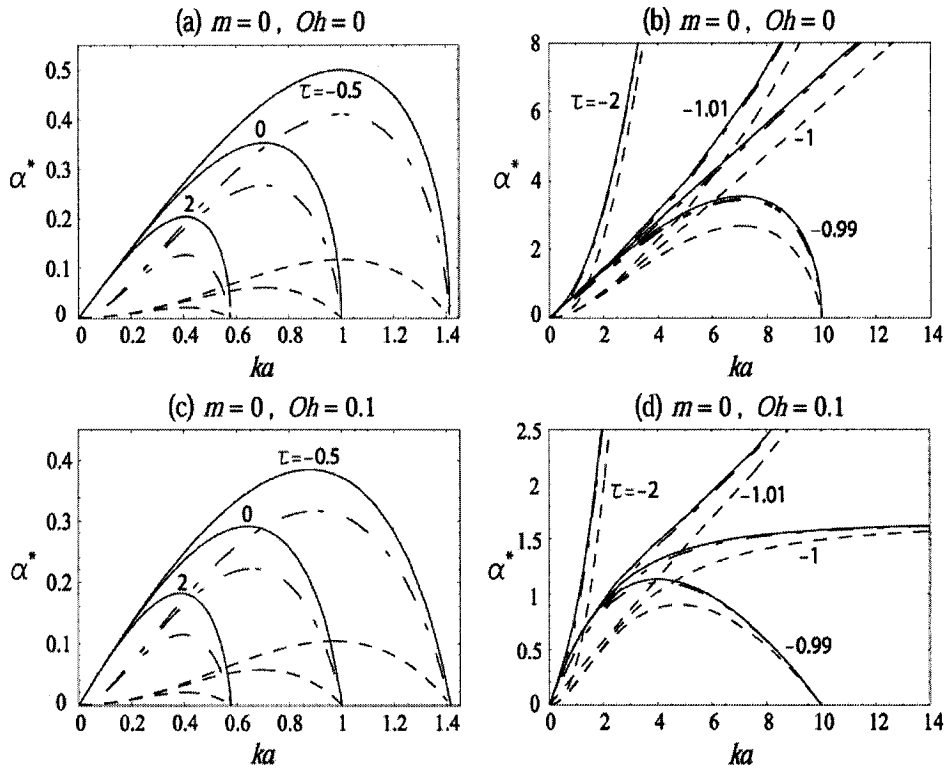

Figure 3-14: Dimensionless growth rate curves α^* as a function of dimensionless wavenumber ka, for m_0 and $Oh_m = 0$ (solid curves), 0.1 (dash-dot curves), 1 (dashed curves), when (a, b) $Oh = 0$ and (c, d) $Oh = 0.1$, for (a, c) $\tau = -0.5, 0, 2$, and (b, d) $\tau = -2, -1.01, -1, -0.99$. (a, c) corresponds to Region I in Table 3.1, and to the MR/A instability. In (b, d) the dimensionless anisotropic elasticity values are close to $\tau = -1$ (C/A instability at the transition between Regions I and II), when controlled by the MR ($\tau = -0.99$; Region I) and C ($\tau = -1.01$; Region II) instability mechanisms, respectively.

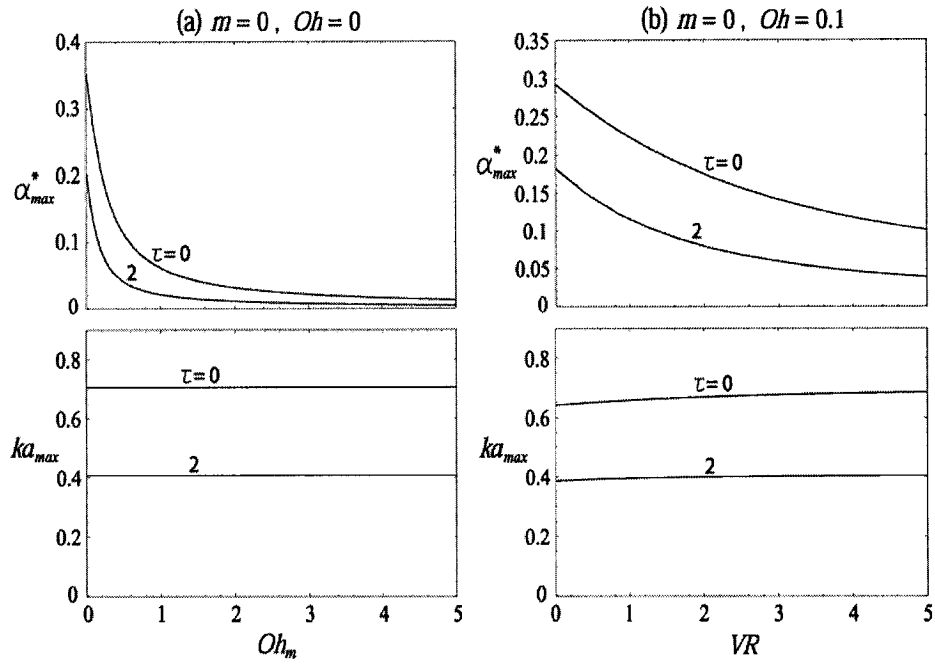

Figure 3-15: Maximum growth rate $\alpha^*_{\max}$, and the corresponding maximum dimensionless wavenumber $ka_{\max}$ (a) as a function of matrix Ohnesorge number Oh_m, for m_0 and $Oh = 0$, for $\tau = 0$ and 2, and (b) as a function of viscosity ratio VR, for m_0 and $Oh = 0.1$, for $\tau = 0$ and 2. The figure corresponds to Region I in Table 3.1, and to the MR/A instability.

When comparing Fig. 3-14(c, d) with Fig. 3-14(a, b), the growth rate decreases with increasing Oh as well as increasing Oh_m. For the MR/A instabilities, besides decreasing the maximum growth rate, the effect of increasing Oh is to shift horizontally the maximum growth rate to lower ka values as shown in Fig. 3-12(a). Meanwhile, increasing Oh_m (increasing VR) shifts the maximum growth rate to higher ka values for a viscous fiber ($Oh = 0.1$) as shown in Fig. 3-12(c) (see also Fig. 3-15(b)). When $Oh > 0$, for $\tau = -1$ the growth rate increases with wavenumber but, after leveling off, it is almost bounded without ka_{cutoff}.

Figure 3-15 shows the maximum growth rate $\alpha^*_{\max}$, and the corresponding maximum dimensionless wavenumber $ka_{\max}$ (a) as a function of matrix Ohnesorge number Oh_m, for m_0 and $Oh = 0$, for $\tau = 0$ and 2, and (b) as a function of viscosity ratio VR, for m_0 and $Oh = 0.1$, for $\tau = 0$ and 2. This figure corresponds to Region I in Table 3.1, and to the MR/A instability. The suppressing effect of the matrix viscosity is evident that as Oh_m (or VR) increases $\alpha^*_{\max}$

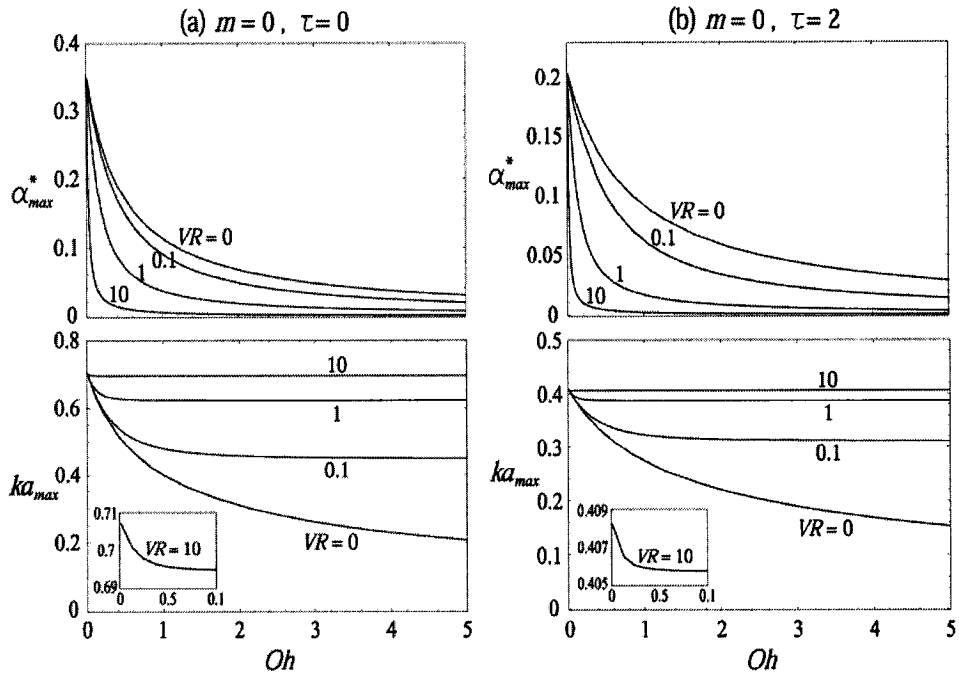

Figure 3-16: Maximum growth rate $\alpha^*_{\max}$, and the corresponding maximum dimensionless wavenumber $ka_{\max}$ as a function of fiber Ohnesorge number Oh, for m_0 and $VR = 0, 0.1, 1, 10$, for (a) $\tau = 0$ and (b) $\tau = 2$. Small in-boxes in the figure for $ka_{\max}$ at $VR = 10$ magnifies the original curve to clearly show the initial sharp decreasing of $ka_{\max}$ with increasing Oh. This figure corresponds to Region I in Table 3.1, and to the MR/A instability.

decreases sharply and then decreases at a much slower rate. However, it is shown in Fig. 3-15(a) that $ka_{\max}$ does not change with increasing Oh_m for either isotropic ($\tau = 0$) or nematic ($\tau = 2$) fiber when the fiber is inviscid ($Oh = 0$), while increasing VR (or Oh_m) shifts the maximum growth rate to higher ka values for a viscous fiber ($Oh = 0.1$). It is also clearly seen that increasing surface elasticity τ tends to stabilize the fiber.

Figure 3-16 shows the maximum growth rate $\alpha^*_{\max}$, and the corresponding maximum dimensionless wavenumber $ka_{\max}$ as a function of fiber Ohnesorge number Oh, for m_0 and $VR = 0, 0.1, 1, 10$, for (a) $\tau = 0$ and (b) $\tau = 2$. Small in-boxes in the figure for $ka_{\max}$ at $VR = 10$ magnifies the original curve to clearly show the initial sharp decreasing of $ka_{\max}$ with increasing Oh. This figure corresponds to Region I in Table 3.1, and to the MR/A instability. Similar to the matrix viscosity, the suppressing effect of the fiber viscosity is evident that as Oh

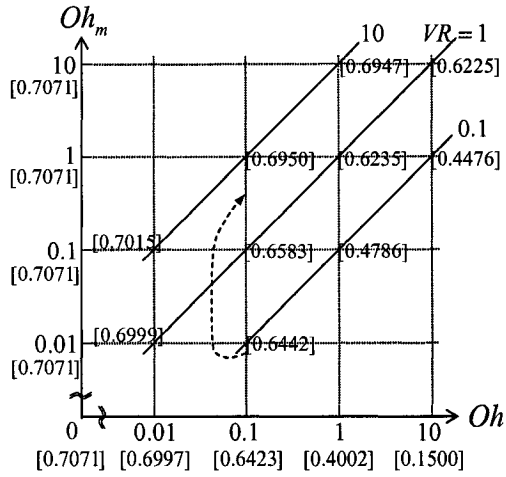

Figure 3-17: Dependence of the maximum dimensionless wavenumber $ka_{\max}$ on the fiber and matrix viscosities, for m_0 and $\tau = 0$. The lines correspond to $VR = 0.1, 1, 10$. The values in parentheses represent $ka_{\max}$ at crossing points of Oh and Oh_m (or VR). The dashed curve represents a path on which $ka_{\max}$ as a function of VR has a local maximum.

increases $\alpha^*_{\max}$ decreases sharply and then decreases at a much slower rate. The combined effect of the fiber and matrix viscosities (increasing VR) further decreases $\alpha^*_{\max}$. On the other hand, it is shown that $ka_{\max}$ decreases with increasing Oh but rather increases with increasing VR when the fiber is viscous ($Oh \neq 0$), meaning that the fiber viscosity increases the length scales of the unstable mode while the matrix viscosity decreases the length scales. When comparing Fig. 3-16(b) with Fig. 3-16(a), it is also seen that increasing surface elasticity τ tends to dampen the fiber instability.

Figure 3-17 shows the dependence of the maximum dimensionless wavenumber $ka_{\max}$ on the fiber and matrix viscosities, for m_0 and $\tau = 0$, and establishes the consistency of the present results for nematic fibers with previous studies on viscous Newtonian fibers [15, 17, 18]. The lines correspond to $VR = 0.1, 1, 10$. On the axis of Oh, where $VR = 0$, the maximum dimensionless wavenumber $ka_{\max}$ decreases with increasing Oh. On the axis of Oh_m, where $VR \rightarrow \infty$, the maximum dimensionless wavenumber $ka_{\max}$ has a constant value, $ka_{\max} = 1/\sqrt{2} \approx 0.7071$. As VR increases from 0 to ∞, the maximum dimensionless wavenumber $ka_{\max}$ increases along either a constant Oh line or a constant Oh_m line. The dashed curve in the figure represents a path on which $ka_{\max}$ as a function of VR has a local maximum, as reported

Table 3.2: Dependence of the maximum dimensionless wavenumber on the viscosity ratio.

VR	Tomotika Ref. [15]	Ref. [18] ($0.002 \leq Oh \leq 0.01$)	Ref. [17] ($0.002 \leq Oh \leq 0.01$)	This study ($0.04 \leq Oh \leq 0.1$)
0.06	0.353	0.611	0.623	0.643
0.1	0.409	0.643	0.688	0.679
0.66	0.53	0.659	0.682	0.681
1.15	0.568	0.643	0.682	0.682
2.56	0.583	0.666	0.702	0.686
4.33	0.581	0.651	0.693	0.683

in other studies [15, 17, 18]. The path shown in Fig. 3-17 covers a certain range of Oh, which was not considered as a parameter in Tomotika's results [15]. The change of $ka_{\max}$ on the path is qualitatively consistent with the results of previous studies [15, 17, 18], as shown in the comparative study summarized in Table 3.2. Table 3.2 shows the dependence of the maximum dimensionless wavenumber $ka_{\max}$ on the viscosity ratio VR calculated in Ref. [15, 17, 18] and in the present work. Except for Tomotika's results, all other studies considered Oh as well as VR as parameters. In our study the path shown as a dashed curve in Fig. 3-17 demonstrates the characteristic behavior of $ka_{\max}$ as a function of VR in the range $0.04 < Oh < 0.1$. The tabulated results from all the studies clearly show that $ka_{\max}$ as a function of VR has a local maximum. In partial summary, our model of bounded axisymmetric capillary instability of a nematic liquid crystalline fiber embedded in a viscous matrix predicts a dependence of maximum wavenumber on the matrix-to-fiber viscosity ratio that is in qualitative agreement with other computational models found in the literature for Newtonian fluids.

3.6 Conclusions

Capillary instabilities in nematic fibers reflect the anisotropic nature of liquid crystals. The surface elasticity of nematics contains orientation contributions that allow for the existence of bending stresses. Surface gradients of bending stresses provide additional anisotropic contributions to the capillary pressure of fibers that renormalize the classical displacement and curvature forces that exist in any fluid fiber. The exact nature and magnitude of the renormalization of the displacement and curvature forces depend on the nematic liquid crystal orientation and the anisotropic contribution to the surface energy. If the orientation is along the fiber axis,

capillary instabilities may be axisymmetric or non-axisymmetric, and if the anchoring energy strongly promotes normal (homeotropic) orientation to the surface, the usually stabilizing curvature forces become destabilizing and capillary instabilities with fibrillation phenomena arise. We have been pursuing experimental verification of non-axisymmetric capillary instability using rheological microscopy methods [30]. The phenomenology predicted in this chapter is accessible, in principle, by changes in temperature, since the anchoring energy of a given interface is temperature dependent [7]. Thus, the classical fiber-to-droplet transformation is one of several possible instability pathways while others include surface fibrillation.

The effect of the viscous shear force at the fiber surface due to the viscous matrix on the bounded axisymmetric capillary instability was also taken into account, and characterized in terms of the Ohnesorge numbers and the matrix-to-fiber viscosity ratio. The capillary instabilities of a thin fiber in a viscous matrix are suppressed by increasing either the fiber or matrix Ohnesorge number, but estimated droplet sizes after fiber break-up in axisymmetric instabilities substantially decrease with increasing matrix Ohnesorge number. In a certain range of the fiber Ohnesorge number, the dependence of the wavenumber corresponding to the maximum growth rate on the viscosity ratio is in qualitative agreement with previous studies on models for Newtonian fluids.

Bibliography

[1] D. A. Edwards, H. Brenner, and D. T. Wasan, *Interfacial Transport Processes and Rheology* (Butterworths-Heinemann, Boston, 1989).

[2] V. G. Levich, *Physicochemical Hydrodynamics* (Prentice-Hall, Englewood Cliffs, NJ, 1962).

[3] C. Pozrikidis, *Introduction to Theoretical and Computational Fluid Dynamics* (Oxford University Press, New York, 1997).

[4] P. G. de Gennes and J. Prost, *The Physics of Liquid Crystals* (Oxford University Press, London, 1993).

[5] H. Ehrentraut and S. Hess, Phys. Rev. E **51**, 2203 (1995).

[6] R. G. Larson, *The Structure and Rheology of Complex Fluids* (Oxford University Press, New York, 1999).

[7] A. A. Sonin, *The Surface Physics of Liquid Crystals* (Gordon and Breach Publishers, Amsterdam, 1995).

[8] H. Yokoyama, in *Handbook of Liquid Crystal Research*, edited by P. J. Collins and J. S. Patel (Oxford University Press, New York, 1997).

[9] A. D. Rey, Ind. Engin. Chem. Res. **36**, 1114 (1997).

[10] A. D. Rey, J. Phys. II France **7**, 1001 (1997).

[11] H. Q. Yang, Phys. Fluids A **4**, 681 (1992).

[12] E. Avital, Phys. Fluids **7**, 1162 (1995).

[13] X. Li, Atomization and Sprays **5**, 89 (1995).

[14] A. D. Rey, Phys. Rev. E **61**, 1540 (2000).

[15] S. Tomotika, Proc. R. Soc. A **150**, 322 (1935).

[16] L. Rayleigh, Proc. R. Soc. London **29**, 71 (1879).

[17] C. M. Kinoshita, H. Teng, and S. M. Masutani, Int. J. Multiphase Flow **20**, 523 (1994).

[18] Y. Kitamura, H. Mishima, and T. Takahashi, Can. J. Chem. Eng. **60**, 273 (1982).

[19] S. P. Lin, *Breakup of Liquid Sheets and Jets* (Cambridge University Press, Cambridge, 2003).

[20] P. G. Drazin, *Introduction to Hydrodynamic Stability* (Cambridge University Press, Cambridge, 2002).

[21] S. Chandrasekhar, *Liquid Crystals* (Cambridge University Press, Cambridge, 1992).

[22] E. G. Virga, *Variational Theories for Liquid Crystals* (Chapman Hall, London, 1994).

[23] A. Rapini and M. Papoular, J. Phys. (Paris), Colloq. C4, **30**, 54 (1969).

[24] T. J. Sluckin and A. Poniewierski, in *Fluid Interfacial Phenomena*, edited by C. A. Croxton (Wiley, Chichester, 1986).

[25] S. Faetti, in *Physics of Liquid Crystalline Materials*, edited by I-C Khoo and F. Simoni (Gordon and Breach, Philadelphia, 1991).

[26] C. Papenfuss and W. Muschik, Mol. Mat. **2**, 1 (1992).

[27] S. Middleman, *Modeling Axisymmetric Flows: Dynamics of Films, Jets, and Drops* (Academic Press, San Diego, 1995).

[28] D. D. Joseph, *Fluid Dynamics of Viscoelastic Liquids* (Springer-Verlag, New York, 1990).

[29] J. N. Anno, *Mechanics of Liquid Jets* (Lexington Books, Toronto, 1977).

[30] P. T. Mather, H. G. Jeon, C. D. Han, and S. Chang, Macromol. **33**, 7594 (2000).

Chapter 4

Temperature Effects on Capillary Instabilities in a Thin Nematic Liquid Crystalline Fiber Embedded in a Viscous Matrix

4.1 Summary

Linear stability analysis of capillary instabilities in a thin nematic liquid crystalline cylindrical fiber embedded in an immiscible viscous matrix is performed by formulating and solving the governing nemato-capillary equations, that include the effect of temperature on the nematic ordering as well as the effect of the nematic orientation. A representative axial nematic orientation texture with the planar easy axis at the fiber surface is studied. The surface disturbance is expressed in normal modes, which include the azimuthal wavenumber m to take into account non-axisymmetric modes. Capillary instabilities in nematic fibers reflect the anisotropic nature of liquid crystals, such as the ordering and orientation contributions to the surface elasticity and surface normal and bending stresses. Surface gradients of normal and bending stresses provide additional anisotropic contributions to the capillary pressure that may renormalize the classical displacement and curvature forces that exist in any fluid fiber. The exact nature

(stabilizing and destabilizing) and magnitude of the renormalization of the displacement and curvature forces depend on the nematic ordering and orientation, i.e., the anisotropic contribution to the surface energy, and accordingly capillary instabilities may be axisymmetric or non-axisymmetric. In addition, when the interface curvature effects are considered as contributions of the work of interfacial bending and torsion to the total energy of the system, the higher order bending moment contribution to the surface stress tensor is critical in stabilizing the fiber instabilities. For the planar easy axis, the nematic ordering contribution to the surface energy, which renormalizes the effect of the fiber shape, plays a crucial role to determine the instability mechanisms. Moreover, the unstable modes, which are most likely observed, can be driven by the dependence of surface energy on the surface area. Low ordering fibers display the classical axisymmetric mode since the surface energy decreases by decreasing the surface area. Decreasing temperature gives rise to the encounter with a local maximum or to monotonic increase of the characteristic length of the axisymmetric mode. Meanwhile, in the presence of high surface ordering, non-axisymmetric finite wavelength instabilities emerge, with higher modes growing faster since the surface energy decreases by increasing the surface area. As temperature decreases, the pitches of the chiral microstructures become smaller. However, this non-axisymmetric instability mechanism can be regulated by taking account of the surface bending moment, which contains higher order variations in the interface curvatures. More and more non-axisymmetric modes emerge as temperature decreases, but, at constant temperature, only a finite number of non-axisymmetric modes are unstable and a single fastest growing mode emerges with lower and higher unstable modes growing slower. For nematic fibers, the classical fiber-to-droplet transformation is one of several possible instability pathways while others include chiral microstructures. The capillary instabilities' growth rate of a thin nematic fiber in a viscous matrix is suppressed by increasing either the fiber or matrix viscosity, but estimated droplet sizes after fiber break-up in axisymmetric instabilities decrease with increasing the matrix viscosity.

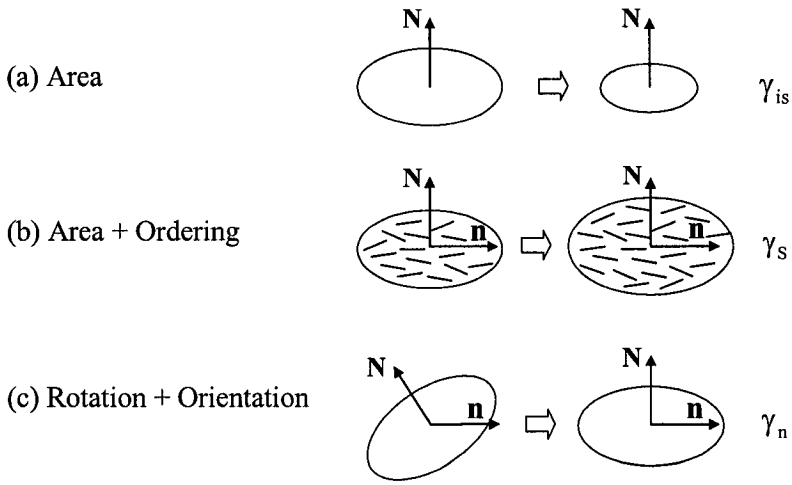

Figure 4-1: Three contributions to the surface free energy density of a nematic interface: γ_{is} is the isotropic contribution, γ_S is the nematic ordering contribution, and γ_n is the anchoring contribution. The total surface energy can decrease by area reduction (γ_{is}), by area dilation (γ_S), and by area rotation (γ_n).

4.2 Introduction

A question of fundamental importance in capillary instabilities of thin fibers is the nature of the modes that arise when driven by surface tension forces. For isotropic fluid fibers, surface tension is isotropic, and thus only surface area reduction plays a role to select an unstable mode since the surface energy decreases by decreasing the surface area [1]. In addition, it is known that when surface curvature effects are important in isotropic fluids, the contribution of the work of surface bending and torsion to the total energy of the system can be included since the bending and torsion deformation is related to variations in the two principal curvatures of the interface [2, 3, 4, 5]. On the other hand, the surface tension of nematic liquid crystals contains anisotropic contributions [7, 8, 9] known as nematic ordering and anchoring energies [10, 11, 6] as well as an isotropic contribution. Figure 4-1 shows the three contributions to the surface free energy density of a nematic interface: γ_{is} is the isotropic contribution, γ_S is the nematic ordering contribution, and γ_n is the anchoring contribution. The figure shows that the total surface energy can decrease by area reduction (γ_{is}), by area dilation (γ_S), and by area rotation (γ_n). Since chiral non-axisymmetric fiber instability modes increase the surface area,

and for that reason are never observed in isotropic material interfaces, nematic interfaces can, as shown in this chapter, promote the instability through the nematic ordering and anchoring energy mechanisms.

Capillary instabilities in liquid crystal fibers have been analyzed with and without viscous matrix effects in Chapter 3 [12, 13], and in this chapter we extend the previous work and analyze the temperature dependence of the instability mechanisms and thresholds. We adopt the nemato-capillary equation for the fiber which contains the viscous stress force at the interface, and thus show the effect of the viscosity ratio on the capillary instabilities using the fiber and the matrix Ohnesorge numbers (i.e. ratio of viscous to surface forces).

The specific objectives of this chapter are to: (1) present a general equation that describes capillary instabilities in a thin nematic liquid crystal fiber embedded in a viscous matrix; (2) characterize all the possible capillary instability modes and elucidate the physical mechanisms that drive and quench the instabilities; (3) establish parametric conditions that lead to axisymmetric and non-axisymmetric capillary instabilities; (4) characterize the nematic ordering and anchoring energy contributions to capillary instabilities; and (5) characterize the surface bending and torsion moment contributions to capillary instabilities.

The organization of this chapter is as follows. In Section 4.3, we present the governing nemato-capillary equations and derive the instability criteria for a representative nematic texture. In Section 4.4, we characterize all possible instability modes and the geometry of the evolving unstable fiber. The instability mechanisms are clearly identified and discussed in terms of capillary forces. All results are summarized in compact tabular form and discussed in detail, emphasizing the physical as well as mathematical aspects. Representative computed visualizations of unstable fibers are included to complement the tabulated and graphical information. In Section 4.5, we further investigate the stabilizing mechanism when the contributions of the work of surface bending and torsion to the total energy of the system are included. Section 4.6 presents conclusions.

4.3 Governing Equations

We consider the stability of a thin, initially axisymmetric, cylindrical nematic fiber embedded in an immiscible viscous matrix. The nematic liquid crystal is assumed to be incompressible, and its orientation is homogeneous and constant. Linear stability analysis is used to analyze the complete set of axisymmetric and non-axisymmetric capillary instabilities in nematic liquid crystalline fibers.

In this chapter, we use the same geometry and texture of a liquid crystalline fiber with a fixed director field, as shown in Chapter 3 (see Figure 3-1). The fixed director assumption holds when the fiber radius is smaller than the extrapolation length ℓ. The extrapolation length is the ratio of characteristic bulk elastic energy to surface anchoring energy [6]. When $a < \ell$, it is less costly to store surface energy than bulk energy, and hence under this condition the director is spatially homogeneous (see Chapter 1 section 1.3.7). Since the director is fixed, only the linear momentum balance equation for the bulk and surface defines the evolution of the fiber's shape. In this work, the mechanical response of the nematic fluid is that of an anisotropic viscoelastic material [14, 6], where the bulk is viscous and the surface is elastic.

4.3.1 Constitutive equations

While the viscous stress tensor $\mathbf{t}^v$ is described by Ericksen's Transversely Isotropic Fluid (TIF) constitutive equation (3.7), the surface elastic stress tensor $\mathbf{t}^{se}$ is expressed by one of extensions of the Rapini-Papoular constitutive equation. Extensions of the Rapini-Papoular constitutive equation are used in the literature, specifically to describe thermally-induced surface orientation transitions [15]. A well-known phenomenological expression for the surface free energy density of the nematic liquid crystal was proposed by Sluckin and Poniewierski [8] where the surface free energy was expanded to the second order in terms of the symmetric, traceless, 3×3 tensor order parameter $\mathbf{Q}$ [7, 8, 9] and is given by

$$\begin{aligned} \gamma &= \gamma_{is} + \gamma_{an}(\mathbf{N}, \mathbf{Q}, \mathbf{Q}\cdot\mathbf{N}) \\ &= \gamma_{is} + \beta_{11}\mathbf{N}\cdot\mathbf{Q}\cdot\mathbf{N} + \beta_{20}\mathbf{Q}:\mathbf{Q} + \beta_{21}\mathbf{N}\cdot\mathbf{Q}\cdot\mathbf{Q}\cdot\mathbf{N} + \beta_{22}\left(\mathbf{N}\cdot\mathbf{Q}\cdot\mathbf{N}\right)^2 , \end{aligned} \tag{4.1}$$

where γ_{is} is the isotropic surface tension, γ_{an} is the anisotropic surface energy, and $\{\beta_{ij}\}$, $ij = 11, 20, 21, 22$, are the phenomenological parameters that are independent of temperature. For instance, β_{11} represents the effects due to the Van der Waals interaction between the nematic and isotropic (matrix) phases. The anisotropic (nematic) contribution γ_{an} arises whenever the surface tensor order parameter deviates from the surface 'easy tensor order parameter', which minimizes the surface free energy. In the uniaxial nematic state, the tensor order parameter is given by

$$\mathbf{Q} = S\left(\mathbf{nn} - \frac{1}{3}\mathbf{I}\right), \tag{4.2}$$

where S is the scalar order parameter. Since the anisotropic surface energy γ_{an} is a function of $\mathbf{N}$ and $\mathbf{Q}$, there are two mechanisms for storing surface elastic energy, one is through nematic ordering (S) and the other through nematic orientation ($\mathbf{n}$). Then, the surface free energy density, Eq. (4.1), is rewritten by making use of Eq. (4.2) as [9]

$$\gamma = \gamma_{is} + \gamma_{\mathbf{S}}(S) + \gamma_{\mathbf{n}}(S, (\mathbf{n}\cdot\mathbf{N})^2), \tag{4.3}$$

where

$$\gamma_{\mathbf{S}}(S) = \frac{1}{3}\left[-\beta_{11}S + \frac{1}{3}(\beta_{21} + 2\beta_{20} + \beta_{22})S^2\right], \tag{4.4}$$

$$\gamma_{\mathbf{n}}(S, (\mathbf{n}\cdot\mathbf{N})^2) = \left[\beta_{11}S + \frac{1}{3}(\beta_{21} - 2\beta_{22})S^2\right](\mathbf{n}\cdot\mathbf{N})^2, \tag{4.5}$$

where $\gamma_{\mathbf{S}}(S)$ represents the anisotropic contribution due to the nematic ordering, and $\gamma_{\mathbf{n}}(S, (\mathbf{n}\cdot\mathbf{N})^2)$ the anisotropic contribution due to the nematic orientation at the surface as well as due to the nematic ordering.

The surface 'easy axis', the director orientation which minimizes the surface free energy, may be parallel to the surface (planar anchoring), perpendicular to the surface (homeotropic anchoring), or tilted according to the signs and magnitudes of the phenomenological parameters β_{ij}. In this chapter, we consider the planar easy axis since the director field is fixed along the fiber axis, which is close to the planar anchoring condition. It is assumed that $\beta_{20} = 0$, i.e., the nematic-nematic interaction is negligible with respect to the nematic-isotropic phase interaction. The signs of the phenomenological parameters β_{ij}, which satisfy conditions that minimize the

surface free energy in terms of the surface nematic orientation, are given as [9]

$$\beta_{11} > 0\,, \qquad \beta_{22} > 0\,, \qquad \beta_{21} < 0\,, \tag{4.6}$$

and further restrictions are obtained as

$$\beta_{22} < \frac{1}{4}\left|\beta_{21}\right|\,, \qquad \beta_{11} < \frac{1}{3}\left(\left|\beta_{21}\right| - 4\beta_{22}\right)\,. \tag{4.7}$$

From Eq. (4.6), the planar surface orientation is stable when

$$S < S_p\,, \tag{4.8}$$

where S_p is the scalar order parameter for the planar easy axis and is expressed as

$$S_p = \frac{3\beta_{11}}{\left|\beta_{21}\right| + 2\beta_{22}}\,. \tag{4.9}$$

The planar surface orientation is stable when $T > T_p$, where T_p is the temperature which corresponds to S_p. By assuming that the scalar order parameter is uniform across the fiber but a function of temperature, the surface free energy depends only on temperature and the surface nematic orientation. Then, the scalar order parameter is assumed as [9]

$$S(T) = c\sqrt{\frac{T_0 - T}{T_0}}\,, \tag{4.10}$$

where T_0 is a few degrees lager than the nematic-isotropic transition temperature and c is a constant. By using Eq. (4.6) and Eq. (4.10), the surface free energy is derived for a small distortion from the planar easy axis and finally given as

$$\gamma = \gamma_{is} + \gamma_{\mathrm{S}}\left(T\right) + \gamma_{\mathrm{n}}(T, (\mathbf{n}\cdot\mathbf{N})^2), \tag{4.11}$$

where

$$\begin{aligned}\gamma_{\mathbf{S}}(T) &= -\frac{1}{3}\beta_{11}S_p\sqrt{\frac{T_0-T}{T_0-T_p}}\left[1+\left(1-\frac{3\beta_{22}}{|\beta_{21}|+2\beta_{22}}\right)\sqrt{\frac{T_0-T}{T_0-T_p}}\right] \\ &= -\frac{1}{3}\beta_{11}S_p\sqrt{\Delta T^*}\left[1+(1-b)\sqrt{\Delta T^*}\right], \end{aligned} \tag{4.12}$$

$$\begin{aligned}\gamma_{\mathbf{n}}(T,(\mathbf{n}\cdot\mathbf{N})^2) &= \beta_{11}S_p\sqrt{\frac{T_0-T}{T_0-T_p}}\left(1-\sqrt{\frac{T_0-T}{T_0-T_p}}\right)(\mathbf{n}\cdot\mathbf{N})^2 \\ &= \beta_{11}S_p\sqrt{\Delta T^*}\left(1-\sqrt{\Delta T^*}\right)(\mathbf{n}\cdot\mathbf{N})^2, \end{aligned} \tag{4.13}$$

$$b=\frac{3\beta_{22}}{|\beta_{21}|+2\beta_{22}}, \tag{4.14}$$

$$\Delta T^*=\frac{T_0-T}{T_0-T_p}, \tag{4.15}$$

where $\gamma_{\mathbf{S}}(T)$ represents the anisotropic contribution due to the nematic ordering, $\gamma_{\mathbf{n}}(T,(\mathbf{n}\cdot\mathbf{N})^2)$ represents the anisotropic contribution due to the anchoring (nematic orientation at the surface) energy, b is the ratio of two anchoring phenomenological parameters, i.e., $\frac{|\beta_{21}|}{\beta_{22}}$, and ΔT^* is the dimensionless nematic temperature. Using Eqs. (4.6) and (4.7) and the range restriction of $S(T)$ in Eq. (4.8), we obtain that

$$0<b<\frac{1}{2}, \qquad 0<\Delta T^*<1. \tag{4.16}$$

It is noted that, as ΔT^* increases from 0 to 1, the temperature T actually decreases from T_0 to T_p. Finally, Eq. (4.11) can be rewritten as

$$\begin{aligned}\gamma &= \gamma_{is}+C(\Delta T^*)+W_p(\Delta T^*)(\mathbf{n}\cdot\mathbf{N})^2 \\ &= \gamma_{is}\left[1+\frac{C(\Delta T^*)}{\gamma_{is}}+\frac{W_p(\Delta T^*)}{\gamma_{is}}(\mathbf{n}\cdot\mathbf{N})^2\right], \end{aligned} \tag{4.17}$$

using

$$C(\Delta T^*)=-\frac{1}{3}\beta_{11}S_p\sqrt{\Delta T^*}\left[1+(1-b)\sqrt{\Delta T^*}\right], \tag{4.18}$$

$$W_p(\Delta T^*)=\beta_{11}S_p\sqrt{\Delta T^*}\left(1-\sqrt{\Delta T^*}\right), \tag{4.19}$$

where C is the nematic ordering coefficient, and W_p the anchoring strength of the anisotropic surface energy in the Rapini-Papoular form. It is noted that the nematic ordering coefficient C is negative while the anchoring strength W_p is positive.

It is noted that since the two contributions to the capillary pressure are expressed by Eq. (3.21), the nematic ordering coefficient C and the anchoring strength W_p contribute to the capillary pressure through both the normal and bending stresses. Nevertheless, when considering the linear regime of capillary instability of a nematic liquid crystal fiber, second order terms involving $H(\mathbf{n}\cdot\mathbf{N})^2$ cancel out and the only remaining anchoring (surface orientation) contribution to the capillary pressure is that from the bending stresses. Thus, any model that attempts to capture the linear regime of capillary instability in a nematic liquid crystal fiber must include all contributions arising from the bending stress tensor as well as the normal stress tensor.

4.3.2 Governing equations for an axial nematic fiber

In this section, the governing equation of the surface disturbance $\xi(z,\theta,t)$, Eq. (3.3), is derived for the axial fiber in the viscous matrix by combining the linear momentum balance equation, Eq. (3.56), and the normal stress boundary condition, Eq. (3.19).

Using Eqs. (3.23) and (3.24) in Eq. (3.20), the capillary pressure p_c becomes

$$\begin{aligned} p_c &= \gamma_{is}\left\{\left[1+\frac{C(\Delta T^*)}{\gamma_{is}}\right]\left(\frac{1}{a}-\frac{1}{a^2}\xi-\frac{1}{a^2}\frac{\partial^2\xi}{\partial\theta^2}-\frac{\partial^2\xi}{\partial z^2}\right)-2\frac{W_p(\Delta T^*)}{\gamma_{is}}\frac{\partial^2\xi}{\partial z^2}\right\} \\ &= \gamma_{is}\left[S_n\left(\frac{1}{a}-\frac{1}{a^2}\xi-\frac{1}{a^2}\frac{\partial^2\xi}{\partial\theta^2}\right)-S_{nb}\frac{\partial^2\xi}{\partial z^2}\right], \end{aligned} \tag{4.20}$$

where

$$S_n = \left[1+\frac{C(\Delta T^*)}{\gamma_{is}}\right] = 1-a^*\sqrt{\Delta T^*}\left[1+(1-b)\sqrt{\Delta T^*}\right], \tag{4.21}$$

$$S_{nb} = \left[1+\frac{C(\Delta T^*)}{\gamma_{is}}+2\frac{W_p(\Delta T^*)}{\gamma_{is}}\right] = 1+a^*\sqrt{\Delta T^*}\left[5+(b-7)\sqrt{\Delta T^*}\right], \tag{4.22}$$

$$a^* = \frac{S_p}{3}\frac{\beta_{11}}{\gamma_{is}}, \tag{4.23}$$

where a^* is the ratio of nematic ordering energy to isotropic surface energy. Table 4.1 sum-

Table 4.1: Parametric definitions.

Parameters	Equations	Definitions
$C(\Delta T^*)$	(4.18)	nematic ordering coefficient
$W_p(\Delta T^*)$	(4.19)	anchoring strength
a^*	(4.23)	ratio of nematic ordering energy to isotropic surface energy
b	(4.14)	ratio of two anchoring phenomenological parameters, i.e., $\frac{\lvert\beta_{21}\rvert}{\beta_{22}}$
ΔT^*	(4.15)	dimensionless nematic temperature

marizes all parameters, which appear in Eqs. (4.21) and (4.22), and their definitions for easy reference.

Since the total surface free energy and the isotropic surface tension are always positive in Eq. (4.17), we deduce that S_n can be either positive or negative but S_{nb} is always positive. Eq. (4.20) properly reduces to the Newtonian capillary pressure when $\Delta T^* = 0$, i.e., when surface tension is isotropic. Importantly, when the normal and bending stresses contribute to the capillary pressure of an axial fiber, forces appear that are given respectively by

$$p_c\,|_{nf} = \gamma_{is}\left[1+\frac{C(\Delta T^*)}{\gamma_{is}}\right]\left(\frac{1}{a}-\frac{1}{a^2}\xi-\frac{1}{a^2}\frac{\partial^2\xi}{\partial\theta^2}-\frac{\partial^2\xi}{\partial z^2}\right), \tag{4.24}$$

$$p_c\,|_{bf} = -2W_p(\Delta T^*)\frac{\partial^2\xi}{\partial z^2}, \tag{4.25}$$

where $p_c\,|_{nf}$ can compete or cooperate with the usual isotropic contribution since the sign of the normal force coefficient $\left[1+\frac{C(\Delta T^*)}{\gamma_{is}}\right]$ is not fixed, whereas $p_c\,|_{bf}$ cooperates with the usual isotropic contribution as seen in Eq. (4.20) since the sign of the anchoring strength W_p is positive.

Combining Eqs. (3.57), (3.34), and (3.58) in conjunction with Eq. (4.20) gives the differential equation for ξ:

$$\frac{\partial^2\xi}{\partial t^2}-\left(\frac{3\eta}{\rho}+\frac{2\mu}{\rho k^2a^2}\right)\frac{\partial^3\xi}{\partial z^2\partial t}+\frac{\gamma_{is}a}{2\rho}\frac{\partial^2}{\partial z^2}\left[S_n\left(\frac{\xi}{a^2}+\frac{1}{a^2}\frac{\partial^2\xi}{\partial\theta^2}\right)+S_{nb}\frac{\partial^2\xi}{\partial z^2}\right]=0. \tag{4.26}$$

Eq. (4.26) properly reduces to the Newtonian fiber embedded in a Newtonian matrix when $\Delta T^* = 0$, i.e., when surface tension is isotropic. By substituting Eq. (3.3) into Eq. (4.26), a

quadratic equation for the dimensionless growth rate, $\alpha^* = \alpha\sqrt{\rho a^3/\gamma_{is}}$, is obtained:

$$\alpha^{*2} + \left[3Oh\,(ka)^2 + 2Oh_m\right]\alpha^* - \frac{(ka)^2}{2}\left[S_n(1-m^2) - S_{nb}\,(ka)^2\right] = 0\,, \tag{4.27}$$

where ka is the dimensionless wavenumber, $Oh = \eta/\sqrt{\rho a\gamma_{is}}$ the fiber Ohnesorge number, and $Oh_m = \mu/\sqrt{\rho a\gamma_{is}}$ the matrix Ohnesorge number. These two Ohnesorge numbers are the ratios of the viscous to surface forces. Solving the quadratic equation for α^*, Eq. (4.27), we find

$$\alpha^* = \frac{1}{2}\left\{-\left[3Oh\,(ka)^2 + 2Oh_m\right] + \sqrt{\left[3Oh\,(ka)^2 + 2Oh_m\right]^2 + 2\,(ka)^2\left[S_n(1-m^2) - S_{nb}\,(ka)^2\right]}\right\}. \tag{4.28}$$

Thus, the axial fibers are unstable when the following inequality is satisfied:

$$-\left[3Oh\,(ka)^2 + 2Oh_m\right] + \sqrt{\left[3Oh\,(ka)^2 + 2Oh_m\right]^2 + 2\,(ka)^2\left[S_n(1-m^2) - S_{nb}\,(ka)^2\right]} > 0\,. \tag{4.29}$$

The maximum growth rate $\alpha^*_{\max}$ and the corresponding wavenumber $ka_{\max}$ are obtained by solving Eq. (4.27), which properly reduce to the well-known results for Newtonian fluids surrounded by an inviscid matrix when the viscoelastic anisotropy and the non-axisymmetric dependence vanish; i.e., $\mu = 0$, $\eta_1 = \eta_2$, $\eta_3 = 0$, $\Delta T^* = 0$, and $m = 0$. In more detail, the asymptotic results for the highly viscous fiber are $\alpha^*_{\max} = 1/(6Oh)$ and $ka_{\max} = 1/\sqrt{3\sqrt{2}Oh}$, while the asymptotic results for the inviscid fiber are $\alpha^*_{\max} = 1/\left(2\sqrt{2}\right)$ and $ka_{\max} = 1/\sqrt{2}$. Moreover, when only axisymmetric disturbances become unstable, i.e., $m = 0$, the results predict the axial fiber break-up into droplets with a characteristic size of $2\pi/(ka_{\max})$ [16]. For the axisymmetric disturbances in the nematic inviscid fiber with the inviscid matrix, i.e., $Oh = Oh_m = 0$ and $m = 0$, Eq. (4.27) reduces to

$$\alpha^* = \frac{ka}{\sqrt{2}}\sqrt{S_n - S_{nb}\,(ka)^2}\,, \tag{4.30}$$

and the maximum growth rate $\alpha^*_{\max}$ and the corresponding wavenumber $ka_{\max}$ are given by

$$\alpha^*_{\max} = \frac{1}{\sqrt{8}}\sqrt{\frac{S_n^2}{S_{nb}}}\,, \qquad ka_{\max} = \frac{1}{\sqrt{2}}\sqrt{\frac{S_n}{S_{nb}}}\,. \tag{4.31}$$

The physics of capillary instabilities in axial nematic fibers can be elucidated by rewriting

Eq. (4.20) as

$$p_c = \gamma_{is}\left[S_n\left(\frac{1}{a} - \frac{1}{a^2}\xi - \frac{1}{a^2}\frac{\partial^2\xi}{\partial\theta^2}\right) - S_{nb}\frac{\partial^2\xi}{\partial z^2}\right] = \frac{\gamma_{is}}{a}S_n + f_d + f_c\,, \tag{4.32}$$

$$f_d = -\frac{1}{a^2}C_\xi\xi, \quad f_c = -\frac{1}{a^2}C_{\xi_{\theta\theta}}\xi_{\theta\theta} - C_{\xi_{zz}}\xi_{zz}, \quad C_\xi = C_{\xi_{\theta\theta}} = \gamma_{is}S_n, \quad C_{\xi_{zz}} = \gamma_{is}S_{nb}\,. \tag{4.33}$$

The capillary pressure contains two (ξ-dependent) deformation effects: a displacement force, f_d, and a curvature force, f_c. Capillary instabilities occur because a spatially periodic pressure gradient develops, inducing macroscopic flow. The driving force for creating a pressure gradient is denoted as a destabilizing force, while a force resisting it is denoted as a stabilizing force. The nature of the two capillary forces depends only on the sign of their coefficients, C_ξ, $C_{\xi_{\theta\theta}}$, and $C_{\xi_{zz}}$, which are the effective surface tensions for both forces. Thus the displacement force is destabilizing (stabilizing) for $C_\xi > 0$ ($C_\xi < 0$), while the curvature force is stabilizing (destabilizing) for $C_{\xi_{\theta\theta}} > 0$ and $C_{\xi_{zz}} > 0$ ($C_{\xi_{\theta\theta}} < 0$ and $C_{\xi_{zz}} < 0$). In isotropic fibers ($\Delta T^* = 0$), the displacement force is always destabilizing and the curvature force is always stabilizing, thus explaining the existence of lower cutoff in the instability wavelength, as in the classical Rayleigh fiber instability. This occurs because the stabilizing curvature force for sufficiently short wavelengths overpowers the driving displacement force. Since for axial fibers $S_{nb} > 0$ as explained below Eq. (4.20), the curvature force from ξ_{zz} is always stabilizing. On the other hand, since S_n can be either positive or negative depending on magnitudes of a^*, b, and ΔT^* (see Eq. (4.21)), the displacement force and the curvature force from $\xi_{\theta\theta}$ can be stabilizing or destabilizing. If $S_n > 0$ ($S_n < 0$), the curvature force from $\xi_{\theta\theta}$ is stabilizing (destabilizing) while the displacement force is destabilizing (stabilizing).

4.4 Results and Discussion

The characterization of capillary instabilities in nematic fibers requires the specification of two features: (i) instability mechanism; (ii) symmetry of deformation modes. These two features are embedded in Eq. (4.28) and must be considered separately.

(i) *Instability mechanism*

The capillary instabilities in nematic liquid crystalline fibers are found to follow two different routes:

(a) Modified Rayleigh (MR) instability mechanism

The modified Rayleigh instability is characterized by a single $m = 0$ mode. There is an upper cutoff wavenumber ka_{cutoff} above which disturbances do not grow. The axial fibers have no azimuthal dependence and thus axisymmetric.

(b) Bounded Simultaneous (BS) instability mechanism

The bounded simultaneous instability is characterized by simultaneous occurrence of azimuthal modes $m \geq 2$ with bounded growth rate. The following ordering in growth rates is found:

$$\alpha^{*2}_{\max} < \alpha^{*3}_{\max} < \cdots < \alpha^{*n}_{\max} < \alpha^{*n+1}_{\max} < \cdots , \tag{4.34}$$

where $\alpha^{*}_{\max}(m_n) \equiv \alpha^{*n}_{\max}$ while m_n represents $m = n$ mode hereafter.

(ii) *Symmetry of deformation modes*

The symmetry of the deformation in this chapter is restricted to axisymmetric and non-axisymmetric modes, axisymmetric modes being rotationally invariant. It is noted that for axial fibers the mode $m = 0$ is, as usual, an axisymmetric mode.

Based on this general discussion, the criteria required to classify the capillary instability are given by specification of: Instability mechanism/Symmetry. The following two cases emerge:

(a) Modified Rayleigh/Axisymmetric (MR/A)

(b) Bounded Simultaneous/Non-Axisymmetric (BS/NA).

In what follows we discuss these two different capillary instabilities in axial fibers, and determine the parametric dependence of the deformation and growth rates.

4.4.1 Capillary instabilities in axial fibers

To further analyze our results, we define a critical value of a^* as:

$$a^*_c = \frac{1}{2-b} , \tag{4.35}$$

which satisfies $S_n = S_{nb} = 0$ at $\Delta T^* = 1$ and $S_{nb} > S_n > 0$ for $0 < \Delta T^* < 1$.

Table 4.2: Capillary instabilities in axial fibers according to Eq.(4.29).

a^*	Instability type	**Region I** $0 < \Delta T^* < 1$		
$a^* \leq a_c^*$	MR/A	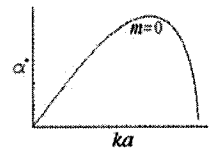		
a^*	Instability type	**Region II** $0 < \Delta T^* < \Delta T^*_{S_n=0}$	$\Delta T^*_{S_n=0}$	**Region III** $\Delta T^*_{S_n=0} < \Delta T^* < \Delta T^*_{S_{nb}=0}$
$a^* > a_c^*$	MR/A	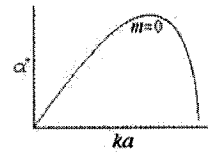	No	No
	BS/NA	No	No	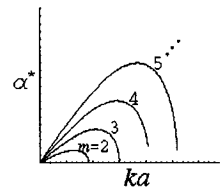 $\alpha^{*2}_{\max} < \alpha^{*3}_{\max} < \alpha^{*4}_{\max} < \cdots$

Table 4.2[1] summarizes the complete phenomenology of the two capillary instabilities in axial fibers, as computed from Eq. (4.28). If $a^* \leq a_c^*$, there is only one regime, where ΔT^* ranges from 0 to 1. If $a^* > a_c^*$, there are two regimes according to the signs of S_n (the values of ΔT^*: see Table 4.3 and discussion below). The first column shows the regions of a^*, the second column shows the instability type, and the entries show characteristic growth rate curves for each instability mechanism. For the MR instability in the second row (Regime I) and the third column (Regime II), the growth rate curve is bounded, and an upper ka_{cutoff} exists. For the BS instability in the fifth column (Regime III), the growth rate curves are bounded with upper ka_{cutoff}, and higher modes grow faster than lower modes.

Table 4.3[2] summarizes the fundamental features of the two types of capillary instabilities

[1] MR/A: Modified Rayleigh/Axisymmetric instability
BS/NA: Bounded Simultaneous/Non-Axisymmetric instability
$\alpha^{*i}_{\max}$: Maximum growth rate of ith mode for BS instabilities
[2] Three contributions to the surface free energy density in Eq. (4.11):

Table 4.3: Fundamental features of capillary instabilities in axial fibers.

Instability regime in Table 4.2	**Region I, II** $a^* \leq a_c^*$, $0 < \Delta T^* < 1$ $a^* > a_c^*$, $0 < \Delta T^* < \Delta T^*_{S_n=0}$	**Region III** $a^* > a_c^*$, $\Delta T^*_{S_n=0} < \Delta T^* < \Delta T^*_{S_{nb}=0}$
S_{nb}	+	+
$C_{\xi_{zz}}$	+	+
$f_{c,\xi_{zz}}$	Stabilizing	Stabilizing
S_n	+	−
$C_{\xi_{\theta\theta}}$, C_ξ	+	−
$f_{c,\xi_{\theta\theta}}$ / f_d	Stabilizing / Destabilizing	Destabilizing / Stabilizing
Instability type	MR/A ($m = 0$)	BS/NA ($m \geq 2$)
γ_S with relation to γ_{is}	S_n (+) : cooperating	S_n (−) : competing
Instability mode selection	$\gamma \downarrow$ as surface area $\downarrow$	$\gamma \downarrow$ as surface area $\uparrow$ ($\alpha^{*2}_{\max} < \alpha^{*3}_{\max} < \alpha^{*4}_{\max} < \cdots$)

in Table 4.2, as deduced from Eqs. (4.32) and (4.33). The first column shows properties we investigate, the first row shows instability regimes in Table II, and the entries show features of the properties for each instability type. For long cylindrical fibers, as long as the curvature force from ξ_{zz}, $f_{c,\xi_{zz}}$, is stabilizing ($C_{\xi_{zz}} > 0$), both axisymmetric and non-axisymmetric disturbances are always bounded with an upper cutoff wavenumber (lower cutoff wavelength), meaning that fibers are stable for sufficiently short wavelengths. Otherwise, the instability must be of the Hadamard type, where a lower cutoff wavelength does not exist and short wavelengths lead to catastrophic instability [12, 13]. For nematic fibers, the surface energy is dependent of the surface shape through, in particular, the effects of the nematic ordering contribution as well as the isotropic surface tension, and of the surface nematic orientation (anchoring). As seen in the table, for axial fibers, $S_{nb} > 0$ ($C_{\xi_{zz}} > 0$) and thus $f_{c,\xi_{zz}}$ is always stabilizing by means of its contribution of the anchoring energy, which arises from surface gradients of bending stresses, due to the positive anchoring strength W_p. Meanwhile, similar to the isotropic fiber, when the nematic ordering is small (second column for Regime I, II), the axial fiber is unstable to the axisymmetric m_0 mode, which is least stabilized by the curvature force from $\xi_{\theta\theta}$, $f_{c,\xi_{\theta\theta}}$, and

$$\gamma = \underbrace{\gamma_{is}}_{\text{isotropic}} + \underbrace{\gamma_S(S)}_{\text{nematic ordering}} + \underbrace{\gamma_n(S,(\mathbf{n}\cdot\mathbf{N})^2)}_{\text{nematic orientation}}$$

thus most likely destabilized by the displacement force, since the surface energy is decreased by decreasing surface area (last row). When the nematic ordering is large (third column for Regime III), higher non-axisymmetric modes, which are more destabilized by $f_{c,\xi_{\theta\theta}}$, grow faster than lower modes and $m \leq 1$ modes even do not emerge since the surface energy decreases by increasing the surface area (last row). Since S_n appears as the normal force coefficient while S_{nb} consists of both normal and bending force coefficients (see Eqs. (4.24) and (4.25)), the described phenomenology of capillary instabilities in axial fibers is attributed to anisotropic effects arising from surface gradients of normal and bending stresses. More importantly, the nematic ordering contribution to the surface energy, which renormalizes the effect of the fiber shape, plays a crucial role to determine the instability mechanisms (last two rows).

We next discuss in detail the physical and mathematical aspects of the tabulated information.

Instability characterization in axial fibers

As explained above the physics of capillary instabilities in axial fibers, as summarized in Table 4.2, is elucidated by considering the sign and magnitudes of the displacement and curvature forces. Figure 4-2 shows a representative schematic of the displacement (f_d) and curvature ($f_{c,\xi_{zz}}$, $f^{m1}_{c,\xi_{\theta\theta}}$, $f^{m}_{c,\xi_{\theta\theta}}$) forces as a function of the dimensionless nematic temperature ΔT^*, for (a) $a^* \leq a^*_c$ and (b) $a^* > a^*_c$, where $f_{c,\xi_{zz}}$ represents the curvature forces from ξ_{zz}, $f^{m1}_{c,\xi_{\theta\theta}}$ the curvature force from $\xi_{\theta\theta}$ for mode $m = 1$, and $f^{m}_{c,\xi_{\theta\theta}}$ for $m \geq 2$ modes. The roman numerals (I, II, III) refer to the three regimes of Table 4.2. Since the cross-section of the axisymmetric mode is circular and centered on the z-axis, there is no curvature force from $\xi_{\theta\theta}$ for mode $m = 0$. The figure provides the reasons for the existence of the only regime (I) for $a^* \leq a^*_c$ and of the two regimes (II, III) for $a^* > a^*_c$, and observation of the sign and relative magnitudes of the stabilizing and destabilizing forces explains the phenomenology of Table 4.2. As summarized in Table 4.3, Fig. 4-2(a) shows that in Regime I the displacement forces f_d are destabilizing while the curvature forces $f_{c,\xi_{zz}}$, $f^{m1}_{c,\xi_{\theta\theta}}$, and $f^{m}_{c,\xi_{\theta\theta}}$ stabilizing, showing smaller curvature force for $m = 1$ ($f^{m1}_{c,\xi_{\theta\theta}}$) than for $m \geq 2$ ($f^{m}_{c,\xi_{\theta\theta}}$). It is seen that the stabilizing forces for the non-axisymmetric modes are sufficiently strong to quench the instability, and thus only $m = 0$ is unstable. In other words, it is energetically costly to cause instability modes $m \geq 1$ as seen

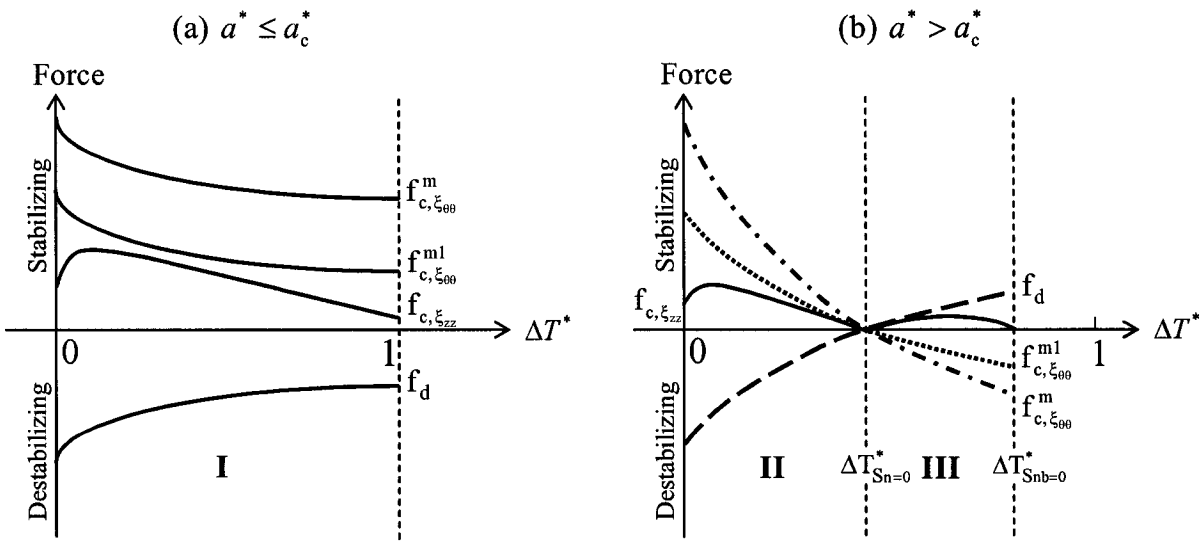

Figure 4-2: Representative schematic of the displacement (f_d) and curvature ($f_{c,\xi_{zz}}$, $f^{ml}_{c,\xi_{\theta\theta}}$, $f^{m}_{c,\xi_{\theta\theta}}$) forces as a function of the dimensionless nematic temperature ΔT^*, for (a) $a^* \leq a_c^*$ and (b) $a^* > a_c^*$, where $f_{c,\xi_{zz}}$ represents the curvature forces from ξ_{zz}, $f^{ml}_{c,\xi_{\theta\theta}}$ the curvature force from $\xi_{\theta\theta}$ for mode $m = 1$, and $f^{m}_{c,\xi_{\theta\theta}}$ for $m \geq 2$ modes. The roman numerals (I, II, III) refer to the three regimes of Table 4.2. Since the cross-section of the axisymmetric mode is circular and centered on the z-axis, there is no curvature force from $\xi_{\theta\theta}$ for mode $m = 0$. The figure provides the reasons for the existence of the only regime (I) for $a^* \leq a_c^*$ and of the two regimes (II, III) for $a^* > a_c^*$, and observation of the sign and relative magnitudes of the stabilizing and destabilizing forces explains the phenomenology of Table 4.2.

by comparing the magnitude of stabilizing forces with that of destabilizing forces. Fig. 4-2(b) shows that in Regime II f_d is destabilizing while $f_{c,\xi_{zz}}$, $f^{m1}_{c,\xi_{\theta\theta}}$, and $f^{m}_{c,\xi_{\theta\theta}}$ are all stabilizing. The stabilizing forces for the non-axisymmetric modes are again sufficiently strong to quench the instability, and thus only $m = 0$ is unstable. In Regime III, f_d becomes stabilizing as well as $f_{c,\xi_{zz}}$ while $f^{m1}_{c,\xi_{\theta\theta}}$ and $f^{m}_{c,\xi_{\theta\theta}}$ become destabilizing, showing smaller destabilizing curvature forces for $m = 1$ than for $m \geq 2$. Since only for $m \geq 2$ the magnitude of the destabilizing forces is relatively greater than that of the total stabilizing forces and $f_{c,\xi_{zz}}$ is stabilizing, the bounded simultaneous instability occurs for $m \geq 2$. Moreover, higher mode shows larger destabilizing forces, resulting in Eq. (4.34). It is noted that since $S_{nb} > 0$, the region of $\Delta T^*_{S_{nb}=0} \leq \Delta T^* < 1$, where $S_n < S_{nb} < 0$, is thermodynamically inaccessible.

The nature of non-axisymmetric instabilities can be explained by referring to the summary of last two rows in Table 4.3. For the cylindrical axial fiber, the surface orientation of the nematic texture is along the fiber axis. Since the planar easy axis of the surface is considered, the misalignment between the actual director and the easy axis is small enough not to cause the non-axisymmetric instability by means of bending stresses. Moreover, the anchoring contribution through surface gradients of bending stresses tends to stabilize the capillary instability due to the positive anchoring strength W_p. On the other hand, since the nematic ordering coefficient C is negative, the nematic ordering contribution to the surface free energy, $\gamma_{\mathbf{S}}$, competes with the usual isotropic and the anchoring contributions (see Eq. (4.17)). For the sufficiently large ratio of nematic ordering energy to isotropic surface energy ($a^* > a^*_c$), if the nematic temperature, which satisfies Eq. (4.8), is low enough (close to T_p), the high degree of nematic ordering gives rise to a large negative value of C and may even cause non-axisymmetric deformation by allowing for surface deformations and rotations in order to decrease the surface energy by increasing the surface area. These observations on the symmetry of the unstable modes can be made quantitative, as follows. When the growth rate α^* is real and positive, the surface disturbances become unstable and grow with time. For the axial fiber, by solving Eq. (4.28) positive real α^* solutions are obtained when the following condition is satisfied:

$$S_n(1 - m^2) - S_{nb}\,(ka)^2 > 0\,, \tag{4.36}$$

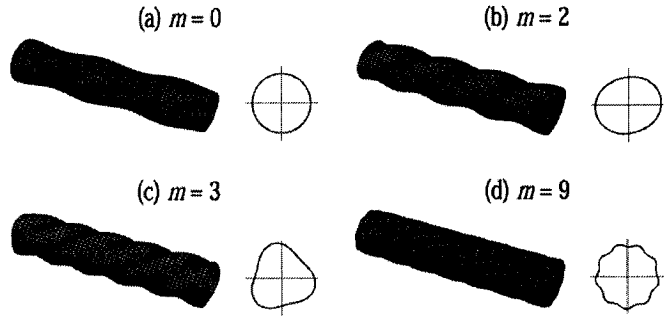

Figure 4-3: Computed visualization of 3D views of unstable fibers (left), and the cross-sectional fiber geometry (right), for $a^* > a_c^*$, and the following azimuthal wavenumbers: $m = 0, 2, 3, 9$. For $m \geq 2$ capillary instabilities result in chiral structures.

which reduces to

$$0 < (ka)^2 < \frac{S_n(1-m^2)}{S_{nb}}. \tag{4.37}$$

Eq. (4.37) gives the upper ka_{cutoff} for the axisymmetric mode $m = 0$ when $S_n > 0$ (Regime I, II in Table 4.2, 4.3) and for the non-axisymmetric modes $m \geq 2$ when $S_n < 0$ (Regime III in Table 4.2, 4.3). In the Newtonian fiber ($S_{nb} = S_n = 1$ since $\Delta T^* = 0$) inequality Eq. (4.36) is never fulfilled for $m \geq 1$, and the positive real α^* is obtained only for the axisymmetric disturbances ($m = 0$), from Eq. (4.28).

Symmetry of deformation modes in axial fibers

In this study, surface disturbances are classified by the mode m in the azimuthal direction given in Eq. (3.3). Because m is an integer, positive and negative signs are equally possible for each value of m. In axial fibers, the sign selects the handedness of the shape deformation but does not affect the growth rate curves due to the m^2 dependence of the growth rate in Eq. (4.28). A positive sign imprints a left-handed rotation to the surface pattern and thus these are chiral modes. The mode m_0, which is a so-called varicose mode, represents the well-known axisymmetric disturbance. Likewise, the m_1 mode is called the sinuous mode, and modes with $m \geq 2$, fluted modes.

Figure 4-3 shows computed visualization of the cross-sections and 3D views of four instability modes, using Eqs. (3.2), (3.3), and (4.28), for $a^* > a_c^*$. In Regime II (see Table 4.2) the

only axisymmetric mode $m = 0$ is unstable while the bounded simultaneous non-axisymmetric instabilities for $m \geq 2$ occur in Regime III, among which m_2, m_3, and m_9 modes are seen in this figure. Fig. 4-3 shows that the cross-sectional shape and position of the fibers are periodic in the z-direction. For $m \geq 2$ the spatial period of the chiral microstructure, called the pitch and given by $\lambda = 2\pi/(ka)$, defines the degree of twisting per unit length. For m_2, the fiber has a constant elliptic cross-section, which rotates along the fiber axis, while for $m \geq 3$ the cross-sectional shape has a regular pattern identified by m axes of rotational symmetry and rotates along the fiber axis. The axial rotation of the anisotropic cross-sectional shape for $m \geq 2$, produces twisted ridged microstructures. For the classical m_0 mode, $\lambda = 2\pi/ka$ is the dimensionless wavelength of the varicose shape in the z-direction. The fiber cross-section is always circular but periodically expands and contracts when traversing the axial fiber direction. Thus, for the m_0 mode the formation of droplets with a characteristic size λ is predicted. It is noted that, while changing Oh and Oh_m change the maximum growth rate and the corresponding wavenumber, they have no effect on the surface deformation pattern.

Parametric effects on capillary instabilities in axial fibers

The contribution of the viscosity ratio to the capillary instabilities of a thin nematic fiber in a viscous matrix is analyzed by two parameters, the fiber and matrix Ohnesorge numbers, where viscosity ratio is defined as

$$VR = \frac{\mu}{\eta} = \frac{Oh_m}{Oh}. \tag{4.38}$$

Following convention, either Oh_m or VR is used to display the results of the effect of viscosities on the capillary instabilities when setting Oh equal to a constant value.

Since, for the m_0 mode (Regime I, II in Table 4.2), the formation of droplets after fiber break-up is predicted due to the axisymmetric instability while the pitch of the chiral microstructures for $m \geq 2$ (Regime III in Table 4.2) is calculated from $ka_{\max}$, we introduce the relative droplet size r^* for $m = 0$ and the dimensionless pitch λ^* for $m \geq 2$ to analyze the nematic temperature effect on the characteristic size of the surface microstructures in capillary instabilities, given by

$$r^* = \frac{r}{r_{\text{ref}}} = \sqrt[3]{\frac{ka_{\max,\,\text{ref}}}{ka_{\max}}}, \qquad \lambda^* = \frac{\lambda}{\lambda_{\text{ref}}} = \frac{ka_{\max,\,\text{ref}}}{ka_{\max}}, \tag{4.39}$$

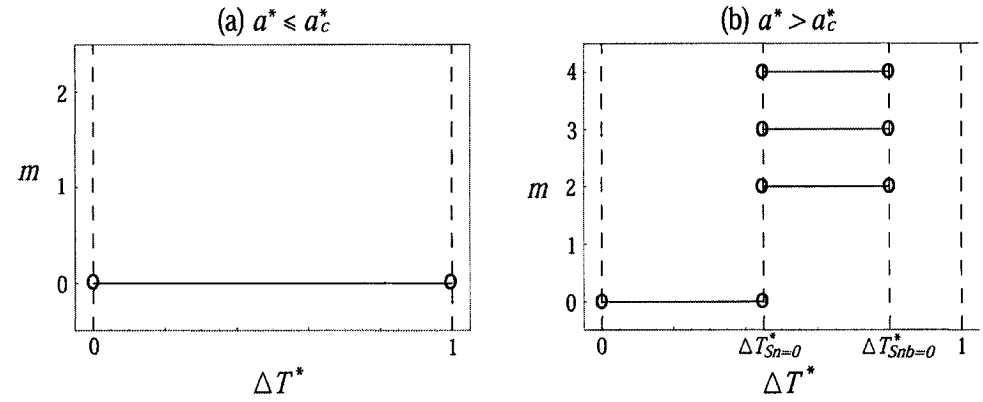

Figure 4-4: Azimuthal wavenumber m as a function of dimensionless nematic temperature ΔT^* for (a) $a^* \leq a_c^*$ and (b) $a^* > a_c^*$. (a) corresponds to Regime I (MR/A instability), and (b) to Regime II and III (MR/A and BS/NA instabilities) in Table 4.2. For $a^* \leq a_c^*$, only the MR mode m_0 persists over the whole range of ΔT^* while, for $a^* > a_c^*$, the transition of instability mechanisms from MR to BS is seen. The region of $\Delta T^*_{S_{nb}=0} \leq \Delta T^* < 1$ is thermodynamically inaccessible.

where $ka_{\max} = 1/\sqrt{2}$, which corresponds to an isotropic fiber ($\Delta T^* = 0$) and inviscid system ($Oh = Oh_m = 0$).

Figure 4-4 shows the azimuthal wavenumber m as a function of dimensionless nematic temperature ΔT^* for (a) $a^* \leq a_c^*$ and (b) $a^* > a_c^*$. Fig. 4-4(a) corresponds to Regime I (MR/A instability), and Fig. 4-4(b) to Regime II and III (MR/A and BS/NA instabilities) in Table 4.2. In Fig. 4-4(a), for $a^* \leq a_c^*$, only the MR mode m_0 persists over the whole range of ΔT^* because the stabilizing curvature forces for modes $m \geq 1$ are sufficiently strong. In Fig. 4-4(b), for $a^* > a_c^*$, the transition of instability mechanisms from MR to BS is seen. The MR mode m_0 persists for $0 < \Delta T^* < \Delta T^*_{S_n=0}$, while $m \geq 2$ modes arise simultaneously for $\Delta T^*_{S_n=0} < \Delta T^* < \Delta T^*_{S_{nb}=0}$ since the curvature forces from $\xi_{\theta\theta}$ are destabilizing and total destabilizing forces for $m \geq 2$ modes are greater than total stabilizing forces. Both types of instabilities are bounded with upper ka_{cutoff} since the curvature forces from ξ_{zz} are always stabilizing. At $\Delta T^* = \Delta T^*_{S_n=0}$, all displacement and curvature forces become equal to 0 (see also Fig. 4-2(b)) and thus instabilities do not occur. Through this temperature the transition of instability mechanisms from MR to BS occurs and is regarded as a transition of a more complicated instability regime (Regime III in Table 4.2). The region of $\Delta T^*_{S_{nb}=0} \leq \Delta T^* < 1$ is

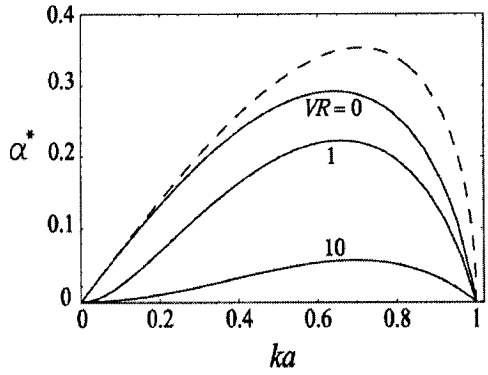

Figure 4-5: Dimensionless growth rate curves α^* as a function of dimensionless wavenumber ka, for m_0 at $\Delta T^* = 0$, for $VR = 0, 1, 10$ when $Oh = 0.1$(solid curves), and $Oh = Oh_m = 0$ (dashed curve). The figure shows the viscous effects of fiber (Oh) and matrix (Oh_m) on capillary instabilities for the isotropic fiber ($\Delta T^* = 0$).

thermodynamically inaccessible.

Figure 4-5 shows the dimensionless growth rate curves α^* as a function of the dimensionless wavenumber ka, for m_0 at $\Delta T^* = 0$, for $VR = 0, 1, 10$ when $Oh = 0.1$(solid curves), and $Oh = Oh_m = 0$ (dashed curve). This figure shows the viscous effects of fiber (Oh) and matrix (Oh_m) on capillary instabilities for the isotropic fiber ($\Delta T^* = 0$). From the dashed curve and the solid curve for $Oh = 0.1$ and $VR = 0$, it is seen that increasing Oh decreases the maximum growth rate and shifts it to lower ka values, meaning that fiber viscosity increases the length scales of the unstable mode. Meanwhile, solid curves show that increasing VR (increasing Oh_m) decreases the maximum growth rate and shifts it to higher ka values, meaning that matrix viscosity decreases the length scales of the unstable mode. In summary, the capillary instabilities of a thin nematic fiber in a viscous matrix are suppressed by increasing either the fiber or matrix Ohnesorge number, but the estimated droplet sizes after fiber break-up in axisymmetric instabilities substantially decrease with increasing the matrix Ohnesorge number.

Figure 4-6 shows the dimensionless growth rate curves α^* as a function of the dimensionless wavenumber ka, for m_0 at $b = 0.25\,(a_c^* = 0.5714)$, for (a) $Oh = Oh_m = 0$ when $a^* = 0.3$ and $\Delta T^* = 0$ (dash), 0.3505 (solid), 0.7092 (dash-dot), 1 (dash), (b) $Oh = Oh_m = 0$ when $a^* = 1$ and $\Delta T^* = 0$ (dash), 0.01, 0.1, 0.3, 0.4, (c) $Oh = 0.1$ and $VR = 1$ when $a^* = 0.3$ and $\Delta T^* = 0$ (dash), 0.3611 (solid), 0.7995 (dash-dot), 1 (dash), and (d) $Oh = 0.1$ and $VR = 1$

when $a^* = 1$ and $\Delta T^* = 0$ (dash), 0.01, 0.1, 0.3, 0.4. This figure shows the effects of ΔT^* on the m_0 instability in two different regions of a^* at a constant b. Fig. 4-6 corresponds to the MR/A instability: Fig. 4-6(a, c) to Regime I ($a^* \leq a_c^*$), and Fig. 4-6(b, d) to Regime II ($a^* > a_c^*$) in Table 4.2. In Fig. 4-6(a, c), according to Eq. (4.28), the only unstable mode is m_0 over the whole range of ΔT^*. For $a^* = 0.3$ and $Oh = Oh_m = 0$ ($Oh = 0.1$ and $VR = 1$), at $\Delta T^* = 0.3505$ (0.3611) $ka_{\max}$ reaches the local minimum while $\alpha^*_{\max}$ reaches the local minimum at $\Delta T^* = 0.7092$ (0.7995). Thus, increasing ΔT^* suppresses the capillary instability until $ka_{\max}$ and $\alpha^*_{\max}$ reach separately the local minima, and then releases the instability fully in $ka_{\max}$ but incompletely in $\alpha^*_{\max}$ as $\Delta T^* \to 1$ (see Fig. 4-7 and discussion below). Besides decreasing the maximum growth rate, the effect of increasing Oh and Oh_m is to increase slightly the nematic temperatures ΔT^* of the local minima of $ka_{\max}$ and $\alpha^*_{\max}$. In Fig. 4-6(b, d), according to Eq. (4.28), the mode m_0 is unstable for $0 < \Delta T^* < \Delta T^*_{S_n=0}$, where $\Delta T^*_{S_n=0} = 0.4444$ at $a^* = 1$. As ΔT^* increases, the maximum growth rate $\alpha^*_{\max}$ and the corresponding wavenumber $ka_{\max}$ decrease and finally the growth rate becomes 0 at $\Delta T^* = \Delta T^*_{S_n=0}$. The cutoff wavenumber ka_{cutoff} is also decreasing with ΔT^* but a function of neither Oh nor Oh_m. It is also noted that the growth rate curves for $\Delta T^* = 0$ when $Oh = Oh_m = 0$ and when $Oh = 0.1$ and $VR = 1$ in Fig. 4-6 (dashed curves) correspond to those in Fig. 4-5, respectively. It is seen in Fig. 4-6 that the suppressing effect of the fiber and matrix viscosities is evident, showing that the values $Oh > 0$ and $Oh_m > 0$ change the maximum growth rate and the corresponding wavenumber. In what follows, we discuss our results only for $Oh = Oh_m = 0$.

Figure 4-7 shows the maximum growth rate $\alpha^*_{\max}$, and the corresponding maximum dimensionless wavenumber $ka_{\max}$ as a function of dimensionless nematic temperature ΔT^*, for m_0 when $Oh = Oh_m = 0$, for (a) $a^* = 0.1$ (solid), 0.3 (solid), 0.5 (solid), 0.5714 (dash), 0.6 (dash-dot), 1 (dash-dot) at $b = 0.25$ and (b) $a^* = 0.1$, 0.3, 0.5, a_c^*, 1, at $b = 0.01$ (dash), 0.25 (solid), 0.49 (dash-dot). Fig. 4-7 corresponds to Regime I and II in Table 4.2, and to the MR/A instability. Fig. 4-7(a) shows the effects of ΔT^* on $\alpha^*_{\max}$ and $ka_{\max}$ of the m_0 instability in three different regions of a^* at a constant b. Referring to the nematic temperature effect on the growth rate shown in Fig. 4-6(a), for $a^* < a_c^*$ (solid curves), $\alpha^*_{\max}$ and $ka_{\max}$ as a function of ΔT^* have local minima. As a^* increases, the local minima for $\alpha^*_{\max}$ and $ka_{\max}$ approach asymptotically the values of $\alpha^*_{\max}$ and $ka_{\max}$, respectively, at $\Delta T^* = 1$ and $a^* = a_c^* = 0.5714$.

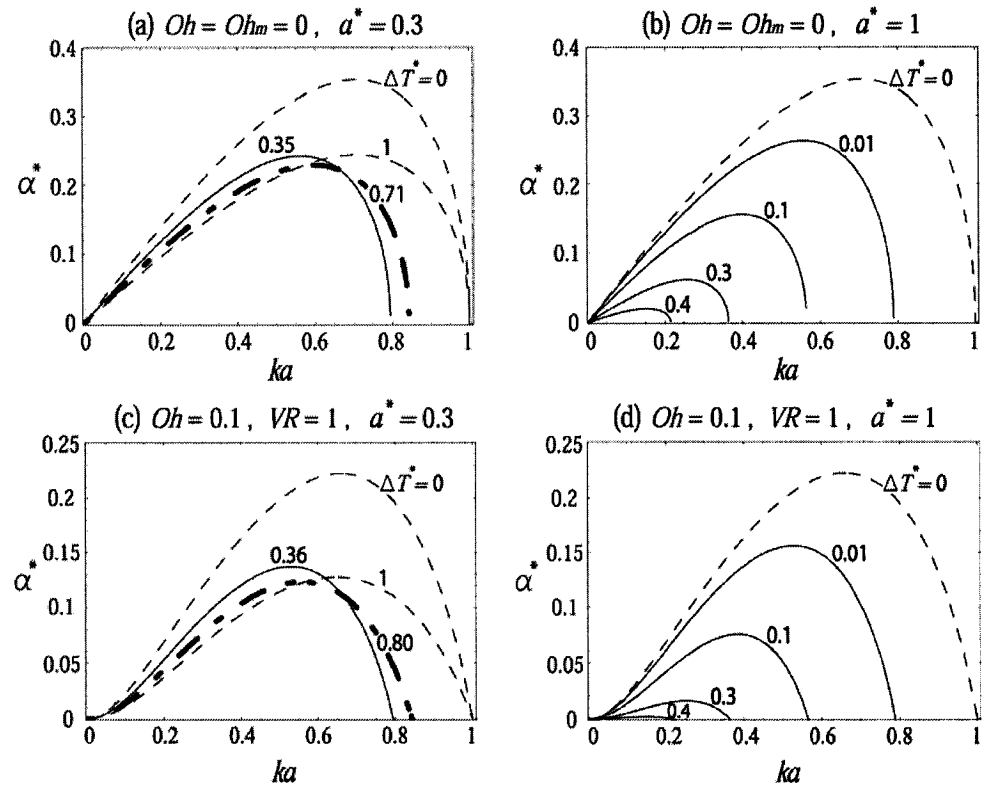

Figure 4-6: Dimensionless growth rate curves α^* as a function of dimensionless wavenumber ka, for m_0 at $b = 0.25\,(a_c^* = 0.5714)$, for (a) $Oh = Oh_m = 0$ when $a^* = 0.3$ and $\Delta T^* = 0$ (dash), 0.3505 (solid), 0.7092 (dash-dot), 1 (dash), (b) $Oh = Oh_m = 0$ when $a^* = 1$ and $\Delta T^* = 0$ (dash), 0.01, 0.1, 0.3, 0.4, (c) $Oh = 0.1$ and $VR = 1$ when $a^* = 0.3$ and $\Delta T^* = 0$ (dash), 0.3611 (solid), 0.7995 (dash-dot), 1 (dash), and (d) $Oh = 0.1$ and $VR = 1$ when $a^* = 1$ and $\Delta T^* = 0$ (dash), 0.01, 0.1, 0.3, 0.4. The figure shows the effects of ΔT^* on the m_0 instability in two different regions of a^* at a constant b. The figure corresponds to the MR/A instability: (a, c) to Regime I ($a^* \leq a_c^*$), and (b, d) to Regime II ($a^* > a_c^*$) in Table 4.2.

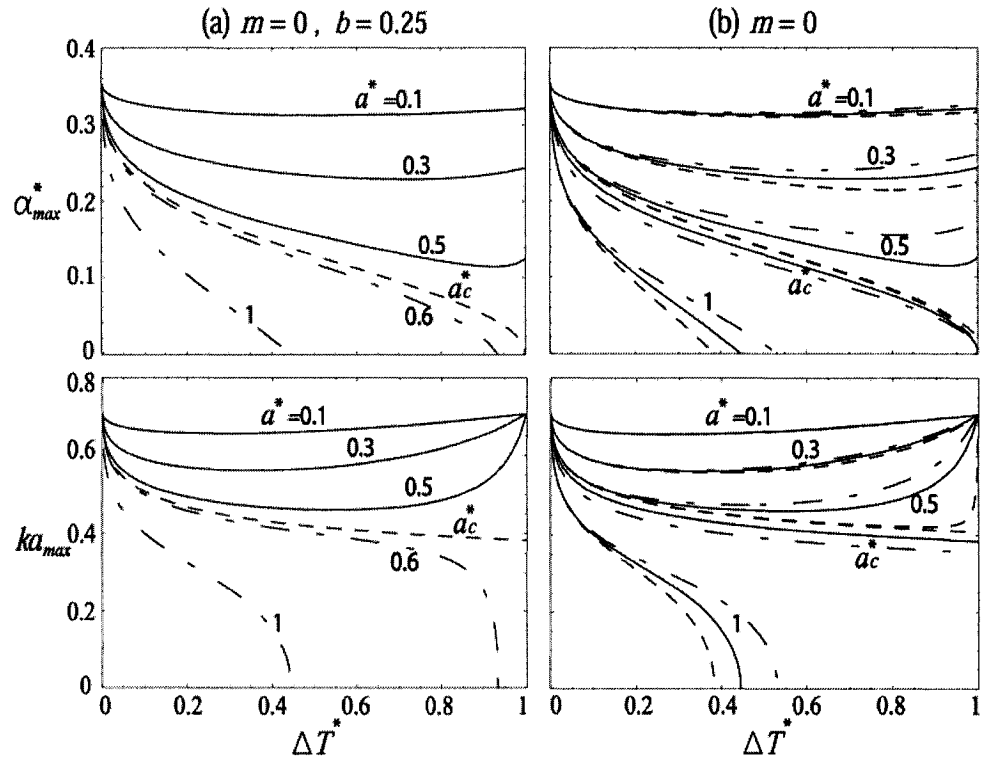

Figure 4-7: Maximum growth rate $\alpha^*_{\max}$, and the corresponding maximum dimensionless wavenumber $ka_{\max}$ as a function of dimensionless nematic temperature ΔT^*, for m_0 when $Oh = Oh_m = 0$, for (a) $a^* = 0.1$ (solid), 0.3 (solid), 0.5 (solid), 0.5714 (dash), 0.6 (dash-dot), 1 (dash-dot) at $b = 0.25$ and (b) $a^* = 0.1$, 0.3, 0.5, a^*_c, 1, at $b = 0.01$ (dash), 0.25 (solid), 0.49 (dash-dot). The figure corresponds to Regime I and II in Table 4.2, and to the MR/A instability. (a) shows the effects of ΔT^* on $\alpha^*_{\max}$ and $ka_{\max}$ of the m_0 instability in three different regions of a^* at a constant b. (b) shows the effect of b on the dependence of $\alpha^*_{\max}$ and $ka_{\max}$ of the m_0 instability on ΔT^* in three different regions of a^*.

Table 4.4: Maximum growth rate, and the corresponding maximum dimensionless wavenumber as a function of dimensionless nematic temperature for constant b.

b = constant : $S_n(a^*, \Delta T^*)$, $S_{nb}(a^*, \Delta T^*)$	At $\Delta T^* = 0$, $S_n = S_{nb} = 1$ For $\Delta T^* > 0$, $S_{nb} > S_n > 0$ $S_n \downarrow$, $S_{nb} \uparrow\downarrow$ as $\Delta T^* \uparrow$	
a^*	$\alpha^*_{\max} \propto \sqrt{\frac{S_n^2}{S_{nb}}}$	$ka_{\max} \propto \sqrt{\frac{S_n}{S_{nb}}}$
$a^* < a^*_c$: At $\Delta T^* = 1$, $S_n = S_{nb} > 0$	$\downarrow$ (local minimum) $\uparrow$	$\downarrow$ (local minimum) $\uparrow$
$a^* = a^*_c$: At $\Delta T^* = 1$, $S_n = S_{nb} = 0$	$\downarrow$ to 0	$\downarrow$ to finite
$a^* > a^*_c$: At $\Delta T^*_{S_n=0}$, $S_n = 0$, $S_{nb} > 0$	$\downarrow$ to 0 at $\Delta T^*_{S_n=0}$	$\downarrow$ to 0 at $\Delta T^*_{S_n=0}$

Accordingly, the droplet size after fiber break-up is predicted to change from small to large to small by increasing ΔT^*, and at a constant ΔT^* the relative droplet size in Eq. (4.39) is bigger for larger a^* in this regime (see Fig. 4-10(a) and discussion below). When $a^* = a^*_c$ (dashed curve), $\alpha^*_{\max}$ and $ka_{\max}$ gradually decrease with ΔT^*. At $\Delta T^* = 1$, the growth rate becomes 0 while $ka_{\max}$ a finite value. Referring to Fig. 4-6(b), for $a^* > a^*_c$ (dash-dot curves), $\alpha^*_{\max}$ and $ka_{\max}$ monotonically decrease with ΔT^* and become 0 at $\Delta T^* = \Delta T^*_{S_n=0}$ ($\Delta T^*_{S_n=0} = 0.9338$ for $a^* = 0.6$, and $\Delta T^*_{S_n=0} = 0.4444$ for $a^* = 1$). Tables 4.4 and 4.5 summarize how and why the $\alpha^*_{\max}$ and $ka_{\max}$ dependence on ΔT^* is different for (a) three different regions of a^* at constant b (Tables 4.4) and for (b) two different regions of a^* at changing b (Tables 4.5). In Table 4.4, the first row shows general conditions which are always satisfied that $S_n = S_{nb} = 1$ at $\Delta T^* = 0$ and $S_{nb} > S_n > 0$ for $\Delta T^* > 0$, and which are obtained from Eqs. (4.21, 4.22) at a constant b that S_n decreases while S_{nb} increases and then decreases with ΔT^*. The $\alpha^*_{\max}$ and $ka_{\max}$ dependence on S_n and S_{nb} is evaluated using Eq. (4.31). The first column shows three different regions of a^* and the corresponding conditions found. The entries show the $\alpha^*_{\max}$ and $ka_{\max}$ dependence, either increasing or decreasing, on ΔT^*. In summary, although the general conditions in the first row are equally applied, the characteristic condition at each region of a^* eventually controls the $\alpha^*_{\max}$ and $ka_{\max}$ dependence. As a^* increases, the combined effects of the nematic ordering and the anchoring tend to quench the m_0 instability by decreasing $\alpha^*_{\max}$ and $ka_{\max}$ and even by shifting $\Delta T^*_{S_n=0}$ to lower values for $a^* > a^*_c$. Fig. 4-7(b) shows the effect of b on the dependence of $\alpha^*_{\max}$ and $ka_{\max}$ of the m_0 instability on ΔT^* in three different regions

Table 4.5: Maximum growth rate, and the corresponding maximum dimensionless wavenumber as a function of dimensionless nematic temperature for changing b.

$b \neq$ constant : $S_n(a^*, b, \Delta T^*)$, $S_{nb}(a^*, b, \Delta T^*)$	At $\Delta T^* = 0$, $S_n = S_{nb} = 1$ For $\Delta T^* > 0$, $S_{nb} > S_n > 0$	
a^*	$\alpha^*_{\max} \propto \sqrt{\frac{S_n^2}{S_{nb}}}$	$ka_{\max} \propto \sqrt{\frac{S_n}{S_{nb}}}$
$a^* \neq a_c^*$: $b \downarrow \Rightarrow S_n(\Delta T^*) \downarrow$, $S_{nb}(\Delta T^*) \downarrow$	$\downarrow$	$\downarrow$
$b \downarrow \Rightarrow a_c^* \downarrow$ ($S_n = S_{nb} = 0$ at $\Delta T^* = 1$)	renormalization of $S_n(\Delta T^*)$ and $S_{nb}(\Delta T^*)$ is more effective at larger ΔT^* and a^*	
$a^* = a_c^*$: $b \downarrow \Rightarrow a_c^* \downarrow \Rightarrow S_n(\Delta T^*) \uparrow$, $S_{nb}(\Delta T^*) \downarrow$	$\uparrow$	$\uparrow$

of a^*. Decreasing b decreases $\alpha^*_{\max}$ and $ka_{\max}$ for any value of a^*, except for a_c^*. The effect of changing b is even more evident for larger a^* and ΔT^*, and thus smaller a^* less sensitive to the effect of b so that differences in $\alpha^*_{\max}$ and $ka_{\max}$ are hardly recognizable for $a^* = 0.1$ in the figure. It is also noted that the effect of b is opposite when $a^* = a_c^*$, i.e., decreasing b increases $\alpha^*_{\max}$ and $ka_{\max}$ but not by a large amount. The reason for the above effects of b is now explained. In Table 4.5, the first column shows two different regions of a^* and the corresponding conditions found by decreasing b. The entries show the $\alpha^*_{\max}$ and $ka_{\max}$ dependence on ΔT^*. In summary, decreasing b decreases a_c^* (see Eq. (4.35)) and tends to decrease $\alpha^*_{\max}$ and $ka_{\max}$ for any value of a^*, except for a_c^*, by decreasing S_n by a larger amount than decreasing S_{nb} (see Eq. (4.31)) since only the nematic ordering coefficient C in both S_n and S_{nb} is a function of b (see Eqs. (4.21, 4.22)). In addition, the renormalization effects of S_n and S_{nb} due to changing a_c^* are taken into account since changing b alters a_c^*, which is obtained in the condition that $S_n = S_{nb} = 0$ at $\Delta T^* = 1$. Since the condition, $S_n = S_{nb} = 1$ at $\Delta T^* = 0$, holds for any values of a^* and b, the renormalization effect on S_n and S_{nb} is more clearly seen far from the fixed point $\Delta T^* = 0$, i.e., near $\Delta T^* = 1$, or at larger a^*. On the other hand, when $a^* = a_c^*$, the renormalization of S_n and S_{nb} with decreasing b results in small amount increase of S_n but decrease of S_{nb}, and thus allows for increasing $\alpha^*_{\max}$ and $ka_{\max}$. Since changing b has a much smaller effect than changing a^*, b is set at 0.25 in most of our results.

Figure 4-8 shows the maximum growth rate $\alpha^*_{\max}$, and the corresponding maximum dimensionless wavenumber $ka_{\max}$ as a function of dimensionless nematic temperature ΔT^*, for $a^* = 1$ and $b = 0.25$ ($a_c^* = 0.5714$) when $Oh = Oh_m = 0$. Since $a^* > a_c^*$, Fig. 4-8 corresponds to

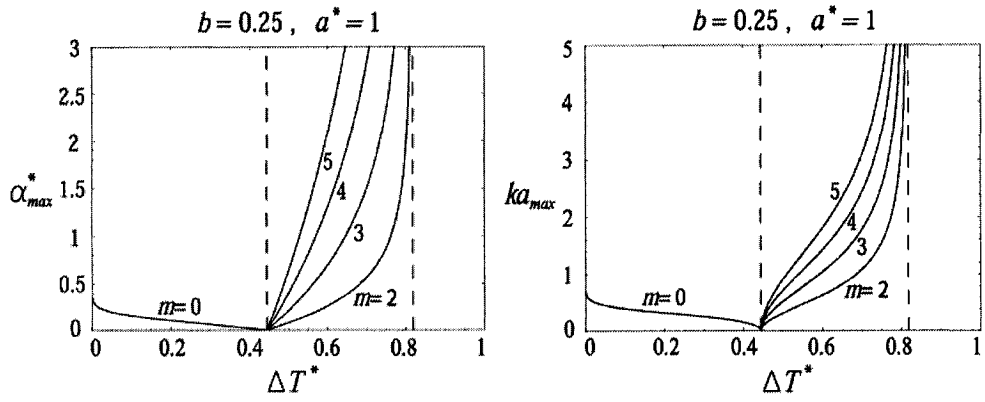

Figure 4-8: Maximum growth rate $\alpha^*_{\max}$, and the corresponding maximum dimensionless wavenumber $ka_{\max}$ as a function of dimensionless nematic temperature ΔT^*, for $a^* = 1$ and $b = 0.25\,(a_c^* = 0.5714)$ when $Oh = Oh_m = 0$. This figure corresponds to Regime II (MR/A instability) and Regime III (BS/NA instability) in Table 4.2.

Regime II (MR/A instability) in Table 4.2 for $0 < \Delta T^* < \Delta T^*_{S_n=0}\,(= 0.4444)$ and to Regime III (BS/NA instability) in Table 4.2 for $\Delta T^*_{S_n=0} < \Delta T^* < \Delta T^*_{S_{nb}=0}\,(= 0.8182\,)$. Referring to Table 4.3, the m_0 mode emerges in Regime II, which grows slower as $\Delta T^* \rightarrow \Delta T^*_{S_n=0}$ and becomes stable at $\Delta T^* = 0.4444$. In this regime, the surface energy decreases by decreasing the surface area (last row in Table 4.3). In Regime III, the bounded simultaneous instabilities are seen for modes $m \geq 2$, but only four modes are presented in the figure, clearly showing that higher modes grow faster than lower modes since the surface energy decreases by increasing the surface area (last row in Table 4.3) and the modes grow even faster near $\Delta T^* = 0.8182$. Referring to Fig. 4-2(b), since at $\Delta T^* = \Delta T^*_{S_n=0}$ all displacement and curvature forces become equal to 0, and thus instabilities do not occur. Considering that nematic temperatures of the transition, $\Delta T^*_{S_n=0}$ and $\Delta T^*_{S_{nb}=0}$, totally change with changing a^*, it seems impossible to analyze the a^* effects on the BS/NA instabilities.

Figure 4-9 shows the dimensionless cutoff wavenumber ka_{cutoff} as a function of dimensionless nematic temperature ΔT^* at $b = 0.25$, for (a) $a^* = 0.3$, $0.5714\,(a_c^*)$, 1, for m_0, and (b) $a^* = 1$, for m_2 to m_5. Figure 4-9(c) shows the dimensionless cutoff wavenumber ka_{cutoff} as a function of mode number m at $\Delta T^* = 0.6$ for $a^* = 1$. Fig. 4-9(a) corresponds to Regime I and II in Table 4.2, and to the MR/A instability. ka_{cutoff} shows the same pattern as $ka_{\max}$ in Fig. 4-7(a) that for

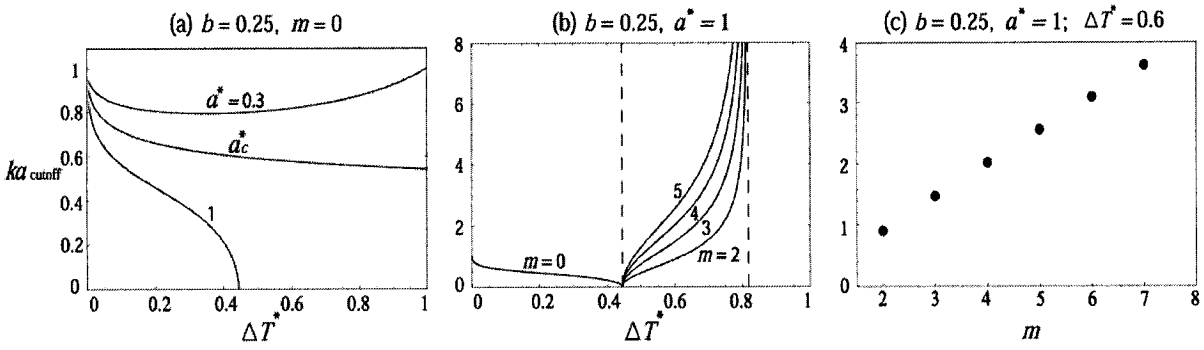

Figure 4-9: Dimensionless cutoff wavenumber ka_{cutoff} as a function of dimensionless nematic temperature ΔT^* at $b = 0.25$, for (a) $a^* = 0.3$, $0.5714\,(a_c^*)$, 1, for m_0, and (b) $a^* = 1$, for m_2 to m_5. (c) Dimensionless cutoff wavenumber ka_{cutoff} as a function of mode number m at $\Delta T^* = 0.6$ for $a^* = 1$. (a) corresponds to Regime I and II for MR/A instability, (b) to Regime II for MR/A instability and Regime III for BS/NA instability, (c) to Regime III for BS/NA instability in Table 4.2.

$a^* < a_c^*$ ka_{cutoff} has a local minimum. Fig. 4-9(b) corresponds to Regime II (MR/A instability) in Table 4.2 for $0 < \Delta T^* < \Delta T^*_{S_n=0}\,(= 0.4444)$ and to Regime III (BS/NA instability) in Table 4.2 for $\Delta T^*_{S_n=0} < \Delta T^* < \Delta T^*_{S_{nb}=0}\,(= 0.8182)$. ka_{cutoff} shows the same pattern as $ka_{\max}$ in Fig. 4-8, i.e., in Regime III higher modes range to larger wavenumbers than lower modes and thus are less stable. Fig. 4-9(c) corresponds to Regime III (BS/NA instability) in Table 4.2. The ka_{cutoff} dependence on m is clearly shown as linear, meaning that higher modes are unstable for larger wavenumbers (smaller wavelength). It is reminded that the cutoff wavenumber ka_{cutoff} is a function of neither Oh nor Oh_m (see also Fig. 4-6).

Figure 4-10 shows the relative droplet size predicted after fiber break-up, r^*, for $m = 0$ and the dimensionless pitch λ^* of the chiral microstructures for $m \geq 2$ as a function of ΔT^*, when $Oh = Oh_m = 0$, at $b = 0.25\,(a_c^* = 0.5714)$, for (a) m_0 and $a^* = 0.3$, 0.5, 0.5714, and (b) $a^* = 1$ and $m = 0$, 2, 3, 5, 9. Fig. 4-10(a) corresponds to Regime I (MR/A instability), and Fig. 4-10(b) to Regime II (MR/A instability) and III (BS/NA instability) in Table 4.2. The droplet size r^* and the pitch λ^* are calculated by using Eq. (4.39). Fig. 4-10(a) shows that, referring to the nematic temperature effect on $ka_{\max}$ for $a^* \leq a_c^*$ shown in Fig. 4-7(a), the droplet size r^* for $a^* < a_c^*$ increases, reaches a local maximum, and then decreases as the nematic temperature ΔT^* increases while r^* monotonically increases for $a^* = a_c^* = 0.5714$.

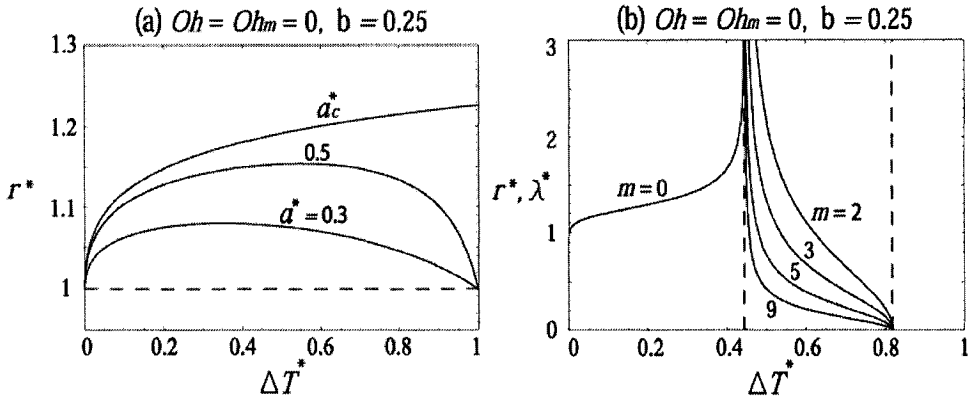

Figure 4-10: Relative droplet size predicted after fiber break-up, r^*, for $m = 0$ and the dimensionless pitch λ^* of the chiral microstructures for $m \geq 2$ as a function of ΔT^*, when $Oh = Oh_m = 0$, at $b = 0.25\,(a_c^* = 0.5714)$, for (a) m_0 and $a^* = 0.3$, 0.5, 0.5714, and (b) $a^* = 1$ and $m = 0$, 2, 3, 5, 9. (a) corresponds to Regime I (MR/A instability), and (b) to Regime II (MR/A instability) and III (BS/NA instability) in Table 4.2. The droplet size r^* and the pitch λ^* are calculated by using Eq. (4.39).

In Fig. 4-10(b), the droplet size r^* for $a^* > a_c^*$ increases and diverges as ΔT^* approaches the transition temperature $\Delta T^*_{S_n=0}$. As ΔT^* further increases, large pitch microstructures at the fiber surface emerge for non-axisymmetric $m \geq 2$ modes, and then the pitches become shorter and shorter. Although only four modes are presented in Regime III, it is clearly seen that higher modes are patterned by much smaller pitches than lower modes, meaning that higher modes grow faster and are more likely observed. Considering that, as ΔT^* increases from 0 to 1, the temperature T actually decreases from T_0 to T_p (see Eq. (4.15)), decreasing temperature T gives rise to the encounter with a local maximum of the characteristic length of the axisymmetric instability for $a^* < a_c^*$ but to monotonic increase of the characteristic length for $a^* \geq a_c^*$. For $a^* > a_c^*$, further decreasing T shortens the characteristic length of the non-axisymmetric instabilities and thus the instabilities become stronger.

Figure 4-11 shows representative structures that summarize capillary instabilities in axial fibers. Fig. 4-11(a) corresponds to Regime I (MR/A instability) while Fig. 4-11(b) to Regime II and III (MR/A and BS/NA instabilities) in Table 4.2. Axial fibers display two types of instabilities, whose symmetry and existence are controlled by the sign and magnitude of S_n in Eq. (4.28). It is seen in Fig. 4-11(a) that small values of a^* lead to the axisymmetric modified

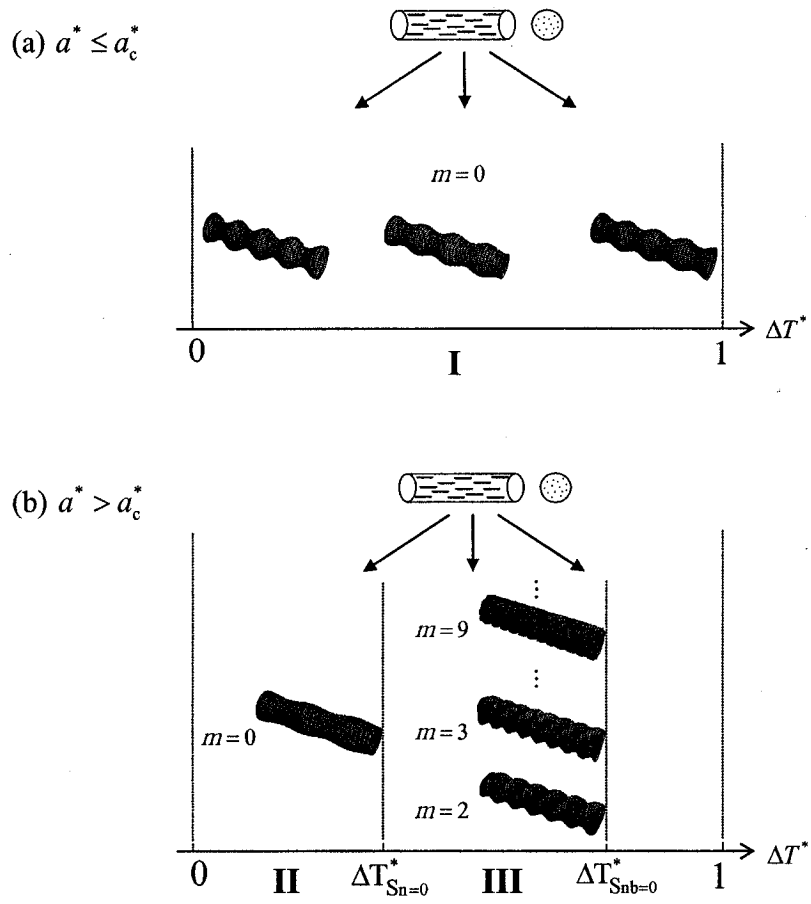

Figure 4-11: Representative structures that summarize capillary instabilities in axial fibers. (a) corresponds to Regime I (MR/A instability) while (b) to Regime II and III (MR/A and BS/NA instabilities) in Table 4.2. Axial fibers display two types of instabilities, whose symmetry and existence are controlled by the sign and magnitude of S_n in Eq. (4.28). Small values of a^* lead to the axisymmetric modified Rayleigh (MR/A) instability over the whole range of ΔT^*, and to an eventual fiber break-up into droplets. Intermediate or large values of a^* lead to the MR instability for small ΔT^* but ignite non-axisymmetric bounded simultaneous (BS/NA) instabilities for intermediate ΔT^*, leading to the distortion of the fiber into lower-symmetry cylindrical fibers.

Rayleigh (MR/A) instability over the whole range of ΔT^*, and to an eventual fiber break-up into droplets. In Fig. 4-11(b), intermediate or large values of a^* lead to the MR instability for small ΔT^* but ignite non-axisymmetric bounded simultaneous (BS/NA) instabilities for intermediate ΔT^*, leading to the distortion of the fiber into lower-symmetry fibers.

4.5 Bending and Torsion Effects on Capillary Instabilities

4.5.1 Modified governing equations

In this section we further investigate the stabilizing mechanism of simultaneous instabilities in Regime III of Table 4.2, in which growth rates infinitely grow with increasing azimuthal wavenumber m. The governing nemato-capillary equation is modified by the fact that the interface curvature effects can be accounted for as contributions of the work of interfacial bending and torsion to the total energy of the system since the bending and torsion deformation is related to variations in the two principal curvatures of the interface [2, 3, 4, 5]. The coefficients of the work of deformation are the interfacial bending and torsion moments, defined below.

The surface stress tensor taking into account the surface moments, in general, consists of the tangential (perpendicular to $\mathbf{N}$) and transversal (parallel to $\mathbf{N}$) contribution [2, 4]:

$$\boldsymbol{\sigma} = \boldsymbol{\sigma}_s + \sigma^{\alpha \mathrm{N}} \mathbf{i}_\alpha \mathbf{N}\,; \qquad \alpha = 1, 2\,, \tag{4.40}$$

where $\mathbf{i}_\alpha$ is the orthonormal unit surface base vector. At the fluid interface, the tangential part of the surface stress tensor $\boldsymbol{\sigma}$ is given as

$$\boldsymbol{\sigma}_s = \frac{1}{2}(\sigma_1 + \sigma_2)\mathbf{I}_s\,, \tag{4.41}$$

where σ_1 and σ_2 are the eigenvalues of $\boldsymbol{\sigma}_s$. The transversal component $\sigma^{\alpha \mathrm{N}}$ is given by

$$\sigma^{\alpha \mathrm{N}} = -\mathbf{i}_\alpha \cdot (\nabla_s \cdot \mathbf{M})\,. \tag{4.42}$$

The bending moment tensor $\mathbf{M}$ in Eq. (4.42) is defined as

$$\begin{aligned}\mathbf{M} &= \frac{1}{2}(M_1 + M_2)\mathbf{I}_s + \frac{1}{2}(M_1 - M_2)\mathbf{q} \\ &= \frac{1}{2}B\mathbf{I}_s + \frac{1}{2}\Theta\mathbf{q}\,,\end{aligned} \tag{4.43}$$

where M_1 and M_2 are the eigenvalues of $\mathbf{M}$, and B and Θ are the surface bending and torsion moments, respectively. The curvature deviatoric tensor $\mathbf{q}$ in Eq. (4.43) is defined as

$$\mathbf{q} = \frac{1}{D}(\mathbf{b} - H\mathbf{I}_s)\,, \qquad \mathbf{b} = -\nabla_s\mathbf{N}\,, \tag{4.44}$$

where $\mathbf{b}$ is the curvature tensor, and D denotes the deviatoric curvature expressed as

$$D = -\frac{1}{2}\left(\frac{1}{R_{r\theta}} - \frac{1}{R_{rz}}\right)\,. \tag{4.45}$$

In conjunction with Eq. (3.14), the total surface elastic stress tensor for the nematic fiber can be rewritten as

$$\mathbf{t}^{\mathrm{se}} = \boldsymbol{\sigma} + \mathbf{t}^{\mathrm{se}}_B\,. \tag{4.46}$$

As derived in Eq. (3.19), the normal component of the surface gradient of $\mathbf{t}^{\mathrm{se}}$ gives rise to the generalized Laplace equation:

$$-p_c = (\nabla_s \cdot \mathbf{t}^{\mathrm{se}}) \cdot \mathbf{N} = (\nabla_s \cdot \boldsymbol{\sigma}) \cdot \mathbf{N} + (\nabla_s \cdot \mathbf{t}^{\mathrm{se}}_B) \cdot \mathbf{N}\,. \tag{4.47}$$

The first term of Eq. (4.47) is obtained by making use of the expressions for $\sigma^{\alpha\mathrm{N}}$ and $\mathbf{b}$, Eqs. (4.42, 4.44), and the given relationship between the mechanical and thermodynamical surface tensions and moments [2, 3, 4, 5]:

$$\begin{aligned}(\nabla_s \cdot \boldsymbol{\sigma}) \cdot \mathbf{N} &= \boldsymbol{\sigma} : \mathbf{b} - \nabla_s^2\mathbf{M} \\ &= 2H(\sigma_1 + \sigma_2) - \nabla_s^2\mathbf{M} \\ &= 2H(\gamma - \frac{1}{2}BH - \frac{1}{2}\Theta D) - \nabla_s^2\mathbf{M}\,.\end{aligned} \tag{4.48}$$

The Helfrich model for the work of flexural deformation is employed and hence gives the ex-

pressions of the bending and torsion moments [2, 3, 4, 5]:

$$\begin{aligned} B &= B_0 + (4k_c + 2\bar{k}_c)H \; ; \qquad B_0 = -4k_c H_0 \, , \\ \Theta &= -2\bar{k}_c D \, , \end{aligned} \tag{4.49}$$

where k_c and $\bar{k}_c$ are the bending and torsion elastic moduli, respectively, H_0 is the spontaneous curvature, and B_0 represents the bending moment of a flat interface. By substituting Eq. (4.49) for Eq. (4.43), we obtain

$$-\nabla_s^2 \mathbf{M} = -2k_c \nabla_s^2 H \, . \tag{4.50}$$

Replacing Eqs. (4.49, 4.50) into Eq. (4.48) yields

$$(\nabla_s \cdot \boldsymbol{\sigma}) \cdot \mathbf{N} = 2H\gamma - (B_0 + 4k_c H)H^2 - 2\bar{k}_c HK - 2k_c \nabla_s^2 H \, , \tag{4.51}$$

where K is the Gaussian curvature, i.e., $K = H^2 - D^2$. Using Eq. (4.51) and the expression in Eq. (3.20) for the second term of Eq. (4.47), the capillary pressure becomes

$$-p_c = 2H\gamma - (B_0 + 4k_c H)H^2 - 2\bar{k}_c HK \; - 2k_c \nabla_s^2 H - 2H \left(\frac{\partial \gamma}{\partial \mathbf{N}} \cdot \mathbf{N} \right) - \nabla_s \cdot \left(\frac{\partial \gamma}{\partial \mathbf{N}} \right) . \tag{4.52}$$

By using Eq. (3.22), the capillary pressure p_c is derived as

$$\begin{aligned} -p_c &= \frac{\gamma_{is}}{a} \left[S_n \left(-1 + \frac{\xi}{a} + \frac{\xi_{,\theta\theta}}{a} \right) + S_{nb} a \xi_{,zz} + \frac{M_{SC}}{2} \left(-\frac{1}{2} + \frac{\xi}{a} + \frac{\xi_{,\theta\theta}}{a} + a\xi_{,zz} \right) - M_T a \xi_{,zz} \right. \\ &\quad \left. - \frac{M_B}{2} \left(-1 + 3\frac{\xi}{a} + 5\frac{\xi_{,\theta\theta}}{a} + 5a\xi_{,zz} + 2\frac{\xi_{,\theta\theta\theta\theta}}{a} + 4a\xi_{,zz\theta\theta} + 2a^3 \xi_{,zzzz} \right) \right] , \end{aligned} \tag{4.53}$$

where

$$\begin{aligned} M_{SC} &= \frac{B_0}{\gamma_{is} a} = \frac{\text{bending moment of flat interface}}{\text{isotropic surface tension}} \, , \\ M_T &= \frac{\bar{k}_c}{\gamma_{is} a^2} = \frac{\text{torsion surface elastic modulus}}{\text{isotropic surface energy}} \, , \\ M_B &= \frac{k_c}{\gamma_{is} a^2} = \frac{\text{bending surface elastic modulus}}{\text{isotropic surface energy}} \, , \end{aligned}$$

$\xi_{,\theta\theta} = \frac{\partial^2 \xi}{\partial \theta^2}$, $\xi_{,zz} = \frac{\partial^2 \xi}{\partial z^2}$, $\xi_{,\theta\theta\theta} = \frac{\partial^4 \xi}{\partial \theta^4}$, $\xi_{,zzzz} = \frac{\partial^4 \xi}{\partial z^4}$, and $\xi_{,zz\theta\theta} = \frac{\partial^4 \xi}{\partial z^2 \partial \theta^2}$. Taking the same

procedure as shown previously, the growth rate equation for the instabilities is finally obtained:

$$\alpha^* = \frac{1}{2}\left\{-\left[3Oh\,(ka)^2 + 2Oh_m\right] + \sqrt{\left[3Oh\,(ka)^2 + 2Oh_m\right]^2 + 2\,(ka)^2\,P}\right\} \quad > 0\,, \qquad (4.54)$$

where

$$\begin{aligned} P \;\equiv\; & \left(S_n + \frac{M_{SC}}{2}\right)(1-m^2) - \left(S_{nb} + \frac{M_{SC}}{2} - M_T\right)(ka)^2 \\ & -\frac{M_B}{2}\left[3 + 2m^4 - 5m^2 + 4m^2\,(ka)^2 - 5\,(ka)^2 + 2\,(ka)^4\right]. \end{aligned} \qquad (4.55)$$

4.5.2 Results and discussion

By solving Eq. (4.54), positive real α^* solutions are obtained when the following condition is satisfied:

$$P > 0\,. \qquad (4.56)$$

In comparison with Eq. (4.36) there are three new parameters, i.e., M_{SC}, M_T, and M_B, in Eq. (4.56). Although, in the literature, data of the three parameters for liquid crystals are not available, data for other material systems enable us to assume that the orders of magnitude for the parameters are similar and to further assume that M_{SC} and M_B are positive while M_T is negative [2, 3]. To analyze the new effects, we use the same parameters as in section 4.4. Therefore, the parameter b in S_n and S_{nb} is set at 0.25. Since we already discussed the effect of viscosities on the instabilities in section 4.4, the results in this section are given only for $Oh = Oh_m = 0$. As representative results, we show calculations for $M_{SC} = M_B = -M_T = 0.01$. As seen in Table 4.2, there are three instability regimes according to choices of a^* and ΔT^*. Table 4.6[3] summarizes the complete phenomenology of the two capillary instabilities in axial fibers, as computed from Eq. (4.54). If $a^* \leq a_c^*$, there is only one regime, where ΔT^* ranges from 0 to 1. If $a^* > a_c^*$, there are two regimes according to the signs of $\left(S_n + \frac{M_{SC}}{2}\right)$, i.e., the values of ΔT^*, in Eq. (4.56). When $\left(S_n + \frac{M_{SC}}{2}\right)$ is positive, only the Modified Rayleigh (MR) instability occurs while, when $\left(S_n + \frac{M_{SC}}{2}\right)$ is negative, the Bounded

[3] MR/A: Modified Rayleigh/Axisymmetric instability
BSq/NA: Bounded Sequential/Non-Axisymmetric instability
m_i: ith mode of the azimuthal wavenumber m for BSq instabilities

Table 4.6: Capillary instabilities in axial fibers according to Eq.(4.54).

a^*	Instability type	**Region I** $0 < \Delta T^* < 1$
$a^* \leq a_c^*$	MR/A	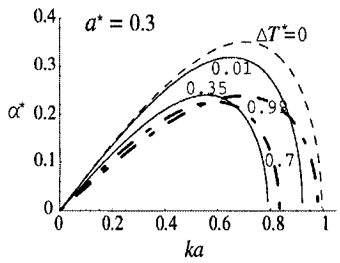

a^*	Instability type	**Region II** $0 < \Delta T^* < \Delta T_{II}^*$	Stable regime	**Region III** $\Delta T_{III}^* \leq \Delta T^* < \Delta T_{S_{nb}=0}^*$
$a^* > a_c^*$	MR/A	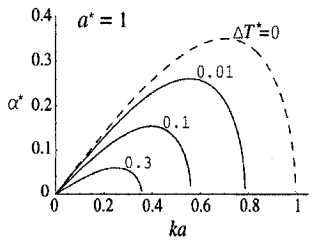	No	No
	BSq/NA	No	No	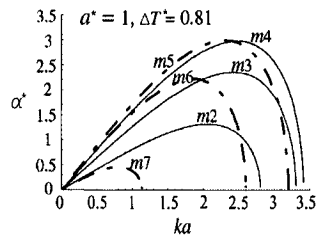

Sequential (BSq) instability emerges. The first column shows the regions of a^*, the second column shows the instability type, and the entries show characteristic growth rate curves for each instability mechanism. For the MR instability in the second row (Regime I) and the third column (Regime II), the growth rate curve is bounded, and an upper ka_{cutoff} exists. Under the bounded sequential (BSq) mechanism in the fifth column (Regime III), unstable modes appear sequentially with ΔT^*, and the growth rate curves are bounded with upper ka_{cutoff}. For the BSq instability, a fastest growing mode exists at constant ΔT^*, which is faster than growth rates of any other lower or higher unstable modes.

(a) Regime I: $a^* \leq a_c^*$ and $0 < \Delta T^* < 1$

The critical value of a^*, $a_c^* = 0.5657$, is obtained when a^* satisfies $P = 0$ for m_0 at $\Delta T^* = 1$ since only the MR mode m_0 is unstable over the whole range of ΔT^*. Similar to the results in Fig. 4-6(a) and Fig. 4-7(a) for $a^* = 0.3$, the growth rate curves for m_0 in Table 4.6 show that α^*_{max} and ka_{max} as a function of ΔT^* have local minima. Accordingly, the droplet size after fiber break-up is predicted to change from small to large to small by increasing ΔT^*.

(b) Regime II: $a^* > a_c^*$ and $0 < \Delta T^* < \Delta T^*_{II}$

The upper temperature limit of Regime II, $\Delta T^*_{II} = 0.4378$, is obtained for positive $\left(S_n + \frac{M_{SC}}{2}\right)$ and satisfies $P = 0$ for m_0 since, in this regime, only the MR mode m_0 occurs, i.e., $P > 0$ for m_0:

$$\left(S_n + \frac{M_{SC}}{2}\right) - \frac{3M_B}{2} > 0\,. \tag{4.57}$$

Similar to the results in Fig. 4-6(b) and Fig. 4-7(a) for $a^* = 1$, the growth rate curves for m_0 in Table 4.6 show that, as ΔT^* increases, the maximum growth rate α^*_{max} and the corresponding wavenumber ka_{max} decrease and finally the growth rate becomes 0 at $\Delta T^* = \Delta T^*_{II}$. The cutoff wavenumber ka_{cutoff} is also decreasing with ΔT^*.

(c) Regime III: $a^* > a_c^*$ and $\Delta T^*_{III} \leq \Delta T^* < \Delta T^*_{S_{nb}=0}$

The lower temperature limit of Regime III, $\Delta T^*_{III} = 0.4646$, is obtained for negative $\left(S_n + \frac{M_{SC}}{2}\right)$ and satisfies $P = 0$ for m_2 since the BSq instability emerges, i.e., $P > 0$ for $m \geq 2$:

$$\left(S_n + \frac{M_{SC}}{2}\right)(1 - m^2) - \frac{M_B}{2}\left(3 + 2m^4 - 5m^2\right) > 0\,, \tag{4.58}$$

while the upper temperature limit is $\Delta T^*_{S_{nb}=0} (= 0.8182)$. In comparison with Fig. 4-8 and

Fig. 4-9(b), the growth rate curves for $m \geq 2$ in Table 4.6 show the most striking result that emerging higher azimuthal modes are suppressed by means of the bending moment contribution to the surface elastic stress tensor. As ΔT^* increases, more and more azimuthal modes emerge, but a fastest growing mode exists at constant ΔT^* and thus lower and higher unstable modes only grow slower than the fastest growing mode (see Fig. 4-12 and discussion below). At $a^* = 1$ and $\Delta T^* = 0.81$, five azimuthal modes are unstable from m_2 to m_7, among which growth rates become faster up to m_4 and then decline toward m_7.

It is noted that there is also a stable regime, i.e., $a^* > a_c^*$ and $\Delta T_{II}^* \leq \Delta T^* < \Delta T_{III}^*$, where no instability occurs since both conditions of Eq.(4.57) and Eq. (4.58) are not satisfied.

Figure 4-12 shows the dimensionless cutoff wavenumber ka_{cutoff} as a function of dimensionless nematic temperature ΔT^* at $b = 0.25$, $a^* = 1$, and $M_{SC} = M_B = -M_T = 0.01$. The figure corresponds to Regime II (MR/A instability) for $0 < \Delta T^* < \Delta T_{II}^* (= 0.4378)$ and to Regime III (BSq/NA instability) for $\Delta T_{III}^* (= 0.4646) \leq \Delta T^* < \Delta T_{S_{nb}=0}^* (= 0.8182)$ in Table 4.6. In Regime II, the growth rate of m_0 decreases with ΔT^* and becomes 0 at ΔT_{II}^*, so does ka_{cutoff}. In Regime III, unstable modes appear from m_2 sequentially in ascending order of the azimuthal wavenumber m with increasing temperature ΔT^*. Hence, at constant ΔT^* only a finite number of azimuthal modes are unstable and a fastest growing mode exists. At the upper temperature limit $\Delta T_{S_{nb}=0}^*$, for instance, m_2 to m_7 modes arise, among which the m_4 mode grows faster than other unstable modes. Meanwhile, between the two vertical dashed lines, i.e., $\Delta T_{II}^* \leq \Delta T^* < \Delta T_{III}^*$, no instability arises.

4.5.3 Analysis of bending moment effects

In this section, we focus on the specific effects of the bending moment (see Eq. (4.50)). The physics behind the noticeable stabilizing mechanism in Regime III of the sequential instabilities of Table 4.6 compared with the simultaneous instabilities of Table 4.2 can be elucidated by analyzing the role of three new parameters, M_{SC}, M_T, and M_B, in Eq. (4.55). Since it is assumed that M_{SC} and M_B are positive while M_T is negative, the positive terms $\frac{M_{SC}}{2}$ and $\frac{M_{SC}}{2} - M_T$ added to S_n and S_{nb}, respectively, tend to cooperate with the usual isotropic contribution (see Eqs. (4.24, 4.25) and discussion below). Meanwhile, by comparing Eq. (4.56) with Eq. (4.36), the third term in Eq. (4.55), which is combined with higher orders of curvature gradients, plays

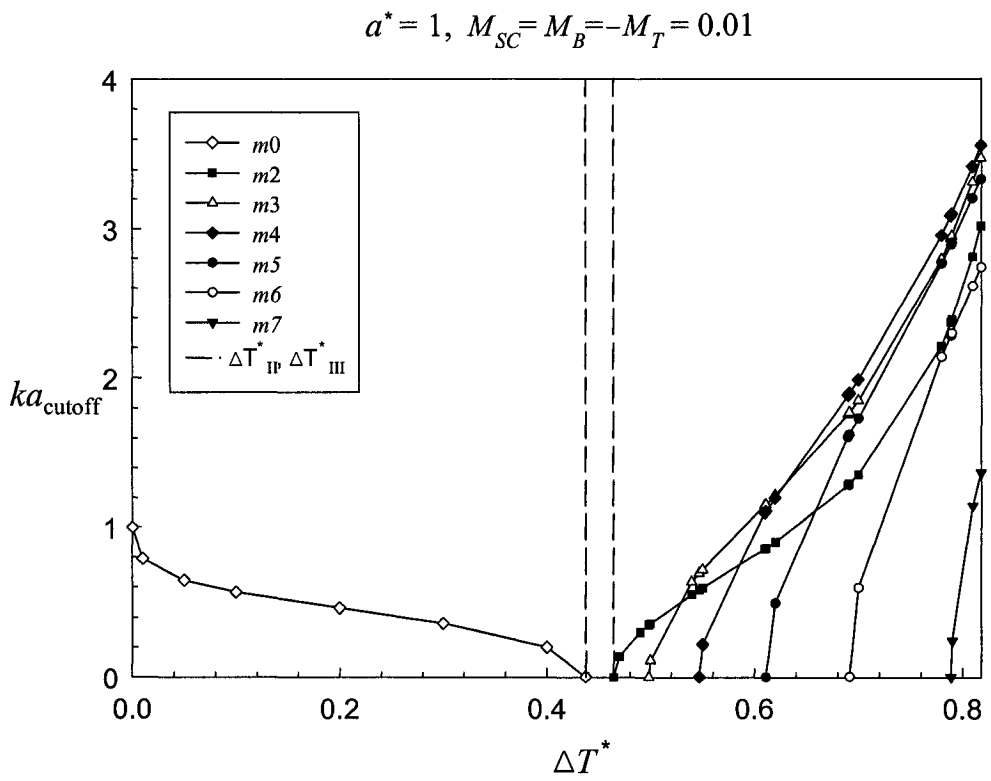

Figure 4-12: Dimensionless cutoff wavenumber ka_{cutoff} as a function of dimensionless nematic temperature ΔT^* at $b = 0.25$, $a^* = 1$, and $M_{SC} = M_B = -M_T = 0.01$. The figure corresponds to Regime II (MR/A instability) for $0 < \Delta T^* < \Delta T^*_{II}\,(= 0.4378)$ and to Regime III (BSq/NA instability) for $\Delta T^*_{III}\,(= 0.4646) \leq \Delta T^* < \Delta T^*_{S_{nb}=0}\,(= 0.8182)$ in Table 4.6. Between the two vertical dashed lines, i.e. $\Delta T^*_{II} \leq \Delta T^* < \Delta T^*_{III}$, no instability arises.

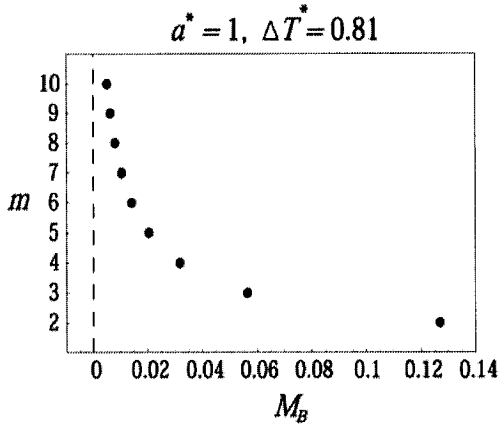

Figure 4-13: Upper limit of the azimuthal wavenumber m as a function of the dimensionless bending surface elastic modulus M_B at $b = 0.25$, $a^* = 1$, and $\Delta T^* = 0.81$, for the cutoff wavenumber ka_{cutoff}. The figure corresponds to Regime III (BSq/NA instabilities) in Table 4.6.

a crucial role in stabilizing the nematic fiber since the coefficient $\frac{M_B}{2}$ is positive. Hence, to focus on the role of the higher order terms, we consider a special case in which only the bending moment contribution is taken into account through the transversal component of the surface stress tensor given by Eq. (4.42), and thus the capillary pressure in Eqs. (4.47, 4.52) reduces to

$$\begin{aligned} -p_c &= 2H\gamma - \nabla_s^2 \mathbf{M} + (\nabla_s \cdot \mathbf{t}_B^{\text{se}}) \cdot \mathbf{N} \\ &= 2H\gamma - 2k_c \nabla_s^2 H - 2H \left(\frac{\partial \gamma}{\partial \mathbf{N}} \cdot \mathbf{N} \right) - \nabla_s \cdot \left(\frac{\partial \gamma}{\partial \mathbf{N}} \right) . \end{aligned} \tag{4.59}$$

Using the same procedure, the following instability criterion is obtained:

$$P \equiv S_n(1 - m^2) - S_{nb}\,(ka)^2 - M_B \left[m^4 - m^2 + 2m^2\,(ka)^2 - (ka)^2 + (ka)^4 \right] \quad > 0\,. \tag{4.60}$$

Figure 4-13 shows the upper limit of the azimuthal wavenumber m as a function of the dimensionless bending surface elastic modulus M_B at $b = 0.25$, $a^* = 1$, and $\Delta T^* = 0.81$, for the cutoff wavenumber ka_{cutoff}. This figure corresponds to Regime III (BSq/NA instabilities) in Table 4.6. It is clearly seen that more and more azimuthal modes can emerge as M_B decreases, and infinite m modes are unstable as $M_B \to 0$ (see Table 4.2 and Fig. 4-9(b)). The limit value of M_B for m_7 is 0.0103, and thus m_2 to m_7 modes are unstable at $M_B = 0.01$, which is consistent

with the result in Fig. 4-12.

Finally it is noticed that a dramatic change is observed when M_B is negative that in all three regimes (Regime I-III) catastrophic instability emerges, and we deduce that the sign of the bending modulus k_c as well as its magnitude are most critical in implementing the curvature effects through the bending and torsion deformation although k_c, $\bar{k}_c$, and H_0 are system-dependent properties.

4.6 Conclusions

Capillary instabilities in nematic fibers reflect the anisotropic nature of liquid crystals. The surface elasticity of nematics contains both ordering and orientation contributions. The nematic ordering contribution allows for the existence of normal stresses while the nematic orientation contribution allows for the existence of bending stresses as well as normal stresses. Thus, surface gradients of normal and bending stresses provide additional anisotropic contributions to the capillary pressure of fibers that renormalize the classical displacement and curvature forces that exist in any fluid fiber. The exact nature and magnitude of the renormalization of the displacement and curvature forces depend on the nematic ordering and orientation, and thus on the anisotropic contribution to the surface energy. In addition, when the interface curvature effects are accounted for as contributions of the work of interfacial bending and torsion to the total energy of the system, the higher order bending moment contribution to the surface stress tensor through the transversal component in the generalized form is proved to be critical in stabilizing higher order non-axisymmetric fiber instabilities.

For the planar easy axis, if the nematic orientation is along the fiber axis, capillary instabilities may be axisymmetric or non-axisymmetric depending on the nematic ordering contribution since the misalignment between the actual director and the easy axis is small so that the bending stresses alone cannot cause non-axisymmetric instabilities. In other words, the nematic ordering contribution to the surface energy, which renormalizes the effect of the fiber shape, plays a crucial role to determine the instability mechanisms. Low ordering fibers display the classical axisymmetric mode ($m = 0$) since the surface energy decreases by decreasing the surface area. Decreasing temperature T for this mode gives rise to a local maximum or to a monotonic

increase of the characteristic length of the axisymmetric mode. Thus, the phenomenology discussed above is accessible by changes in temperature since the anisotropic surface energy is temperature dependent. For the m_0 mode, the characteristic size of droplets formed after fiber break-up may be controlled by tuning the temperature under the small or moderate nematic ordering effects. Meanwhile, in the presence of high surface ordering, non-axisymmetric ($m \geq 2$) finite wavelength instabilities emerge, with higher modes growing faster since the surface energy decreases by increasing the surface area. As the temperature T decreases, the pitches of the chiral microstructures become smaller. However, this non-axisymmetric instability mechanism due to high surface ordering can be regulated by taking account of the surface bending moment, which contains higher order variations in the curvatures of the interface. More and more azimuthal modes emerge as the temperature T decreases, but, at constant temperature, only a finite number of azimuthal modes are unstable and a fastest growing mode exists with lower and higher unstable modes growing at a slower rate.

The predicted ability of capillary instabilities in nematic fibers to produce surface structures of well-defined symmetry and length scales, as well as chiral microstructures is an important result that augments the pathways for targeted pattern formation.

The effect of the viscous shear force at the fiber surface due to the viscous matrix on the bounded axisymmetric capillary instability was also taken into account, and characterized in terms of the Ohnesorge numbers and the matrix-to-fiber viscosity ratio. The capillary instabilities of a thin fiber in a viscous matrix are suppressed by increasing either the fiber or matrix Ohnesorge number, but estimated droplet sizes after fiber break-up in axisymmetric instabilities substantially decrease with increasing matrix Ohnesorge number.

Bibliography

[1] A. D. Rey, Ind. Eng. Chem. Res. **36**, 1114 (1997).

[2] P. A. Kralchevsky, *Particles at Fluids Interfaces and Membranes* (Elsevier, New York, 2001).

[3] P. A. Kralchevsky, J. C. Eriksson, and S. Ljunggren, Adv. Colloid Interface Sci. **48**, 19 (1994).

[4] S. Ljunggren, J. C. Eriksson, and P. A. Kralchevsky, J. Colloid Interface Sci. **191**, 424 (1997).

[5] P. A. Kralchevsky, J. Colloid Interface Sci. **137**, 217 (1990).

[6] P. G. de Gennes and J. Prost, *The Physics of Liquid Crystals* (Oxford University Press, London, 1993).

[7] W. J. A. Goossens, Mol. Cryst. Liq. Cryst. **124**, 305 (1985).

[8] T. J. Sluckin and A. Poniewierski, *Fluid Interfacial Phenomena* (John Wiley, Chichester, 1986).

[9] G. Barbero, Z. Gabbasova, and M. A. Osipov, J. Phys. II **1**, 691 (1991).

[10] A. A. Sonin, *The Surface Physics of Liquid Crystals* (Gordon and Breach Publishers, Amsterdam, 1995).

[11] H. Yokoyama, in *Handbook of Liquid Crystal Research*, edited by P. J. Collins and J. S. Patel (Oxford University Press, New York, 1997).

[12] A.-G. Cheong, A. D. Rey, and P. T. Mather, Phys. Rev. E **64**, 041701 (2001).

[13] A.-G. Cheong and A. D. Rey, Cont. Mech. Therm. **14**, 263 (2002).

[14] S. Chandrasekhar, *Liquid Crystals* (Cambridge University Press, Cambridge, 1992).

[15] S. Faetti, in *Physics of Liquid Crystalline Materials*, edited by I.-C. Khoo and F. Simoni (Gordon and Breach, Philadelphia, 1991).

[16] A. D. Rey, J. Phys. II France **7**, 1001 (1997).

Chapter 5

Texture Dependence of Capillary Instabilities in Nematic Liquid Crystalline Fibers

5.1 Summary

Static and dynamic linear analyses of axisymmetric capillary instabilities in textured nematic liquid crystalline fibers are performed using the equations of nemato-statics and inviscid nemato-dynamics. Three representative textures, i.e., axial, onion, and radial, are analyzed to show all possible effects of Frank gradient elasticity on the wavelength selection and growth rate of peristaltic modes driven by surface area reduction. It is found that Frank elasticity may tend to stabilize or destabilize the fiber, depending on the initial fiber texture. Axial textures tend to stabilize the fiber through the director splay-bend distortions driven by surface tilting. Onion textures are destabilized by decreasing azimuthal bend elastic energy caused by surface displacement. Radial textures exhibit a stabilizing tilt mechanism due to bend modes and a destabilizing displacement mechanism due to splay modes, but the former is predicted to be dominant. The static analysis provides good estimates of the instability thresholds while the transient energy balance provides information on the fastest growing modes. The static and dynamic results are compared and shown to be fully consistent. The couplings between

splay and/or bend distortions, surface tilting, and surface displacement in nematic fibers are characterized and used to explain the deviations from the classical Rayleigh instability.

5.2 Introduction

A question of fundamental importance in capillary instabilities of liquid crystalline fibers is to identify possible mechanisms that promote stability and hence widen the processing windows for these materials. In isotropic fluid fibers, the surface tension driven fiber-to-droplet transformation is well understood and known as the Rayleigh instability [1, 2, 3]. In the static thermodynamical analysis, the Rayleigh threshold shows that the isotropic fiber is unstable for the wavelength of the surface disturbance exceeding the perimeter of the fiber. Meanwhile, Rayleigh also predicted a fastest growing wavelength that governs the capillary instability of an isotropic fluid fiber and thus makes the fiber break up into a trail of droplets with a specific size in the linear regime using a transient analysis. For isotropic fluid fibers, only surface area reduction plays a role to promote instability since the surface energy decreases by decreasing the surface area [4]. On the other hand, an essential characteristic of nematic liquid crystals is mechanical anisotropy and bulk gradient elasticity [5]. Bulk gradient elasticity, also known as Frank elasticity, in nematic liquid crystals is due to orientation gradients and hence is known as curvature elasticity. Capillary instabilities in liquid crystalline fibers have been analyzed in terms of surface anisotropies [6, 7, 8], and in this chapter we analyze the bulk anisotropy effects on the instability mechanisms and thresholds. For clarification, we note that anisotropy in this chapter refers to the unique direction imposed by the average molecular orientation, known as the nematic director, and hence different director fields correspond to different types of anisotropy. Thermodynamic stability analyses of nematic LC fibers have been performed for different nematic textures [4, 9]. In this chapter we extend the previous work by considering the time evolution of unstable modes in axial, onion, and radial textures (see figure 5-2 below), as well as by establishing the correspondence between instability criteria found using thermodynamical and dynamical analyses. The fiber is assumed to have nematic orientation, where the rod-like molecules are more or less parallel to each other but otherwise free to translate past each other [5]. As mentioned above the theories and analyses are based on transient integral

energy balances as well as free-energy calculations so that we capture growth rate patterns of instabilities as well as static instability thresholds.

The specific objectives of this chapter are to: (1) formulate a thermodynamic model for the static analysis and present an integral energy balance equation for the transient analysis that describes and identifies the bulk elastic energy contributions to capillary instabilities of nematic liquid crystalline fibers; (2) derive instability criteria for static and transient analyses in three characteristic nematic textures and elucidate the physical mechanisms that promote and suppress the instabilities; (3) establish parametric conditions that lead to capillary instabilities; (4) characterize the nematic orientation contributions to capillary instabilities; and (5) relate the Frank distortion energy contribution in the static analysis to that in the transient analysis.

The organization of this chapter is as follows. In Section 5.3, we present the thermodynamic model for static analysis, the integral energy balance equation for transient analysis, and the equilibrium condition for distorted director fields. In Section 5.4, we derive the instability criteria for static and transient energy analyses in three characteristic nematic textures. The instability mechanisms for static and transient analyses are clearly identified and discussed in terms of Frank distortion elastic energy. Section 5.5 presents conclusions.

5.3 Governing Equations

5.3.1 Geometry and texture of nematic liquid crystalline fibers

Figure 5-1 shows definitions of the fiber geometry. Figure 5-1(a) shows that the fiber is initially a uniform cylinder with radius a, with its axis collinear with the z-axis of a cylindrical coordinate system. In the cross-sectional view, unit vectors $\mathbf{i}_r$ and $\mathbf{i}_\theta$ are shown in the direction of the r- and θ-axes, respectively. Figure 5-1(b) shows the periodically deformed fiber with unit surface normal $\mathbf{N}$, radius R and wavelength λ. The fiber radius R and unit surface normal $\mathbf{N}$ periodically change with a wavelength λ along the z-direction. In this chapter, we apply our analysis to three characteristic nematic textures of initially constant director fields, denoted as axial, onion, and radial textures, and accordingly the nematic fiber with each texture is called axial fiber, onion fiber, and radial fiber, respectively. Figure 5-2 shows the schematic of undeformed fibers with (a) axial, (b) onion and (c) radial textures. In the cross-sectional view,

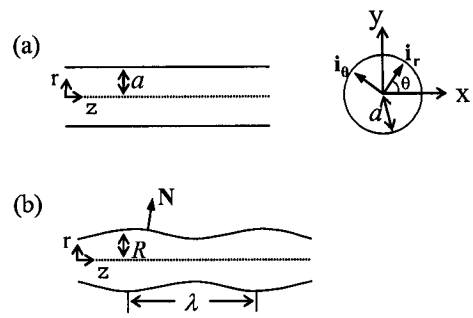

Figure 5-1: (a) Unperturbed fiber with radius a is aligned in the z-axis of a cylindrical coordinate system (r, θ, z). Cross-sectional view in Cartesian coordinates (x, y) shows the unit vectors $\mathbf{i}_r$ and $\mathbf{i}_\theta$ and azimuthal angle θ. (b) Periodically deformed axisymmetric fiber with unit surface normal vector $\mathbf{N}$, radius R and wavelength λ. Fiber radius R and unit surface normal $\mathbf{N}$ periodically change with a wavelength λ along the z-direction. The figure is representative of the peristaltic (axisymmetric) mode.

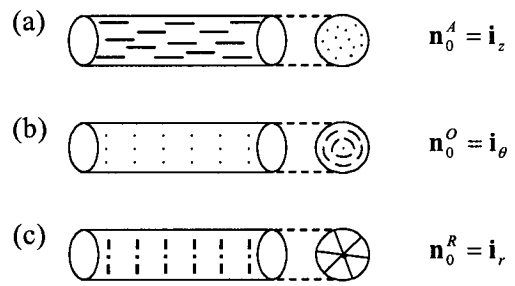

Figure 5-2: Schematic of undeformed fibers with (a) axial, (b) onion and (c) radial textures. In the cross-sectional view, the director field $\mathbf{n}$ is shown as dots, curves, or lines in each texture. Defect cores are seen at the centre of onion and radial textures. The corresponding director field is shown on the right side.

the director field $\mathbf{n}$ is shown as dots, curves, or lines in each texture. The fiber nematic texture is expressed by the director field using unit vectors $\mathbf{i}_z$, $\mathbf{i}_\theta$, and $\mathbf{i}_r$ in the direction of the z-, θ-, and r-axes, respectively. Defect cores are seen at the centre of onion and radial textures. In this chapter, we assume that these defects have already nucleated.

It is noted that escaped radial textures in cylindrical cavities are well understood experimentally and theoretically. The escaped radial texture where the director escapes into the third dimension along the cylinder axis has been shown to be more stable than the radial texture with a line defect at the center [5, 10, 11], and was observed for MBBA in cylindrical cavities [11, 12]. The escaped radial textures with singular point defects along the cylinder axis were also observed in cylindrical cavities of $20 \sim 200\mu m$ in radius by optical studies [12, 13] and of as small as $0.3\mu m$ in radius by deuteron NMR, where the density of singular point defects was obtained in the strong-anchoring limit [14]. Meanwhile, the radial texture with a line defect at the centre of the fiber can also be stable, for instance, in the vicinity of a nematic/smectic-A transition [5] or when the fiber radius is small enough [5, 10, 11].

Linear stability analysis is used to describe peristaltic axisymmetric capillary instabilities in nematic liquid crystalline fibers for the three textures. Static energy analysis based on thermodynamic stability is presented to obtain a critical wavelength for the capillary instability while transient energy analysis to construct a growth rate curve and thus obtain the fastest growing wavelength as well as to establish the consistency of the results. Twist distortions are beyond the scope of this chapter, and only splay and/or bend modes are taken into account. Likewise, chiral non-axisymmetric distortion modes are not taken into account in this chapter.

5.3.2 Static energy analysis

We consider the thermodynamic stability of an infinitely long cylindrical nematic LC fiber subjected to infinitesimal periodic surface disturbances. The nematic liquid crystal is assumed to be incompressible, and its initial orientation is homogeneous and constant in each of three characteristic textures: axial, onion, and radial. Then, the constant director fields evolve as the shape of nematic fibers changes.

As seen in figure 5-1(b), the fiber radius R and the unit surface normal $\mathbf{N}$ change along the z-direction. In the static analysis, the fiber shape with a periodic surface disturbance is given

at any position z by

$$R(z) = R_0 + \xi(z) \,. \tag{5.1}$$

The periodic surface disturbance ξ is expressed as

$$\xi(z) = \xi_0 \cos[kz] \,, \tag{5.2}$$

where ξ_0 is the initial amplitude of the disturbance and k the axial wavenumber. The average fiber radius R_0 in Eq. (5.1) is required, for a fixed volume, to be

$$R_0 = a\sqrt{1 - \frac{\xi_0^2}{2a^2}} \approx a\left(1 - \frac{\xi_0^2}{4a^2}\right) \,, \tag{5.3}$$

where the approximation is valid in the linear regime of the capillary instability, i.e., when

$$\frac{\xi}{a} \ll 1 \,. \tag{5.4}$$

The unit surface normal $\mathbf{N}$ is given in the linear regime by

$$\mathbf{N} = \mathbf{i}_r - \frac{\partial R}{\partial z}\mathbf{i}_z \,. \tag{5.5}$$

During the capillary instability, the fiber geometry evolution is captured by the principal radii of curvature ($R_{r\theta}$, R_{rz}) as well as the fiber's radius R and its unit surface normal $\mathbf{N}$. In the linear regime, the principal radii of the curvature are expressed as [3]

$$\frac{1}{R_{r\theta}} = \frac{1}{R} \,, \qquad \frac{1}{R_{rz}} = -\frac{\partial^2 R}{\partial z^2} \,. \tag{5.6}$$

To discuss capillary instabilities, it is also useful to introduce the following expression for the mean curvature H in cylindrical coordinates:

$$H = -\frac{1}{2}\nabla_s \cdot \mathbf{N} = -\frac{1}{2}\left(\frac{1}{R_{r\theta}} + \frac{1}{R_{rz}}\right) \tag{5.7}$$

$$= -\frac{1}{2}\left(\frac{1}{R} - \frac{\partial^2 R}{\partial z^2}\right) \,, \tag{5.8}$$

where ∇_s is the surface gradient operator.

Distorted director fields

As seen in Fig. 5-2(a), in the axial texture, the director is initially oriented along the fiber axis and it is given by

$$\mathbf{n}_0^A = \mathbf{i}_z \,, \tag{5.9}$$

where the superscript ^{A} denotes the axial texture and the subscript $_0$ the initial director field. Likewise, in Fig. 5-2(b), the director is initially along the azimuthal direction in the onion texture:

$$\mathbf{n}_0^O = \mathbf{i}_\theta \,, \tag{5.10}$$

and, in Fig. 5-2(c), along the fiber radius in the radial texture:

$$\mathbf{n}_0^R = \mathbf{i}_r \,, \tag{5.11}$$

where the superscripts ^{O} and ^{R} denote the onion and radial textures, respectively. The director field in each texture is expected to evolve as the nematic fibers are subjected to infinitesimal surface disturbances. Since the surface disturbances are very small, only a slight distortion from the initial director field is assumed [5]:

$$\mathbf{n} = \mathbf{n}_0 + \boldsymbol{\epsilon} \,, \tag{5.12}$$

where $\mathbf{n}_0$ is the initial director field and $\boldsymbol{\epsilon}$ is the slight distortion normal to $\mathbf{n}_0$.

To find the distorted director field in each texture, we apply conditions for equilibrium in the nematic bulk by introducing the distortion free energy. The distortion free energy density, known as Frank distortion energy, stored in a nematic LC fiber is simplified using one constant approximation to [5]

$$F_d = \frac{K}{2} \left[(\nabla \cdot \mathbf{n})^2 + (\nabla \times \mathbf{n})^2 \right] \,, \tag{5.13}$$

where F_d is the Frank distortion free energy density and K the Frank elastic constant in the

one constant approximation. In equilibrium, the following condition is satisfied:

$$\mathbf{n} \times \mathbf{h} = \mathbf{0}\,, \tag{5.14}$$

where $\mathbf{h}$ is the molecular field expressed as [5]

$$\begin{aligned} \mathbf{h} &= -\left[\frac{\partial F_d}{\partial \mathbf{n}} - \nabla \cdot \frac{\partial F_d}{\partial(\nabla \mathbf{n})}\right] \\ &= K\nabla^2 \mathbf{n}\,. \end{aligned} \tag{5.15}$$

Eq. (5.14) means that the director is parallel to the molecular field in equilibrium.

Free energy of nematic liquid crystalline fibers

The total free energy density for a nematic LC fiber with distorted director orientation is given by [5]

$$F = F_d + F_s = \frac{K}{2}\left[(\nabla \cdot \mathbf{n})^2 + (\nabla \times \mathbf{n})^2\right] + \gamma\delta\left(r - R\right)\,, \tag{5.16}$$

where F_s is the surface free energy density for the surface director orientation along the easy axis, γ the surface free energy density, and δ the Dirac delta function. Since the strong anchoring condition is assumed at the fiber surface, the surface free energy density γ only represents the isotropic surface tension. Thus, the surface free energy contribution to the total free energy does not contain any elastic distortion effect and remains unchanged in the three nematic textures. Meanwhile, the Frank distortion energy contribution differs in one texture from another since the director variation in the bulk of the fiber is the origin of the elastic distortion energy.

5.3.3 Transient energy analysis

We consider the transient stability of an infinitely long cylindrical nematic LC fiber subjected to infinitesimal periodic surface disturbances. The geometry of the LC fiber and the director field are a function of time as well as of space. In this section, the general equation of the transient integral energy balance is derived.

In the transient analysis, the fiber shape at any time t and position z is given by

$$R(z,t) = R_0 + \xi(z,t) \,. \tag{5.17}$$

The surface disturbance ξ is expressed by assuming its exponential growth as

$$\xi(z,t) = \xi_0 \cos[kz]\, e^{\alpha t} \,, \tag{5.18}$$

where α is the growth rate for real and positive values.

Transient integral energy balance equation

The conservation of energy under isothermal condition, and under the absence of body forces, director inertia and director surface force is given by [15]

$$\frac{d}{dt}\int_V \left(\frac{1}{2}\rho \boldsymbol{v}\cdot\boldsymbol{v} + F_d\right) dV + \int_V T\dot{S} dV = \int_A \mathbf{N}\cdot\mathbf{t}\cdot\boldsymbol{v} dA \,, \tag{5.19}$$

where $\frac{d}{dt}$ and the superposed dot denote material time derivatives, ρ is the density, $\boldsymbol{v}$ the velocity, T the temperature, S the entropy per unit volume, $\mathbf{t}$ the stress tensor, V the volume, and A the surface area. If the only entropy source is the viscous dissipation, the second integral in Eq. (5.19) becomes [5]

$$\int_V T\dot{S} dV = \int_V \mathbf{A} : \mathbf{t}^v dV \,. \tag{5.20}$$

The rate of deformation tensor $\mathbf{A}$ is expressed as

$$\mathbf{A} = \frac{1}{2}\left[(\nabla \boldsymbol{v}) + (\nabla \boldsymbol{v})^{\mathrm{T}}\right] \,, \tag{5.21}$$

where the superscript $^{\mathrm{T}}$ denotes the transpose. The viscous stress tensor $\mathbf{t}^v$ is given as

$$\mathbf{t}^v = 2\mu\mathbf{A} \,, \tag{5.22}$$

where μ is the viscosity. It is noted that in the linear regime distortions are insignificant and the rheology is Newtonian [5]. By making use of Eqs. (5.21) and (5.22) in Eqs. (5.20) and (5.19)

can be rewritten in the linear regime such that

$$\int_V \left[\frac{\partial}{\partial t}\left(\frac{1}{2}\rho \boldsymbol{v}\cdot\boldsymbol{v}\right)+\dot{F}_d\right]dV+\int_V \frac{1}{2}\mu\left[(\nabla \boldsymbol{v})+(\nabla \boldsymbol{v})^{\mathrm{T}}\right]:\left[(\nabla \boldsymbol{v})+(\nabla \boldsymbol{v})^{\mathrm{T}}\right]dV=\int_A \mathbf{N}\cdot\mathbf{t}\cdot\boldsymbol{v}dA\,. \tag{5.23}$$

Because strong anchoring condition is imposed at the fiber surface, the surface behaves like an isotropic material and only the contribution of $\dot{F}_d$ reflects the anisotropic elasticity of the LC fiber. Using Eq. (5.13), the contribution of $\dot{F}_d$ in Eq. (5.23) is expressed in terms of $\nabla\mathbf{n}$:

$$\dot{F}_d=\frac{\partial F_d}{\partial(\nabla\mathbf{n})}:\frac{d}{dt}(\nabla\mathbf{n})^{\mathrm{T}}=K\left[(\nabla\cdot\mathbf{n})\,(tr\mathbf{D})+\nabla\mathbf{n}:\mathbf{D}-\nabla\mathbf{n}:\mathbf{D}^{\mathrm{T}}\right], \tag{5.24}$$

where $tr\mathbf{D}$ denotes the trace of tensor $\mathbf{D}$ and

$$\mathbf{D}\equiv\frac{d}{dt}(\nabla\mathbf{n})^{\mathrm{T}}=\frac{\partial(\nabla\mathbf{n})^{\mathrm{T}}}{\partial t}+(\boldsymbol{v}\cdot\nabla)(\nabla\mathbf{n})^{\mathrm{T}}\,. \tag{5.25}$$

The contribution of $\mathbf{D}$ to $\dot{F}_d$ appears to be different in the three nematic textures, which allows for identifying the contributions to elastic storage due to bulk orientation distortions. In this chapter, we investigate the effect of anisotropic elasticity through the Frank distortion energy on the capillary instability of the LC fibers displaying the axial, onion, and radial textures. The LC fibers are assumed inviscid so that the viscous dissipation term in Eq. (5.23) drops out and the transient integral energy balance equation becomes

$$\int_V \left[\frac{\partial}{\partial t}\left(\frac{1}{2}\rho \boldsymbol{v}\cdot\boldsymbol{v}\right)+\dot{F}_d\right]dV=\int_A \mathbf{N}\cdot\mathbf{t}\cdot\boldsymbol{v}dA\,. \tag{5.26}$$

The role of viscosity on the capillary instability of LC fibers has been studied with the governing nemato-capillary equations [6].

5.4 Results and discussion

The characterization of linear capillary instabilities in nematic fibers is based on the observation that there are two mechanisms associated with the coupling between director, and hence the Frank distortion (gradient) elasticity, and the geometrical changes in the fiber: (i) surface tilting and (ii) surface displacement mechanisms. These two mechanisms are embedded in total

distortion energy equations for statics:

$$\mathcal{F}_d = \int_V F_d dV \,, \tag{5.27}$$

and for dynamics:

$$\frac{d\mathcal{F}_d}{dt} = \int_{V(t)} \dot{F}_d dV \,, \tag{5.28}$$

and are activated for specific textures, as follows.

(i) *Surface tilting mechanism* (M_T)

The surface tilting mechanism is activated when surface tilting (undulation) changes the director orientation. When splay and/or bend distortions arise due to the surface tilting driven by the re-orientation of the fiber surface, they tend to stabilize the fibers by increasing the Frank distortion energy. Hence, the M_T mechanism always promotes stability.

(ii) *Surface displacement mechanism* (M_D)

The surface displacement mechanism is characterized by decreasing the Frank distortion energy and thus destabilizing the nematic fibers. When splay and/or bend distortions are uncoupled from the surface orientation, the surface displacement due to a decrease in average radius may destabilize the fibers by decreasing the Frank distortion energy.

In what follows we discuss these two different instability mechanisms in axial, onion, and radial fibers for statics and dynamics, respectively, and determine the parametric dependence of the nematic capillary instabilities on each mechanism of the Frank distortion elasticity.

5.4.1 Static energy analysis

In this section we present the thermodynamic analysis of the nematic fiber capillary instability for the axial, onion, and radial textures and establish the parametric conditions that lead to the Rayleigh instability.

Using Eqs. (5.1), (5.2), and (5.3), the surface free energy of the deformed LC fiber, $\mathcal{F}_{s,f}$, is obtained by integrating the second term in Eq. (5.16) over the surface with a unit wavelength,

$\lambda = \frac{2\pi}{k}$, to order ξ_0^2:

$$\begin{aligned} \mathcal{F}_{s,f} &= \gamma 2\pi \int_0^{\lambda} R(z)\sqrt{1+\left(\frac{dR}{dz}\right)^2}\,dz \\ &= \gamma 2\pi a\lambda - \gamma 2\pi a\lambda \frac{\xi_0^2}{4a^2}\left(1-\frac{4\pi^2 a^2}{\lambda^2}\right), \end{aligned} \tag{5.29}$$

Hence, the surface free energy change, Δ_s, is given as

$$\begin{aligned} \Delta_s &\equiv \mathcal{F}_{s,f} - \mathcal{F}_{s,i} = -\gamma 2\pi a\lambda \frac{\xi_0^2}{4a^2}\left(1-\frac{4\pi^2 a^2}{\lambda^2}\right) \\ &= -\gamma \pi^2 \xi_0^2 \frac{1}{ka}\left(1-k^2a^2\right), \end{aligned} \tag{5.30}$$

where $\mathcal{F}_{s,i}$ is the initial surface free energy of the cylindrical fiber:

$$\mathcal{F}_{s,i} = \gamma 2\pi a\lambda\,. \tag{5.31}$$

Axial fibers

The distorted director field for each texture is obtained by solving Eq. (5.14) with Eq. (5.15). Using Eqs. (5.9) and (5.12), the distorted director field of the initially axial texture can be written as

$$\mathbf{n}^A(r,z) = \mathbf{i}_z + n_r(r,z)\mathbf{i}_r\,, \tag{5.32}$$

where n_r is the slight splay-bend director distortion as a function of r and z. Substituting Eqs. (5.32) and (5.15) into Eq. (5.14) results in

$$\left(\nabla^2\mathbf{n}\right)_r = \frac{\partial^2 n_r}{\partial r^2} + \frac{1}{r}\frac{\partial n_r}{\partial r} + \frac{\partial^2 n_r}{\partial z^2} - \frac{n_r}{r^2} = 0\,, \tag{5.33}$$

where $\left(\nabla^2\mathbf{n}\right)_r$ is the r-component of the vector $\nabla^2\mathbf{n}$. By solving Eq. (5.33) and using periodic and finite boundary conditions in the z and r-directions, respectively, the splay-bend distortion is found to be

$$n_r(r,z) = -\xi_0 k \sin\left[kz\right]\frac{I_1\left[kr\right]}{I_1\left[ka\right]}\,, \tag{5.34}$$

where the strong anchoring condition that the director field is parallel to the planar easy axis (perpendicular to the unit surface normal) at the surface is applied. Thus, the distorted director field for the axial texture is

$$\mathbf{n}^A(r,z) = \mathbf{i}_z - \xi_0 k \sin[kz] \frac{I_1[kr]}{I_1[ka]} \mathbf{i}_r \,. \tag{5.35}$$

The elastic energy for the axial fiber is initially zero because no director gradients initially exist, and only arises with the distorted director field due to surface tilting. Using Eq. (5.35), the elastic distortion free energy, $\mathcal{F}_{d,f}$, is obtained by integrating the first term in Eq. (5.16), Eq. (5.27), over the volume with a unit wavelength, $\lambda = \frac{2\pi}{k}$, to order ξ_0^2:

$$\begin{aligned} \mathcal{F}_{d,f} &= 2\pi \int_0^{\frac{2\pi}{k}} \int_0^{R(z)} \frac{K}{2} \left[(\nabla \cdot \mathbf{n})^2 + (\nabla \times \mathbf{n})^2 \right] r dr dz \\ &= \pi^2 \xi_0^2 \frac{K}{a} k^2 a^2 \frac{I_0[ka]}{I_1[ka]} \,. \end{aligned} \tag{5.36}$$

The distortion free energy change, Δ_d, is given as

$$\Delta_d \equiv \mathcal{F}_{d,f} - \mathcal{F}_{d,i} = \pi^2 \xi_0^2 \frac{K}{a} k^2 a^2 \frac{I_0[ka]}{I_1[ka]} \,. \tag{5.37}$$

From Eq. (5.30) and Eq. (5.37), the net change in the total free energy, Δ, for the axial fiber is given by

$$\Delta = \Delta_s + \Delta_d = \pi^2 \xi_0^2 \frac{\gamma}{ka} \left[(k^2 a^2 - 1) + \frac{K}{a\gamma} k^3 a^3 \frac{I_0[ka]}{I_1[ka]} \right] \,. \tag{5.38}$$

By setting

$$\Delta = 0 \,, \tag{5.39}$$

meaning that no total free energy change occurs, the dimensionless critical wavenumber $(ka)_c$ and the critical wavelength λ_c are found as

$$(ka)_c = \frac{2\pi a}{\lambda_c} = \frac{1}{\sqrt{1 + 2\frac{K}{\gamma a}}} \,, \qquad \lambda_c = \lambda_R \sqrt{1 + 2\frac{K}{\gamma a}} \,, \tag{5.40}$$

$$\lambda_R = 2\pi a \,, \tag{5.41}$$

where λ_R is the critical wavelength for isotropic liquid fibers, known as Rayleigh capillary instability threshold. From Eq. (5.40), the net effect of Frank elasticity is to stabilize the fiber by splay-bend distortions in the rz-plane. In other words, the surface tilting mechanism, $\mathrm{M_T}$, acting through splay-bend modes due to $n_r(r,z)$ created on the rz-plane tends to stabilize the fiber by increasing the Frank distortion energy:

$$\mathrm{M_T}: \ \mathbf{n}_0^A = (0,0,1) \Longrightarrow \mathbf{n}^A = (n_r(r,z),0,1) \ . \tag{5.42}$$

Onion fibers

In the onion texture, axial (z-directional) periodic surface disturbances do not affect the azimuthal (θ-directional) director field because the fiber shape and the director field are uncoupled. Thus, the director field remains unchanged by changes in the geometry:

$$\mathbf{n}^O = \mathbf{n}_0^O = \mathbf{i}_\theta \, . \tag{5.43}$$

The Frank elasticity for the onion texture is pure bend and arises because the molecules bend azimuthally (see figure 5-2(b)), then the initial elastic distortion energy $\mathcal{F}_{d,i}$ is obtained as

$$\mathcal{F}_{d,i} = 2\pi \int_0^{\frac{2\pi}{k}} \int_{r_0}^{a} \frac{K}{2} (\nabla \times \mathbf{n})^2 r dr dz = \pi K \frac{2\pi}{k} \ln \frac{a}{r_0} \, , \tag{5.44}$$

where r_0 is the defect core radius [5]. Because of the existence of the defect core at the centre of the onion fiber (see figure 5-2(b)), the lower integration limit in the r-direction is r_0. It is known that the defect core radius r_0 is in the order of nanometers [5]. Although the director field remains unchanged during the fiber deformation, the elastic distortion energy $\mathcal{F}_{d,f}$ changes due to the fiber displacements and is obtained to order ξ_0^2:

$$\mathcal{F}_{d,f} = 2\pi \int_0^{\frac{2\pi}{k}} \int_{r_0}^{R(z)} \frac{K}{2} (\nabla \times \mathbf{n})^2 r dr dz = \pi K \frac{2\pi}{k} \left[\ln \frac{a}{r_0} - \frac{\xi_0^2}{2a^2} \right] . \tag{5.45}$$

The distortion free energy change Δ_d is given as

$$\Delta_d = -\pi^2 \xi_0^2 \frac{K}{a} \frac{1}{ka} \, . \tag{5.46}$$

From Eqs. (5.30) and (5.46), the net change in the total free energy Δ for the onion fiber is given by

$$\Delta = \pi^2 \xi_0^2 \frac{\gamma}{ka} \left[\left(k^2 a^2 - 1\right) - \frac{K}{a\gamma} \right] . \tag{5.47}$$

Using Eq. (5.39), the dimensionless critical wavenumber and the critical wavelength are found as

$$(ka)_c = \frac{2\pi a}{\lambda_c} = \sqrt{1 + \frac{K}{\gamma a}} , \qquad \lambda_c = \frac{\lambda_R}{\sqrt{1 + \frac{K}{\gamma a}}} . \tag{5.48}$$

From Eq. (5.48), it is found that the net effect of Frank elasticity is to destabilize the fiber by reducing azimuthal bend energy. In other words, the surface displacement mechanism, $\mathrm{M_D}$, acting on the azimuthal bend modes tends to destabilize the fiber by decreasing the Frank distortion energy:

$$\mathrm{M_D} \text{ for } \mathbf{n}^O = (0,1,0) = \text{constant} : \quad \int_V F_d\left(\mathbf{n}^O\right) dV \Longrightarrow \int_{V^*} F_d\left(\mathbf{n}^O\right) dV^* , \tag{5.49}$$

where V^* is the fiber volume with surface disturbances.

Radial fibers

Using Eqs. (5.11) and (5.12), the distorted director field of the initially radial texture can be written as

$$\mathbf{n}^R(r,z) = \mathbf{i}_r + n_z(r,z)\mathbf{i}_z , \tag{5.50}$$

where n_z is the slight bend distortion as a function of r and z. Substituting Eqs. (5.50) and (5.15) into Eq. (5.14) results in

$$\left(\nabla^2 \mathbf{n}\right)_z - n_z \left(\nabla^2 \mathbf{n}\right)_r = \frac{\partial^2 n_z}{\partial r^2} + \frac{1}{r}\frac{\partial n_z}{\partial r} + \frac{\partial^2 n_z}{\partial z^2} + \frac{n_z}{r^2} = 0 , \tag{5.51}$$

where $\left(\nabla^2 \mathbf{n}\right)_z$ is the z-component of the vector $\nabla^2 \mathbf{n}$. Since the second partial derivative of n_z with respect to z in Eq. (5.51) is much smaller than the other terms when estimating the order of magnitude, adopting the long wavelength approximation, i.e.,

$$\frac{\lambda}{a} \gg 1 , \tag{5.52}$$

enables us to solve a quasi-one dimensional ordinary differential equation:

$$\frac{\partial^2 n_z}{\partial r^2} + \frac{1}{r}\frac{\partial n_z}{\partial r} + \frac{n_z}{r^2} = 0\,. \tag{5.53}$$

By using boundary conditions that the director field is perpendicular to the fiber axis at the defect core and periodic and parallel to the unit normal at the surface, the bend distortion is found to be

$$n_z(r,z) = \xi_0 k \sin[kz] \frac{\sin\left[\ln\frac{r}{r_0}\right]}{\sin\left[\ln\frac{a}{r_0}\right]}\,. \tag{5.54}$$

Thus, the distorted director field for the radial texture is

$$\mathbf{n}^R(r,z) = \mathbf{i}_r + \xi_0 k \sin[kz] \frac{\sin\left[\ln\frac{r}{r_0}\right]}{\sin\left[\ln\frac{a}{r_0}\right]}\mathbf{i}_z\,. \tag{5.55}$$

Therefore, in the long wavelength approximation, bend distortions on the rz-plane are taken into account. The Frank elasticity for the initially radial texture is pure splay and arises because the molecules splay radially (see figure 5-2(c)), then the initial elastic distortion energy $\mathcal{F}_{d,i}$ is obtained as

$$\mathcal{F}_{d,i} = 2\pi \int_0^{\frac{2\pi}{k}} \int_{r_0}^{a} \frac{K}{2}(\nabla\cdot\mathbf{n})^2 r dr dz = \pi K \frac{2\pi}{k} \ln\left(\frac{a}{r_0}\right)\,. \tag{5.56}$$

It is also noticed that the lower integration limit in the r-direction is r_0 because of the existence of the defect core at the centre of the radial fiber. Using Eq. (5.55), the elastic distortion free energy $\mathcal{F}_{d,f}$ is obtained for the deformed fiber to order ξ_0^2:

$$\begin{aligned}
\mathcal{F}_{d,f} &= 2\pi \int_0^{\frac{2\pi}{k}} \int_{r_0}^{R(z)} \frac{K}{2}\left[(\nabla\cdot\mathbf{n})^2 + (\nabla\times\mathbf{n})^2\right] r dr dz \\
&= \pi K \frac{2\pi}{k}\left[\ln\frac{a}{r_0} - \frac{\xi_0^2}{2a^2} + \frac{1}{4}\xi_0^2 k^2 \left\{\frac{\ln\frac{a}{r_0}}{\sin^2\left[\ln\frac{a}{r_0}\right]} + \frac{\cos\left[\ln\frac{a}{r_0}\right]}{\sin\left[\ln\frac{a}{r_0}\right]}\right\}\right]\,.
\end{aligned} \tag{5.57}$$

The distortion free energy change Δ_d is given as

$$\Delta_d = \pi^2 \xi_0^2 \frac{K}{a}\frac{1}{ka}\left[-1 + \frac{1}{2}k^2a^2\left\{\frac{\ln\frac{a}{r_0}}{\sin^2\left[\ln\frac{a}{r_0}\right]} + \frac{\cos\left[\ln\frac{a}{r_0}\right]}{\sin\left[\ln\frac{a}{r_0}\right]}\right\}\right]\,. \tag{5.58}$$

From Eqs. (5.30) and (5.58), the net change in the total free energy Δ for the radial fiber is given by

$$\Delta = \pi^2 \xi_0^2 \frac{\gamma}{ka} \left[(k^2a^2 - 1) - \frac{K}{a\gamma} \left\{ 1 - \frac{1}{2} k^2 a^2 \left(\frac{\ln \frac{a}{r_0}}{\sin^2 \left[\ln \frac{a}{r_0} \right]} + \frac{\cos \left[\ln \frac{a}{r_0} \right]}{\sin \left[\ln \frac{a}{r_0} \right]} \right) \right\} \right] . \tag{5.59}$$

Using Eq. (5.39), the dimensionless critical wavenumber and the critical wavelength are found as

$$(ka)_c = \frac{2\pi a}{\lambda_c} = \sqrt{\frac{1+S}{1+B}}, \qquad \lambda_c = \lambda_R \sqrt{\frac{1+B}{1+S}}, \tag{5.60}$$

$$S = \frac{K}{a\gamma}, \qquad B = \frac{1}{2} \frac{K}{a\gamma} \left(\frac{\ln \frac{a}{r_0}}{\sin^2 \left[\ln \frac{a}{r_0} \right]} + \frac{\cos \left[\ln \frac{a}{r_0} \right]}{\sin \left[\ln \frac{a}{r_0} \right]} \right) . \tag{5.61}$$

From Eq. (5.60), the radial texture contains two competing elastic modes: the destabilizing splay Frank elasticity mode, S, causing a decrease in the critical wavelength and the stabilizing bend Frank elasticity mode, B, causing an increase in the critical wavelength.

Using Eq. (5.13), the splay elastic energy scales with $1/r^2$ and the surface displacement plays a role to redistribute the nematic LC away from the high energy core while the bend elasticity arises due to the director variation along the fiber axis driven by surface shape undulation and thus increases the Frank elastic energy by director distortions. In other words, the surface displacement mechanism, $\mathrm{M_D}$, acting on the splay modes on the $r\theta$-plane tends to destabilize the fiber by decreasing the Frank distortion energy:

$$\mathrm{M_D} \text{ for } \mathbf{n}^R = (1,0,0) = \text{constant} : \quad \int_V F_d \left(\mathbf{n}^R \right) dV \Longrightarrow \int_{V^*} F_d \left(\mathbf{n}^R \right) dV^* , \tag{5.62}$$

while the surface tilting mechanism, $\mathrm{M_T}$, acting through bend modes due to $n_z(r,z)$ created on the rz-plane tends to stabilize the fiber by increasing the Frank distortion energy:

$$\mathrm{M_T} : \quad \mathbf{n}_0^R = (1,0,0) \Longrightarrow \mathbf{n}^R = (1,0,n_z(r,z)) . \tag{5.63}$$

For micrometer-size fibers, we assume that $a = 10^{-5}m$ and $r_0 = 10^{-9}m$ [1]. Using these values, the splay mode S is approximately one hundred times smaller than the bend mode B so that the net effect of Frank elasticity on the capillary instability is to increase the critical wavelength

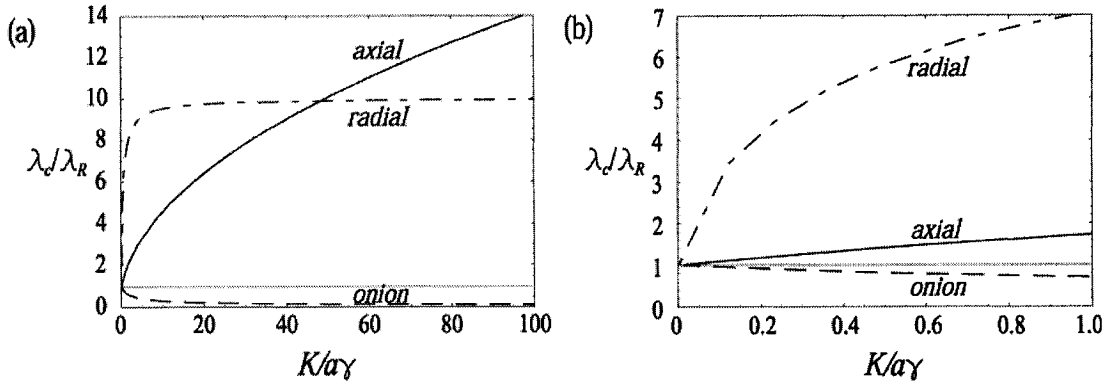

Figure 5-3: (a) Scaled critical wavelength $\frac{\lambda_c}{\lambda_R}$ as a function of the dimensionless energy ratio $\frac{K}{a\gamma}$; the dimensionless number $\frac{K}{a\gamma}$ is the ratio of the bulk elastic energy to the isotropic surface energy, for the three nematic textures. In both plots, the reference horizontal line corresponds to the Rayleigh instability threshold for isotropic materials. The symbol λ_R is the critical Rayleigh wavelength given in Eq. (5.41). Frank elasticity stabilizes the axial and radial fibers, but destabilizes the onion texture. (b) Same as (a) but $0 < \frac{K}{a\gamma} < 1$. For this parametric window, Frank elasticity has the strongest impact on stability of the radial texture.

above the Rayleigh threshold.

Figure 5-3 shows the scaled critical wavelength $\frac{\lambda_c}{\lambda_R}$ as a function of the dimensionless energy ratio $\frac{K}{a\gamma}$; the dimensionless number $\frac{K}{a\gamma}$ is the ratio of the bulk elastic energy to the isotropic surface energy, for the three nematic textures. In both plots, the reference horizontal line corresponds to the Rayleigh instability threshold for isotropic materials. Figure 5-3(a) shows the global features of the effect of texture on the instability. The axial and radial textures tend to stabilize the fiber while the onion texture tends to destabilize the fiber. Thus, the effect of the energy ratio $\frac{K}{a\gamma}$ on the instability is texture dependent. The strongest effect is for the axial texture, where no saturation is observed. This is due to the fact that the stabilizing surface tilting mechanism, M_T, increases monotonically. On the other hand, for the radial texture, as the energy ratio increases above a value of approximately ten, the stabilizing surface tilting mechanism, M_T, and destabilizing surface displacement mechanism, M_D, described above cancel each other, and the dimensionless critical threshold saturates at a value of 9.97. The threshold of the onion texture decreases to zero, since only the purely destabilizing surface displacement mechanism, M_D, is present. For nematic liquid crystals and micrometer-size fibers, it is expected

that $\frac{K}{a\gamma} \leq 1$. For typical low molecular-weight nematic LC fibers at temperatures sufficiently far from the smectic A transition (if any), using $\gamma = 10^{-2} Nm^{-1}$ [16], $K = 10^{-11} Jm^{-1}$ [17] and $a = 10^{-5} m$, we find $\frac{K}{a\gamma} = 10^{-4}$. Meanwhile, nematic liquid crystalline polymers can have elastic constants of orders of magnitude up to $10^{-8} Jm^{-1}$ [18]. For mesophase carbon pitches, elastic constants were estimated to be of the order of $10^{-8} Jm^{-1}$ [19]. In addition, near the nematic/smectic-A transition, the bend elastic constant diverges [5, 20]. Therefore, with $K = 10^{-8} Jm^{-1}$, the dimensionless parameter $\frac{K}{a\gamma}$ reaches up to one for micrometer-radius fibers, and hence Figure 5-3(b) focuses on the small $\frac{K}{a\gamma}$ regime. This figure shows that in this parametric window the strongest effect of Frank elasticity is on the stabilization of the radial texture.

5.4.2 Transient energy analysis

Figure 5-4 summarizes the complete phenomenology of the two Frank elasticity instability mechanisms in the transient energy analysis. The stabilizing surface tilting mechanism, $\mathrm{M_T}$, contributes to the distortion energy through the local time derivative and acts in the axial fiber by splay-bend modes and in the radial fiber by bend modes, respectively, created on the rz-plane. The destabilizing surface displacement mechanism, $\mathrm{M_D}$, contributes to the distortion energy through the convective change and acts in the onion fiber by constant-azimuthal bend modes and in the radial fiber by constant-radial splay modes, respectively, in the $r\theta$-plane.

We next present the transient integral energy balance equation for the nematic fiber, derive the instability criteria for the three representative nematic textures (see figure 5-2), and discuss in detail the physical and mathematical aspects of the process.

For the inviscid liquid fiber, the velocity field can be obtained by introducing the velocity potential and solving Laplace's equation of the velocity potential, which satisfies the continuity equation [2, 21, 22]:

$$v_r(r,z,t) = \xi_0 \alpha e^{\alpha t} \cos[kz] \frac{I_1[kr]}{I_1[ka]}, \qquad v_z(r,z,t) = -\xi_0 \alpha e^{\alpha t} \sin[kz] \frac{I_0[kr]}{I_1[ka]}. \tag{5.64}$$

Using this velocity field in Eq. (5.64), the rate of change of kinetic energy in Eq. (5.26) is

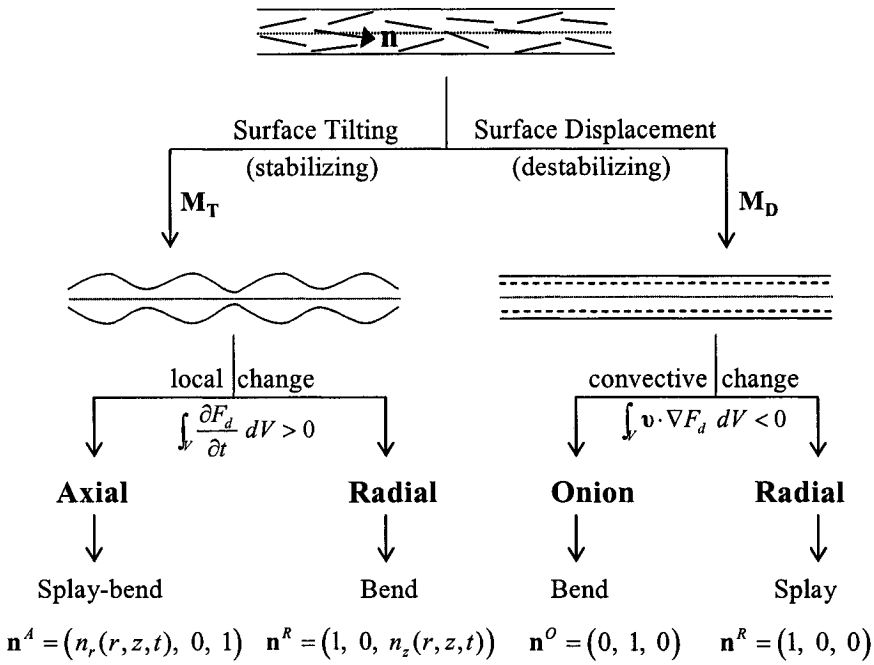

Figure 5-4: Frank elasticity instability mechanisms in the transient energy analysis. The stabilizing surface tilting mechanism, M_T, arises through the local time derivative and acts in the axial fiber by splay-bend modes and in the radial fiber by bend modes, respectively. The destabilizing surface displacement mechanism, M_D, arises through the convective change and acts in the onion fiber (constant azimuthal bend modes) and in the radial fiber (constant radial splay modes), respectively.

calculated in a unit wavelength $\lambda = \frac{2\pi}{k}$ to order ξ_0^2 as

$$\int_V \frac{\partial}{\partial t}\left(\frac{1}{2}\rho \boldsymbol{v}\cdot\boldsymbol{v}\right) dV = \xi_0^2 \alpha^3 e^{2\alpha t}\frac{2\pi^2\rho a}{k^2}\frac{I_0[ka]}{I_1[ka]}\,. \tag{5.65}$$

By assuming no surface shear, the surface integral term in Eq. (5.26) is rewritten as [6]

$$\int_A \mathbf{N}\cdot\mathbf{t}\cdot\boldsymbol{v}dA = \int_A (\nabla_s\cdot\mathbf{t}^{se})\cdot\boldsymbol{v}dA = \int_A -p_c v_r dA\,, \tag{5.66}$$

where $\mathbf{t}^{se}$ is the surface elastic stress tensor and p_c is the capillary pressure that is the magnitude of the surface normal force and is given using Eqs. (5.8) and (5.17):

$$-p_c = 2H\gamma = -\frac{\gamma}{a} + \frac{\gamma}{a^2}\left(1-k^2a^2\right)\xi_0 e^{\alpha t}\cos[kz]\,. \tag{5.67}$$

By substituting Eqs. (5.64) and (5.67) into Eq. (5.66), the surface integral term is obtained in a unit wavelength $\lambda = \frac{2\pi}{k}$ to order ξ_0^2 as

$$\int_A \mathbf{N}\cdot\mathbf{t}\cdot\boldsymbol{v}dA = \xi_0^2\alpha e^{2\alpha t}\frac{2\pi^2\gamma}{ka}\left(1-k^2a^2\right)\,. \tag{5.68}$$

Capillary instabilities in axial fibers

Referring to Eq. (5.35), the distorted director field in the transient analysis can be written by assuming an exponential change in time:

$$\mathbf{n}^A(r,z,t) = \mathbf{i}_z - \xi_0 k e^{\alpha t}\sin[kz]\frac{I_1[kr]}{I_1[ka]}\mathbf{i}_r\,. \tag{5.69}$$

It is noted that the flow driven by the capillary instability is so weak that the director field is not affected by the flow [5].

As expected from the previous section, the rate of change of Frank distortion energy, $\dot{F}_d$, is different in the three nematic textures. For the distorted axial texture, Eq. (5.69), the convective term in Eq. (5.25) is of higher order and drops out in the linear regime of the capillary instability

while the local time derivative term contributes to $\dot{F}_d$, which by using Eq. (5.24) is given by:

$$\dot{F}_d = K\left[\alpha\left(\frac{-\xi_0 k}{I_1[ka]}e^{\alpha t}\right)^2\left\{(\sin[kz]\,kI_0[kr])^2 + (\cos[kz]\,kI_1[kr])^2\right\}\right]. \tag{5.70}$$

Thus, using Eq. (5.70), Eq. (5.28) is obtained in a unit wavelength $\lambda = \frac{2\pi}{k}$ to order ξ_0^2:

$$\int_V \dot{F}_d dV = 2\pi^2 K\xi_0^2 k\alpha e^{2\alpha t} ka\frac{I_0[ka]}{I_1[ka]}. \tag{5.71}$$

Substituting Eqs. (5.65), (5.68), and (5.71) into Eq. (5.26) gives a quadratic equation for the dimensionless growth rate, $\alpha^* = \alpha\sqrt{\rho a^3/\gamma}$:

$$\alpha^{*2} - \frac{(ka)^2}{2}\left[1 - \left(2\frac{K}{a\gamma} + 1\right)(ka)^2\right] = 0, \tag{5.72}$$

where ka is the dimensionless wavenumber. Solving the quadratic equation for α^*, Eq. (5.72), we find

$$\alpha^* = (ka)\sqrt{\frac{1 - \left(2\frac{K}{a\gamma} + 1\right)(ka)^2}{2}}. \tag{5.73}$$

Thus, the axial fibers are unstable when the following inequality is satisfied:

$$1 - \left(2\frac{K}{a\gamma} + 1\right)(ka)^2 > 0. \tag{5.74}$$

The maximum growth rate $\alpha^*_{\max}$ and the corresponding wavenumber $ka_{\max}$ are obtained by solving Eq. (5.72):

$$ka_{\max} = \sqrt{\frac{1}{2\left(2\frac{K}{a\gamma} + 1\right)}}, \qquad \alpha^*_{\max} = \frac{1}{2}\sqrt{\frac{1}{2\left(2\frac{K}{a\gamma} + 1\right)}}, \tag{5.75}$$

which predict the axial fiber break-up into droplets with a characteristic size of $2\pi/ka_{\max}$ [23]. Eq. (5.75) properly reduces to the well-known results [21] when the bulk elastic anisotropy vanishes, i.e., $K = 0$, and the asymptotic results for the inviscid fiber are

$$\alpha^*_{\max} = \frac{1}{2\sqrt{2}}, \qquad ka_{\max} = \frac{1}{\sqrt{2}}. \tag{5.76}$$

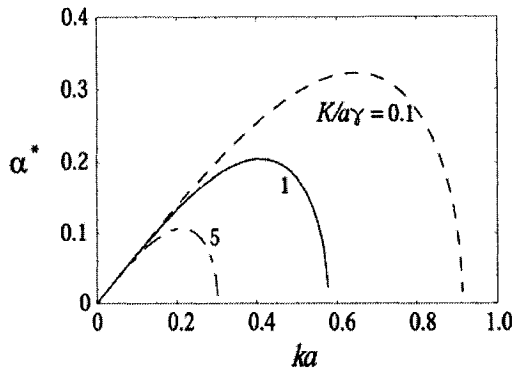

Figure 5-5: Dimensionless growth rate curves α^* as a function of the dimensionless wavenumber ka for $\frac{K}{a\gamma} = 0.1,\ 1,\ 5$ for the axial fiber. Frank elasticity decreases the growth rate and increases the wavelength of the fastest growing mode.

Solving Eq. (5.73) by setting $\alpha^* = 0$ gives the cutoff wavenumber:

$$ka_{\text{cutoff}} = \frac{1}{\sqrt{1 + 2\frac{K}{\gamma a}}}, \tag{5.77}$$

which is consistent with the critical wavenumber in the static energy analysis, Eq. (5.40).

Figure 5-5 shows the dimensionless growth rate curves α^* as a function of dimensionless wavenumber ka at $\frac{K}{a\gamma} = 0.1,\ 1,\ 5$ for the axial fiber. Not only ka_{cutoff} but α^*_{max} and ka_{max} decrease as $\frac{K}{a\gamma}$ increases, meaning that the bulk elasticity suppresses the axial fiber instability by increasing the length scale of the capillary instability as well as slowing down its growth rate.

Consistent with the static energy analysis, the effect of Frank distortion energy change $\dot{F}_d$ on the capillary instability for the transient energy analysis is now explained in detail (see figure 5-4). From Eq. (5.71), it is seen that the net effect of Frank elasticity is to stabilize the fiber by increasing splay-bend elastic energy. The distorted axial texture contributes to $\dot{F}_d$ only through the local time derivative term in Eq. (5.25). The stabilization mechanism $\mathrm{M_T}$ through splay-bend distortions in the rz-plane is generated by changes in the surface orientation, and hence no contribution arises from the convective term which is related to changes in surface displacement.

Capillary instabilities in onion fibers

For the onion texture, the director field remains constant and the local time derivative term in Eq. (5.25) is zero while the convective term contributes to the Frank distortion energy change $\dot{F}_d$. In order to simplify the calculation of $\dot{F}_d$, we adopt standard approximations for the velocity field used previously in the literature [22]. From Eq. (5.64), it is evident that v_z is only weakly dependent on r and is assumed to be only a function of z while v_r is approximated linearly dependent on r. These approximations are considerably accurate when $ka < 1$. Then, the velocity field for the inviscid liquid is given as [22]

$$v_r(r,z,t) = \xi_0 \alpha e^{\alpha t} \frac{r}{a} \cos[kz] \,, \qquad v_z(z,t) = -\xi_0 \alpha e^{\alpha t} \frac{2}{ka} \sin[kz] \,, \tag{5.78}$$

which satisfies the continuity equation. Using Eqs. (5.24) and (5.78), it is found that

$$\dot{F}_d = -K \frac{\xi_0 \alpha e^{\alpha t}}{a} \frac{\cos[kz]}{r^2} \,. \tag{5.79}$$

Thus, using Eq. (5.79), Eq. (5.28) is obtained in a unit wavelength $\lambda = \frac{2\pi}{k}$ to order ξ_0^2 by

$$\int_V \dot{F}_d dV = -2\pi^2 \xi_0^2 \alpha e^{2\alpha t} \frac{K}{a} \frac{1}{ka} \,. \tag{5.80}$$

Substituting Eqs. (5.65), (5.68), and (5.80) into Eq. (5.26) gives a quadratic equation for the dimensionless growth rate:

$$\alpha^{*2} - \frac{(ka)^2}{2} \left[1 + \frac{K}{a\gamma} - (ka)^2 \right] = 0 \,. \tag{5.81}$$

Solving the quadratic equation for α^*, Eq. (5.81), we find

$$\alpha^* = (ka) \sqrt{\frac{1 + \frac{K}{a\gamma} - (ka)^2}{2}} \,. \tag{5.82}$$

Thus, the onion fibers are unstable when the following inequality is satisfied:

$$1 + \frac{K}{a\gamma} - (ka)^2 > 0 \,. \tag{5.83}$$

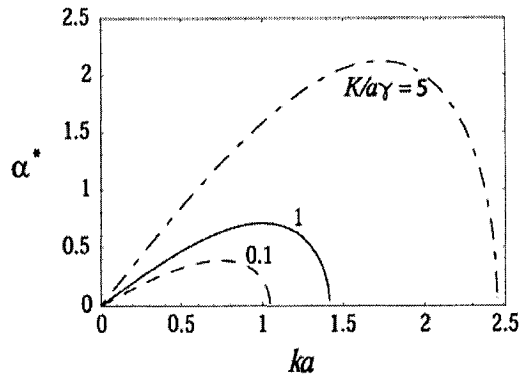

Figure 5-6: Dimensionless growth rate curves α^* as a function of the dimensionless wavenumber ka at $\frac{K}{a\gamma} = 0.1,\ 1,\ 5$ for the onion fiber. Frank elasticity increases the growth rate and decreases the wavelength of the fastest growing mode.

The maximum growth rate $\alpha^*_{\max}$ and the corresponding wavenumber $ka_{\max}$ are obtained by solving Eq. (5.81):

$$ka_{\max} = \sqrt{\frac{1+\frac{K}{a\gamma}}{2}}, \qquad \alpha^*_{\max} = \frac{1+\frac{K}{a\gamma}}{2\sqrt{2}}, \tag{5.84}$$

which predict the onion fiber break-up into droplets with a characteristic size of $2\pi/ka_{\max}$ [23]. Eq. (5.84) properly reduces to the well-known results, Eq. (5.76), when the bulk elastic anisotropy dependence vanishes, i.e., $K = 0$. Solving Eq. (5.82) by setting $\alpha^* = 0$ gives the cutoff wavenumber:

$$ka_{\text{cutoff}} = \sqrt{1+\frac{K}{\gamma a}}, \tag{5.85}$$

which is consistent with the critical wavenumber in the static energy analysis, Eq. (5.48).

Figure 5-6 shows the dimensionless growth rate curves α^* as a function of dimensionless wavenumber ka at $\frac{K}{a\gamma} = 0.1,\ 1,\ 5$ for the onion fiber. Not only ka_{cutoff} but $\alpha^*_{\max}$ and $ka_{\max}$ increase as $\frac{K}{a\gamma}$ increases, meaning that the bulk elasticity promotes the onion fiber instability by decreasing the length scale of the capillary instability as well as increasing its growth rate. From Eq. (5.80), it is seen that the net effect of Frank elasticity is to destabilize the fiber by decreasing the azimuthal bend Frank elastic energy. The surface displacement that leads to a decrease in the azimuthal bend energy contributes to $\dot{F}_d$ only through the convective term in Eq. (5.25). Under the destabilization mechanism $\mathrm{M_D}$, the destabilizing azimuthal bend modes

arise from changes in the location of the surface, and hence no contribution from local time derivatives appears. The local time derivative contribution is, as noted above (see figure 5-4), only ignited by couplings between surface orientation and the director field. Since the director is uncoupled from surface orientation, only positional effects promote the instability.

Capillary instabilities in radial fibers

Referring to Eq. (5.55), the distorted director field in the transient analysis can be written by assuming an exponential change in time:

$$\mathbf{n}^R(r,z,t) = \mathbf{i}_r + \xi_0 k e^{\alpha t} \sin[kz] \frac{\sin\left[\ln\frac{r}{r_0}\right]}{\sin\left[\ln\frac{a}{r_0}\right]} \mathbf{i}_z \,. \tag{5.86}$$

It is also noted that the flow driven by the capillary instability is so weak that the director field is not affected by the flow.

For the radial texture, Eq. (5.86), both the convective and the local time derivative terms in Eq. (5.25) remain and contribute to the Frank distortion energy change $\dot{F}_d$, which is given using Eqs. (5.24) and (5.78):

$$\dot{F}_d = K\left(-\alpha e^{\alpha t}\frac{\xi_0}{a}\cos[kz]\frac{1}{r^2} + \alpha e^{2\alpha t}\frac{\xi_0^2 k^2}{\sin^2\left[\ln\frac{a}{r_0}\right]}\sin^2[kz]\frac{\cos^2\left[\ln\frac{r}{r_0}\right]}{r^2}\right) . \tag{5.87}$$

Thus, using Eq. (5.87), Eq. (5.28) is obtained in a unit wavelength $\lambda = \frac{2\pi}{k}$ to order ξ_0^2 by

$$\int_V \dot{F}_d dV = -2\pi^2 \alpha e^{2\alpha t}\xi_0^2 \frac{K}{a}\frac{1}{ka}\left\{1 - k^2a^2\frac{1}{2}\left(\frac{\ln\frac{a}{r_0}}{\sin^2\left[\ln\frac{a}{r_0}\right]} + \frac{\cos\left[\ln\frac{a}{r_0}\right]}{\sin\left[\ln\frac{a}{r_0}\right]}\right)\right\} . \tag{5.88}$$

Substituting Eqs. (5.65), (5.68), and (5.88) into Eq. (5.26) gives a quadratic equation for the dimensionless growth rate:

$$\alpha^{*2} - \frac{(ka)^2}{2}\left[\left(1+\frac{K}{a\gamma}\right) - (ka)^2\left\{1 + \frac{1}{2}\frac{K}{a\gamma}\left(\frac{\ln\frac{a}{r_0}}{\sin^2\left[\ln\frac{a}{r_0}\right]} + \frac{\cos\left[\ln\frac{a}{r_0}\right]}{\sin\left[\ln\frac{a}{r_0}\right]}\right)\right\}\right] = 0 . \tag{5.89}$$

Solving the quadratic equation for α^*, Eq. (5.89), we find

$$\alpha^* = \frac{ka}{\sqrt{2}}\sqrt{\left(1+\frac{K}{a\gamma}\right) - (ka)^2\left\{1+\frac{1}{2}\frac{K}{a\gamma}\left(\frac{\ln\frac{a}{r_0}}{\sin^2\left[\ln\frac{a}{r_0}\right]}+\frac{\cos\left[\ln\frac{a}{r_0}\right]}{\sin\left[\ln\frac{a}{r_0}\right]}\right)\right\}}. \tag{5.90}$$

Thus, the radial fibers are unstable when the following inequality is satisfied:

$$\left(1+\frac{K}{a\gamma}\right) - (ka)^2\left\{1+\frac{1}{2}\frac{K}{a\gamma}\left(\frac{\ln\frac{a}{r_0}}{\sin^2\left[\ln\frac{a}{r_0}\right]}+\frac{\cos\left[\ln\frac{a}{r_0}\right]}{\sin\left[\ln\frac{a}{r_0}\right]}\right)\right\} > 0\,. \tag{5.91}$$

Meanwhile, Eq. (5.90) properly reduces to the well-known result of Rayleigh when the bulk elastic anisotropy dependence vanishes, i.e., $K = 0$:

$$\alpha^* = \frac{ka}{\sqrt{2}}\sqrt{1-(ka)^2}, \tag{5.92}$$

and thus Eq. (5.76) is also obtained for $K = 0$. Solving Eq. (5.90) by setting $\alpha^* = 0$ gives the cutoff wavenumber:

$$ka_{\text{cutoff}} = \sqrt{\frac{1+\frac{K}{a\gamma}}{1+\frac{1}{2}\frac{K}{a\gamma}\left(\frac{\ln\frac{a}{r_0}}{\sin^2\left[\ln\frac{a}{r_0}\right]}+\frac{\cos\left[\ln\frac{a}{r_0}\right]}{\sin\left[\ln\frac{a}{r_0}\right]}\right)}}, \tag{5.93}$$

which is consistent with the critical wavenumber in the static energy analysis, Eq. (5.60).

Figure 5-7 shows the dimensionless growth rate curves α^* as a function of dimensionless wavenumber ka , for $\frac{K}{a\gamma} = 0.323$, 1, 5 for the radial fiber. As $\frac{K}{a\gamma}$ increases, ka_{cutoff} and ka_{max} decrease while α^*_{max} decreases until $\frac{K}{a\gamma} \sim 1$ and then increases, meaning that the bulk elasticity contains two competing effects on the radial fiber instability: (i) the suppressing effect shown by increasing the length scales of the capillary instability and (ii) the non-monotonic maximum growth rate. Surface tilting on the radial fiber ignites stabilizing bend modes on the rz-plane. These bending distortions under the M_T mechanism increase the energy and are thus stabilizing. On the other hand, the initial splay distortion is destabilizing under the M_D mechanism and promotes the instability. The stabilizing bend modes are driven by the orientation of the fiber surface (surface tilting), while the destabilizing splay modes act through changes in the position of the surface (surface displacement). The destabilizing splay modes in the radial

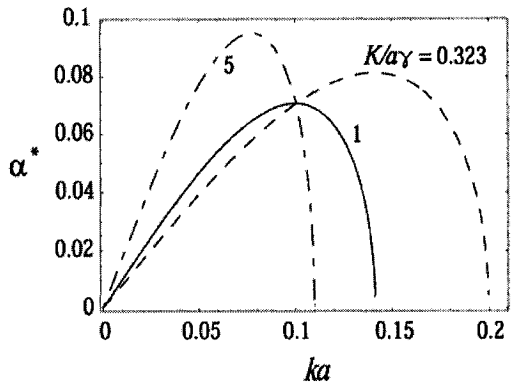

Figure 5-7: Dimensionless growth rate curves α^* as a function of the dimensionless wavenumber ka at $\frac{K}{a\gamma} = 0.323, 1, 5$ for the radial fiber. Frank elasticity increases the wavelength of the fastest growing mode. On the other hand, the maximum growth rate is non-monotonic, first decreases and then increases with increasing $\frac{K}{a\gamma}$.

textures are equivalent to the destabilizing azimuthal bend modes in the onion texture since they are controlled by the M_D mechanism (see figure 5-4). On the other hand, the stabilizing bend modes in the radial texture are equivalent to the stabilizing splay-bend modes in the axial texture since they are controlled by the M_T mechanism (see figure 5-4).

In partial summary, when splay and/or bend distortions are created by surface tilting they tend to stabilize the fiber by increasing the energy, and when splay and/or bend distortions are uncoupled from the surface orientation, the surface displacement may destabilize the fibers by decreasing the Frank distortion energy. In the transient integral energy analysis, surface tilting effects enter through local time derivatives (see Eq. (5.25)) while surface displacement effects through convective terms (see Eq. (5.25)).

5.4.3 Bulk elastic energy contributions to capillary instabilities

This section briefly compares the Frank distortion energy contribution for each texture in the static energy analysis to that in the transient energy analysis, with the objective of elucidating the dual nature of orientation gradients in growing peristaltic modes, as discussed in the previous section.

By making use of the divergence theorem and Eqs. (5.24) and (5.25), Eq. (5.28) is rewritten

as

$$\frac{d\mathcal{F}_d}{dt} = \int_V \frac{\partial F_d}{\partial (\nabla \mathbf{n})} : \frac{\partial (\nabla \mathbf{n})^{\mathrm{T}}}{\partial t} dV + \oint_S \mathbf{N} \cdot \boldsymbol{\upsilon} F_d dA \,. \tag{5.94}$$

In statics, the change of the distortion free energy corresponding to Eq. (5.94) can be expressed using the variational symbol δ:

$$\delta\mathcal{F}_d = \int_V \frac{\partial F_d}{\partial (\nabla \mathbf{n})} : \delta (\nabla \mathbf{n})^{\mathrm{T}} \, dV + \oint_S \mathbf{N} \cdot \delta \mathbf{s} F_d dA \,. \tag{5.95}$$

where $\delta\mathbf{s}$ is the variation of the position vector at the surface.

From Eqs. (5.94) and (5.95), it is clearly seen that in the linear regime considered here, the first integral represents the surface tilting contribution to the Frank distortion energy in the presence of director distortions while the second represents the surface displacement contribution. The difference between the static and the transient analyses comes from time dependence of the system. Without time dependence, the free energy change is obtained for the system before and after surface disturbances as shown in the statics results. In both statics and dynamics, the stabilizing $\mathrm{M_T}$ mechanism is included in the first integral while the destabilizing $\mathrm{M_D}$ mechanism in the second integral. The correspondence between the statics and dynamics is shown by the consistency between results in Eqs. (5.37), (5.46), and (5.58), and results in Eqs. (5.71), (5.80), and (5.88). In all textures, the static thresholds, shown in Eqs. (5.40), (5.48), and (5.60), are consistent with the corresponding cutoff results from the transient analysis, shown in Eqs. (5.77), (5.85), and (5.93). This consistency establishes the correctness of the two distinct approaches.

5.5 Conclusions

Capillary instabilities in nematic fibers reflect the anisotropic nature of liquid crystals. Classical theories of liquid crystalline materials are used to develop static and transient thermodynamic models of linear axisymmetric capillary instabilities driven by surface area reduction. Since the bulk gradient elasticity of nematics contains orientation gradient contributions that couple with surface distortions, the thermodynamic models on three representative nematic fiber textures identify the most likely effects. The axial texture tends to stabilize the fiber by increasing

splay-bend elastic energy created by the surface tilting mechanism. The onion texture tends to destabilize the fiber by decreasing azimuthal bend elastic energy created by the surface displacement mechanism. The peristaltic distortion in the radial texture creates two competing splay and bend elastic modes driven by surface displacement and surface tilting, respectively. By estimating the model parameters using published data for typical low molecular-weight nematic LC fibers, it is found that the net effect of Frank elasticity is to increase the length scales of the capillary instability in the radial fiber. The use of static and dynamic formulations gives mutually consistent results, and shows that the role of Frank elasticity in capillary instabilities is a function of the initial fiber texture. Splay and/or bend modes on the rz-plane stabilize the fiber by the surface tilting mechanism while splay and/or bend modes on the $r\theta$-plane destabilizes it by the surface displacement mechanism. Gradient elasticity offers another tool to control soft evolving surfaces.

Bibliography

[1] D. A. Edwards, H. Brenner, and D. T. Wasan, *Interfacial Transport Processes and Rheology* (Butterworths-Heinemann, Boston, 1989).

[2] V. G. Levich, *Physicochemical Hydrodynamics* (Prentice-Hall, Englewood Cliffs, 1962).

[3] C. Pozrikidis, *Introduction to Theoretical and Computational Fluid Dynamics*, (Oxford University Press, New York, 1997).

[4] A. D. Rey, *Ind. Eng. Chem. Res.* **36**, 1114 (1997).

[5] P. G. de Gennes and J. Prost, *The Physics of Liquid Crystals* (Oxford University Press, London, 1993).

[6] A.-G. Cheong, A. D. Rey, and P. T. Mather, Phys. Rev. E **64**, 041701 (2001).

[7] A.-G. Cheong and A. D. Rey, *J. Chem. Phys.* **117**, 5062 (2002).

[8] A.-G. Cheong and A. D. Rey, *Eur. Phys. J. E* **9**, 171 (2002).

[9] A. D. Rey, *Modelling Simul. Mater. Sci. Eng.* **7**, 147 (1999).

[10] P. E. Cladis, and M. Kleman, *J. Phys.* **33**, 591 (1972).

[11] R. B. Meyer, *Philos. Mag.* **27**, 405 (1973).

[12] C. Williams, P. Pieranski, and P. E. Cladis, *Phys. Rev. Lett.* **29**, 90 (1972).

[13] C. E. Williams, P. E. Cladis, and M. Kleman, *Mol. Cryst. Liq. Cryst.* **21**, 355 (1973).

[14] G. P. Crawford, M. Vilfan, and J. W. Doane, *Phys. Rev. A* **43**, 835 (1991).

[15] S. Chandrasekhar, *Liquid Crystals* (Cambridge University Press, Cambridge, 1992).

[16] A. A. Sonin, *The Surface Physics of Liquid Crystals* (Gordon and Breach Publishers, Amsterdam, 1995).

[17] M. Kreuzer and R. Eidenschink, in *Liquid Crystals in Complex Geometries*, edited by G. P. Crawford and S. Zumer (Taylor & Francis, London, 1996).

[18] T. De'neve, M. Kleman, and P. Navard, Liq. Cryst. **18**, 67 (1994).

[19] O. Fleurot and D. D. Edie, J. Rheol. **42**, 781 (1998).

[20] L. Cheung and R. B. Meyer, Phys. Lett. A **43**, 261 (1973).

[21] S. Middleman, *Modeling Axisymmetric Flows: Dynamics of Films, Jets, and Drops* (Academic Press, San Diego, 1995).

[22] J. N. Anno, *Mechanics of Liquid Jets* (Lexington Books, Toronto, 1977).

[23] A. D. Rey, J. Phys. II France **7**, 1001 (1997).

Chapter 6

Conclusions and Contributions to Original Knowledge

6.1 Conclusions

A demand to understand surface physics of nematic liquid crystals has been rapidly growing, due to its importance in many practical applications. Interfacial thermodynamics and transport phenomena of liquid crystals are an emerging area of research since not many liquid crystalline materials have been characterized. The most well-characterized liquid crystals are low-molecular-weight calamitic (rod-like) nematics such as 5CB, PAA, and MBBA. However, non-equilibrium surface phenomena are not well understood. In addition, force balance equations describing static and dynamical interfacial phenomena are available but have not been widely used to describe the mechanics of fiber and film microstructures. Therefore, this thesis explores the mechanics and stability of nematic liquid crystalline fibers. The motivation for this thesis is to create new knowledge and principles that conform to the restrictions of thermodynamics, and thus the parametric studies performed in the thesis are restricted by thermodynamics.

In this thesis, linear stability analysis of capillary instabilities in a nematic liquid crystalline fiber was performed by formulating and solving the governing nemato-capillary equations. The main parameters affecting the capillary instabilities are the isotropic and anisotropic surface tensions, the anisotropic viscosities, the bulk orientational elasticity, the isotropic viscosity of

the matrix, and the surface bending modulus.

6.1.1 Cahn-Hoffman capillarity vector thermodynamics for curved liquid crystal interfaces

The Cahn-Hoffman capillarity vector thermodynamics for curved anisotropic interfaces was adapted to liquid crystal interfaces. The thermodynamic formalism was derived and expressed in terms of nematic surface energies. The connection between interfacial rotational effects, surface tension anisotropy, and bending stresses is established. The thermodynamic formalism was used to derive the capillary pressure equation for liquid crystal interfaces that have three distinct contributions: (i) surface area reduction, (ii) surface area rotations, and (iii) director curvature. The classical Rayleigh instability in isotropic liquid fibers is of the peristaltic (axisymmetric) mode since the instability is only driven by the area reduction mechanism. For liquid crystalline fibers, chiral (non-axisymmetric) instabilities, which cause an increase in the surface area, may occur when driven by the area rotation and director curvature mechanisms. The chiral modes produce twisted microstructure and lead to novel structuring and patterning of liquid crystalline fibers. The capillarity vector formalism was shown to be a tractable and simple method to analyze capillarity processes in nematic liquid crystals.

6.1.2 Surface orientation effect on capillary instabilities in a thin nematic fiber

Capillary instabilities in the nematic fiber with the fixed director field along the fiber axis (axial texture) reflect the anisotropic nature of liquid crystals through the orientation contribution to the surface elasticity that gives rise to surface bending stresses. Surface gradients of bending stresses provide the orientation contribution to the capillary pressure that renormalize the classical displacement and curvature forces which exist in any liquid fibers. If the planar easy axis or weak homeotropic anchoring is imposed on the surface, the peristaltic mode is unstable and the classical fiber-to-drop transformation is predicted. If the anchoring energy strongly promotes homeotropic orientation at the surface, the surface orientation contribution due to the misalignment between the actual director and the easy axis becomes so large that the bending stresses can cause non-axisymmetric instabilities, and capillary instabilities with fibrillar phe-

nomena arise. Meanwhile, the suppressing effect of the fiber viscosity on capillary instabilities shifts the fastest growing wavenumber and its growth rate towards significantly smaller values for the bounded peristaltic mode, or decreases the growth rate for the unbounded (catastrophic) instabilities.

6.1.3 Viscous matrix effect on capillary instabilities in a thin nematic fiber

The effect of the viscous shear force at the fiber surface due to the viscous matrix on the capillary instability is characterized in terms of the fiber and matrix Ohnesorge numbers, which represent the ratio between viscous and interface forces in each phase, and the matrix-to-fiber viscosity ratio. The capillary instabilities are suppressed by increasing either the fiber or matrix Ohnesorge number, but estimated drop sizes after fiber break-up in the peristaltic instability substantially decrease with increasing matrix Ohnesorge number. For the peristaltic instability of the isotropic case, in a certain range of the fiber Ohnesorge number, the dependence of the wavenumber corresponding to the fastest growth rate on the viscosity ratio is in qualitative agreement with other computational models found in the literature for Newtonian fluids.

6.1.4 Surface ordering effect on capillary instabilities in a thin nematic fiber

When the surface elasticity of nematics contains both ordering and orientation contributions, the nematic ordering contribution allows for the existence of normal stresses while the nematic orientation contribution allows for the existence of bending stresses as well as normal stresses. Thus, surface gradients of normal and bending stresses provide additional anisotropic contributions to the capillary pressure of the nematic fiber, which renormalize the classical displacement and curvature forces that exist in any liquid fibers. In addition, when the interface curvature effects are taken into account, the higher order bending moment contribution to the surface stress is proved to be critical in stabilizing higher order non-axisymmetric fiber instabilities.

For the planar easy axis, if the nematic orientation is fixed along the fiber axis, capillary instabilities depend on the surface ordering contribution since the surface orientation contribution due to the misalignment between the actual director and the easy axis is so small that the bending stresses alone cannot cause non-axisymmetric instabilities. Low ordering fibers display the classical peristaltic (axisymmetric) mode since the area reduction mechanism is

dominant. Decreasing temperature for this axisymmetric mode gives rise to a local maximum or a monotonic increase of the characteristic length. Therefore, the characteristic size of drops formed after fiber break-up can be controlled by tuning temperature under small or moderate nematic ordering effects. In the presence of high surface ordering, chiral (non-axisymmetric) finite wavelength (bounded) instabilities emerge, with higher modes growing faster since the area dilation mechanism dominates: The surface ordering increases as temperature decreases, which results in decreasing the surface energy to meet the requirement of negative surface excess entropy, and the surface energy decreases with increasing the surface area in this instability regime. The pitches of the chiral microstructure become smaller with decreasing temperature. However, this chiral instability mechanism due to high surface ordering can be regulated by considering the surface bending moment which contains higher order variations in the interface curvatures. As temperature decreases, more and more chiral modes emerge but, at a constant temperature, there are only a finite number of unstable chiral modes among which a fastest growing mode exists.

6.1.5 Bulk gradient elasticity effect on capillary instabilities in a thick nematic fiber

Classical theories of liquid crystals were used to develop static and transient thermodynamic models of linear peristaltic capillary instabilities driven by surface area reduction: The strong anchoring condition is imposed on the fiber surface, and hence only the isotropic surface tension plays a role. The director variation in the bulk of the fiber is the origin of the elastic distortion energy that differs from one texture to another. Since the bulk distortion elasticity contains orientation gradient contributions that couple with surface deformations, the thermodynamic models on three representative nematic textures identify the most likely effects. The axial texture tends to stabilize the fiber by increasing splay-bend elastic energy created by the surface tilting mechanism. The onion texture tends to destabilize the fiber by decreasing azimuthal bend elastic energy created by the surface displacement mechanism. The radial texture exhibits a stabilizing surface-tilting-mechanism due to bend elastic modes and a destabilizing surface-displacement-mechanism due to splay elastic modes, but the former is predicted to be dominant. The use of static and dynamic formulations gives mutually consistent results, and shows that

the role of Frank distortion elasticity in capillary instabilities is a function of the initial fiber texture. Splay and/or bend modes on the axial plane stabilize the fiber by the surface tilting mechanism, whereas splay and/or bend modes on the cross-sectional plane destabilizes it by the surface displacement mechanism. Therefore, bulk gradient elasticity offers another tool to control soft evolving surfaces.

6.2 Contributions to Original Knowledge

1. A new capillarity vector thermodynamic formalism for anisotropic liquid crystal interfaces, which takes into account the essential elastic anisotropies, is developed.

2. Rigorous capillary pressure equations at liquid crystal interfaces are derived using the capillarity vector formalism.

3. Linear stability analysis of capillary instabilities in a nematic liquid crystalline fiber is performed by formulating and solving the governing nemato-capillary equations. The results are analyzed in terms of instability mechanisms/modes which are affected by the main parameters: the isotropic and anisotropic surface tensions, the anisotropic viscosities, the bulk orientational elasticity, the isotropic viscosity of the matrix, and the surface bending modulus.

4. All possible resulting morphologies and fiber surface patterns in capillary instabilities of nematic liquid crystalline fibers are characterized: drops, surface fibrillation, and helical or chiral fibers with twisted ripple patterns on the surface.

5. The predicted ability of capillary instabilities in nematic fibers to produce surface structures of well-defined symmetry and length scales, as well as chiral microstructures is an important result that augments the pathways for targeted pattern formation.